MTA Doktori Értekezés

Nagy porozitású szilárd gélek (aerogélek) szerkezete, fizikai-kémiai tulajdonságai és alkalmazásai

Kalmár József

Debreceni Egyetem

2025.

„Ez csak ürügy valami csalafintaságra ...”

Bastiano Coimbra de la Coronilla y Azevedo (Terence Hill)

Structure, physico-chemical properties and applications of high-porosity solid gels (aerogels)

József Kalmár

University of Debrecen

2025

TABLE OF CONTENTS

ABBREVIATIONS AND ACRONYMS

Abbreviation	Definition
ACS	American Chemical Society
APTMS	(3-aminopropyl)trimethoxy silane
ATR	attenuated total reflectance
BDP	beclomethasone dipropionate
BET	Brunauer-Emmett-Teller [theory]
BIPLED	bipolar gradients and longitudinal eddy current delay [NMR pulse sequence]
BJH	Barrett-Joyner-Halenda [theory]
BQ	benzoquinone
BS	borosilicate aerogel
BSA	bovine serum albumin
BSP	borosilicate-PVA hybrid aerogel
BSPH	borosilicate-PVA aerogel with added microcrystalline hydroxyapatite
CaAG	Ca-alginate aerogel
CAT-B	cathepsin B enzyme
CE	capillary electrophoresis
CONTIN	[CONTIN is a portable Fortran IV package for inverting noisy linear operator equations: S. W. Provencher, Comput. Phys. Commun. 27, 213–227 (1982).]
COSY	COrrelation SpectroscopY [2D NMR method]
CPMAS	cross-polarization magic angle spinning
CPMG	Carr-Purcell-Meiboom-Gill [NMR pulse sequence]
CPTMS	3-chloropropyl-trimethoxysilane
Cu-Clam-AG	Cu(II)-cyclam containing aerogel
Cu-Clen-AG	Cu(II)-cyclen containing aerogel
DDS	drug delivery system
DH	dihydroxybenzene
DLS	dynamic light scattering
DMA	dynamic mechanical analysis
DMEM-HAM’S	nutrient mixture of dulbecco's modified eagle's medium and Ham's F-12 [cell culture medium]
DNA	deoxyribonucleic acid
DSC	differential scanning calorimetry
EDC	1-ethyl-3-(3-dimethylaminopropyl) carbodiimide
EDC	1-ethyl-3-(3-dimethyl-aminopropyl) carbodiimide hydrochloride
EDS / EDX	energy dispersive X-ray spectroscopy
EPR	electron paramagnetic resonance spectroscopy
FBS	fetal bovine serum
FDA	US Food and Drug Administration
FITC	fluorescein isothiocyanate

FSGM	fluorescein-labeled silica-gelatin aerogel microparticles
FT-IR	Fourier-transformed infrared spectroscopy
G	α-L-guluronate
GEAR	[An efficient numerical method for solving stiff ordinary differential equation (ODE) systems.]
G-MTX	gelatin-methotrexate conjugate
GPTMS	3-glycidoxy-propyl-trimethoxysilane
HaCaT	human epidermal keratinocyte cell line
HAp	hydroxyapatite
HG	Na-alginates with high guluronic acid content (70:30 G/M ratio)
HL-60	[a long-term human acute promyelocytic leukemia cell line]
HPLC	high-performance liquid chromatography
HPMC	hydroxypropyl methylcellulose
HSQC	heteronuclear single quantum coherence [2D NMR technique]
I	“loaded with ibuprofen only”
IA	“loaded with ibuprofen and ascorbic acid”
IBU	ibuprofen
IC_{50}	half-maximal inhibitory concentration
IR	infrared
IUPAC	International Union of Pure and Applied Chemistry
KET	ketoprofen
LDLS	laser diffraction light scattering
LG	Na-alginates with low guluronic acid content (30/70 G/M ratio)
M	β-D-mannuronate
MAS	magic angle spinning [NMR spectroscopy]
MB	methylene blue
MeOH	methanol
MERA	multi-exponential relaxation analysis
MS	mass spectrometry
MTT	3-(4,5-dimethylthiazol-2-yl)-2,5-diphenyltetrazolium bromide
MTX	methotrexate
NBT	nitroblue tetrazolium
NL-DFT	non-local density functional theory
NMP	N-methylpyrrolidone
NMR	nuclear magnetic resonance [spectroscopy technique]
PA	polyamide
PAA	polyamide aerogel
PBS	phosphate-buffered saline solution
PGSTE	pulse gradient stimulated echo [NMR pulse sequence]
PGSTE	stimulated echo [NMR pulse sequence]
PTFE	polytetrafluoroethylene

PVA	polyvinyl alcohol
RF	radio frequency
RP-HPLC	reversed-phase high-performance liquid chromatography
SANS	small angle neutron scattering
SAXS	X-ray scattering
SCC	squamous cell carcinoma [cell line]
scCO_2	supercritical carbon-dioxide
SEM	scanning electron microscopy
SGM	silica-gelatin hybrid aerogel
SLD	scattering length densities
SOD	Superoxide Dismutase
ssNMR	solid-state nuclear magnetic resonance [spectroscopy technique]
TEM	transmission electron microscopy
TEOS	tetraethyl orthosilicate
TG	thermogravimetry
TMOS	tetramethyl orthosilicate
TOCSY	total correlation spectroscopy [2D NMR method]
TUHH	Technische Universität Hamburg
UD	University of Debrecen
USC	University of Santiago de Compostela
X-Ca-alg-X	X-Ca-alginate aerogels
XPS	X-ray photoelectron spectroscopy
XRD	X-ray powder diffraction
ZiTa	[A complex program package for reaction kinetics applications.]

I. INTRODUCTION

Nanostructured highly porous solids, such as xerogels and aerogels are in the focus of global research and development efforts in the last decades. Similarly to other nanostructured materials, the huge specific surface areas of such solid gels provide unique physico-chemical properties that are distinct from those of their bulk parent materials. Several methods are published in the literature for the fabrication of solvated gels including the gelation of polymers and macromolecules, as well as, the in-situ formation of three dimensional solvated networks. The nanostructured skeleton of such gels can be made of inorganic oxides, metals, carbon, biopolymers, synthetic polymers; either amorphous or crystalline. The conversion of solvated gels to dry solid gels is often simply termed "drying", which process has an additional impact on the architecture of the final solid skeleton. Intensive research is dedicated to the development of new functional porous solids for energy, biomedical, environmental and electrochemical applications with the promise of transformative innovations. In relation to the emergence of several new deep tech companies specializing in aerogels, the International Union of Pure and Applied Chemistry (IUPAC) listed "Aerogels" as one of the Top10 Emerging Technologies in Chemistry in 2022, ranking aerogels research competitive among such hot areas as "Sodium Batteries", "Solar Fuels" and "Nanozymes". In spite of the rapid development in the tailored fabrication of nanostructured solid gels, the mechanism based understanding of their interfacial physical and chemical features that determine their application related performance remains inadequately explored for driving potent innovations in the field. Therefore, our team at University of Debrecen (UD) defined such research aims that offer a niche direction for the European aerogels community. Specifically, we intend to contribute to the development of high performance functional solid gels for drug delivery, advanced catalysis and environmental technology, while simultaneously harnessing a molecular level mechanistic understanding on the physico-chemical processes that govern the advantageous features of the new gels in the targeted application. Our strong background in homogeneous phase reaction kinetics and mechanistic chemistry provides us the tools to tackle with such challenging experimental problems as following fast heterogeneous physico-chemical processes in suspensions with high time resolution, and giving the adequate mathematical description of these phenomena. In the past years, we adapted advanced techniques for the characterization of porous solids both in their dry and partially solvated states. We have established strong partnerships with excellent European research groups to utilize the state-of-the-art in the fabrication of advanced aerogels. This dissertation is the summary of our results achieved under my supervision between 2015 and 2025 in mechanistic based surface science and materials chemistry focusing on solid gels.

II. RESEARCH DIRECTIONS AND AIMS

My return to the University of Debrecen (UD) in 2014 was possible by agreeing to pursue a new research direction besides solution phase mechanistic chemistry, which was the core topic of my Ph.D. studies. This new research line was preferred to connect with materials science, as the foundations for the fabrication of nanostructured aerogels were already laid by the work of Prof. István Lázár and Prof. István Fábián. Thus, I decided to move into the research of functional porous solids with a focus on novel aerogels addressing commercial applications. However, I aimed to do so by introducing a rigorous new approach by developing an in-depth mechanistic understanding the physico-chemical phenomena governing the application related features of the new aerogels fabricated in our group. Our application oriented aim is to systematically design, prepare and benchmark novel functional aerogels as *i*) new stimuli responsive drug delivery systems, and *ii*) immobilized redox catalysts with enhanced activity. In line with these, we aim for delivering mechanistically precise models for *i*) the hydration induced structural changes of functional aerogels, *ii*) the sorption properties and the surface reactions of functional aerogels and *iii*) describing the intimate relationship between the key structural features and the application related properties of aerogels, as visualized in **Scheme 1**.

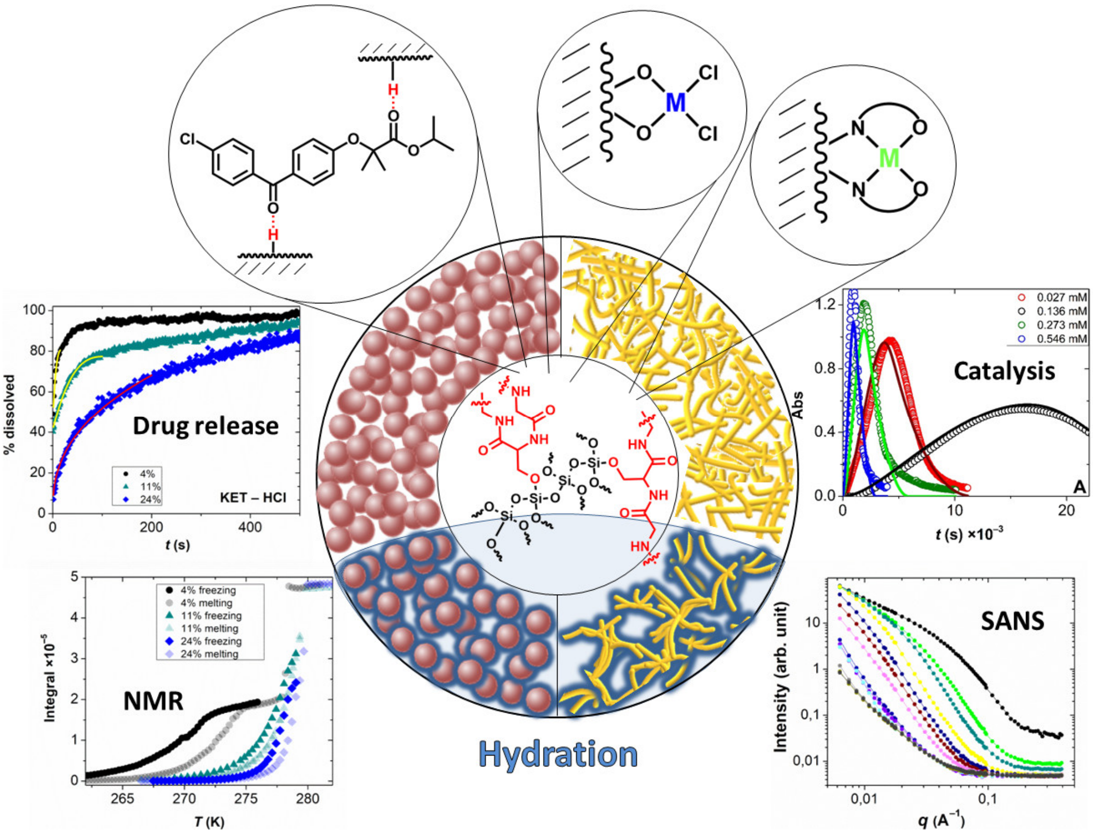

Scheme 1. The visual summary of our research approach. The design of the novel aerogels is fine-tuned in a concerted manner with developing an in-depth mechanism-based understanding of their hydration, sorption and surface chemical properties.

I developed these research lines in order to coherently increase our knowledge in the utilization, modification and state-of-the-art characterization of interfacial phenomena taking place on the solid skeletons of aerogels. The ultimate reason behind this approach is considering that understanding structure-property-function relationships in these systems will facilitate the systematic design and timely delivery of new functional aerogels, which in turn will facilitate their industrial translation. In order to achieve these aims I have integrated chemical, physical and engineering approaches in our research team. In this regard, I build on my research expertise in solution phase reaction kinetics, mechanistic chemistry, and coordination chemistry.

In this dissertation, I summarized what I believe to be our key findings in the interfacial chemistry of functional aerogels. The characterization and the benchmarking of our novel functional aerogels are discussed in a concerted manner with exploring the mechanisms of key physico-chemical processes that determine their performance. The results are collected in three major chapters in the ***Result and Discussion*** section of this thesis, as follows.

In the first chapter, the mechanistic aspects of hydration induced structural changes of selected polymer and silica-polymer hybrid aerogels are detailed together with the application related consequences. Our achievements in the incremental development of non-conventional characterization techniques, such as special solution phase, and solid state NMR methods, and small angle neutron scattering (SANS) of partially hydrated aerogels are also highlighted. The motivation is that most of the aerogels are utilized in aqueous media (e.g. for drug delivery, sorption, catalysis), and their hydration and wetting mechanisms are key factors setting the final gel architectures that in turn determine mass transport characteristics, accessibility of pores, release of impregnated molecules, kinetic cage effects.

The second chapter focuses on novel aerogels for drug delivery applications, including their characterization, in vitro biological benchmarking and mechanistic investigations. Details are given on the improvements we achieved with different alginate aerogels modified either in their chemical structure or surface properties. Our stepwise endeavor for the preparation and in vivo evaluation of methotrexate containing hybrid aerogel microparticles is also detailed.

The third chapter focuses on the features and mechanisms of selected sorption processes taking place on silica aerogels, and catalytic redox reactions taking place on metal-complex functionalized silica aerogels. High time-resolution kinetic experiments were designed and performed in these systems in order to gain a molecular level understanding of the processes involved. Detailed kinetic models are discussed in view of mathematical simulations. The key aspects of the increased reactivities of the immobilized metal complexes are highlighted.

III. LITERATURE REVIEW

III-1. Introduction to aerogels

III-1.1. Nanoscale structures of aerogels

Aerogels are a family of solid porous materials. [1] They can be regarded as a subtype of xerogels, but distinguished from the xerogels by the architecture of their solid skeletons. [1]The skeleton of an aerogel is nanostructured, which is the result of the manner of their fabrication. Generally, the smallest characteristic size of the main solid structural elements is in the range of 1–100 nm. Naturally, size is meaningless without defining the shape or more precisely the morphology of such structural elements. Aerogels show a very wide variety of architectural elements, depending on the chemical composition of the skeleton and its fabrication procedure. Typically, silica (SiO_2) based aerogels are built of spherical nanoparticles ($d_{\text{particle}} = 1 – 10$ nm) attached together like a pearl-necklace. Biopolymer aerogels (e.g. cellulose, Ca-alginate, chitosan, gelatin) most commonly constitute of fibrous skeletons, where the fibers can be branched, entangled and interconnected, usually in an isotropic manner. Synthetic polymer aerogels can be fabricated in a controlled way in various morphologies depending on the gelation procedure (**Fig. 1**). [2] The various nanoscale architectures still yield some common properties classifying aerogels. Their porosity is characteristically high (> 90%), their pore structure is open and interconnected, and the characteristic size of the pores is in the mesoporous range (2 – 50 nm), while some aerogels also display micropores or macropores.

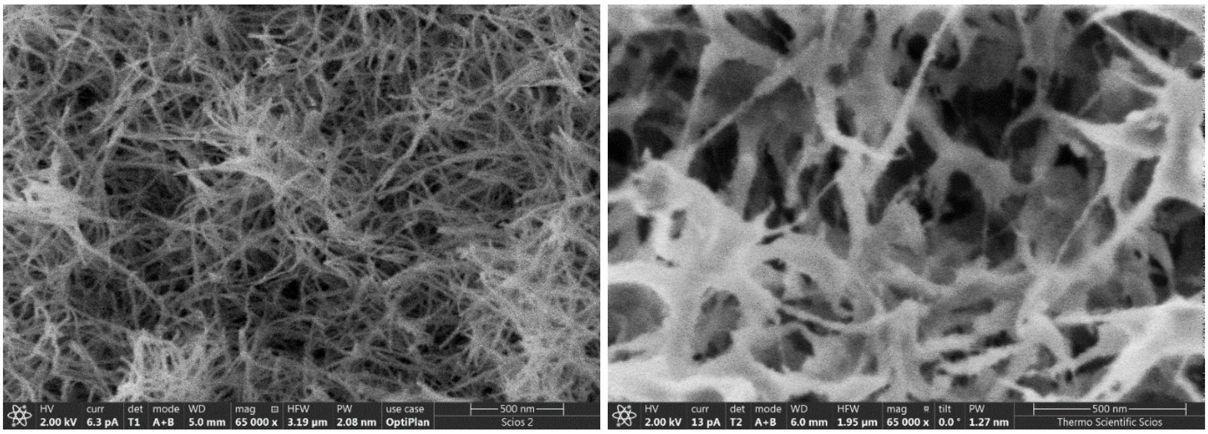

Figure 1. SEM images at 65k× magnification of a polyimide (left) and a polyamide aerogel (right). [3]

III-1.2. Fabrication of aerogels

From the fabrication point of view, aerogels are derived from solvated gels in which the liquid component is replaced by a gas without collapsing the three-dimensional solid skeleton of the parent gel. Thus, the fabrication of aerogels starts with constructing the gel network in a solvent, and the architecture of this gel network is intended to be preserved in the final aerogel.

The solvated gel can be constructed from already existing macromolecules. In this case, the homogeneous solution of the macromolecules is perturbed in a way that the macromolecules attach to each other in a loose but continuous isotropic network dispersed in the solvent. This process can be induced by changing the temperature, applying an antisolvent, dissolving ionic substances, acids, bases, or adding chemical agents that react with the macromolecules and cross-link them. Biopolymer gels are usually constructed this way, termed simply as “gelation”. The key aspect is finding the right conditions for the formation of phase separated open porous gel networks, and avoiding the precipitation of the macromolecules in a single dense bulk phase. For constructing e.g. inorganic oxide and synthetic polymer gels, chemical precursors are dissolved, chemically initiated, and the desired 3D network of the dispersed solid phase forms in their reaction. The directed linking of pre-synthesized dispersed nanoparticles has also been realized. [4,5] The molecular level mechanisms of both the gelation of macromolecules and the reactive formation of 3D networks from chemical precursors are heavily researched. [6,7] The reason is that understanding these mechanism gives control over them, enabling the fine tuning of both the chemical composition and the nanoscale architecture of the gels, resulting distinct final materials even from the same chemical composition. These processes generally involve the initial formation of nanosized but individually dispersed objects that later aggregate into a continuous 3D network. Thus they are generally termed as “sol-gel” processes (**Scheme 2**).

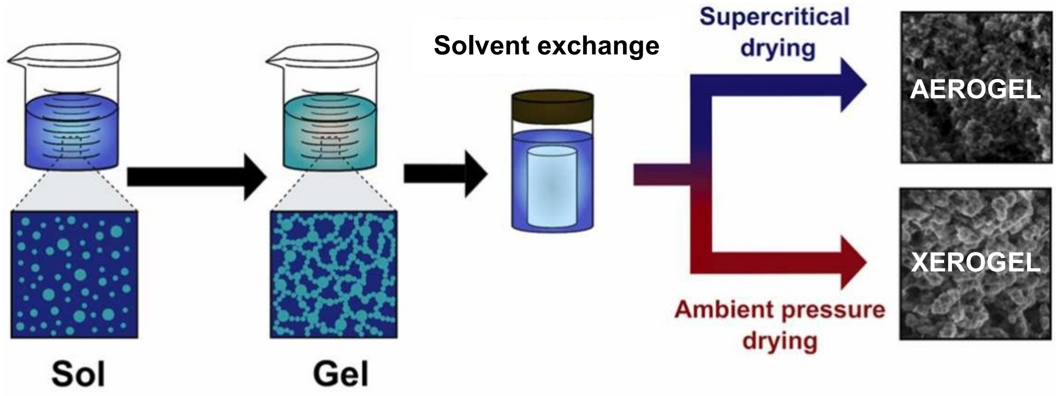

Scheme 2. The main steps of the preparation of aerogels and xerogels. [8]

The next step in the preparation of aerogels is the treatment of the solvated gels. This can involve chemical and physical modifications, including impregnation. When necessary, the mother liquid in which the gel was prepared is exchanged to another liquid. This procedure is termed as “solvent exchange”. The reason is either the further manipulation of the gel network, or it is the pre-requisite for the effective removal of the solvent in a way to best conserve the nanoscale architecture of the solvated gel. Importantly, when the solvent is exchanged, the solvated solid skeleton undergoes structural changes. The reason is that the mother liquid usually well-solvates the skeleton, whereas the new liquid not necessarily does. [9] This has a pronounced effect on the nanoscale architecture on the skeleton, and it is one of the main reasons for the difference between the architecture of the original gel and the final aerogel. In the case of dramatic changes in the nanoscale architecture, the gel macroscopically shrinks (or swells), which modifies its porosity and macroscopic rheological and mechanical properties. Additionally, the surface properties of the skeleton can change, because the conformation of the macromolecules (polymers) can be markedly different in different polarity solvents. If a given conformation is conserved during drying, it determines the surface properties, e.g. hydrophilicity of the final aerogel. It is a practical observation that the timeframe of the solvent exchange is also a key factor and a point in controlling the final architecture. If solvent exchange is stationary, similar control can be achieved by the gradient composition change of the liquid.

The final step in the preparation of aerogels is the controlled extraction of the liquid from the parent solvated gel in a way to preserve the architecture of its solid skeleton. Even the careful evaporation of the liquid leads to some damage because the strong capillary tension that develops during solvent evaporation collapses some of the nanosized pores. These products are generally termed xerogels (**Scheme 2**). The liquid in the gel can be transformed instead to its supercritical state and then gasified, but the needed high temperature and pressure makes this process unpractical and hazardous. A more feasible way of extraction utilizes that some organic solvents (most notably acetone, methanol and ethanol) are well miscible with CO_2 in a wide temperature and pressure range. These organic solvents can be extracted with liquid CO_2. When only pure liquid CO_2 remains in the gel pores, it can be transferred to its supercritical state (T_{critical} = 31 °C, p_{critical} = 74 bar). [10] A more effective process is transforming the organic solvent–CO_2 mixture into the supercritical state close to the critical point of CO_2. In this case, a continuous supercritical solvent extraction can be realized by pumping CO_2 through the system until the gel is free of the organic solvent. In both cases, the remaining supercritical CO_2 in the gel is gasified by depressurizing the system, avoiding the formation of a liquid phase. [11] The CO_2 assisted supercritical processes for the extraction of solvents are less expensive, greener and safer than other alternatives, therefore most of the experimental and commercial aerogels are produced this way. The skeleton architectures are generally well-conserved this way, which is also a driving force for using acetone, ethanol, or methanol as the final solvent in the parent gels. Nevertheless, both the choice of solvent and the exact conditions of its extraction have to be fine-tuned taking into account the chemical composition of the gel skeleton in order to achieve the desired final aerogel nanoscale architecture.

III-1.3. Structural characterization of aerogels

The purpose of the structural characterization of aerogels is to meticulously explore both the chemical composition and the nanoscale morphology of the given aerogel, and necessarily do so in multiple size scales. [12] In-depth material characterization is often a demanding and challenging experimental endeavor, yet it is pivotal to provide information for understanding the connection between structure and properties. One general objective of characterization is to explain the experimentally determined macroscopic features of aerogels. Another goal is to provide a basis for understanding the mechanisms of physical and chemical processes that determine the performance of the given nanostructured material in a specific application.

The chemical structure of dry as-prepared aerogels is most often explored by solid state nuclear magnetic resonance (NMR) spectroscopy. When necessary, the chemical intermediates of the fabrication process can be studied in the solution phase using NMR. The as-prepared aerogels can be studied by infrared (IR) and Raman spectroscopy methods. X-ray photoelectron spectroscopy (XPS) is often utilized to identify the different bonding states of the atoms in the skeleton. The elemental composition of an aerogel is usually mapped using energy dispersive X-ray spectroscopy (EDS), which is often an extra detector option in the scanning electron microscopy (SEM) instrument. When precise elemental composition is needed, the sample is solubilized using chemical digestion, and the resulting solution analyzed by atomic emission or absorption spectrometry methods. The crystalline states of the components in the aerogel are explored using powder state X-ray diffraction (XRD). The main challenge in the chemical characterization of aerogels is to distinguish among the components of composites and hybrids, as they usually produce convoluted and overlapping signals. It is also challenging to identify small scale chemical modifications, e.g. the formation of new bonds between the components.

The nanoscale imaging of the aerogels is realized by scanning and transmission electron microscopy methods (SEM and TEM, respectively). With special detector systems, these can reveal chemical information, as well, e.g. by detecting backscattered electrons in SEM. [3] Information on the nanoscale structural characteristics of aerogels can be obtained by measuring the adsorption-desorption isotherms of small sorbates, usually N_2, CO_2, Ar, H_2O under strictly controlled conditions. The challenge is the interpretation of these sorption data. The only more or less assumption-free theory for this purpose is based on non-local density functional theory (NL-DFT) calculations. [13] However this is possible only if the model function (kernel) of the solid surface of the aerogel skeleton is available. Kernel functions are widely available for metal oxide and carbon surfaces, but are scarce for polymers, especially for biopolymers. In such cases, the classical models such as the Brunauer-Emmett-Teller (BET) model and the Barrett-

Joyner-Halenda (BJH) model are accepted for estimating the structural parameters of the porous sorbents from the experimental sorption isotherms. Importantly, the restrictions and limitations of these classical models have to be observed when interpreting the experimental data. [14] The nanoscale architectures of aerogels are commonly studied by small angle X-ray and neutron scattering (SAXS and SANS, respectively) methods, which is discussed later in this thesis in a dedicated section. Non-conventional liquid phase NMR methods for exploring the interaction of small molecular liquids with aerogel surfaces are also discussed later in a dedicated section.

The macroscopic material characteristics of aerogels as envelope density, compressive strength, tensile strength are measured using the same classical techniques as for bulk materials. Skeletal density is usually measured using helium gas pycnometry. Phase transitions, chemical decomposition and other thermal processes are characterized by thermogravimetry (TG) and differential scanning calorimetry (DSC) methods. Dynamic mechanical analysis (DMA) is a valuable tool for detecting the change of the mechanical properties of aerogels as a function of temperature. The precise characterization of the acoustic properties, the thermal conductivity and the electric conductivity of aerogels require the modification of conventional instrumental hardware, setup and data evaluation. The reason is that these properties of the aerogels are drastically different from those of the bulk materials and foams that directed the design and evolution of the measurement instrumental hardware and software. The details of good practice for these measurements regarding aerogels are given in dedicated publications. [15-17]

The colloidal properties of suspended aerogel particles are characterized by the classical methods of colloid chemistry, including laser diffraction light scattering (LDLS), dynamic light scattering (DLS) and combined electrophoretic mobility measurements. [18,19]

III-1.4. Unique properties and applications of aerogels

Aerogels in general have extremely low envelop density (0.02–0.20 g/cm^3), high porosity (90–99%), and a large specific surface area (400–1300 m^2/g). [20] The combination of these properties makes aerogels a unique family of materials that are versatile in many modern applications. Naturally, the specific physico-chemical properties of aerogels that determine their application specific performance is dually determined by their chemical composition and the nanoscale architecture of their solid backbones. The desired chemical composition evidently limits the available fabrication strategies together with the available morphological designs, but careful control in these yield distinctly different material properties for aerogels of identical chemical composition. [21] The most common types of aerogels are inorganic oxide aerogels (e.g., silica, titania, alumina) [22], carbon aerogels [23], metal aerogels (e.g. gold, silver, platinum) [24], biopolymer aerogels (e.g. cellulose, alginate, chitosan, pectin, lignin, gelatin, whey protein) [25], and synthetic polymer aerogels (e.g. polyurea, polyurethane, polyimide, resorcinol-formaldehyde, polyamide) [26-28]. Special attention is dedicated to the research of multi-component aerogels, where the skeleton forming polymeric components interpenetrate in the skeleton in the molecular level and join by chemical bonding, which results in the macroscopic reinforcement of the mechanical properties. [29]

Today, the only industrial scale application of aerogels is in advanced thermal insulation solutions. Commercial aerogel "superinsulation" panels are available for insulating *i*) piping in the chemical and oil industries (**Scheme 3**), *ii*) buildings, and *iii*) electric vehicle battery packs. The two globally leading aerogel producers both in production capacity and in capital are Aspen Aerogels (USA) and IBIH Aerogel (PRC). [30] Future applications under research are drug delivery devices [31,32], tissue engineering scaffolds [33], environmental separation devices [34], various catalysts [35], and high performance electrode materials [36]. Recently introduced novel applications are as stretchable electronics [37], thermal energy storage [38], and solar water harvesting [39]. Following the global trends, a growing emphasis is put on the sustainable production of aerogels [40,41], and on additive manufacturing methods as 3D printing and direct-ink writing [42]. Despite the significant advances, there are still remaining challenges for the further industrialization of specialty aerogels. The most pressing are high production costs, limited scalability, mechanical fragility, and poor durability under long-term stress.

Thanks to Prof. Ioannis Michaloudis' creativity, dedication and expertise, aerogel-based sculptures, art installations and fashion items are now globally renowned and awarded. [43,44]

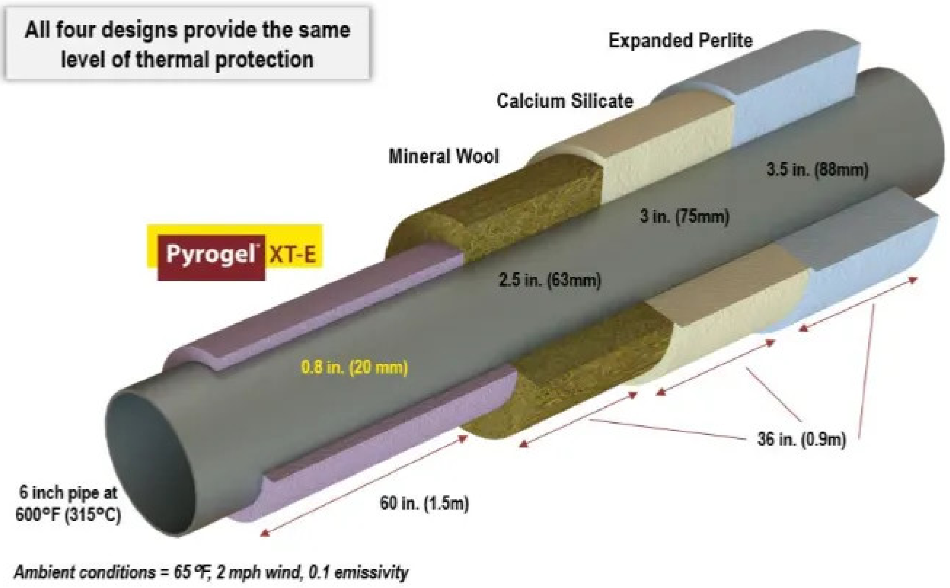

Scheme 3. Comparison of thermal insulation designs for an industrial pipe of 315 °C. Pyrogel® is a commercially available aerogel product of Aspen Aerogels (source: Aspen Aerogels).

III-2. Aerogels in drug delivery

There are only a handful of studies published in the literature that report the molecular-level investigation of the physico-chemical factors that govern the drug delivery properties of advanced porous materials. [45-50] Very few of the published studies deal with the physico-chemical investigation of the drug delivery features of mesoporous aerogels. [32,51] A variety of novel mesoporous inorganic and biopolymer (polysaccharide and protein) aerogels have recently been prepared only in the last decade. [52-57] Aerogels dried under supercritical conditions are promising platforms for oral and pulmonary drug delivery applications. [58-60] Novel administration routes and other biomedical applications are also intensively investigated. [25,32,61-64] Biocompatible aerogels are emerging vessels for musculoskeletal drug delivery. [65] Biopolymers and composite systems are now intensively investigated for oral, transdermal (wound treatment) and nasal delivery. [58,59,66,67] Inorganic-biopolymer hybrid aerogels have been synthesized for targeting local delivery and tissue engineering. [33,68]

III-2.1. Aerogels as advanced drug delivery systems for oral and local administration

Aerogel carriers with high specific surface area and open mesopores are promising drug solubilizing aids because nonpolar active ingredients can easily be deposited (e.g. during their preparation, or from supercritical CO_2) in the pores of these carriers in amorphous forms. [32,51,61] Subsequent release of the physically deposited amorphous drug can be burst-like, which can lead to an exceptional increase in bioavailability compared to microcrystalline drugs. This has high valorization potential for orally administered high potent agents (e.g. Pazopanib). [69] Retarded drug release can be achieved by hydrogel-forming (e.g. biopolymer) carriers that could be useful in wound treatment, locally administering antibiotics (e.g. Vancomycin). [70] Biopolymers (chitosan, hyaluronic acid, casein, gelatin) hybridized with silica offer the control of hydration and matrix erosion. Another factor is the highly pH dependent hydration and swelling of the selected biopolymers. [71,72] Furthermore, $–NH_2$ and –COOH groups can relatively easily be grafted into the inorganic component of the hybrid aerogel that can form specific interactions (e.g. H-bonding, Coulomb interaction) with active ingredients. Finally the morphology determine the permeability of the porous system and consequently the transport of the dissolved active ingredient. The combination of these effects are ultimately utilized to control the rate and kinetics of drug release from the carriers. These unexploited properties were targeted by our group for developing aerogel-based stimuli responsive drug delivery systems.

In order to optimize the functionality of an aerogel based drug delivery system, it is necessary to develop feasible strategies for fine-tuning its release properties. One possibility is to modify the surface of the carrier and tune its hydrophilicity and/or hydrophobicity, which directly sets the strength of interaction of the drug with the backbone of the aerogel. [32,33] Preparing core-shell or coated aerogel carriers has been proved to be a straightforward strategy to achieve retarded release in the case of otherwise rapid release aerogel systems. [64,73-75] Coating silica-alginate hybrid aerogel with hydroxypropyl methylcellulose (HPMC) and Ca(II)-alginate results in ca. 3-times slower drug release compared to the uncoated aerogel. [73] The coating of silica aerogel with Eudragit introduces pH control. Compared to the uncoated silica aerogel carrier, the rate of drug release from the coated aerogel is ca. 5-times slower in pH = 1.0 HCl solution, but it is intact in pH = 7.2 PBS. [64,75] Another strategy for the optimization of carrier functionality is to implement aerogels of hybrid inorganic-organic backbones. The physico-chemical properties of these hybrids, and thus, their release properties can easily be tuned by changing the ratio of their constituents. [59,68,74,76-78]

Our idea is that stimuli (pH or redox) responsive hydration and dissolution properties can be achieved by hybridizing biopolymers (e.g. chitosan, hyaluronic acid, gelatin, denatured DNA) with biocompatible inorganic oxides (silica) and introducing further functional groups ($–NH_2$, –COOH, –SH) to these hybrids using well-establish synthetic strategies. Inorganic-biopolymer hybrids have been synthesized targeting local delivery and tissue engineering. [33,68] Surface functionalized and composite aerogels are prepared for numerous applications for the biomedical and biotech fields. The combination of these strategies have not been explored in drug delivery and can lead to advanced, yet non-expensive controlled release devices. It is expected that both the hydration properties and the specific chemical interactions can be tuned in functionalized hybrid aerogels of controlled hydration properties leading to controlled release delivery systems with responsiveness towards pH and redox environment. Biopolymer and biocompatible macromolecule based hydrogels have successfully used for the development of pH responsive delivery systems. [71,79-81]

III-2.2. Adsorptive deposition of drugs in aerogels and consequences in drug release

It is well-established that aerogels due to their open mesopores can efficiently be impregnated with active ingredients by adsorptive precipitation (also termed as adsorptive deposition) using supercritical CO_2. This technique yields the highest possible loadings, and also ensures that the active ingredients condense in their amorphous forms inside the porous carrier matrices. [82-85] Adsorptive precipitation also ensures the homogeneous distribution of the active ingredients inside the porous matrices. The distribution of the drug is cooperatively dictated by the thermodynamics of the multilayer adsorption of the drug molecules on the inner pore walls, and the intimate conditions of the pressure-drop induced precipitation of the drugs from supercritical CO_2. [83,86,87] In general, the rate of the release of the amorphous active ingredient from the drug-impregnated carrier is significantly faster than the dissolution of the (micro)crystalline forms of the same drug. Furthermore, the total drug concentration is also elevated, because the solution is in quasi-equilibrium with the amorphous solid temporarily, as its recrystallization and precipitation is slow. Thus, this carrier strategy effectively enables fast drug dissolution and release, which ultimately leads to temporal concentration increase and thus, enhanced bioavailability. [62-64,83] As an example, high temporal concentration increase has been achieved with fat soluble vitamins when loaded into aerogels. [84,88]

The relative rates of the dissolution of the deopsited drug, its diffusion from the porous carrier and its final recrystallization from solution determine the maximum drug concentration and the timeframe of the temporal solubilization effect, i.e. the overall drug release profile. [89,90] When the relative rates of drug dissolution and release are significantly higher than its recrystallization, a dramatic and long lasting temporal concentration increase is achieved. This kinetic phenomenon is termed as the “spring effect” in the literature. A mathematical model was developed by Hirai et.al. to describe such uniques drug release profiles. [91]

III-2.3. Mechanism of drug release from aerogels

Understanding drug release mechanisms is important to tune the features of carriers and facilitate the design of new devices with advanced functionalities. General considerations can be formulated when the drug is physically deposited in aerogels, but such responsive systems where the active ingredient is chemically conjugated to the backbone have to be evaluated individually. When the drug is dispersed on the surface and inside the pores of aerogel particles, drug release can be divided into two main mechanistic steps. The first step is the dissolution of the drug, which is followed by its transport from the device to the dissolution medium. Both of these processes are governed by such physico-chemical factors that determine the limiting step in the mechanism, and eventually the rate of drug release. The most fundamental of these factors are the following. *i*) Hydration characteristics of the deposited drug and the carrier matrix, including erosion and swelling. *ii*) Specific interactions between the aerogel backbone and drug molecules. *iii*) Mass transport processes effective in the hydrated delivery device. These factors have profound effects on both drug dissolution and transport that should carefully be assessed in order to get a comprehensive idea on drug release mechanisms and kinetic profiles.

When the drug loaded aerogel particles get in contact with a body fluid, their hydration starts on the surface and penetrates into the pore network. Consequently, the deposited solid drug is also hydrated, which leads to its dissolution; first on the surface of the particles and afterwards inside the pores. The hydrophilicity of the drug and that of the aerogel carrier can significantly be different, taking into account that the solubility characteristics of the drug markedly depend on its crystallinity, as well. When the carrier is hydrated, the chemical conditions in the release medium (pH, temperature, ionic strength, presence of surfactants) have profound effects on the nature of specific interactions, via the change of the conformation, protonation state, effective charge of the drug molecule and the aerogel backbone. Strong interaction between the drug and the aerogel results in the establishment of dynamic adsorption-desorption equilibrium between hydrated and bound drug molecules. Importantly, effective mass transport is governed by the architecture of the wet device, which can be very different from that of the dry aerogel. As an approximate trend, those aerogels that extensively erode do not swell or collapse (e.g. silica, alumina, cross-linked biopolymers), and erosion is negligible in those aerogels that extensively swell or collapse in water (e.g. natural biopolymers).

Simple semi-realistic models can be utilized to describe cumulative drug release from aerogel carriers only such cases where specific interactions between the aerogel skeleton and the drug are negligible. In such particular situations where aerogel erosion, swelling or collapse are very well-defined, the drug release profiles can adequately be modelled. [92-94]

III-2.4. Metal ion crosslinked alginate aerogels

Alginate is an anionic biomacromolecule, the copolymer of β-D-mannuronate (M) and α-L-guluronate (G) single carbohydrate (monosaccharide) units, as depicted in **Scheme 4**.

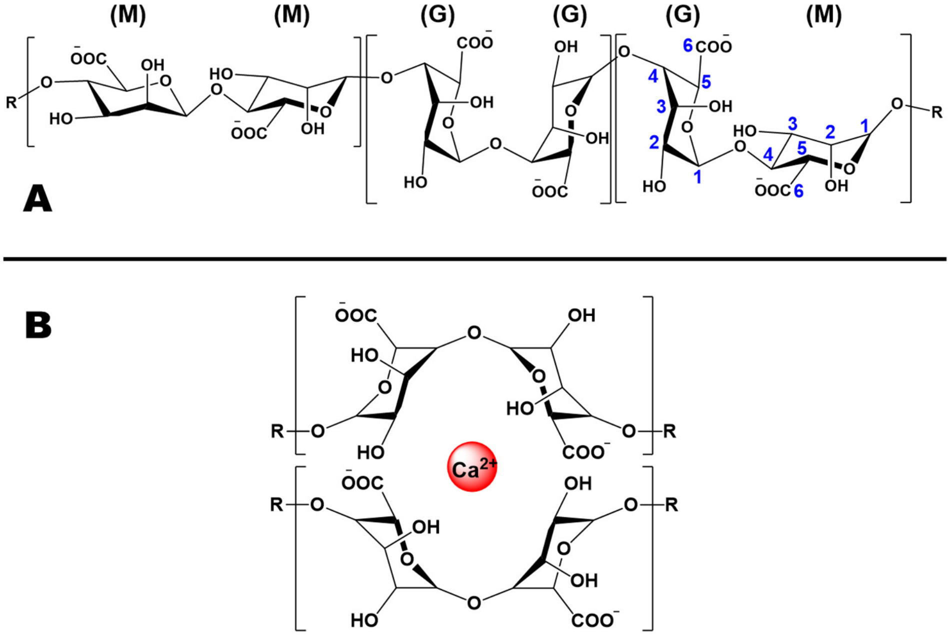

Scheme 4. Molecular structure of alginate (A), and the structure of the "eggbox" coordination pocket of the Ca^{2+} crosslinked alginate macromolecules (B). M = β-D-mannuronate, G = α-L-guluronate. [95]

The molar ration of the G and M units depends on source of the alginate, and can shows a large variation. Usually brown algae species are processed as biological (marine agricultural) sources of alginates, resulting in water soluble sodium alginate. The solubility of sodium alginate in neutral aqueous solutions is good, however the polyanions react with aqueous multivalent metal cations (typically Ca^{2+}, Cu^{2+}, Ni^{2+}, Co^{2+}, Fe^{3+}, Gd^{3+}) that ionotropically cross-link the macromolecules. Such metal ion crosslinked alginates result hydrogels even in low alginate concentrations. The coordination pocket of the metal ion that is responsible for the cross-linking of alginate molecules is usually described as an “egg-box” (**Scheme 4**). However, these metal ion crosslinked alginate gels readily dissolve in neutral or slightly acidic ($7 > pH > 4$) solutions where the concentration of the cross-linking metal ion is low. [96,97]

III-2.5. Bioconjugate aerogels as drug delivery systems

The application of biopolymers opens the way of conjugating active ingredients by covalent bonds and formulating bioconjugate aerogels. [98-100] Several drug delivery strategies have been developed for methotrexate, which is one of the most widely used agents in the treatment of some cancers and autoimmune diseases. [101,102] Biodegradable hydrophilic gelatin microspheres functionalized with MTX provide increased anti-tumor activity. [103-105] Prodrug approaches and covalent conjugation have also been extensively studied. It was shown that both strategies were suitable for selective delivery within tissues or cells. [106-110] Biodegradable MTX-gelatin conjugates were synthesized and studied by Narayani and Rao. They used 1-ethyl-3-(3-dimethylaminopropyl) carbodiimide (EDC) to covalently link MTX to the peptide side chains of gelatin. In the final formulation, hydrophilic microparticles were prepared from the conjugates. [104,111,112] Ofner et al. prepared novel gelatin-MTX conjugates that does not release the incorporated MTX under *in vitro* conditions, but a complex enzymatic response is necessary for effective delivery. [113-115]

Our idea was to prepare MTX-gelatin conjugates and hybridize them with silica for the fabrication of MTX functionalized silica-gelatin aerogel microparticles, as microparticles might be particularly useful in the treatment of diffuse or partially inoperable tumors as suspensions.

III-2.6. Biological experiments with aerogels

The biocompatibility and biodistribution of all new aerogels intended to be used as drug delivery systems have to be investigated in order to provide information on their health effects. [116] In addition, understanding the biodistribution of i.p. injected aerogel particles may facilitate the development of passively targeted delivery systems. Unfortunately, there are only a handful of studies reporting the in vitro biocompatibility of aerogels tested on different cell cultures, and the number of published in vivo studies is even lower. These mainly focus on the oral administration of drug-loaded aerogels, and aerogels for tissue regeneration. [117-120] Thus, one of our aims in full cooperation with Dr. Gábor Király and Prof. Gábor Szemán-Nagy working at the Department of Molecular Biotechnology and Microbiology at UD is to establish biological experimental strategies for benchmarking aerogels in living environments.

III-3. Interfacial processes in aerogels

Mechanism based understanding on the functionality of an advanced material demands the utilization of an array of state-of-the-art physico-chemical methods that are rarely accessible in one research group. [12] Consequently, very few reports are available in the literature for such approaches. [121-123] To the best of our knowledge, the combined use of liquid state NMR, solid state NMR and SANS methods have been introduced for the elucidation of hydration induced structural changes in aerogels at UD (**Scheme 5**). [124-129] High resolution (fast) kinetic methods are rarely utilized for studying heterogeneous sorption/desorption and redox reactions, which could be a bottleneck in connecting structure and functionality. The coordination mode of the metal ion in immobilized complexes are often overlooked when postulating mechanistic models for catalytic reactions. [130] The combination of kinetic experiments, structural studies and application related benchmarking could lead to the unprecedentedly deep understanding of the mechanisms of reactions on aerogel surfaces.

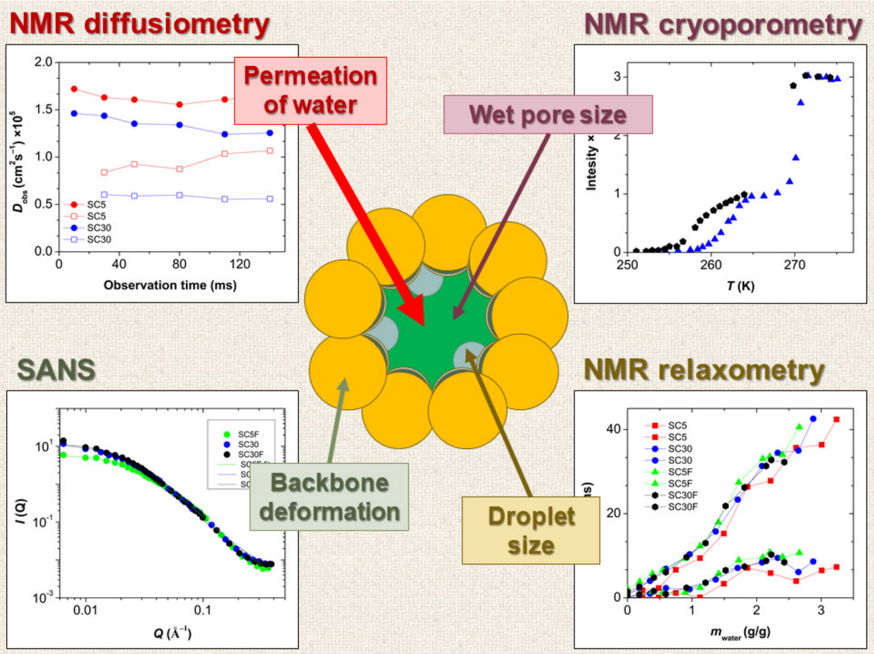

Scheme 5. Complementary information form non-conventional liquid state NMR and SANS methods for elucidating the hydration properties and consequent structural changes in hydrophilic aerogels. [125]

III-3.1. Nuclear magnetic resonance spectroscopy (NMR) methods for characterizing gels

Nuclear magnetic resonance (NMR) methods have been proven to be powerful tools for exploring the physical interactions of water molecules and other molecular liquids with the nanostructured skeletons of mesoporous materials. This is possible through the exchange of magnetization between water and the adjacent solid skeleton, the alteration of the translational (equilibrium) diffusion of water, and the alteration of the phase transition temperatures of water due to its nanostructuring in confinement in the porous material. These properties of water molecules can be measured by liquid state NMR relaxometry, diffusiometry and cryoporometry methods that are complemented by the solid state NMR measurements of partially hydrated samples providing information on the chemical structure and magnetization dynamics of the solid skeleton in interaction with water. [131-134]

III-3.1.1. NMR relaxometry of liquids confined in porous solids

The basic idea of the NMR relaxometric investigation of hydrated porous solids is, that the spin-lattice (T_1) and spin-spin (T_2) relaxation times of the protons in the water molecules hydrating the solid backbone fundamentally depend on their localization and chemical environment in the sample. [135-139] Water molecules that are strongly bound to the solid backbone (e.g. in the primary hydration sphere) relax significantly faster than water molecules which form (quasi-bulk) droplets or puddles and are not involved in direct interactions with the solid backbone. The simultaneous localization of water molecules in different spatially (magnetically) separated structural regions may yield different relaxation domains depending on the rate of chemical exchange between these regions. [140-142] If the exchange between the micro-environments is relatively slow on the timescale of the relaxometric experiments (ca. 1 ms), multiple relaxation domains are observed. [122] In contrast, only one relaxation domain is observed in the case of limiting fast exchange, even for water molecules located in different micro-environments in the hydrated porous solid.

The relaxation time characteristic for a single domain is the combination of the different relaxation times of the water protons located in the different micro-environments of the domain participating in the fast exchange of water among the micro-environments. The characteristic spin-spin relaxation time of a given domain (T_2) can be expressed by the following equation in the simplest case, when water in the bulk of a quasi-spherical droplet is in fast exchange with the adjacent hydration sphere ("non-freezing" water layer) of the backbone: [135-137]

$$\frac{1}{T_2} = \frac{V_\mathrm{S}}{V_0} \times \frac{1}{T_{2\mathrm{S}}} + \frac{V_\mathrm{L}}{V_0} \times \frac{1}{T_{2\mathrm{L}}} \qquad (1)$$

Here, V_0 is the total volume of water in the domain, V_S is the volume of water on the surface of the droplet that is part of the hydration sphere of the backbone, and V_L is the volume of water in the bulk of the droplet ($V_0 = V_S + V_L$). T_{2S} is the relaxation time of water in the hydration sphere ("non-freezing" water layer), T_{2L} is the relaxation time of bulk water and T_2 is the observed relaxation time of the domain. Usually, T_{2S} is significantly smaller than T_{2L}. In the case when the relaxation domain consists of a quasi-spherical water droplet in exchange with the adjacent hydration sphere of the backbone, the observed relaxation time (T_2) increases with the increasing water content of the domain (V_0) if the droplet size increases. When the size of the droplet increases, the ratio of bulk water (V_L) over surface water (V_S) also increases, which in turn results in the increase of the observed T_2 according to **eq. 1**.

This theory assumes the projection of the strong surface relaxation of primary "non-freezing" water layer into the quasi-bulk water in the pores via fast chemical exchange. It can be operational in the case of such porous solids, where the structure and the morphology of the pore wall does not change due to its hydration. This is the case in porous silicas, cements, shale minerals, etc. In these cases **eq. 1** can be re-formulated to include the filling factor (f) parameter, which shows how much of the available pore volume is filled with liquid water, where f=0 is empty, and f=1 is completely filled. [137,142,143].

$$\frac{1}{T_2} = \frac{1}{T_{2L}} + \lambda \frac{S_{\mathrm{pore}}}{V_{\mathrm{pore}}} \left(\frac{1}{T_{2S}} - \frac{1}{T_{2L}} \right) \frac{1}{f^k} \qquad (2)$$

Here, T_2 is the measured relaxation time in pore water, λ is approximately the thickness of the fast relaxing primary "non-freezing" water layer on the solid surface, T_{2S} is the relaxation time in this layer and T_{2L} is the relaxation time in bulk water. Parameter f is the fraction of the pore volume that is filled with water, S_{pore} is the total apparent surface area of the porous material and V_{pore} is its total pore volume. When the solid backbone is hydrophilic and wetted evenly, the k parameter is 1, but it is lower than 1 in the case of partially hydrophobic skeletons reflecting the uneven wetting [142,144]. When the amount of water is increased in the solid porous sample, the filling ratio of the pores is higher.

At higher filling ratios, multiple quasi-bulk regions (puddles) can form atop the primary "non-freezing" water layer, e.g. in the corners of concave pores. If these puddles are large, the exchange of water molecules between the quasi-bulk phase and the primary layer can be slow enough for the observation of multiple T_2 relaxation times. [121] Multiple relaxation domains can also be observed when water is localized in spatially (magnetically) separated spots in the porous matrix. An example is a mixed micro- and mesoporous matrix that has well separated micropores. However, the spatial separation of water is uncommon in highly hydrophilic open porous solids, because thermodynamics dictates the even wetting of the solid backbone controlled by the nanoscale morphology (curvature) of the walls. [145] In such cases, the above described simple, purely geometry-based theories are not valid. [140,141]

The T_2 relaxation times are measured using the Carr-Purcell-Meiboom-Gill (CPMG) sequence. The different relaxation domains yield individual exponential decay components (with different T_2 relaxation times) in the CPMG intensity decay. Thus, the first step of data evaluation is the deconvolution of the individual relaxation decays, which is usually done using the combination of invers Laplace transformation on non-linear model regression. The signal amplitudes of the individual exponential components of the experimental relaxation decays can convey additional information. The signal amplitudes can be quantitatively associated to the individual relaxation processes (i.e. the distinct relaxation domains) when chemical exchange among the domains is limiting slow. In this case, the signal amplitudes are independent from one another and directly proportional to the amount of water in the given domain. [136] This enables the direct quantification of the water contents of the different chemical environments (relaxation domains) as a function of the total water content of the sample, or filling factor.

III-3.1.2. NMR cryoporometry theory

The main information in NMR cryoporometry measurements is the melting and freezing point depressions of probe liquid droplets in nanoscale confinement inside the studied solvated porous solid. [133,146] This information can be translated to droplet size distribution, which is equivalent to pore size distribution when the liquid completely fills the pores. [147] In this case, the dominating shape of the pores is also reflected in the melting – freezing hysteresis curves.

The primary data in the NMR cryoporometry measurements are the relaxation filtered intensities of the liquid water (or other probe liquid) protons as a function of temperature. Most commonly, the CPMG spin-echo pulse sequence is applied to eliminate the broad ^{1}H signal of the solid phase during the echo time. The relaxation delay in the applied CPMG sequence is long enough to achieve the complete transversal relaxation of the water molecules in the frozen phase and those in strong interactions with the solid skeleton. [123,148,149] Consequently, only those molecules contribute to the ^{1}H NMR signal that are situated in quasi-bulk droplets and puddles confined by the nanoscale components of the solid backbone, because they have high enough T_2 relaxation times to pass the CPMG filter. [150,151] The objective is the detection of the shift of the phase transition temperatures of water confined in various geometries by the aerogel backbone by changing the temperature of the sample in small steps. [133,134] The sizes and the shapes of these water bodies, referred to as droplets and puddles can be reconstructed based on the measured shifts of the melting and freezing temperatures. The melting and freezing points of liquids confined in nanometer wide spaces are lowered, as given by the modified Gibbs-Thomson equations:

$$\Delta T_\mathrm{m} = T_\mathrm{m} - T_0 = -\frac{n_\mathrm{m} K_\mathrm{c}}{r_\mathrm{p}} \qquad (3)$$

$$\Delta T_\mathrm{f} = T_\mathrm{f} - T_0 = -\frac{n_\mathrm{f} K_\mathrm{c}}{r_\mathrm{p}} \qquad (4)$$

In **eq. 3**, ΔT_m is the melting point depression expressed as a difference between the phase transition temperature of the bulk (T_0) and the confined liquid (T_m). K_c is the cryoporometric constant, n_m is the geometric factor describing melting and r_p stands for the average pore radius. In **eq. 4**, the symbols denote the corresponding parameters for freezing. The values of ΔT_m and ΔT_f, and n_m and n_f are different, because melting and freezing of liquids in confined spaces show a hysteresis in general. [133,146,150] The hysteresis is due to the different mechanisms of the propagation of the phase change fronts in the nanostructure as function of temperature. Thus, depending on the starting point (molten or frozen sample), the structure of the sample is different at a given temperature. The exact differences are dictated by the geometrical features of the confining solid skeleton. These geometrical features are in turn reflected in the measured NMR intensity versus temperature data, termed as the melting-freezing hysteresis curve.

An important aspect of the cryoporometry experiments is that the forming ice crystals might deform the nanostructured skeleton. This is indicated by the distortion of the melting-freezing hysteresis loop in repeated subsequent measurement cycles. Data interpretation should be very careful if these signs are observed.

The size distribution of (water) droplets confined in aerogels is most often calculated using the methodology of Petrov and Furó. The measured water peak integrals are plotted against the temperature, and the intensity versus temperature data are transformed to intensity versus pore size data using the modified Gibbs-Thomson equations (**eqs. 3-4**). The numerical derivation of these yields pore size distribution plots. Importantly, “droplet shape / size”, is intentionally used instead of “pore shape / size” to indicate that the primary data determined by this method is the shape and the size of the water bodies that are confined by the solid skeleton. For instance, the primary fibrils of polymer aerogels passing through larger bodies of water can change the geometry of confinement, leading to the change of the shape of the melting-freezing hysteresis loop with the changing water content of the hydrated aerogel sample.

III-3.1.3. Pulse gradient stimulated echo (PGSTE) NMR diffusiometry theory

The observed self-diffusion (also termed as equilibrium diffusion) coefficient (D_{obs}) of a liquid is altered compared to its bulk phase value, when the liquid is confined in the pores of a nanostructured solid network. This apparent self-diffusion coefficient characteristic for the confinement significantly depends on the length of the observation time applied in the diffusion experiment (Δ). At limiting-short observation times, the molecules travel shorter distances than the size of the pores and do not collide with walls. In this case, the observed self-diffusion coefficient is equivalent to that of measured in the bulk phase. [152,153] At longer observation times, collisions with the walls reduce the effective distance covered by the molecules, and the apparent self-diffusion coefficient is lowered. In other words, the effective displacement of the water molecules in the tortuous network is a function of the observation time, and thus, affects D_{obs}. Therefore, information can be obtained on the confinement of the liquid, and on the permeability and morphology of the solid network by changing the observation time. [153-157]

Furthermore, the observed self-diffusion coefficient (D_{obs}) depends on the localization water and the morphology of the porous system at the given hydration level. The behavior of water molecules can be distinct at different hydration levels depending on the size, geometry and chemical environment of the different water bodies in partially hydrated aerogels. [152,157] It is possible that water is found in multiple diffusion domains (e.g. in the primary hydration sphere and in quasi-bulk phases) in the same nanostructured sample. If the exchange of water molecules among the different diffusion domains is slow in the timescale of the measurement, multiple self-diffusion coefficients are obtained for the same sample. [154-157] An important feature of the liquid phase NMR approaches is that the diffusiometry timescale is ca. 100 ms, which is much longer than that of the relaxometry experiments.

A stimulated echo sequence is used for measuring the diffusion features including bipolar gradient pulses, longitudinal eddy current delay and two spoiler gradients. Here, the single gradient pulses of the PGSTE sequence are split into a pair of two pulses with opposite signs enclosing a π pulse. The time between the two π pulses is the observation time of the diffusion experiment (Δ). In the PGSTE sequence, the sample magnetization is longitudinal, thus the T_1 decay is operative during most of the diffusion time, which eliminates most of the adverse effects arising from sample inhomogeneity. The total time the magnetization remains in transversal direction (T_2 decay) is twice the period between the first two π/2 pulses, which is approximately equivalent to the length of the gradient pulse (δ). The observation time of the diffusion experiments (Δ) is usually varied between 8 and 130 ms. The length of the gradient pulse (δ) is changed from 2 to 6 ms. The obtained NMR intensity decay data is evaluated using the general expression: [158,159]

$$I = I_0 \exp\{-D_{\mathrm{obs}}\gamma^2(\Delta - \delta/3)\delta^2 G^2\} \qquad (5)$$

The coefficient $D_{\mathrm{obs}}\gamma^2$ is calculated for each experiment by fitting the exponential curve of **eq. 5** to the measured echo intensity (I) as a function of G^2, and using the known parameters. The real self-diffusion coefficient (D_{obs}) is calculated after calibration, which is usually based on measuring the diffusion of D_2O in water by this method.

When multiple diffusion domains are present in the sample, each domain is represented by a different single-exponential function of a given D_{obs} according to **eq. 5**, and the observed decay is the sum of these functions. If the exchange of water is slow between these domains, the different D_{obs} values can be separated effectively. [152,156,157] In order to determine the number of diffusion domains, primary data can effectively be transformed by inverse Laplace transformation using the same algorithms as for the evaluation of NMR relaxometry data.

III-3.1.4. Magic angle spinning (MAS) solid state NMR spectroscopy of gels

Magic angle spinning solid state NMR spectroscopy methods provide effective tools to explore the structural changes of synthetic polymer an biopolymer aerogels upon hydration, mainly by following the ^{13}C and ^{1}H MAS NMR chemical shifts and linewidths as a function of the water content of the partially hydrated aerogel sample. Starting from the as-prepared dry sample, primary information is obtained on the chemical composition and molecular structure of the aerogel skeleton. The primary to quaternary structures of the macromolecules reflecting their conformation and crystallinity, and the state and extent of hydrogen bonding in the solid skeleton can be deduced by the careful assignment of the NMR peaks. When water is added to the aerogels, additional information can be obtained on the state and the localization of water molecules in the hydrated sample. [160-164] Importantly, the hydration of macromolecules (e.g. polysaccharides, polyamides) may cause significant changes in their conformations and crystalline states. Thus, the positioning and the chemical environment of the water molecules in interaction with the macromolecules can be deduced. In the case of higher water contents, the separation of macromolecules that were originally bound together in the dry state of the aerogel by intermolecular ionotropic or hydrogen bonds is well-expressed in the ^{13}C and ^{1}H MAS NMR spectra. [165] Cross-polarization magic angle spinning (CPMAS) experiments can reveal changes in the segmental motion of macromolecules as a consequence of their hydration.

In this case, the polarization transfer from the ^{1}H to the ^{13}C nuclei is less effective, which alters the NMR peaks proportionally to the increased mobility of that given segment.

III-3.2. Small angle neutron scattering (SANS) characterization of gels

The SANS measurements were performed at the Budapest Neutron Centre – BNC (part of HUN-REN Centre of Energy Research) in the Yellow Submarine pin-hole type instrument. A detailed description of this particular instrument design is given in Ref. [166]

Neutrons scattered coherently in elastic events in less than 10° are analyzed in SANS experiments. The size range where SANS can yield information on nanostructured sample is typically 1–100 nm. Any nanosized object, structural element, inhomogeneity, or discontinuity in the sample that display different neutron scattering length densities (SLDs) are regarded as different scattering objects. The primary difference in SLDs in dry mesoporous aerogels, i.e. the contrast, is between the solid backbone and the air filled pores. [150,167] In the case of composite and hybrid aerogels, the different components of the backbone can also give distinct contrasts, depending on the spatial separation of the components. Porous materials can be filled with liquids of different SLDs. In the case of composites and hybrids, this can be utilized to match the contrast of one of the components, which enables the measurement of the exclusive scattering of the other component. This “contrast variation” strategy is a powerful tool in SANS to explore the different components of complicated nanostructured system separately, which usually reveals extra levels of structural information. Care must be taken however in order to understand whether structural changes are taking place or not due to the solvation of the solid skeleton of the sample. Partially solvated samples can be conveniently studied by SANS in order to reveal nanoscale structural changes. However, when the porous sample is partially filled with the liquid, both the well-defined liquid droplets, and the solvated nanoscale structural elements of the skeleton can yield new scattering objects, which complicates data evaluation.

The measured and corrected scattered neutron intensity (*I*) in SANS is analyzed as a function of the momentum transfer (*Q*), which is the magnitude of the scattering vector.

$$Q = \frac{4\pi}{\lambda}\sin\frac{\theta}{2} \qquad (6)$$

Here, λ is the wavelength of the monochromatic neutron beam and Θ is the scattering angle. The absolute neutron scattering intensity (*I*) can be given as follows:

$$I(\lambda,\theta) = I_0(\lambda)\Delta\Omega\eta(\lambda)TV\frac{\mathrm{d}\Sigma}{\mathrm{d}\Omega}(Q) \qquad (7)$$

Here, I_0 is the incoming neutron flux, $\Delta\Omega$ is the unit solid angle, $\eta(\lambda)$ is the detector efficiency, T and V are the transmission and the volume of the sample, respectively, and $\mathrm{d}\Sigma/\mathrm{d}\Omega$ is the macroscopic differential cross section as a function of Q. The mathematical analysis of the differential cross section is a conventional way for extracting information on the nanoscale architecture of the studied sample. When measuring the scattering intensity on a relative scale, and dealing with correlation free scattering objects, the mathematical analysis usually focuses on the description of only one of the components of $\mathrm{d}\Sigma/\mathrm{d}\Omega$ termed as the form factor. This can effectively be performed by the direct mathematical analysis of the corrected $I(Q)$ curves using more or less sophisticated models to represent the nanoscale architecture of the sample. The classical assumption free and simple geometrical models are usually effective for aerogels.

The SANS scattering curves of aerogels can be modelled by the combination of Guinier and power-law approximations, generally referred to as the Beaucage model. This model can be used to describe the scattering from such nanostructured systems, where different structural levels appear in different size scales. [168,169] It can provide information on the size and the shape of scattering objects in the nanometers range, and describe the characteristics (fractal dimensions and roughness) of the main interfaces in the sample. The first level (**eq. 8**) or the second level (**eq. 9**) Beaucage models were used to cover the entire experimental Q range depending on the morphologies of the different aerogels.

$$I(Q) \cong G_1 \exp\left(-\frac{Q^2 R_{g1}^2}{3}\right) + B_1 \left\{\frac{\left[\mathrm{erf}\left(\frac{QR_{g1}^2}{\sqrt{6}}\right)\right]^3}{Q}\right\}^{p_1} + \mathrm{C} \tag{8}$$

$$I(\mathrm{Q}) \cong G_1 \exp\left(-\frac{Q^2 R_{g1}^2}{3}\right) + B_1 exp\left(-\frac{Q^2 R_{g2}^2}{3}\right)\left(\frac{\left[erf\left(\frac{QR_{g1}}{\sqrt{6}}\right)\right]^3}{Q}\right)^{p_1}$$

$$+ G_2 \exp\left(-\frac{Q^2 R_{g2}^2}{3}\right) + B_2 \left(\frac{\left[erf\left(\frac{QR_{g2}}{\sqrt{6}}\right)\right]^3}{Q}\right)^{p_2} + C \tag{9}$$

Several geometrical models (e.g. based on elongated cylinders) have been explored for fitting the SANS data for various aerogels with different morphological features. [170,171] In many cases adequate fitting could not be achieved with the conventional geometric models. [172] The approach of using multiple levels of the Beaucage or the Porod approximations is frequently found suitable to describe the series of SANS curves measured in a given system, thus enabling the direct comparison of the estimated structural parameters for the same set of gel samples, e.g. as function of their preparation conditions, pH or water contents.

The radius of gyration in SANS quantifies the distribution of scattering length densities (SLDs) of the scattering object around its SLD center of mass. Therefore, the radius of gyration is an important shape-independent parameter, which can be used both for solid and liquid state samples, if the Guinier approximation conditions are fulfilled ($Q \times R_g \leq 3$). In the case of mesoporous aerogels, when approximating the dominant pore geometry to be spherical; the mean pore size (d_{pore}) can be estimated from the R_g value as follows. [173]

$$d_{\text{pore}} = 2r_{\text{pore}} \cong 2\sqrt{\frac{5}{3}}R_g \qquad (10)$$

III-3.3. Sorption processes in hydrated silica aerogel particles

Sorption processes on suspended aerogel particles are usually fast, and thus their mechanisms are often only semi-quantitatively explored. The reason is that the evaluation of the experimental data on liquid phase sorption kinetics – either involving suspended particles or immobilized surfaces – often has to be simplified, because the process usually cannot be followed with sufficiently high time resolution, i.e. there are not enough data points in the time resolved experiments for a sophisticated evaluation. The main reason for the low time resolution is that the kinetic data are collected by off-line analysis in most cases. Measuring a data point by sampling and analyzing the system off-line takes at least 1 to 5 min, while fast sorption processes are usually complete in a few minutes. To overcome this problem and follow fast adsorption processes with high time resolution, specialized on-line analytical techniques such as quartz microbalance measurements, [174,175] laser optical spectrometry [176,177] and flow-cell spectrophotometry [178,179] have been implemented.

We aimed to adopt our experience in solution phase reaction kinetics and develop high-time resolution experimental methods for investigating the intimate mechanisms of the sorption of representative model compounds from aqueous solution on suspended silica aerogel microparticles. For these mechanistic studies, the molecular model compound of choice was methylene blue (MB), while bovine serum albumin (BSA) was chosen as a protein of interest.

The thermodynamic and UV-Vis spectroscopic features of MB adsorbed on silica surface are well characterized. [180-183] There is a consensus in the literature that MB forms a monolayer on silica when adsorbed from solutions of high micromolar concentrations at short contact times. The UV-Vis spectrum of adsorbed MB shows a blue shift at around 600 nm, which has been attributed to dimer formation on the surface. This hypothesis is based on a similar blue shift in the spectrum of solvated dimers. [184]

BSA is a soft protein, therefore its aqueous tertiary structure is significantly influenced by the pH of the solution. [185,186] This feature is fundamental in understanding its properties for binding to solid surfaces and transport. [187] The mechanisms of BSA sorption on various silica surfaces have been studied in the pH range between 3 and 9. [188-190] The protein starts to unfold only at pH values lower than 4 and higher than 9. BSA first forms protein islands on a silica surface, and finally completes the monolayer. Multilayer sorption and irreversible binding have also been observed. Protein sorption and binding on solid surfaces are a complex processes that are sensitive to the physico-chemical environment (temperature, pH, ionic strength, etc.), as well as, the chemical characteristics and the morphology of the sorbent. [189,191] Several authors have proposed a two-state model for the sorption of proteins on solid surfaces resulting in weaker (reversible) or stronger (irreversible) binding modes. [192-195] Turbidimetry and UV-vis measurements have been shown to be fundamental in quantifying the interactions of proteins with surfaces including sorption and aggregation. [178,196]

III-3.4. Metal complexes immobilized in aerogels showing enhanced catalytic activity

Mesoporous silica materials have high apparent surface areas, highly permeable pore networks and good mechanical and chemical stabilities that make them ideal catalyst supports. [35] An important aspect of utilizing porous catalyst supports is that the reactions take place in confinement inside the pores. Such confinement of the reactants can alter the frequency of the reactive collisions, which can affect the kinetics of the overall catalytic reactions. This could lead to the alteration of the specific activity or the selectivity of the immobilized catalyst compared to the dissolved counterpart. For instance, phenanthroline based dinuclear Cu(II) complexes immobilized in mesoporous silica have elevated catechol oxidase activity. [197] An imidazolato-bridged Cu(II)-Zn(II) complex is a functional model of the CuZnSOD enzyme, which shows elevated SOD activity in a silica support. [198] Generalized theories, such the “confinement effect”, also termed as the “nest effect” have been proposed to account for the enhanced reactivities. [199-201] We intend to explore the intimate role of mesoporous catalyst supports by performing the in depth characterization of selected functionalized aerogels, and propose a mechanistic model for their reactivities using the tools of reaction kinetics.

IV. EXPERIMENTAL METHODS

IV-1. Preparation of aerogels

IV-1.1. Materials and solutions: All raw chemicals for the preparation of the aerogels were purchased from quality assured commercial vendors, such as Sigma-Aldrich, Merck, Fluka and VWR in the highest available purity, typically above 99%. HPLC grade solvents were used for the synthesis procedures. Other common chemicals (acids, bases, inorganic salts, etc.) were purchased from the same vendors in ACS reagent grade, Puriss, or higher. The source of gelatin was food-grade gelatin sheets from Dr. Oetker. This is a type-A gelatin derived from porcine with a mean molecular weight of 150 kDa and a Bloom strength of 240. Its consistent quality control and high purity make it suitable for research purposes. The source of casein was “MPI 85” casein powder, manufactured and provided by the Hungarian Dairy Research Institute (Mosonmagyaróvár, Hungary). The source of sodium alginate is specified in each of the preparation procedures. 99.5% pure carbon dioxide gas was purchased from Linde. Ultrapure water (“Type I grade water”, $\rho = 18.2$ MΩ cm) was used for all experiments.

IV-1.2. Silica aerogels: Silica aerogels were synthesized by the classical sol-gel process. First, two solutions (“A” and “B”) were prepared. Solution “A” was made from tetramethyl orthosilicate (TMOS, 3.00 mL) dissolved in methanol (7.00 mL). Solution “B” contained methanol (15.0 mL), distilled water (3.00 mL) and aqueous ammonia solution (1.00 ml of 6.2 M). Solutions “A” and “B” were mixed under stirring, then poured into a PTFE-lined plastic mold and sealed. An alcogel formed in 24 h, which was transferred into a perforated frame and aged in a mixture of methanol (250 mL) and ammonia solution (25wt%, 20 mL) for one day. After 24 h, the sample was soaked in 300 ml of methanol twice, then in 300 ml of acetone-methanol mixtures, in which the acetone content was increased in 25% (v/v) steps. Finally, the sample was stored in pure acetone. Acetone was extracted from the gel by liquid carbon dioxide and the gel was dried under supercritical conditions (constant 80 °C, max. pressure 140 bar). The maximum pressure was maintained for 3 h, then released at a rate of 2 bar/min in a custom-made autoclave system. [10] In some cases, a calcined form was used produced by heating the as-prepared silica aerogel at 500 °C for 8 h in a furnace in air.

IV-1.3. Silica-gelatin aerogels: The synthesis of silica-gelatin hybrid aerogels was developed by Dr. Péter Veres and Prof. István Lázár and first published in Ref. [202]. First, the desired amount of gelatin (from 0.10 g to 1.0 g) and 70.0 mg of $(NH_4)_2CO_3$ were dissolved in 20.0 g of hot water. After cooling to room temperature, a second solution containing 3.30 g of TMOS and 5.55 g of MeOH was added to the gelatin solution under vigorous stirring. The mixture was poured in a cylindrical plastic mold for gelation for 24 h. First, the sample was soaked in methanol for 24 h, then, methanol was replaced by acetone in four 24 h soaking steps, and acetone was replaced 2 more times after 24 h soaking. Finally, acetone was extracted with liquid CO_2 at 5.4 MPa at ca. 25 ºC, and the gel was dried using $scCO_2$ at 140 kPa and 80 ºC. [10]

IV-1.4. Fluorescein-labelled silica-gelatin aerogels: Both gelatin and silica can be labeled via linking fluorescein moieties to them with covalent binding. [203,204] First, an aqueous solution containing 0.10 g gelatin in 20 g water was mixed with 1.8 mg fluorescein isothiocyanate (FITC) under reflux for 3 h. After this, 70.0 mg solid ammonium carbonate was dissolved in the mixture. A second solution of 3.00 mL tetramethyl orthosilicate (TMOS) in 7.00 mL methanol was added after cooling to room temperature, and the mixture was poured into a cylindrical plastic mold for gelation. Excess FITC does not react with silica moieties under these conditions. In order to covalently link fluorescein to the silica backbone, a two-step synthesis route was implemented. First 10.0 mg FITC and 16.25 µL (3-aminopropyl)trimethoxy silane (APTMS) was mixed at room temperature for 3 h in 7.00 mL methanol, then 3.00 mL TMOS was introduced into the mixture. A second aqueous solution of 0.10 g gelatin and 70.0 mg $(NH_4)_2CO_3$ in 20 g water was were added, and the resulting mixture was poured into a plastic mold for gelation. In this case, the unreacted FITC from the first solution reacts with gelatin. The gels were solvent exchanged, and dried in $scCO_2$ as given above. [10]

IV-1.5. Methotrexate functionalized silica-gelatin aerogel: Gelatin-methotrexate (G-MTX) conjugate was prepared by following the synthesis route detailed in Ref. [113]. 0.50 g gelatin was dissolved in 30 mL 0.05 M $NaHCO_3$ solution, and mixed with a solution of 150 mg MTX in 15 mL 0.05 M $NaHCO_3$. The pH of the mixture was set to 6.0 with HCl, and stirred at room temperature for 2 h. 750 mg 1-ethyl-3-(3-dimethyl-aminopropyl) carbodiimide hydrochloride (EDC) was added and the mixture was stirred overnight. The conjugate was purified using 7000 MWCO Dialysis Tubing (Thermo) in phosphate buffer (0.05 M, pH = 7.4), and later in water. The aqueous medium was replaced after 24 h soaking, and 5 dialysis cycles were performed. The final, dry G-MTX conjugate was obtained by lyophilization. G-MTX contains ca. 16wt% MTX by dry weight according to capillary electrophoresis (CE) analysis.

A co-gelation strategy was used to prepare methotrexate functionalized silica-gelatin hybrid aerogel (SGM). [205,206] 0.55 g G-MTX and 70 mg $(NH_4)_2CO_3$ were dissolved in 20 mL warm water. After cooling to room temperature, a second solution of 3.0 mL TMOS dissolved in 7.0 mL methanol was mixed into it. After 24 h gelation, the alcogel was subjected to multiple step solvent exchange. First, the alcogel was soaked in methanol for 24 h to remove water. Next, methanol was replaced by acetone in four 24 h soaking steps. The gels were dried in scCO_2 as in the case of pristine silica-gelatin gels. [10]

The composition of the hybrid aerogel was estimated by thermal analysis to be ca. 65wt% silica and 35wt% G-MTX. As no leaching of MTX was detected during the preparation of the hybrid aerogel, the total MTX content of the hybrid material is ca. 6wt% by dry weight. This means an SGM concentration of 2.0 mg/mL is equivalent ca. 0.12 mg/mL free MTX.

IV-1.6. Silica-casein aerogels: Three reactant solutions were prepared: A, B and C. In solution A, the silane reagent TMOS (2.5 cm^3, 13.7 mmol) was dissolved in methanol (15cm^3, 371 mmol). Solution B contained aqueous ammonia solution (1 cm^3, 12.1 mmol NH_3 and ca. 34 mmol water) and water (1 cm^3, 55.6 mmol) mixed with methanol (5 cm^3, 124 mmol). In solution C, 0.05 – 0.40 g of the MPI 85 casein powder was completely dispersed in water (4 cm^3, 222 mmol), For the preparation of the hybrid gels, solution B was added to solution A during constant stirring. After a few minutes of mixing, solution C was also added. The forming gel was kept in the mold for 3 days. For solvent exchange, the gels were kept in methanol, acetone: methanol 1:1 mixture, and pure acetone for at least 2-2days. The extraction of acetone was performed using CO_2 by the technique described in the case of silica-gelatin gels. [10]

IV-1.7. Borosilicate aerogels: Pristine borosilicate aerogel, (termed as BS), borosilicate-PVA hybrid aerogel (termed as BSP), and borosilicate-PVA aerogel with added microcrystalline hydroxyapatite (termed as BSPH) were prepared. [207] Briefly, the synthesis of the skeleton was achieved by co-gelation in a sol-gel procedure in all cases. Tetraethyl orthosilicate (TEOS) was dissolved in a water-ethanol mixture. This mixture was slightly acidified and stirred for 1 h before the addition of the boric acid solution. For synthesizing a hybrid skeleton, the aqueous solution of PVA was added to the TEOS and boric acid solution. In the case of the BSPH, powdered hydroxyapatite (HAp) was also added under vigorous stirring as the last component. The final step was the addition of the NH_4F catalyst to accelerate the gelation. After 24 h gelation, the solvent mixture was exchanged to pure ethanol, which was subsequently exchanged in multiple steps to pure acetone. Acetone was extracted by supercritical CO_2 in an autoclave using the procedure given above. [10]

IV-1.8. Ca-alginate aerogels (TUHH): Aerogel samples were prepared in collaboration with Prof. Pavel Gurikov at TUHH from sodium alginate purchased from Sigma Life Science (catalogue no. 71238). Spherical Ca-alginate aerogel (CaAG) beads of ca. 0.2 mm were synthesized using the jet cutting method. [57,208] 1.0 w/w% aqueous solution of Na-alginate was dropped into 20 g/L $CaCl_2$ solution. The gel beads were subjected to multiple step solvent exchange: the beads were placed for 24 h into 30, 60 and 90 w/w% ethanol-water mixtures and then into anhydrous ethanol. The drying procedure was initiated only when the ethanol content reached min. 98.5 w/w% in order to ensure single phase conditions during supercritical drying. The gel beads were dried by extraction of ethanol with a continuous flow of supercritical CO_2 in a high-pressure autoclave. The autoclave was sealed and preheated to 313 – 323 K. Preheated carbon dioxide was supplied into the autoclave until the desired working pressure (120 kPa) was achieved. The outlet flow rate of carbon dioxide was ca. 25 g min^{-1}. The as-prepared aerogel samples were kept in a desiccator under freshly dried silica gel.

IV-1.9. Fe(III)-alginate aerogels (TUHH): Aerogel samples were prepared in collaboration with Prof. Pavel Gurikov at TUHH from 2 different Na-alginates with high guluronic acid content (HG; 70:30 G/M ratio) and low guluronic acid content (LG; 30/70 G/M ratio) from FMC Biopolymer (Norway). The 2 w/w% aqueous solution of either the low G or the high G alginate was dropped into 0.05 M $FeCl_3$ solution (gelation bath). After gelation, the beads were placed into a fresh 0.05 M $FeCl_3$ solution for 24 h. This was followed by multiple step solvent exchange. The alginate beads were placed for 24 h into 30 V/V%, 60 V/V%, 90V/V% ethanol-water mixtures and two times into pure ethanol. The samples were dried with supercritical CO_2 at 45 °C and 140 bar using a continuous flow process, as given above.

IV-1.10. Ca-alginate aerogels (USC): Aerogel samples were prepared in collaboration with Prof. Carlos A. García-González at USC from sodium alginate (guluronic acid/mannuronic acid ratio of 70/30, M_w =403 kDa) from Sigma-Aldrich. Alginate aerogel powder was prepared by a prilling gelation method using a compressed air-assisted spraying equipment. An aqueous sodium alginate solution of 1.75% (w/v) was transferred to a nozzle for spraying into 200 mL of an aqueous 150 mM $CaCl_2$ solution. Ageing of alginate hydrogels took place for 2 h in the $CaCl_2$ solution before solvent exchange with ethanol. The hydrogels were directly placed in absolute ethanol, which was changed three times in every 24 h. Alginate alcogels were dried using $scCO_2$ (40 °C, 120 bar) at a flow of 5 g/min during 3.5 h in an autoclave.

IV-1.11. Polyurea cross-linked X-Ca-alginate aerogels: Two different types of polyurea cross-linked X-Ca-alginate aerogels (X-Ca-alg-N3300 and X-Ca-alg-RE) were kindly provided by Prof. Patrina Paraskevopoulou together with the parent Ca-alginate aerogel as a reference. The preparation procedures and material characteristics are reported in Refs. [209,210]

IV-1.12. Aerogel from Kevlar-like linear polyamide: The full preparation procedure was taken from a previous publication and reproduced without any modification. [211] Briefly, $CaCl_2$ (2.25 g, 20.3 mmol) and p-phenylenediamine (3.45 g, 31.9 mmol) were dissolved in NMP (90.0 mL) and cooled to 0 °C. Solid terephthaloyl chloride (6.32 g, 31.1 mmol) was added, which resulted in the formation of a transparent homogeneous yellow solution. After 5 min of stirring, the solution became cloudy and the viscosity increased due to the formation of polyamide. The thick suspension aged for 16 h at room temperature. The gel monoliths were soaked in anhydrous ethanol for 5 days with the solvent replaced with fresh each day. Once this solvent exchange process was complete, the gels were dried using supercritical CO_2. [10]

IV-1.13. Cu(II)-cyclen and Cu(II)-cyclam functionalized silica aerogels: The functionalized silica aerogels were prepared using sol-gel synthesis procedures adopted from the literature and optimized. [212] The choice of the ligands limited the synthetic options for immobilization. (3-glycidoxy-propyl)-trimethoxysilane (GPTMS) based arms were attached to cyclen and (3-chloropropyl)-trimethoxysilane (CPTMS) based arms were attached to cyclam. These synthetic precursors were isolated, re-dissolved in the appropriate solvents and characterized in the solution phase by NMR and MS techniques. The complexation of Cu(II) could be achieved in good yields only in the solution phase using the as-prepared macrocyclic precursors. Finally, the functionalized precursors were hydrolyzed and condensed with TMOS using basic catalysts. The functionalized alcogels were transferred to acetone, and dried using $scCO_2$. [10] The chemical structures of the aerogels are discussed in the ***Results and Discussion*** section.

IV-2. Classical characterization of as-prepared aerogels

IV-2.1. Scanning electron microscopy (SEM) with energy dispersive X-ray spectroscopy (EDS): Low voltage scanning electron microscopy (LV SEM) methods were optimized to study the morphology of aerogels. [3] The images were taken in a ThermoFisher Scios 2 instrument under special conditions using very low accelerating voltage and small electron beam current in order to eliminate the charging effects of the aerogel samples. These measurement conditions made it possible to examine the fresh fracture surfaces of the aerogels in their pristine states. A vacuum-resistant carbon tape was used to fix the aerogels, but no further sample treatment was applied. 10 kV accelerating voltage and long measurement time was used for the EDS analysis.

IV-2.2. N_2-sorption porosimetry: Nitrogen adsorption-desorption isotherms were recorded in a Quantachrome Nova 2000e instrument at 77 K. The powdered samples (20 – 80 mg) were degassed under vacuum at different temperatures (50 – 100 °C) depending on the sensitivity of the given aerogel for 24–48 h before the measurements. Based on the measured isotherms, the specific surface area, the pore size distribution and the pore volume of the aerogels were calculated using NovaWin 11.0 software. The $p/p_0 = 0.05 – 0.30$ range was used as input data for the multi-point BET method for calculating the apparent surface area. The pore size distribution and the pore volume were determined by the BJH method using the instrument controlling software. NLDFT calculations were performed in the case of silica-based aerogels.

IV-2.3. Fourier-transformed infrared spectroscopy (FT-IR): The infrared spectra (FT-IR) of the samples were measured with an Agilent Cary 630 FT-IR Spectrometer using a universal ATR head. The measurements were performed on powdered samples that were pressed onto the diamond surface. The IR spectra of the samples were recorded by averaging min. 16 scans.

IV-2.4. X-ray powder diffraction (XRD): Diffraction patterns were collected under Cu-Kα radiation (Kα1= 1.54059 Å) using a Rigaku SmartLab 9.0 kW X-ray diffractometer (XRD) with 200 mA. The measurements were carried out in Bragg-Brentano geometry, between 5 and 90 (2θ) with 5.0 degree/min scan rate, and between 5 and 60 (2θ) with 1.0 degree/min scan rate.

IV-2.5. Compression tests: The compressive strength of dry and partially hydrated aerogel monoliths was measured using an Instron 4302 Universal Strength Testing Apparatus. The crosshead speed of the probe was 1.0 mm/min. A standard strength testing head of 1.0 kN was used. Monolithic test objects of regular cylindrical shape were used with the length of ca. 30 mm and the diameter of ca. 20 mm. Extra care was taken to use monoliths with parallel top and bottom sides. The specimen-to-specimen relative standard deviation of the measured data is ca. 15%. Young’s modulus was calculated by the instrument controlling software.

IV-2.6. Size of suspended aerogel microparticles: The size distribution of aerogel particles was measured by using a hemocytometer in a light-microscopy after wet grinding the samples by a Potter-Elvehjem tissue grinder (10 min) and sonication (5 min). [126,127] Images were taken from c = 0.5 mg/mL suspensions with a microscope camera. The ImageJ software was used for calculating the size distribution of the particles. In some cases, the size distribution of aerogel particles was measured using a laser diffraction light scattering instrument (LDLS).

IV-2.7. Zeta potential of aerogel particles: Aerogels were wet ground by a tissue grinder (see above), and the electrophoretic mobility of the suspended particles was measured at a final aerogel concentration of 0.1 mg/mL in a MALVERN Zetasizer Nano ZS instrument using conventional instrument setup and operation. The Zeta potential values were calculated from the measured electrophoretic mobility and dynamic light scattering data by the instrument controlling software based on the Smoluchowski approximation.

IV-3. Controlled hydration and wetting of aerogels

For preparing partially hydrated aerogel samples, general, the as-prepared dry aerogel sample was gently broken to small pieces, placed onto an analytical balance (min. 50 mg) and aliquots of liquid water were added. Water content is defined as grams of liquid water added to grams of dry aerogel (g/g). The partially hydrated samples were gently mixed and sonicated for using a bath type sonicator. It was tested that sonication does not cause any structural change in the hydrated samples. Each sample was prepared in the corresponding sample holder (e.g. NMR tube), and sealed airtight for a 24–48 h equilibration period before the measurements. The characterization measurements were reproduced in duplicates in such way that the same water content was set by different methods in duplicate samples; either by directly hydrating the dry aerogel, or by adding additional aliquots of water to samples of lower water contents.

Another procedure to prepare partially hydrated aerogel samples was the equilibration of aerogel monoliths with humid air for 84 h in sealed desiccators. The humidity of air was controlled placing saturated solutions of appropriate inorganic salts in the desiccators. [213] The water contents of the samples were calculated from the weight loss after drying at 90 °C.

The macroscopic swelling of aerogels due to hydration and wetting was studied in 5 mm NMR tubes. The dry aerogels were compacted in the tubes by gently pressing the sample and vibrating the tubes. The height of the aerogel column was measured after hydrating and wetting.

IV-4. Liquid phase nuclear magnetic resonance (NMR) methods

The theory of these methods is discussed in details in the ***Literature Review*** section.

IV-4.1. NMR relaxometry: The measurements were performed in a Minispec Bruker mq20 relaxometer instrument. Typically, ca. 50 mg dry aerogel was weighed into an NMR tube, and titrated with water. [132,135,137] The water / dry aerogel mass ratio was increased from 0.1 g/g to 4.0 g/g. The measurements were performed typically at 6 dB. The T_1 (spin-lattice) and the T_2 (spin-spin) relaxation times were determined for every sample. The CPMG (Carr-Purcell-Meiboom-Gill) sequence was used with at least 3 different echo times (0.08 – 0.16 ms) for the T_2 measurements. The parameters of the CPMG sequence were optimized according to the T_1 relaxation times determined using the inversion-recovery method.

The number of exponential functions in the primary CPMG decays was determined by inverse Laplace transformation using the MERA (Multi-Exponential Relaxation Analysis) algorithm on the basis of the CONTIN method in MatLab v.8.5 (MathWorks Inc., USA). After determining the number of exponential decay components, the raw data was fitted by a non-linear Levenberg-Marquardt algorithm using the probe function with the appropriate number of exponential components. As a verification, every experimental data set was additionally fitted with one less exponential component, and the results compared. In the case of ca. the same goodness of fit, the probe function of the least number of exponential components was accepted.

IV-4.2. NMR cryoporometry: Partially hydrated aerogel samples were characterized by NMR cryoporometry at different water contents in a Bruker Avance II 360 MHz NMR instrument. The Carr-Purcell-Meiboom-Gill (CPMG) spin-echo pulse sequence was applied as a relaxation filter. Before every measurement, the length of the 90° pulse was determined (ca. 10 μs). The optimization of the echo time was performed by systematically changing its value between 0.5 and 1.5 ms and monitoring ^{1}H signal intensity in hydrated mesoporous silica aerogel at 265 K as a reference material. Thus, the recorded signal intensity is proportional to the amount of liquid water confined in the porous system. Every aerogel sample was mixed with the proper amount of water, and the mixture was frozen at –20 °C. Multiple melting-freezing cycles were measured between –15 °C and +6 °C in 0.2 – 0.5 °C steps. When the results of the first two cycles were identical within experimental error, the expansion of ice does not damage the aerogel backbone architecture. Temperature was calibrated using glycol and methanol. [214]

The size distribution of the confined water bodies, referred to droplets and puddles, was calculated using the methodology of Petrov and Furó. [133] The measured NMR intensities were plotted against the temperature calculated as the difference (ΔT) from the freezing point of bulk water (273 K). Intensity versus ΔT data were transformed to intensity versus droplet size (d_{droplet}) data using the modified Gibbs-Thomson equations and estimating the geometric factors (spherical, cylindrical or slab-like) from the shape of the melting-freezing hysteresis loop. Density distribution curves were calculated by estimating a log-normal distribution.

IV-4.3. NMR diffusiometry: The self-diffusion of water was studied in partially hydrated aerogel samples at 298 K. A stimulated echo pulse sequence (PGSTE) was used for the measurements featuring bipolar gradients and longitudinal eddy current delay (BIPLED), as described previously. [131,215] The observation time of the diffusion experiments (Δ) was varied between 8 and 120 ms. The length of the gradient pulse (δ) was changed from 2 to 4 ms. The pulsed gradient strength (G) increased in 32 or 64 square distant steps.

The spectra were transformed with the MestReNova 9.0 software and evaluated according to the classical expressions. When multiple diffusion domains are present in the sample, each domain is represented by a single-exponential function of a given D_{obs}. In order to determine the number of diffusion domains and the corresponding D_{obs} values, the primary data were treated using the same algorithms as for the evaluation of the NMR relaxometry data.

IV-5. Magic angle spinning (MAS) solid state NMR measurements

Solid-state NMR spectra were acquired on a Bruker Avance III 500 spectrometer and a wide bore 11.75 Tesla magnet with operational frequencies for ^{1}H and ^{13}C of 500.13 and 125.77 MHz, respectively. A 4 mm triple resonance probe in double resonance mode with magic angle spinning (MAS) was employed. In order to optimize the sensitivity of the probe, the rotor was fitted with Teflon inserts to define a 50 ml volume. [216] The partially hydrated aerogel samples were prepared directly in the 4 mm ZrO_2 rotor. The amount of the dry aerogel was always kept constant, therefore, the NMR spectra are treated as mass-loading normalized data. The rotor was spun at a MAS rate of 15 and 10 kHz for ^{1}H MAS and ^{13}C CPMAS NMR experiments, respectively. For the ^{13}C cross-polarization (CP) MAS experiments, proton radio frequencies (RF) of 55 and 28 kHz were used for initial excitation and decoupling, respectively. During the CP period the ^{1}H RF field was ramped using 100 increments, whereas the ^{13}C RF field was maintained at a constant level. During the acquisition, the protons were decoupled from the carbon using a Spinal-64 decoupling scheme. A cross polarization contact time of 0.5 ms, and a 5 s delay between scans were used. A moderate ramped RF field of 55 kHz was used for spin locking, while the carbon RF field was matched to obtain optimal signal (40 kHz). Spectra were recorded with a spectral width of 42 kHz and 8k transients were accumulated at 298 K.

IV-6. Small angle neutron scattering (SANS)

The measurements were performed by Dr. Adél Len, Dr. Zoltán Dudás and Dr. Zoltán Balogh. Dry, powdered aerogel samples were introduced into 2 mm-thick quartz cuvettes and measured without any pre-treatment. Some samples were wetted either with D_2O or with H_2O

– D_2O mixtures of different composition. The water / dry aerogel mass ratio was at least 3.5 g/g to completely fill the pores of the aerogels. After homogenization, the wet samples were stored for 8 – 24 h at room temperature before SANS measurements.

The measurements were performed at the Budapest Neutron Centre in the Yellow Submarine pin-hole type instrument equipped with a two-dimensional neutron detector. [166] Two sample-to-detector distances (1.2 m and 5.4 m) and two wavelengths ($\lambda = 4.38$ Å and 10.23 Å) were used. The beam diameter was 8.0 mm. The samples were measured for 60 – 180 min at room temperature. The Q range of 0.0065 – 0.4000 Å^{-1} was covered by altering the neutron wavelength and the sample-detector distance. The measured scattering intensity was corrected for sample transmission, empty cell scattering, detector sensitivity and background scattering.

The nano- and microstructural parameters of the scattering objects were estimated by the mathematical analysis of the corrected $I(Q)$ curves. The general considerations used for data evaluation are given in the ***Literature Review*** section. Data fitting was performed using non-linear Levenberg-Marquardt least-squares regression algorithms in the SasView 5.0.3 software.

IV-7. Impregnation of aerogels with active pharmaceutical ingredients

The technique of adsorptive precipitation (adsorptive deposition) was utilized in $scCO_2$ for impregnating the active pharmaceutical ingredients (drugs) into the different as-prepared aerogels, which facilitates the physical deposition of drugs in amorphous state. [61,82,83,205]

Milled and sieved ($d_{\text{particle}} < 125$ μm) silica-gelatin aerogel powders were impregnated with ibuprofen and ketoprofen. The process was realized in an autoclave. Impregnation was performed in $scCO_2$ at 45 °C and 200 bar in a stirred reactor for 6 h. The depressurization rate was 2 bar/min in order to avoid crystallization of the drugs. [205] Drug content was determined with RP-HPLC after soaking 5.0 mg loaded aerogel sample in 10.0 mL methanol for 2 h.

In one set of experiments the Fe(III)-alginate aerogel beads (TUHH) were impregnated with ibuprofen alone, in another set of experiments the beads were simultaneously impregnated with ibuprofen and ascorbic acid. Weighted amounts of aerogel beads and active ingredients were wrapped separately in filter paper and placed into an autoclave. The vessel was warmed up to 45 °C and $scCO_2$ was pumped into it until 200 bar. These conditions were kept for 6 h. The pressure was released first by a 120 bar pressure drop in 10 s, and from there the pressure was released at ca. 3–4 bar/min. The amount of ibuprofen and ascorbic acid were determined by UV-vis spectrophotometry after soaking the loaded aerogel samples in methanol.

As-prepared Ca-alginate aerogel microspheres (USC) were loaded with Beclomethasone dipropionate (BDP). Aerogel (0.40 g) and BDP (0.040 g) powders were poured in separate paper cartridges and placed in a 100 mL autoclave previously loaded with 5 mL (5V/V%) acetone. Impregnation was conducted at 65 °C and 215 bar in $scCO_2$ using different contact times. The depressurization rate was 1 CO_2 g per minute. The BDP-loaded Ca-alginate aerogels were immersed into acetonitrile-water (65-35V/V%), followed by sonication to release all BDP. The BDP concentration was measured by HPLC.

IV-8. High time resolution in vitro drug release tests

Drug release from the impregnated aerogels was studied using a customized fast kinetics method with on-line UV-vis spectrophotometric detection. The drug loaded aerogel was gently crushed, and sieved to uniform size ($d_\text{particle} < 200$ μm) to avoid any particle size-related kinetic effects. This aerogel powder was weighted with 0.01 mg precision into a carefully dried 1.00 cm × 1.00 cm spectrophotometric cuvette. The cuvette was thermostated at 37.0 ± 0.1 °C. On-line detection was started, and 3.0 mL pre-heated release medium was introduced into the cuvette. The suspension was stirred at 300 rpm by a 2 × 8 mm PTFE coated magnetic stir-bar. The UV-vis absorbance change was followed typically in the 200 – 800 nm wavelength range for at least with a time resolution of 1.0 s. As the drug dissolved from the aerogel its characteristic UV-vis spectrum was detected. The concentration of the released nicotinic acid was calculated from the on-line measured absorbance values. It is important to note, that the light scattering (extinction) of the aerogel suspension was taken into correction by subtracting it from each recorded spectrum using the “dual-wavelength method” developed by Liu and Zhu. [178,217] As a verification method, drug release was also followed by HPLC for sustained release systems. Cumulative drug release is given as the percentage of the total amount of loaded drug in the aerogel. All experiments were performed in replicates. Kinetic model fitting was performed based on well-established theories using a non-linear algorithms.

IV-9. In vitro cell viability and cytotoxicity tests, in vivo experiments

The in vitro and in vivo experiments were performed by Dr. Gábor Király and Prof. Gábor Szemán-Nagy at the Department of Molecular Biotechnology and Microbiology at UD.

Generally, the as-prepared aerogel samples were sterilized with UV light for 48 h before the biological experiments. Dry, ground and sieved particles were placed in UV transparent plastic containers and spread to a maximum thickness of 1 – 2 mm. Sterilized aerogel samples were wet-micronized in a laminar box in sterilized PBS and kept there before use.

For the in vitro experiments, suspensions (200 μL) of the selected cell lines (2.5×10^3 – 5.0×10^3 cell/mL) were seeded in 96-well plates and incubated at 37 °C, 5 % CO_2

concentration and 100 % relative humidity. After 24 h, the aerogel suspensions were added to the cells in 200 μL fresh medium. Each microplate contained controls: 1) cells without any treatment, 2) cells treated with pristine silica aerogel. Typically, three different incubations lasting for 24, 48 or 72 h were used. Cell numbers were counted using a hemacytometer and trypan blue dye exclusion. In addition, the MTT viability test was also applied. Percentage of cell growth was expressed relative to control cells. Time-lapse video-microscopy imaging was performed by modified and inverted upright microscopes (Olympus) in a SANYOMCO18-AC CO_2 incubator. The selected cell cultures were grown to ca. 40% confluence, then the cells were treated with the aerogel suspensions (1.0 mg/ml) for 48–72 h. The raw image sequences were evaluated using the ImageJ software. After obtaining the series of x and y positions of the separate cells, the path length and the velocity of their position-changes were determined. All in vitro experiments were performed in triplicates.

Micronized silica-gelatin hybrid aerogel particles suspended in physiological saline were injected carefully into the upper abdominal cavity of 15-22 weeks old C3H mice. Two different concentrations were applied: 52 or 104 mg aerogel in dry weight per kilogram body weight. The control group received an equivalent volume of saline administered in the same way. These experiments aimed to investigate the short-term biodistribution of silica-gelatin microparticles in order to determine their applicability as vehicles for antimetastatic drugs. The histological studies of the abdominal organs and lymphatic tissues were performed at the Department of Pathology of the Kenézy University Hospital of UD.

IV-10. Kinetic experiments in aerogel suspensions

On-line UV-vis spectrophotometry and turbidimetry measurements were carried out in an Agilent 8453 diode array instrument equipped with a built-in temperature control unit and magnetic stirrer to follow fast chemical reactions, and sorption equilibria. A standard quartz cuvette of 1.00×1.00 cm was used for all measurements. All experiments were carried out at constant temperature and under constant stirring using a cuvette sized magnetic stirring rod. Standard external calibration series for UV-vis spectrophotometry and turbidimetry were prepared for the components of the given system. For the time-resolved (kinetic) experiments, 1.0 – 3.0 mL of aerogel suspension was placed in the thermostated spectrophotometric cuvette; and stirring and detection was started. The process was started by promptly injecting the reactant or the sorbate to the aerogel suspension in the cuvette. The absorbance (extinction) change characteristic for the process was followed with a time resolution of 1.0 s. Data evaluation is detailed individually for each system in the ***Results and Discussion*** section.

V. RESULTS AND DISCUSSION

V-1. Hydration mechanisms of aerogels, structures of hydrated aerogels [P1-P7]

When aerogels are designed to be used in aqueous media, e.g. in biomedical or environmental engineering applications, it is essential to understand the mechanism of their hydration and the consequent changes in the aerogel structure. The most important questions are the following. 1) Does the extensive hydration of the backbone cause the erosion of the aerogel monolith? 2) Does the aerogel retain its original morphology and pore structure when hydrated? 3) Are the pores of the aerogels permeable in water, or does the porous structure collapse due to the extensive deformation of the hydrated backbone? 4) What is the stable particle size and surface-layer charge of the hydrated aerogel? Evidently, the answers to these questions are indispensable to understand the properties of hydrated aerogels related to mass transport, adsorption-desorption properties, and suspension stability. [45,47,48,145,218,219]

V-1.1. Hydration and wetting of silica-gelatin hybrid aerogels – relationship between aerogel structure and drug release kinetics [P1, P2]

The mechanistic background of the drug delivery features of silica-gelatin hybrid aerogels were investigated and compared to that of pure silica aerogel using ibuprofen (IBU) and ketoprofen (KET) as model drugs. [202] Importantly, the carriers with low gelatin contents are rapid release systems, while the hybrid aerogels of high gelatin-content show sustained release properties. The factors governing the drug loading and release characteristics were explored by simultaneously investigating the pore structure, surface properties and hydration behavior of the aerogels. Dry aerogels were characterized by scanning electron microscopy (SEM), N_2 adsorption-desorption porosimetry and small-angle neutron scattering (SANS). The mechanism of wetting and hydration is investigated by non-conventional nuclear magnetic resonance (NMR) methods, such as cryoporometry, diffusiometry and relaxometry, and complemented with SANS measurements. The structural information was correlated to high time-resolution drug release experiments.

V-1.1.1. Structural characteristics of silica-gelatin aerogels

First, the structural characteristics and wetting properties of silica and silica-gelatin aerogels are compared. The studied aerogel samples were prepared by the same synthetic procedure, thus, the differences between the aerogels can exclusively be attributed to the incorporation of gelatin into the silica backbone.

V-1.1.1.1. Pore structure and morphology of dry aerogels

Scanning electron microscopy. The fundamental morphologies of the silica and silica-gelatin aerogels are analogous (**Fig. 2**). It is known that silica-based aerogels are built from primary spherical nanoparticles, but these primary particles are not visible in the SEM images, because their size is ca. 5-10 nm (as measured e.g. by SAXS). Some pores are visible in the aerogels, but their sizes cannot be quantified based on the SEM images. It is observable that both the number and the size of macrospores increase with increasing gelatin content. This was further investigated by N_2-adsorption desorption and SANS measurements.

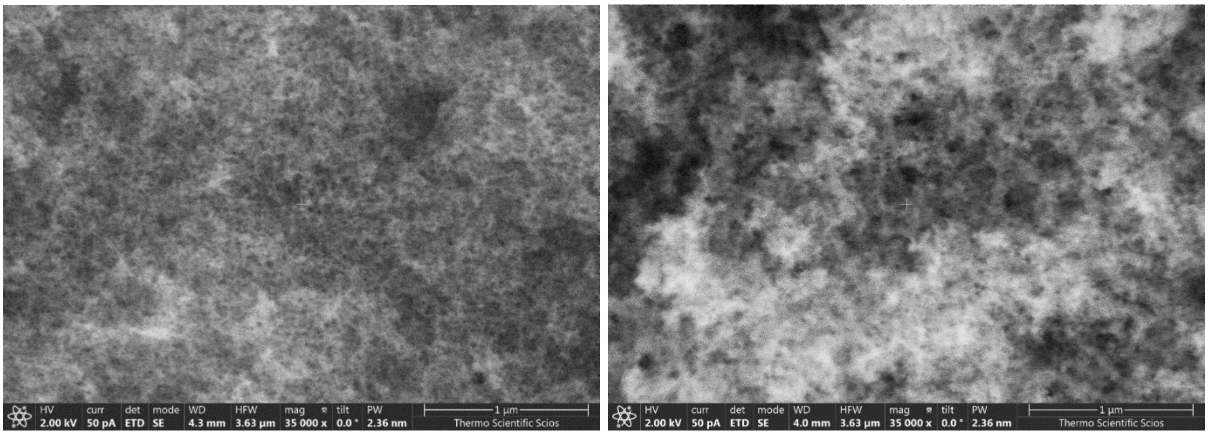

Figure 2. Scanning electron micrographs (SEM) of a pristine silica aerogel (A) and a silica-gelatin hybrid aerogel (B) of 24wt% gelatin content. The scale bars represent 1.0 µm.

N_2-adsorption-desorption porosimetry. All of the experimental hysteresis curves are IUPAC type IV with a H2 loop, which is characteristic for mesoporous materials (**Fig. 3A**). The steep rise of the isotherms at $p/p_0 = 1$ indicates the presence of macropores. [14] The apparent specific surface area (S_{BET}) of the hybrid aerogels systematically decreases with increasing gelatin content (**Table 1**). The pore size distribution curves of the aerogels calculated by the BJH method are shown in **Fig. 3B**. The total specific pore volume (V_{p}) corresponding to $d_{\mathrm{pore}} < 200$ nm systematically decreases with increasing gelatin content (**Table 1**). Pores larger than 200 nm are excluded from the N_2 porosimetry analysis, as a consequence of the working principle of the technique. Thus, the V_{p} value is representative only when the macropore contribution is small. This is further discussed in connection with NMR cryoporometry.

According to the combined SEM and N_2 porosimetry results the increasing amount of incorporated gelatin in the backbone results in the opening and loosening of the dry aerogel matrix resulting in a number of macropores. The contribution of micropores was estimated for each aerogel by using the *t*-plot method, based on the de Boer model of statistical thickness. [220] This indicates that there are no pores present below $d_{\mathrm{pore}} = 2$ nm in any of the aerogels.

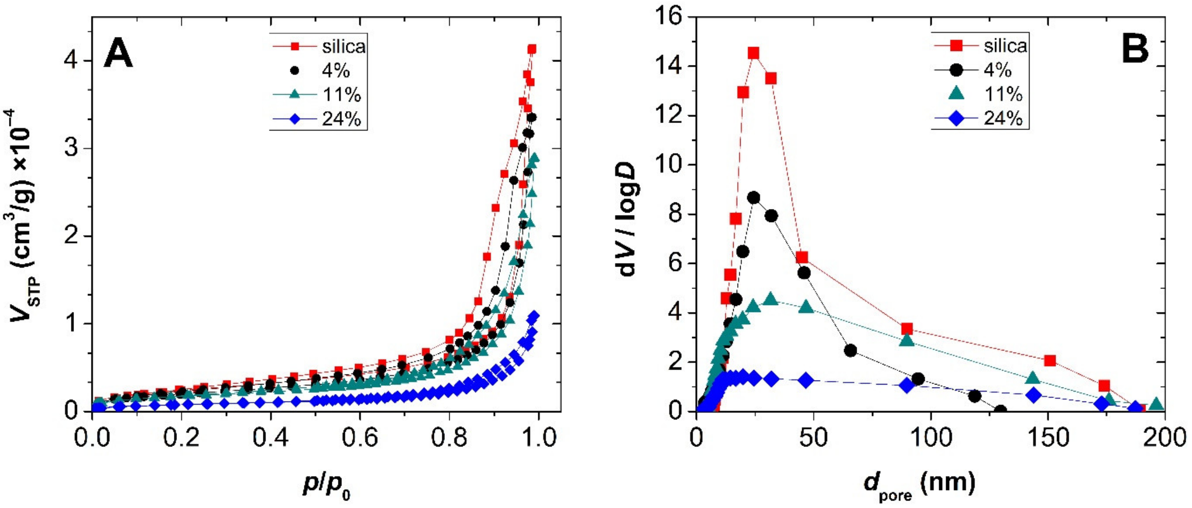

Figure 3. Nitrogen adsorption-desorption isotherms (A) and BJH pore size distribution curves (B) of silica and silica-gelatin hybrid aerogels of different gelatin content (given in the legend as wt%).

Table 1. Morphological data of silica and silica-gelatin hybrid aerogels derived from N_2 gas adsorption-desorption porosimetry data (cf. **Fig. 3**). Mean ± SD values represent 3 replicate measurements.

	S_{BET} (m^2/g) $^{a)}$	V_p (cm^3/g) $^{b)}$	d_{pore} (nm) $^{c)}$	C-constant
silica	812 ± 61	6.20 (198 nm)	32	89
4wt% gelatin	799 ± 72	4.95 (161 nm)	25	73
11wt% gelatin	627 ± 60	4.48 (205 nm)	32	92
18wt% gelatin	416 ± 46	2.31 (213 nm)	17	87
24wt% gelatin	285 ± 32	1.69 (194 nm)	20	85

a) BET specific surface area; b) Total specific pore volume (upper threshold of pore diameter included in the calculation); c) Mean pore diameter: estimated at the maximum of the distribution curve.

Morphology of dry aerogels by SANS. Nanometer sized material inhomogeneities (scattering objects) that have neutron scattering length densities different from their surroundings yield informative SANS curves. The primary difference in neutron scattering length densities in dry mesoporous aerogels, i.e. the contrast, is between the solid backbone and the air filled pores. [146,150,167] In the case of hybrid materials, the different components of the backbone can also give distinct contrasts. All of the SANS curves of the dry aerogels (**Fig. 4A**) can adequately be fitted with the Beaucage model (**eq. 8**). As seen in **Table 2**, the value of the p exponents are between 3 and 4 for silica aerogel and for hybrids of low gelatin content (4wt%). Such p exponents are characteristic for surface fractals. The value of the p exponent is ca. 4 for hybrid aerogels with moderate and high gelatin content (11 – 24wt%), meaning that the boundary between objects of different contrasts is sharp and smooth. [221] This can be attributed to the high number of macropores. For macropores, the area of the pore walls is high and their apparent curvature is low compared to micropores and small mesopores. In line with this explanation, the gyration radius (R_g) is the highest in the case of the aerogel with the highest gelatin content. Thus, the results of the SANS measurements are in excellent agreement with those of the N_2 porosimetry and SEM.

Homogeneity of the hybrid backbone by SANS. The primary observation is that the scattering curves of the dry silica and silica-gelatin aerogels do not show distinct features, i.e. there is no secondary contrast in the hybrid materials. The simplest explanation for this phenomenon is that there is no spatial heterogeneity in the solid silica-gelatin backbones. [222] The hybrid backbones scatter as homogeneous materials, and contrast is the sole result of porosity.

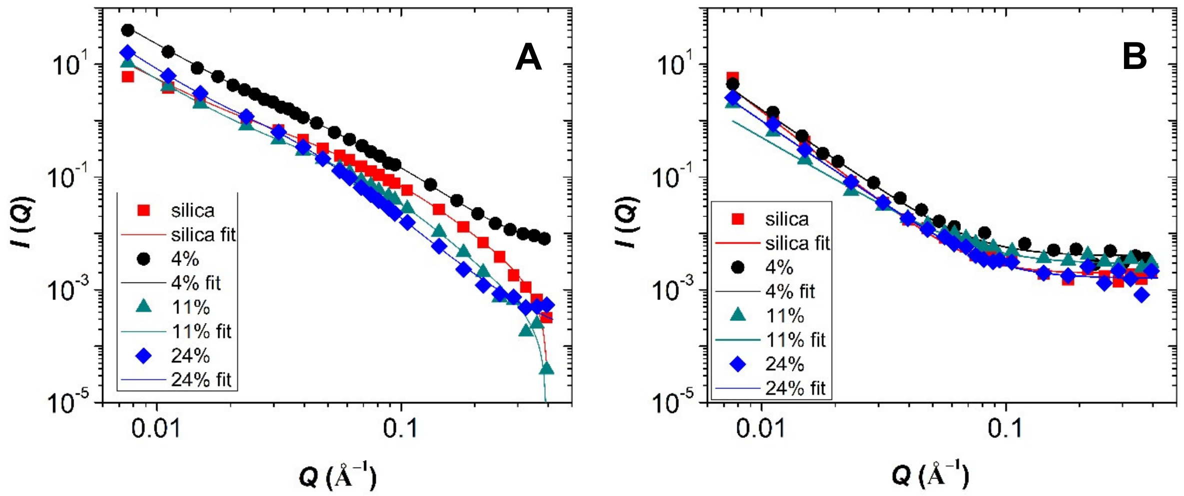

Figure 4. Small angle neutron scattering (SANS) curves of silica and silica-gelatin hybrid aerogels measured in their dry states (A) and when completely hydrated (B) by 1:2 H_2O:D_2O mixture (3.3 g liquid / g dry aerogel). Solid lines represent data fitting to the Beaucage model (**eq. 8**). Estimated structural parameters for the dry aerogels are given in **Table 2**.

In order to verify this theory, contrast-variation SANS experiments were performed. Silica and silica-gelatin aerogels were hydrated (3.3 g liquid / g aerogel) with 1:2 H_2O:D_2O mixture. The SLD of this mixture is ca. equivalent to that of silica. [167] The scattering of such a hydrated silica aerogel is practically equivalent to the background. Interestingly, almost identical, uninformative scattering was measured for the hydrated hybrid aerogels as well, regardless of their gelatin content (**Fig. 4B**). The most feasible explanation is that the contrast of the silica-gelatin matrix approximately matches that of the pure silica. This is a strong indication that the hybridization of the silica-gelatin backbone is homogeneous at molecular level. [222]

Table 2. Structural parameters estimated by fitting the SANS curves of silica and silica-gelatin hybrid aerogels (cf. **Figs. 4 and 11**) with the Beaucage model (**eq. 8**).

	dry	**hydrated (D_2O)**
silica	R_g = 36.8 Å p = 3.28	R_g = 31.9 Å p = 3.87
4wt% gelatin	R_g = 37.3 Å p = 3.44	R_g = 30.3 Å p = 3.97
11wt% gelatin	R_g = 36.4 Å p = 3.98	R_g = 28.2 Å p = 5.15
24wt% gelatin	R_g = 54.0 Å p = 4.22	R_g: N/A p = 2.71

V-1.1.1.2. Pore structure and morphology of hydrated aerogels

Water readily interacts with both silica and silica-gelatin aerogels. Importantly, no macroscopic swelling is detectable for any of the materials. Yet, two concerted processes take place. The backbone is hydrated, and the monolithic structure disintegrates to microparticles. [126,127] Hydration can take different extents based on the composition of the aerogel backbone, which can lead to the alteration of the morphology and the pore structure. The disintegration of the aerogel monoliths is the result of breaking the bonds between the primary building blocks in the solid network due to the surface tension of water and minor hydrolytic reactions. As a result of the two coupled processes, aerogel microparticles form in water. The pore network of these wet particles either retains the original structure of the dry solids, or gets distorted due to the extensive hydration of the backbone. The kinetics of hydration of the silica and silica-gelatin aerogels is fast, and complete in a few seconds when the solid matrices are flooded with water.

Particle size and Zeta potential of hydrated aerogels. Particle size distribution of silica and silica-gelatin aerogels were measured after wet grinding the samples using a standardized protocol ensuring that the difference in particle size is exclusively due to the different composition of the aerogels. Both the position of the maximum and the width of the particle size distribution curve decrease systematically with increasing gelatin content (**Fig. 5**). In hybrid aerogels, the covalent silica network is disrupted by the incorporation of gelatin protein molecules that are bound to each other only by weak secondary forces.

Besides the size of the hydrated aerogel microparticles, the charge of the surface layer has a fundamental influence on the drug delivery properties, because it controls the electrostatic interactions between the aerogel backbone and the drug molecules. The isoelectric point of silica is at ca. pH = 3.5 (**Fig. 6**), which is in good agreement with previously reported values. [223] The E_Z of the hybrid aerogels systematically increases with their increasing gelatin content at all pH values. The proportionality between E_Z and gelatin content is well-expressed at acidic pH (positive E_Z values), but not at neutral pH (negative E_Z values). The isoelectric point of Type A gelatin is at ca. pH = 5.5 [224], which is consistent with the present results.

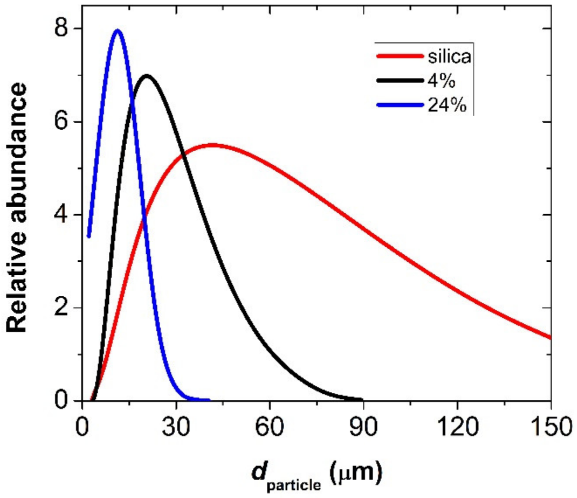

Figure 5. Particle size distribution of wet silica and silica-gelatin hybrid aerogel particles measured by laser diffraction light scattering (LDLS).

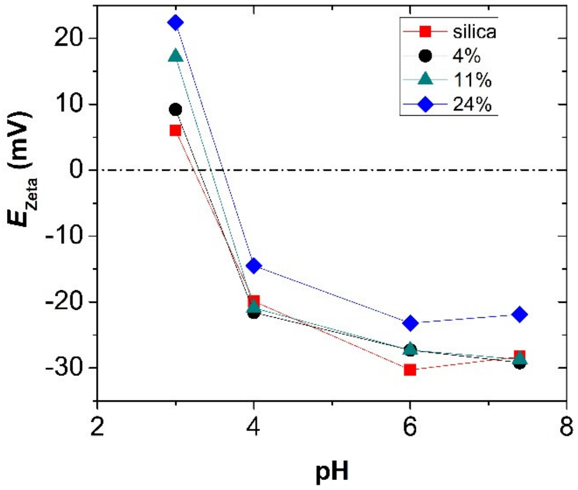

Figure 6. Zeta potential (E_{Zeta}) of silica and silica-gelatin aerogel microparticles as function of pH.

NMR cryoporometry. NMR cryoporometry measurements were conducted with wet silica and silica-gelatin aerogels containing enough water to completely fill their pores. In the case of the silica aerogel, the cryoporometry curves indicate that the pore structure of the hydrated aerogel is nearly identical to that of the dry gel. [126,127] The general conclusion is that during the hydration of silica aerogels, the monoliths disintegrate into microparticles (cf. **Fig. 5**), but the silica network and the pore structure of the microparticles remain intact. [126,127]

Interestingly, no meaningful NMR cryoporometry curves could be recorded for fully hydrated silica-gelatin hybrid aerogels, regardless of their gelatin content. A melting – freezing hysteresis loop was present in the case of the aerogel with the lowest (4wt%) gelatin content, but well-expressed steps were absent (**Fig. 7**). [126,127] In the case of the hybrids with higher gelatin content, practically no melting and freezing point depressions were detected. Thus, NMR cryoporometry measurements verify the presence of a strong, specific interaction between water and silica-gelatin hybrid aerogels, which alters the pore structure, but no well-defined water droplets were detected in the nanoscale confinement of a solid skeleton. [149]

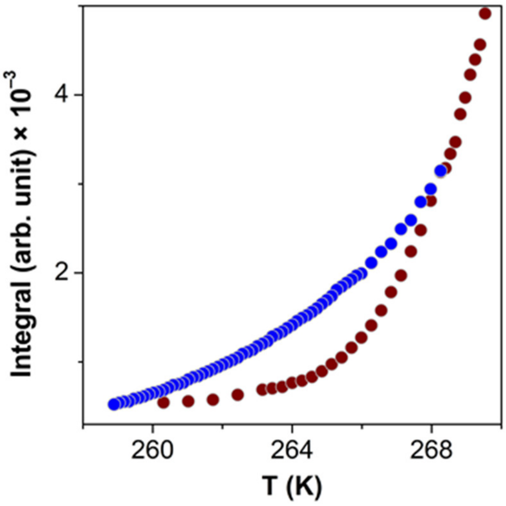

Figure 7. NMR cryoporometry melting (red) and freezing (blue) curves of silica-gelatin aerogel (4wt%) dispersed in water. The absence of inflection points and plateaus on the curves indicates the dense hydrogel like structure of the dispersed aerogel particles with no well-defined pore size distribution.

In order to prove that the observed collapse of the pore network can be attributed to the hydration of the hybrid aerogels, cyclohexane was implemented for cryoporometry. [149] The 1:2 ratio appearance of the melting-freezing hysteresis (**Fig. 8**) suggests the dominating presence of spherical pores in all aerogels. [133] The pore size distribution curves calculated from cyclohexane NMR cryoporometry are in excellent agreement with those measured by N_2 porosimetry for the dry aerogels (cf. **Figs. 3B and 8B**). This means that the pore structures of the dry aerogels are preserved upon solvation by cyclohexane. Total specific pore volume ($V_\mathrm{p}^\mathrm{NMR}$) was calculated from the primary NMR cryoporometry data, specifically from the height of the step associated with the freezing/melting process (see integral values in **Fig. 8A**). [126]

The results show that macropore contribution significantly increases with the increasing gelatin content of the hybrid aerogels. The estimated specific pore volumes (V_p^{NMR}) of the silica-gelatin aerogels are approximately the same regardless of their gelatin content (**Table 3**). This is only an apparent contradiction with the N_2 porosimetry data, where V_p decreases with increasing gelatin content (cf. **Table 1**). Unfortunately, the V_p value is not representative when the macropore contribution is high, because pores larger than ca. 200 nm are excluded from the N_2 porosimetry analysis. Thus, it is more realistic to accept the V_p^{NMR} values measured using cyclohexane to represent the specific pore volumes of the silica-gelatin aerogels.

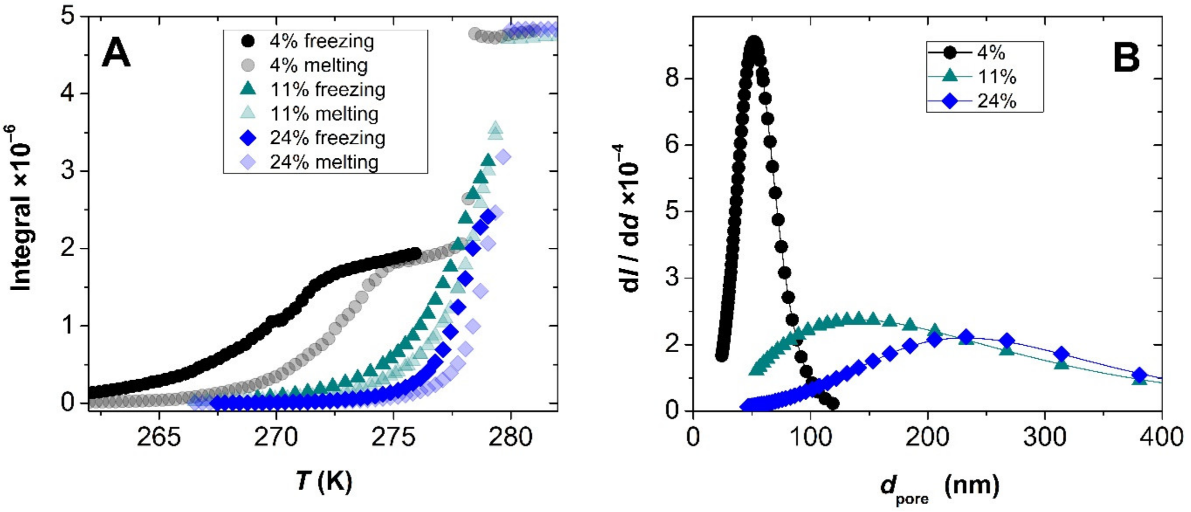

Figure 8. NMR cryoporometry of silica-gelatin hybrid aerogels in cyclohexane. The filling of the pores is complete, and the amount of the bulk-liquid and the pore-liquid is ca. equivalent. Panel A: melting – freezing hysteresis curves. Panel B: Volume equivalent pore size-distribution curves calculated from the data in panel A. The calculation is based on the modified Gibbs-Thompson equations.

Table 3. Structural parameters of silica-gelatin hybrid aerogels estimated from the primary and the derived NMR cryoporometry data (cf. **Fig. 8**).

	V_p^{NMR} (cm³/g) a)	**%mesopore b)**	**%macropore b)**
4wt% gelatin	3.4 ± 0.5	38	62
11wt% gelatin	4.5 ± 0.5	< 10	> 90
24wt% gelatin	4.3 ± 0.5	< 10	> 90

a) Total specific pore volume; b) Cumulative volume equivalent mesopore and macropore contributions derived from pore size distribution.

NMR diffusiometry. When the pores of silica aerogel are completely filled with water, only one characteristic diffusion domain is present. [127] The value of the single observed D_{obs} is set by the ratio of confined water in the pores and bulk water. This indicates that *i*) the primary hydration sphere of the silica network is not large enough to form an independent diffusion domain in the sample, and *ii*) the interchange of water in the pores and in the bulk phase is facile. Accordingly, the pore network of hydrated silica aerogel is open and permeable. [127]

The apparent self-diffusion coefficient of water (D_{obs}) in hydrated silica-gelatin aerogels was measured by PGSTE NMR experiments. The effect of 2 variables was tested: *i*) the water content of the hybrid aerogel samples, and *ii*) the observation time of the diffusion experiments. [158,159] First, it was established that the D_{obs} values are independent of the observation time at $\Delta \geq 40$ ms in all hydrated silica-gelatin aerogels. Thereafter, the effect of water content on D_{obs} was measured using high observation times. Two diffusion domains were detected for aerogels of lower gelatin content (4 – 11wt%) at water contents below 2.0 g/g (**Fig. 9**). The slower diffusion domain is characteristic for water molecules in the primary hydration sphere of the hybrid backbone, [225] while the faster domain represents water molecules moving more freely inside the pores. The 2 domains are in slow exchange with each other, and the slower diffusion domain vanishes when the water content of the sample is increased. After the saturation of the hydration sphere, most of the water diffuses in the pores and this phase dominates the NMR signal. Interestingly, only 1 diffusion domain is present in the hydrated 24wt% gelatin aerogel, regardless of the water content of the sample (**Fig. 9**). This single D_{obs} value systematically increases with increasing water content. Hydrogels typically show this behavior. [226] At high water contents, all hydrated silica-gelatin aerogels display the same, single apparent self-diffusion coefficient for water, independently of the gelatin content of the matrix (**Fig. 9**). The highest observed self-diffusion coefficient of water is ca. 2.0×10^{-5} cm^{2}s^{-1} in the aerogel samples, while that is 2.3×10^{-5} cm^{2}s^{-1} in the pure bulk phase at 25 °C. [227]

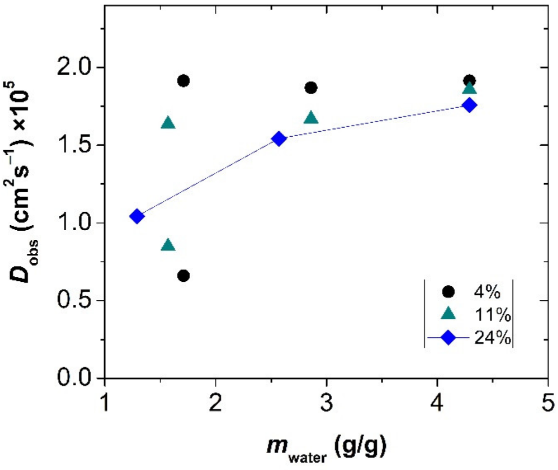

Figure 9. NMR diffusiometry of hydrated silica-gelatin hybrid aerogels. Two diffusion domains are present in aerogels of low gelatin content (4 – 11wt%) at low water content (< 2.0 g/g), and this is reduced to a single diffusion domain at high water content. Only one diffusion domain is present in the hydrated 24wt% gelatin aerogel, regardless of its water content. See legend for gelatin content in wt%.

These results indicate, that hybrid aerogels with lower gelatin content retain a more or less permeable pore structure when treated with water, but hydrated 24wt% gelatin aerogel attains hydrogel-like characteristics even at low water content.

NMR relaxometry. Relaxometry measurements were performed with hydrated silica and silica-gelatin aerogels of different water contents (**Fig. 10**). In accordance with the classical theory, we propose that the faster relaxation domain represents the hydration sphere of the aerogel backbone, and the slower relaxation domain represents water situated farther from the pore walls, e.g. in puddles forming in focal points of the aerogel network. The reciprocal value of T_2 is plotted as function of the reciprocal value of filling factor f (**Fig. 10B**). The total specific pore volumes of the wet aerogels, representing the unity filling factor ($f = 1$), were estimated from NMR cryoporometry data and are referred to as V_p^{NMR} (**Table 3**). The $1/T_2$ vs. $1/f$ plots are meaningful only when constructed for the uppermost water layer, i.e. for the slowest relaxation (high T_2) domain. As seen in **Fig. 10B**, the $1/T_2$ vs. $1/f$ plots are linear, and thus, follow equation (4). [137] Thus, the filling of the pores of the aerogels is assumed to be a continuous process, which begins with the formation of a uniform, thick adsorption layer of water throughout the solid network. At higher water contents, puddles appear inside the pores. The $k = 1$ value suggests that there is a strong interaction between the homogeneous hydration layer and the puddles filling the pore interiors. This is reasonable, since both silica and silica-gelatin are extremely hydrophilic. [225] As seen in **Fig. 10C**, the normalized amplitudes of the two domains are in close correlation with each other in every aerogel sample, especially at low water content (< 2.0 g/g). According earlier considerations, this can be attributed to a moderately fast exchange between the 2 relaxation domains of water in wet aerogels. [136,228]

One remarkable difference can be observed between the hydration mechanism of silica and silica-gelatin aerogels. The observed trend for the T_2 values of hydrated silica aerogel is typical for solid, hydrophilic mesoporous materials that retain their open pore structures, characteristic at their dry state, even when completely filled with water. [135] In contrast, there is an upward break in the trend of the T_2 relaxation times of silica-gelatin samples at around 2.0 g/g water content, as seen in **Fig. 10A**. At water contents lower than this threshold value, the wetting process of silica and silica-gelatin is practically the same, and can be attributed to the hydration of a hydrophilic mesoporous solid network.

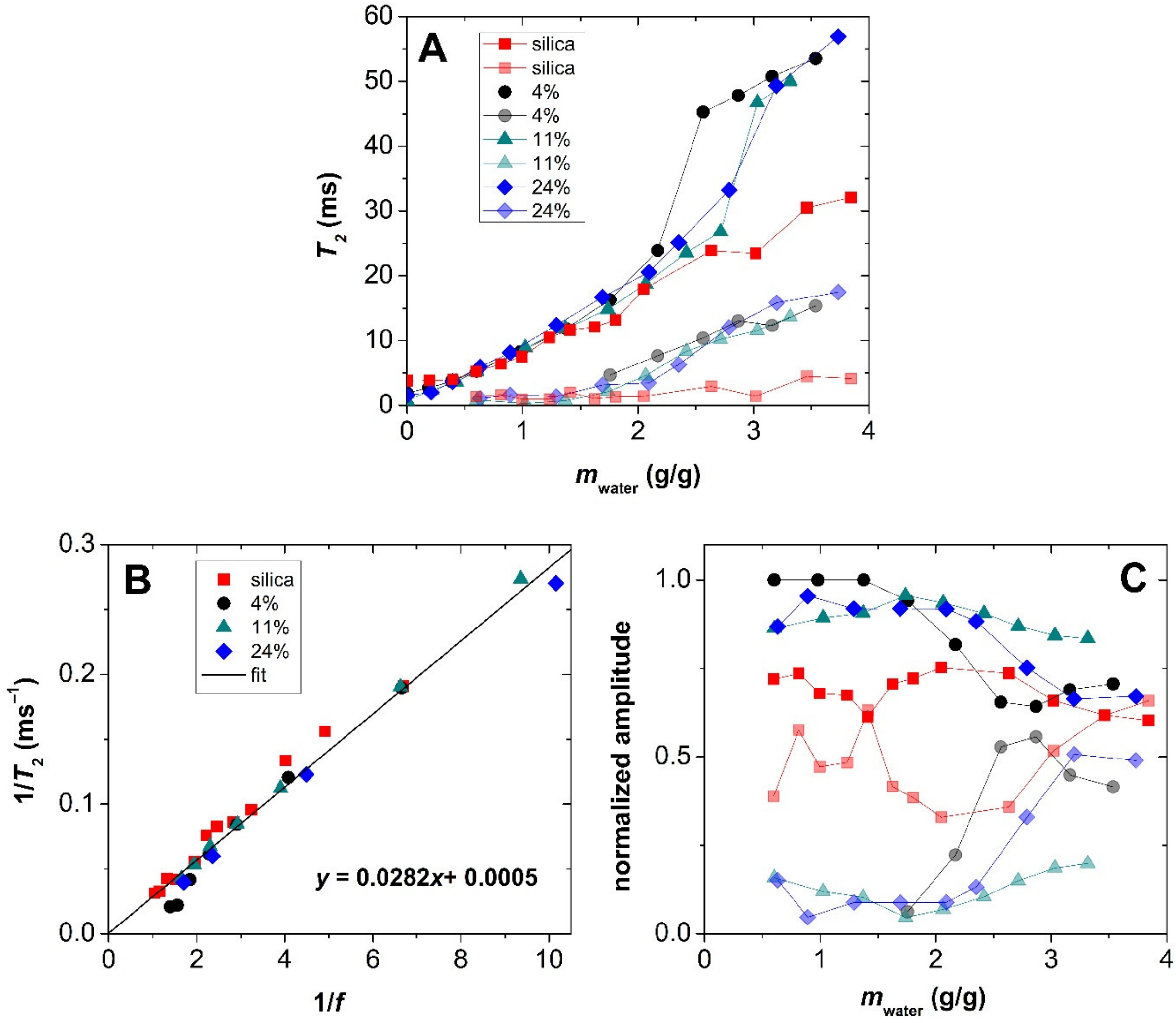

Figure 10. NMR relaxometry of hydrated silica and silica-gelatin hybrid aerogels. Two relaxation domains are present for each aerogel at mass ratios higher than 0.5 g water / g aerogel. Panel A: T_2 as function of water content. Panel B: reciprocal T_2 as function of reciprocal filling factor (f) for the fast relaxation domain. Panel C: normalized amplitude of each relaxation domain (cf. panel A).

At high water contents, the T_2 values steeply increase in silica-gelatin samples for both of the interchanging relaxation domains. This indicates that water is no longer bound to well-defined solid surfaces or confined in well-defined pores in these samples. Thus, it is reasonable to propose that at higher water content (> 2.0 g/g), silica-gelatin matrices reach a critical level of hydration that induces the formation of hydrogel-like structures, which is parallel to the extensive deformation of the hydrated aerogel backbone. This process is also well-expressed by the noted increase of the observed single self-diffusion coefficient of water by increasing water content in the case of the 24wt% gelatin aerogel (cf. **Fig 9**).

SANS of hydrated aerogels. The SANS curves obtained for silica and silica-gelatin aerogels saturated with 3.3 g/g D_2O are shown in **Fig. 11**. No hydration microdomains were observed.

[229] All scattering curves can be fitted with the Beaucage model (cf. **Table 2**). Obvious structural changes can be observed above 11wt% gelatin compared to the dry state. The SANS curve of the hydrated 24wt% gelatin hybrid contains information only in the Porod region meaning that the characteristic mesoporous network does not exist anymore in the sample. This is in-line with the structural information deduced from NMR diffusiometry and relaxometry.

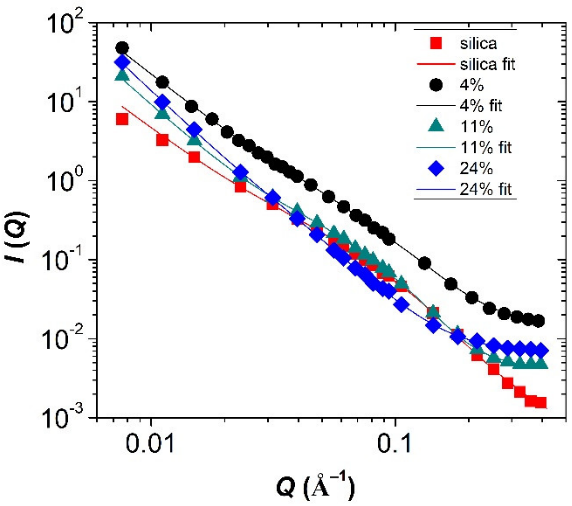

Figure 11. SANS curves of silica and silica-gelatin hybrid aerogels completely filled with D_2O (3.3 g liquid / g aerogel). Solid lines represent data fitting to Beaucage model (cf. **Table 2**).

V-1.1.1.3. Summary of structural characterization

The SANS, SEM and N_2 porosimetry results of the dry aerogels are in good agreement. All techniques suggest that the solid frameworks of the hybrid aerogels are somewhat looser and less barred than that of the parent silica aerogel. The number of macropores is higher, and the total mesopore volume decreases with increasing gelatin content. Contrast variation SANS experiments prove that silica-gelatin is hybridized on the molecular level. Thus, gelatin does not form an outer “layer” on the inner pore walls, or shows any spatial preference in the matrix.

NMR and SANS measurements showed that the well-defined mesoporous structure of pristine silica aerogel is preserved when the material is immersed into water, but the pore-structures of silica-gelatin hybrid aerogels significantly change upon hydration. At low gelatin content (4–11wt%), the structure is permeable and open, yet not as open, as it is in its in dry state. Hybrid aerogels with high gelatin content (18–24wt%) show hydrogel-like characteristics in water, as their open pore structure collapses due to the extensive hydration of their backbones.

V-1.1.2. Mechanism of drug release from aerogel carriers

Structure of active ingredient in aerogel. Silica and silica-gelatin aerogels were impregnated with ibuprofen and with ketoprofen by using the well-established technique of adsorptive precipitation in supercritical CO_2. [83,126,205] The ibuprofen content of the loaded aerogels varies between 19 and 24wt%, and the ketoprofen content varies between 11 and 15wt%. It is proved by XRD that the active ingredients are amorphous in the loaded aerogels.

Kinetics of drug release. The rate of drug release from the hybrid aerogel of the lowest gelatin content (4wt%) is one order of magnitude higher than the rate of drug release from the parent silica aerogel carrier. A possible explanation for this phenomenon is that the facile hydration and erosion of the 4wt% gelatin matrix is the driving factor leading to the rapid desorption and dissolution of the drugs. [126] The kinetics of drug release displays an obvious correlation with the gelatin content of the hybrid aerogel carriers as seen in **Fig. 12**. High gelatin content (11–24wt%) alters both the rate and the mechanism of drug release. The initial stage of release becomes significantly slower, and the overall shape of the kinetic curve reveals a diffusion limited release mechanism. The release curves were fitted with widely accepted semi-empirical models. [92,93] Drug release curves in the case of the 4–11wt% gelatin aerogels can be fitted using the Hopfenberg model, which is a semi-empirical model used to describe drug release from eroding carriers where a zeroth order surface detachment is the limiting step of the release:

$$\frac{M_t}{M_{max}} = 1 - (1 - k_{\mathrm{obs1}} t)^{n_1} \qquad (11)$$

Here, M_t and M_{max} are the cumulative absolute amounts of drug released at time t and at infinite time, respectively. The rate constant is k_{obs1}, which depends on the concentration of drug in the system and on the physical dimensions of the carrier. Parameter n_1 is a shape factor representing the geometry of the carrier: spherical ($n_1 = 3$), cylindrical ($n_1 = 2$) or slab ($n_1 = 1$). The shape factor was fixed at $n_1 = 3$ for fitting release curves in the case of the aerogel carriers. In the case of the aerogels of low-gelatin content, the kinetic curves start with a steep increase, i.e. burst release in the first 30 s. An initial burst, such as this is characteristic for the release curves of erosion driven delivery systems. On the other hand, it is natural to assume that gelatin forms a hydrogel, thus using it as a matrix component leads to slower, diffusion limited drug release. An empirical model to describe diffusion controlled release is the Peppas model:

$$\frac{M_t}{M_{\mathrm{max}}} = k_{\mathrm{obs2}} t^{n_2} \qquad (12)$$

The rate constant is k_{obs2}, which incorporates the structural and geometric characteristics of the delivery system. The limiting value of the n_2 exponent changes with the geometry of the carrier vehicle and it also depends on the particle size distribution of the delivery system. Drug release curves measured in the case of the 18–24wt% gelatin hybrid aerogel carriers cannot be fitted using the Hopfenberg model, but adequate fits were obtained using the Peppas model at fixed $n_2 = 0.43$ value until ca. 65% cumulative release. (The limit of 65% is naturally set by the model itself, because the Peppas model is a short-time approximation.) [230,231] It is evident by examining the first 30 s of the experimental kinetic curves, that the erosion controlled initial burst release is also suppressed in the case of the high-gelatin hybrid aerogel carriers.

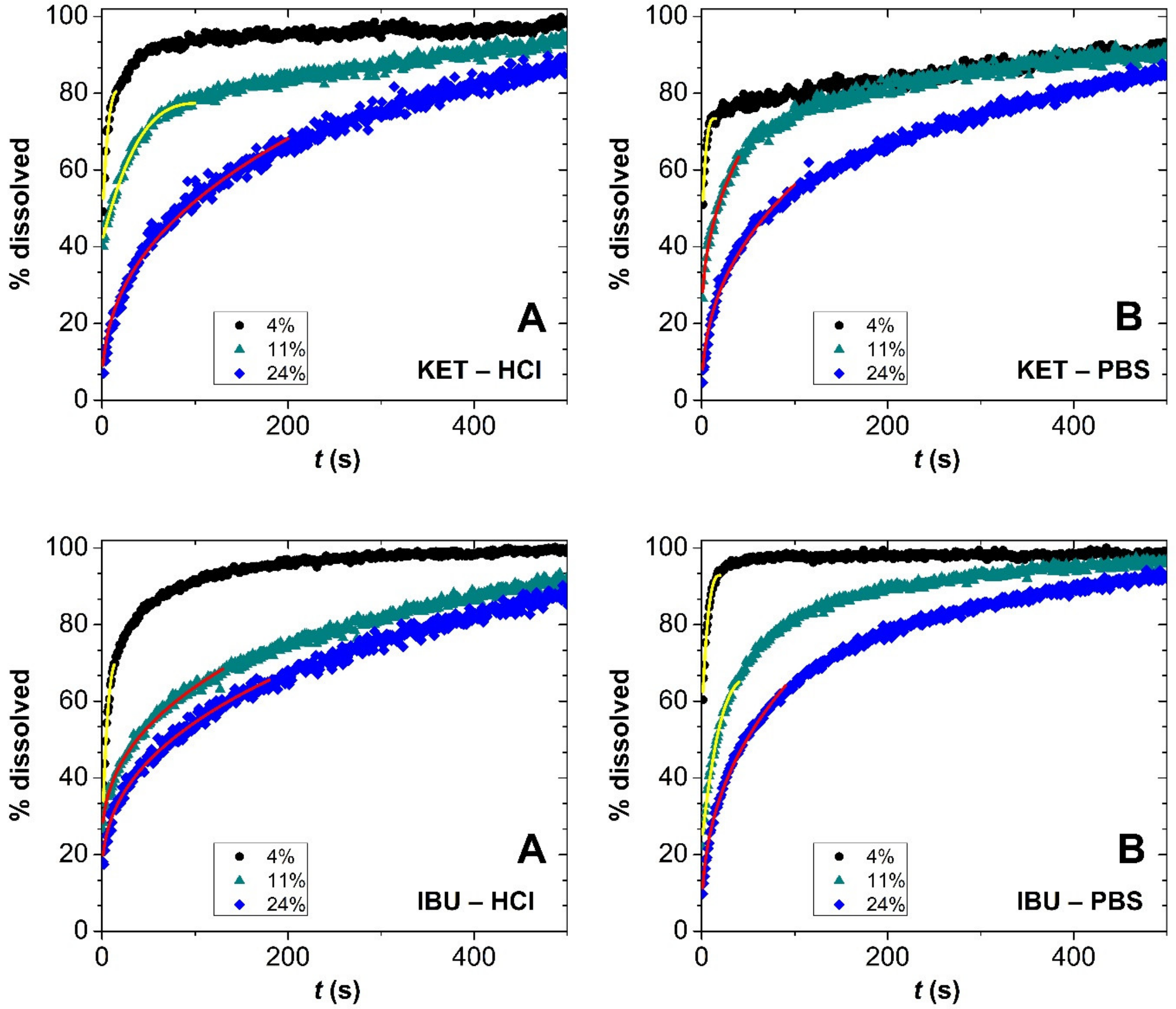

Figure 12. Drug release experiments. The dissolution of ketoprofen (KET) and ibuprofen (IBU) from silica-gelatin hybrid aerogels containing 4 – 24 wt% gelatin in pH = 2.0 HCl solution (A) and in pH = 7.4 PBS (B). Continuous lines represent model fitting: yellow – Hopfenberg, red – Peppas. Mass of loaded aerogel: 1.50 mg, volume of release medium: 3.0 mL, T = 37.0 °C, 300 rpm stirring.

Mechanism of drug release. The main point of the present study is to show that the shifting of the drug release mechanism from erosion facilitated to diffusion controlled in the hybrid aerogels is the direct consequence of the hydration induced structural changes in the backbone in correlation with its gelatin content. [45,47] At low gelatin contents (4–11wt%), erosion and hydration facilitated fast release takes place. The initial aerogel monoliths disintegrate to microparticles, and the adsorbed amorphous drug gets in contact with the release medium through the open pores. The strong interaction between the water molecules and the aerogel backbone repels the adsorbed drug leading to its fast release, as evidenced by the initial burst in the release curves. [126,219] Water hydrates the silica-gelatin backbone, but the gelatin content is too low for the formation of a dense hydrogel at 4–1wt% gelatin. The pores remain open and permeable for the drug molecules. Higher gelatin content (18–24wt%) significantly alters the release mechanism. The disintegration of the monoliths also takes place, but now the gelatin content is sufficiently high for the formation of a continuous hydrogel that practically entraps the loaded drug, and the hindered diffusion of the drug through this hydrogel becomes the rate limiting factor. The formation of the hydrogel also suppresses the initial burst release.

The rate of drug release depends on pH, because the strength of the interactions between the drug molecules and the aerogel skeleton is pH-dependent and changes with the effective charges of these. [46,232] Protonated molecules form hydrogen bonds with polar surface groups, therefore their release is slower than that of the deprotonated species. [46,232] The kinetic curves recorded at pH = 7.4 stop at ca. 90% even at the long time-scale. This suggest that the adsorption-desorption equilibrium of the active ingredient between the carrier and the aqueous medium has an additional influence on drug release at pH = 7.4. [233]

V-1.2. Hydration of hybrid silica-casein aerogels – intact backbone architecture [P3]

One particular characteristic of silica-biopolymer hybrid aerogels is, that the extensive hydration of the biopolymer components in water causes the distortion and the swelling of the backbone, which leads to the partial or complete collapse of the open porous structures. [126,129,234] The collapse of the pores leads to the decrease of the specific surface area and the hindrance of mass transport in the hydrated aerogel particles. Thus, designing hybrids that do not display these adverse hydration properties is in high demand.

In order to meet the above detailed requirements, we synthesized silica-casein hybrid aerogels of casein contents varying from 5wt% (SC5) to 30wt% (SC30). The dry aerogels were characterized by SEM, FT-IR, N_2-sorption porosimetry and SANS. The interaction of the silica-casein aerogels with water was thoroughly investigated by SANS and NMR techniques. [123]

V-1.2.1. Morphology of dry aerogels

Representative SEM images of pristine silica-casein hybrid aerogels are shown in **Fig. 13**, and corresponding N_2 adsorption-desorption isotherms are shown in **Fig. 14**.

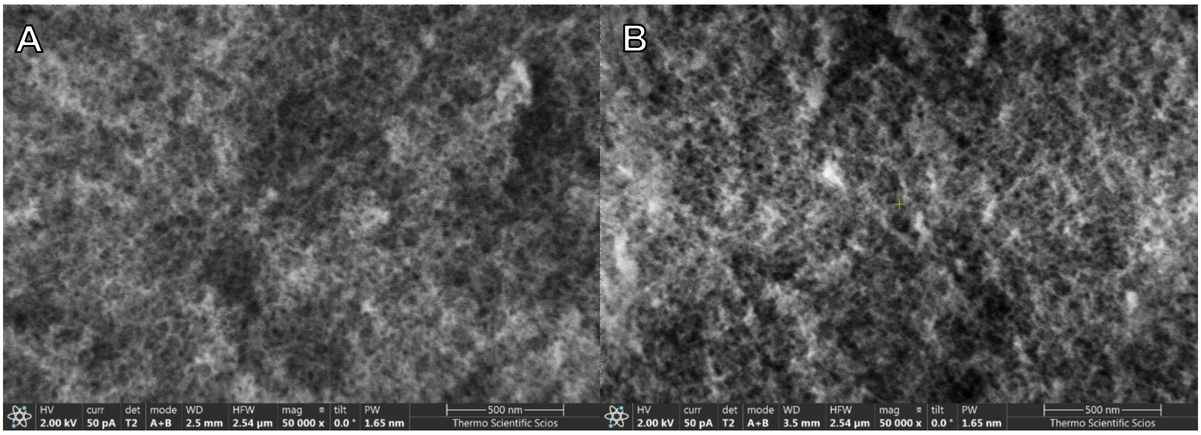

Figure 13. SEM images of silica-casein hybrid aerogels A: 5wt% casein content, B: 30wt% casein content. Magnification is ×50k, and the scale bar shows 500 nm.

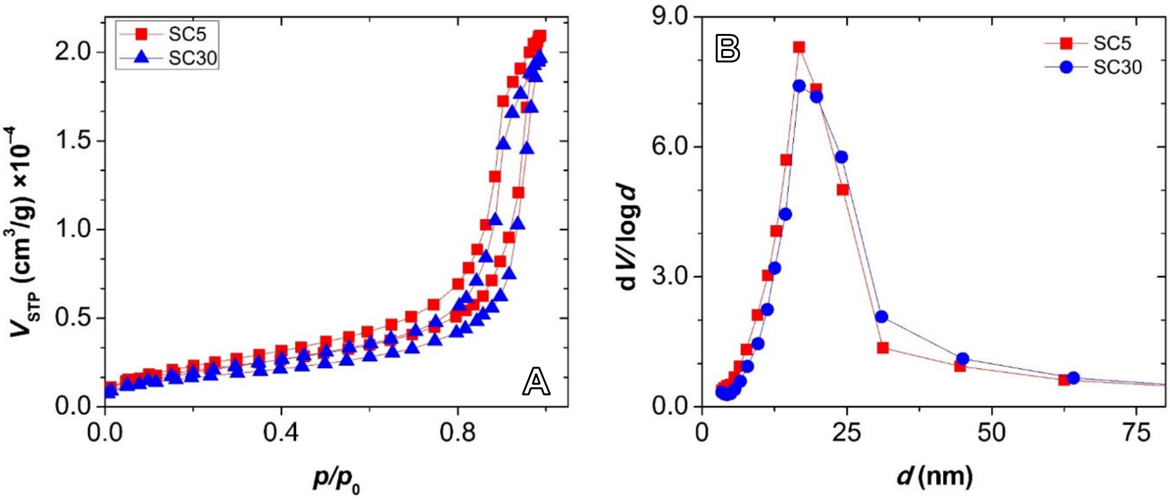

Figure 14. Panel A: Nitrogen adsorption-desorption isotherms of pristine silica-casein aerogels. Panel B: pores size distribution curves calculated from the desorption isotherms using the BJH method. Estimated structural parameters are summarized in **Table 4**.

All N_2-sorption hysteresis curves can be classified as IUPAC IV category with a H3 type loop, which is characteristic for mesoporous materials with a small number of macropores. [14] There is no steep rise in the isotherms at $p/p_0 = 1$, which indicates that the contribution of macropores is negligible. According to the *t*-plot method, the contribution of micropores is also negligible to the total porosity. [220] The specific surface area of the hybrid aerogels decreases with the increase of their casein content (**Table 4**). The pore size distribution curves are practically equivalent for all aerogels with a mean pore size of ca. $d_{\text{pore}} = 20$ nm (**Fig. 14**).

Table 4. Structural parameters of silica-casein aerogels estimated by the BET and the BJH methods from N_2 adsorption-desorption porosimetry data (cf. **Fig. 14**).

Parameter	SC5	SC30	Data evaluation
***C*-constant**	70.7	58.3	BET
Specific surface area (m^2/g)	750	612	BET
Average pore size (nm)	17.3	19.9	BJH
Total pore volume (cm^3/g)	3.22	3.03	BJH

V-1.2.2. Structural characteristics of hydrated aerogels

The morphology of the hydrated hybrid aerogels was investigated by SANS, while the spatial localization and mobility of water was probed by NMR relaxometry, cryoporometry and diffusiometry. Importantly no macroscopic swelling was detectable for any of the materials.

Morphology of hydrated aerogels by SANS. Silica-casein aerogels were hydrated by adding 3.5 g H_2O to 1.0 g aerogel. This amount of water fully hydrates the backbone and fills the pores, as shown by NMR cryoporometry (*vide infra*). The corresponding SANS scattering curves (**Fig. 15**) are practically identical to those measured in the dry states of the aerogels.

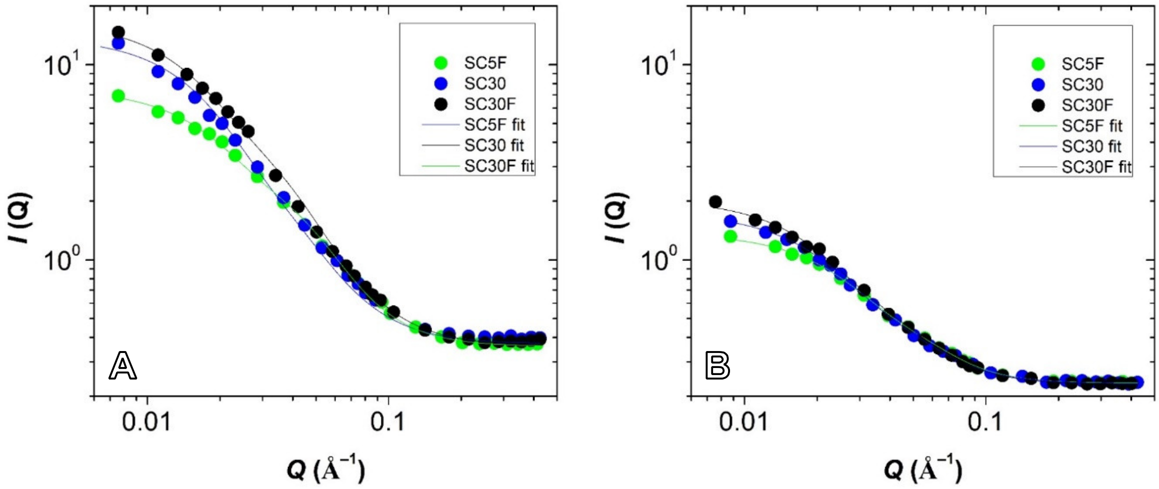

Figure 15. Small angle neutron scattering (SANS) curves of fully hydrated silica-casein aerogels. Panel A: Silica-casein aerogels hydrated by H_2O (3.5 g liquid / g aerogel). Panel B: Silica-casein aerogels hydrated by H_2O:D_2O 2:1 mixture (3.5 g liquid / g aerogel). Solid lines represent data fitting with the Beaucage model. The estimated structural parameters are given in **Table 5**.

The structural parameters (R_g and p) estimated with the Beaucage model are given in **Table 5**. The value of the power law exponent (p) does not change significantly by the hydration of the aerogels, while the value of the gyration radius slightly increases for all hybrids. However, the increase of the value of R_g is negligible compared to the hydration induced alteration of the R_g

values of such silica-gelatin aerogels that significantly swell on the microscopic level. [129] In the case of the silica-casein aerogels, the minor increase of the R_g value is attributed to the formation of an extensive hydration sphere on the solid backbone, which is well expressed in the NMR relaxometry data (*vide infra*). Thus, the high similarity of the SANS curves of the dry and the hydrated silica-casein aerogels indicates that the porous structures of the hybrids are practically not altered upon hydration. [167,229]

Table 5. The values of the gyration radius (R_g) and the power law exponent (p) for dry and hydrated silica-casein aerogel samples. Parameters were estimated by fitting experimental small angle neutron scattering (SANS) curves with the Beaucage model (**eq. 8**).

	dry	**hydrated (H_2O)**	**hydrated (2:1 H_2O:D_2O)**
SC5F	$R_g = 67 \pm 2$ Å $p = 2.6 \pm 0.1$	$R_g = 77 \pm 3$ Å $p = 2.8 \pm 0.1$	$R_g = 59 \pm 2$ $p = 3.0 \pm 0.1$
SC30	$R_g = 78 \pm 2$ Å $p = 3.1 \pm 0.1$	$R_g = 93 \pm 3$ Å $p = 2.5 \pm 0.1$	$R_g = 68 \pm 2$ $p = 2.6 \pm 0.1$
SC30F	$R_g = 81 \pm 2$ Å $p = 3.0 \pm 0.1$	$R_g = 98 \pm 3$ Å $p = 2.6 \pm 0.1$	$R_g = 70 \pm 2$ $p = 2.6 \pm 0.1$

Homogeneity of aerogel backbone by SANS. Contrast variation experiments were performed by filling the silica-casein aerogels with a H_2O:D_2O 2:1 (64wt% H_2O and 36wt% D_2O) mixture, because this liquid has the same SLD value as casein. [235,236] The scattering intensities of the hybrid aerogels filled with this mixture were one order of magnitude lower than those of the aerogels filled by pure H_2O (**Fig. 15**). Nevertheless, the scattering curves are still structured, and can be fitted with the Beaucage model. The values of the power law exponent (p) are similar to those that are characteristic for the silica-casein aerogels in the dry sate, while the R_g values are slightly lower than those measured in the dry state (**Table 5**). This indicates, that the main structural features and the spatial distribution of the silica component in the hybrid backbone is practically the same as in the dry state of the material. When the contrast is reduced, the scattering pattern does not change significantly, suggesting that silica and casein do not form separate nanometer-sized domains and their hybridization is complete.

NMR cryoporometry. The size of the confined water puddles in the silica-casein backbone were determined by NMR cryoporometry at water contents of 5.0 g H_2O / 1.0 g dry aerogel. A representative melting-freezing curve is shown in **Fig. 16** for SC5. The ratio of the height of the two steps in the cryoporometry curve indicates that the ratio of pore water and bulk water is ca. 1:1.7 in the sample of 5.0 g/g water content. The difference between the melting and the freezing points of pore water and bulk water gives a 2:3 ratio, which indicates the dominating presence of spherical pores in the hydrated aerogel. [133,146,150,151] Similar hysteresis curves were obtained for each hybrid aerogel. Pore size distributions (**Fig. 16B**) were calculated by using K_c = 30 nm K^{-1} for water in the Gibbs-Thompson equations (**eqs. 3-4**). [149,237,238] The pore size distribution curves of the hydrated aerogels are in good agreement with those measured by N_2 porosimetry in the dry states of the aerogels (cf. **Fig. 14**). Overall, NMR cryoporometry shows that the porous structures of the silica-casein hybrid aerogels remain intact even when the matrices are fully hydrated and the pores are completely filled by water. [127,147,148] This conclusion is in complete agreement with the SANS results.

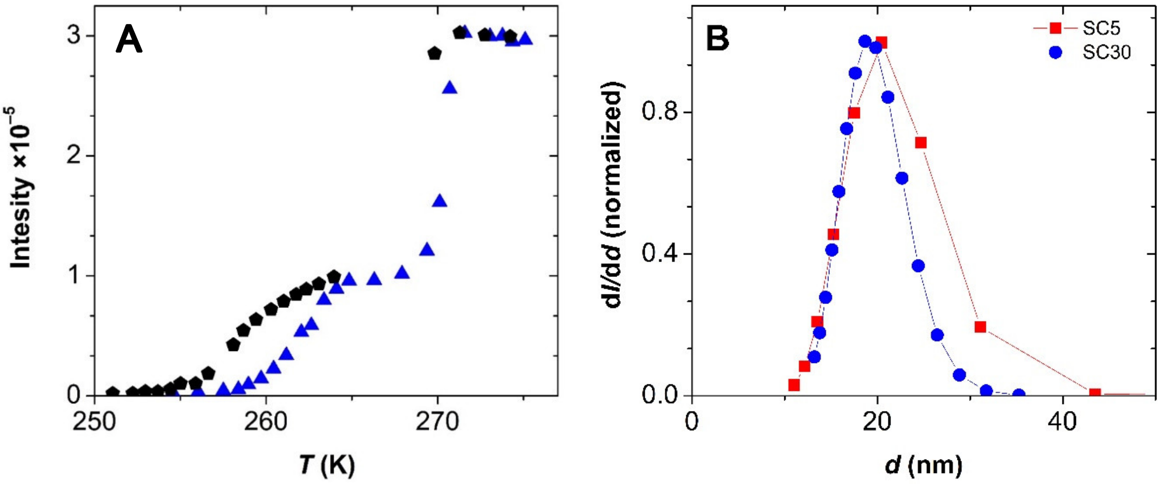

Figure 16. NMR cryoporometry of hydrated silica-casein aerogels. Panel A: Intensity of the water signal as function of temperature during the melting (blue) and the freezing (black) processes of the hydrated SC5 aerogel. Panel B: Pore size distributions calculated using the Gibbs-Thompson equations (**eq. 4**).

NMR relaxometry. Silica-casein aerogels were gradually hydrated until the saturation of the pores at ca. of 3.4 g/g water content. In general, the NMR relaxometry data is almost identical for all silica-casein aerogels. Two relaxation domains can be detected in all hydrated aerogels even at the lowest water content (**Fig. 17**). The domain with the smaller T_2 is attributed to solvent molecules in strong interaction with the surface of the aerogels, i.e. the primary hydration sphere of the silica-casein backbone. [239,240] Accordingly, the value of the smaller T_2 relaxation time only slightly changes with the water content of the aerogel. [241] The higher T_2 values are attributed to the average relaxation of water molecules moving more freely inside the pores. The higher T_2 increases monotonously with increasing water content, because the constraint of the molecules decreases due to the formation of quasi bulk phases by filling the pores. [121,135-138,154] The amplitudes of the 2 relaxation domains are in correlation with each other (**Fig. 17B**). The most feasible explanation for this phenomenon is that water molecules exchange between the 2 domains within the timeframe of the relaxation experiment, but their signals remain mathematically separable. [240] In the case of limiting slow exchange, the amplitude of the high T_2 domain representing the puddles are expected to monotonously increase with increasing water content. [135-137]

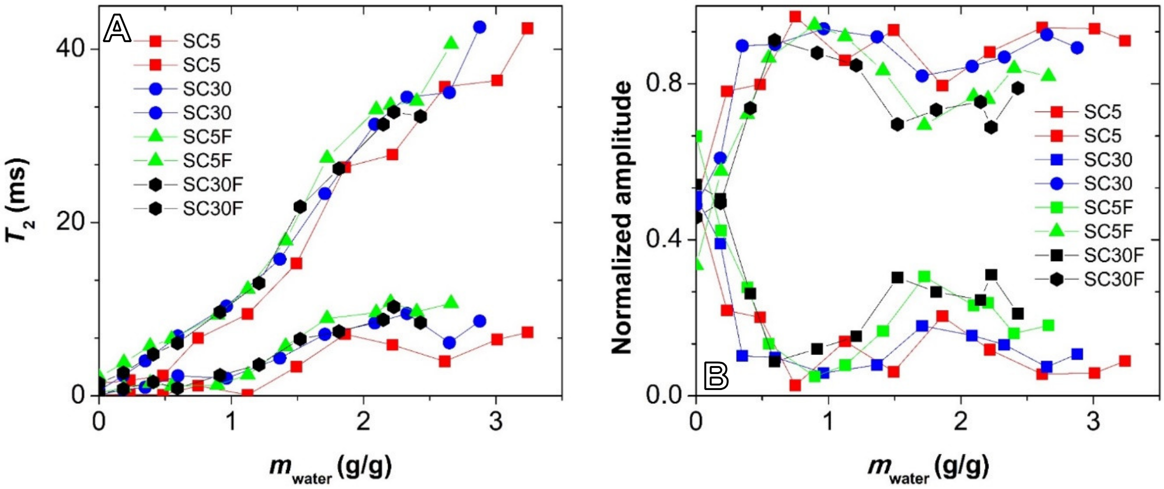

Figure 17. NMR relaxometry of hydrated silica-casein aerogels. Panel A: Experimental T2 relaxation times of water as function of water content of hydrated aerogels. Panel B: The normalized amplitudes corresponding to the relaxation processes shown in panel A.

The above described hydration mechanism is typical for hydrophilic mesoporous silica materials. [122] When water content increases, the puddles (higher T_2) are connected into a coherent fluid layer inside the pores, and partially fill these. The reciprocal filling-factor (1/*f*) plots suggest that the subsequent saturation of the pores by water is monotonous. [137,142]

By compiling the results of NMR relaxometry, two main conclusions can be drawn. 1) The hydration mechanism of all hybrid silica-casein aerogels is practically the same as that of archetypical mesoporous purely silica materials. 2) The amount of the incorporated casein has no detectable effect on this hydration mechanism.

NMR diffusiometry. The self-diffusion of water in the hydrated aerogels were measured by varying the observation time between 10 and 140 ms. [156,157,242] Only one diffusion domain was detected in all samples independently of the observation time, and also independently of the water content of the hydrated aerogels (**Fig. 18**). However, this single D_{obs} value increases with the increasing water content of the hydrated aerogels, regardless of their chemical composition. This indicates that water molecules of different spatial localization are in fast exchange with each other in the timescale of diffusiometry. [243] These results strongly suggest that the porous structure of the hydrated silica-casein aerogels are open and highly permeable, as it is in the case of the hydrated parent silica aerogel. [127,153]

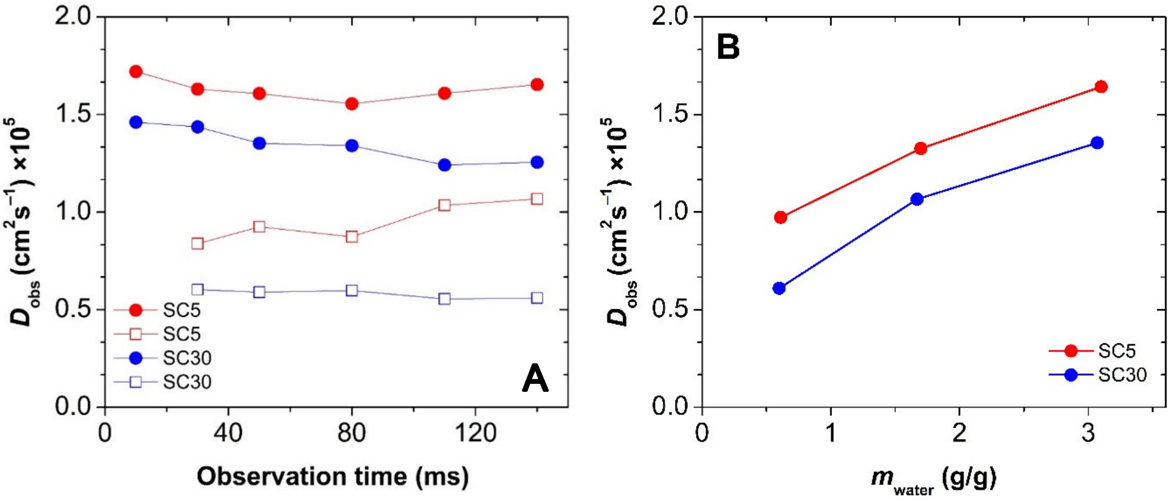

Figure 18. Self-diffusion of water in hydrated silica-casein aerogels measured by NMR diffusiometry. Panel A: Observation time dependence of the self-diffusion coefficient (D_{obs}) of hydrated SC5 (red) and SC30 (blue) aerogels at two different water contents (open symbol: 0.6 g/g; filled symbol: 3.1 g/g). Panel B: Dependence of D_{obs} on the water contents of the hybrid aerogels.

The D_{obs} values are lower at high casein content. As the pore size distributions and the hydration mechanisms are practically the same for all the hydrated silica-casein aerogels, the decrease in D_{obs} is attributed to the assumable higher tortuosity of the high casein content aerogels. For comparison, the D_{obs} value measured in the completely filled parent silica aerogel is 1.9×10^{-5} cm^2 s^{-1}, while this is 2.3×10^{-5} cm^2 s^{-1} in bulk water. [127,227]

Unique hydration and wetting of silica-casein aerogels. As a summary of the characterization of silica-casein aerogels in their wet states, it can be stated that the structural properties of these hydrated hybrids are almost identical to those of the hydrated parent silica aerogel. [127,135] The hydrated silica-casein aerogel particles retain their open mesoporous structures even when completely filled with water. Interestingly, this unique feature of a hybrid inorganic-biopolymer aerogel is almost independent of its casein content. Even partial hydration induces the fast disintegration of the silica-casein aerogel monoliths into microparticles ($d_{particle}$ = 15 µm), but the pores of the hydrated particles remain intact and highly permeable for water. This is highly unusual for inorganic-biopolimer hybrids. [126,129] The hydration of the protein components usually causes the extensive swelling and deformation of the solid backbone of the hybrid, which results in the partial or complete collapse of the pore structure. [154,225,226,228]

V-1.3. Hydration and wetting of borosilicate-PVA hybrid aerogels [P4]

Silica-based hybrid aerogels are of special interest in biomedical research, because of the unique combination of the properties of the inorganic and organic parts that can be utilized in drug delivery and tissue regeneration [244,245]. Borosilicate – polyvinyl alcohol (PVA) hybrid aerogels synthesized previously in our laboratory show promising biological activity when interacting with dental pulp stem cells [207]. This generated the need for the in-depth characterization of the hybrid aerogel microparticles in their fully hydrated states representative to the conditions in bio-fluids. The combination of liquid phase NMR methods and SANS techniques were used [134,246,247]. Three aerogels were studied: pristine borosilicate aerogel (BS), borosilicate-PVA hybrid aerogel (BSP), and borosilicate-PVA hybrid aerogel containing embedded hydroxyapatite (HAp) particles (BSPH). No macroscopic swelling could be detected when wetting these aerogels.

V-1.3.1. Structural characteristics of the dry aerogels

Chemical structures of aerogels. A comprehensive IR and ssNMR study was conducted to investigate the chemical structures of the aerogels [207]. These results show the presence of silica, boria and PVA in the hybrid skeletons, but the existence of Si-O-B or Si-O-C bonds could not be verified unambiguously. [248,249]. Nevertheless, the nanoscale homogeneity of the hybrid skeleton was proved using contrast-variation SANS measurements, as detailed in the next section. Representative TEM-EDS images that display the incorporated HAp particles in the skeleton of the BSPH aerogel are shown in Ref. [207]

Morphologies of dry aerogels. All of the studied aerogels display the classical morphology of silica-based aerogels [127] with few macropores also visible in the SEM images (**Fig. 19**). The hybridization of borosilicate with PVA causes the formation of large aggregates in the skeleton of BSP and BSPH, which results in the formation of a significant number of macropores. A similar effect has been observed earlier when silica was hybridized with biopolymers.

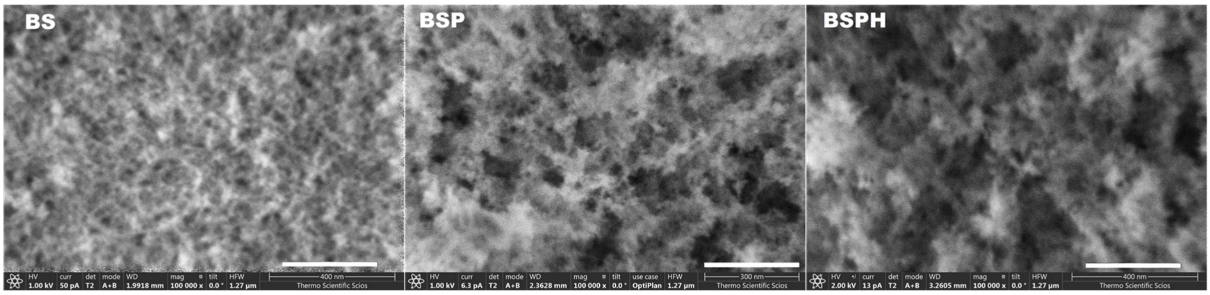

Figure 19. Scanning electron microscopy (SEM) images of the BS, BSP and BSPH aerogels in 100k× magnification. The scale bars are 300 nm.

Interestingly, the incorporation of HAp does not cause any further visible change in the morphology. The explanation is that the shape and the size of the incorporated HAp particles are very similar to those of the aggregates in the hybrid skeleton of BSPH. [207]

Representative N_2-sorption isotherms are shown in **Fig. 20**. All of the hysteresis curves are IUPAC type IVa with H3 class hysteresis loops. These isotherms are characteristic for dominantly mesoporous materials with different proportions of macropores. [14] The structural parameters calculated from the isotherms are given in **Table 6**.

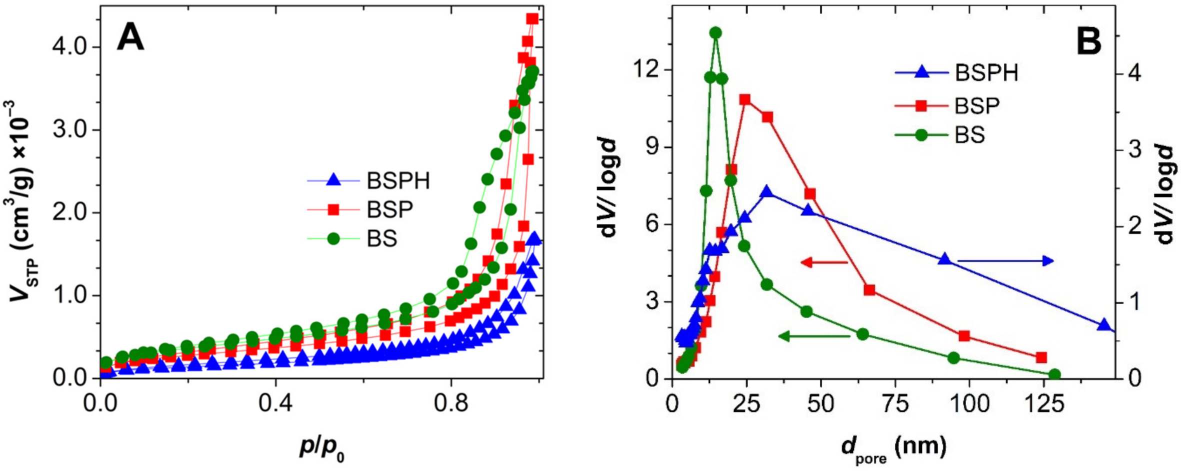

Figure 20. Panel A: N_2 adsorption-desorption isotherms of the as-prepared aerogels. Panel B: pore size distributions calculated from the desorption isotherms using the BJH theory.

Table 6. Morphological parameters of the as-prepared aerogels calculated from the N_2-adsorption-desorption data. (The ±values are the corresponding standard deviations.)

Code name	**Apparent surface area (m^2/g) / 1000**	**Characteristic mesopore diameter (nm)**	**Apparent pore volume (cm^3/g)**
BS	1.3 ± 0.1	17	5.7 ± 0.2
BSP	1.0 ± 0.1	28	6.7 ± 0.3
BSPH	0.52 ± 0.05	42	2.6 ± 0.1

The morphological features of BS are practically the same as those of a typical silica aerogel. The aggregation of the primary particles in the hybrid skeleton of BSP shifts the pore size distribution toward the macropore range, but most of the pores are still smaller than 100 nm. However, the mesoporosity of BSPH is significantly reduced by the incorporation of HAp. The dominant pore sizes are in the macropore range, and mostly outside of the quantification limit of the N_2-sorption technique. This causes the consequent decrease of the apparent surface area and the apparent pore volume in the case of BSPH.

The morphologies of the as-prepared aerogels were additionally studied by SANS. The scattering curves are dramatically different from each other in the low Q region, because this region is sensitive to the presence of large (50 – 100 nm wide) scattering objects. Such objects are present in the backbones of BSP and BSPH in the form of aggregates and HAp particles, but missing from the parent BS. In order to interpret these dual-scale structural features of the aerogels, the primary data were fitted by the two-level Beaucage model. The data at high Q values correspond to the primary particles and the mesopores of the backbone, while the data at low Q values describes the aggregates and the macropores. Characteristic scattering object sizes were calculated from the gyration radius (R_g) values assuming spherical geometry. The object sizes in the high Q region are in good agreement with the pore sizes measured by N_2-sorption, and those in the low Q region correspond roughly to the sizes of the aggregates and the HAp particles in the aerogel skeletons. The p exponent values close to 3 in the high Q region indicate that surface fractals dominate the mesoporous lower structural scale, while the values close to 4 at the higher scale show that the large objects have smooth surfaces. [250,251]

The nanoscale architectures of the hybrid skeletons were further investigated by contrast variation SANS measurements. [207] The aerogels were filled with H_2O:D_2O liquid mixtures, in which the H_2O:D_2O ratio was systematically varied. The contrast of the hybrid skeleton was matched with a single liquid composition (52V/V% D_2O), which has a theoretical scattering length density (SLD) value between those of borosilicate and PVA. This is a strong indication that the hybrid backbone is homogeneous at the low nanometer scale.

V-1.3.2. Hydration and wetting mechanism of borosilicate-PVA aerogels

Morphology of hydrated aerogels. The possibility of hydration induced morphological changes in the aerogels was studied by SANS. All aerogels were completely filled with D_2O, and in another set of experiments with a mixture of 8V/V% D_2O and 92V/V% H_2O. The latter mixture has an SLD value equivalent to that of air, therefore, it is frequently denoted as a zero-SLD probe. [252,253] Unfortunately, it was not possible to carry out conclusive measurements with wet BS, because of the very low hydrolytic stability of this aerogel. In the case of BSP and BSPH, the experimental scattering curves of the hydrated aerogels are very similar to those of the pristine ones (**Fig. 21**). All curves were fitted with the two-level Beaucage model as explained in the previous section. The estimated structural parameters are collected in **Table 7**. Both the shapes of the SANS curves and the estimated structural parameters suggest that only minor morphological changes take place upon the hydration of the hybrid aerogel skeletons.

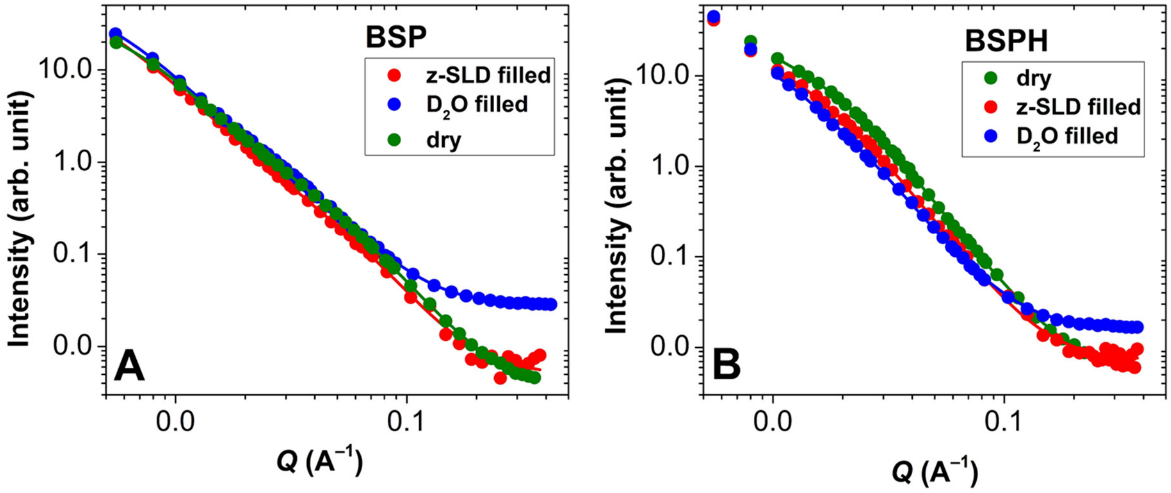

Figure 21. Small angle neutron scattering (SANS) curves of the as-prepared and the hydrated BSP (A) and BSPH (B) samples. Markers: experimental data, lines: results of fitting.

Table 7. Structural parameters estimated from the SANS data using the two-level Beaucage model. Scattering object sizes and *p* exponents of the as-prepared and the hydrated aerogels. (The ± values are the corresponding standard deviations.)

Sample	**Mean object size (nm)** ***high Q region***	***p*** **exponent** ***high Q region***	**Mean object size (nm)** ***low Q region***	***p*** **exponent** ***low Q region***
BSP *dry*	18 ± 1	2.9 ± 0.1	74 ± 5	3.8 ± 0.2
BSP D_2O	18 ± 1	2.9 ± 0.1	83 ± 5	3.4 ± 0.2
BSP D_2O/H_2O	18 ± 4	3.0 ± 0.2	97 ± 14	3.1 ± 0.2
BSPH *dry*	–	–	52 ± 1	3.2 ± 0.1
BSPH D_2O	–	–	49 ± 2	3.0 ± 0.1
BSPH D_2O/H_2O	–	–	52 ± 1	3.2 ± 0.1

NMR cryoporometry measurements were conducted on the wet aerogels with 2.5 g/g water contents to gain further morphological information on their pore systems. [125] The shapes of the melting-freezing hysteresis loops are different for BSP and BSPH (**Fig. 22**). The ratio of the freezing and melting temperature depressions ($\Delta T_f/\Delta T_m$) is close to 2/1 in the case of BSP, which is characteristic to continuous water bodies confined in elongated cylindrical pores. This ratio is 3/2 in the case of BSPH indicating the presence of spherical water droplets confined in the pore system [95,128]. This difference is reasonable in view of the N_2-sorption and SANS results, because both of these methods showed significant morphological differences between these aerogels. It is reasonable to assume that water can form elongated continuous bodies in the smaller interconnected pores of BSP, while the separation of larger spherical droplets is favored in the macropores of BSPH.

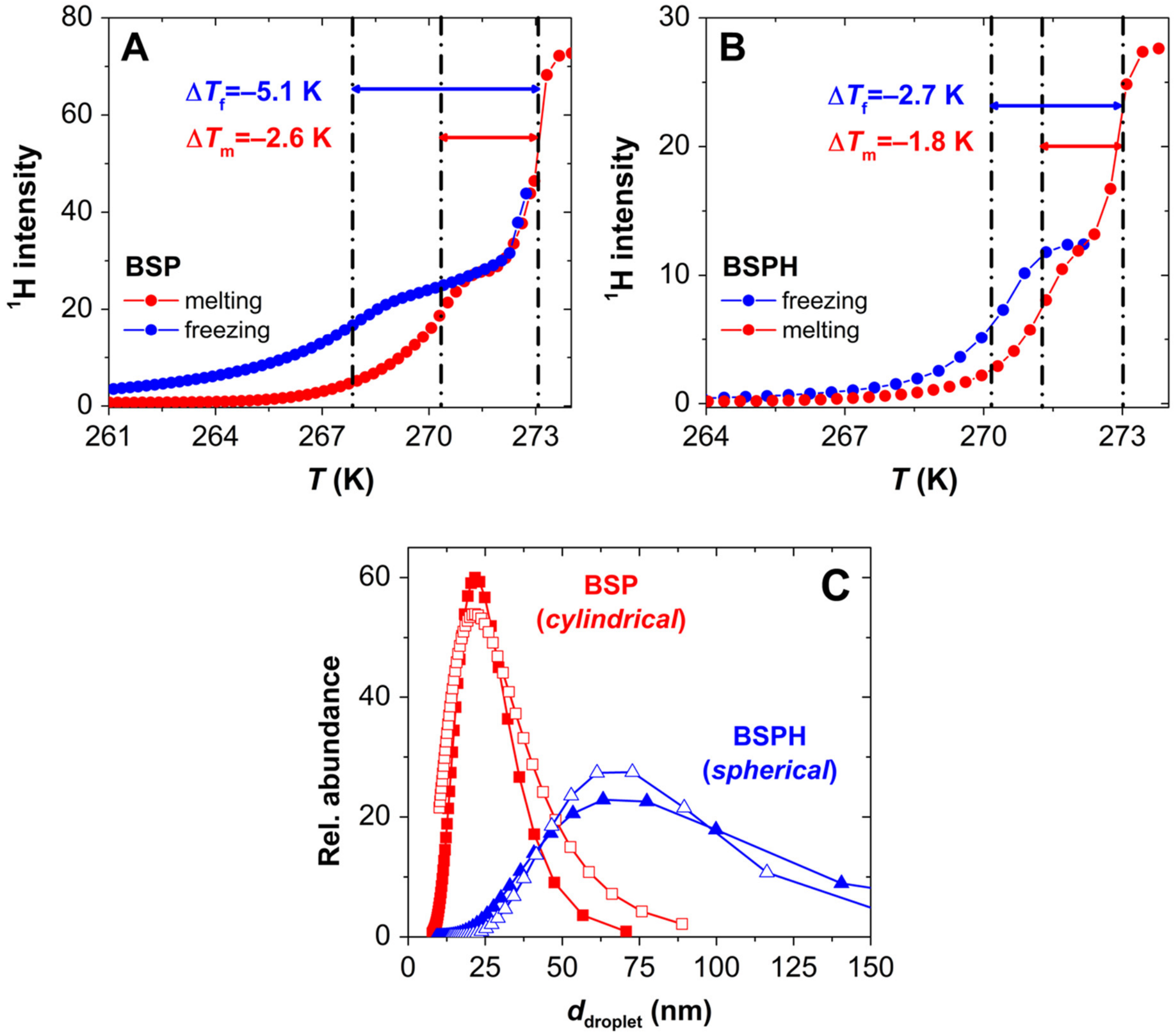

Figure 22. NMR cryoporometry of hydrated BSP and BSPH at 2.5 g/g water contents. Panels A and B: Experimental melting-freezing hysteresis curves. The data points shown are the average of two series of independent experiments. Panel C: Size distributions of water bodies in the aerogels. The empty markers were calculated from the freezing curves, and the filled markers from the melting curves.

The NMR cryoporometry based size distributions resulting from the melting and the freezing curves are practically the same in both systems (**Fig. 22B**). [149,237,238,254] These sizes are in good agreement with the pore size distributions of the dry aerogels calculated from the N_2-desorption isotherms, and with the mesopore sizes estimated from the SANS data.

As a summary, the SANS and the NMR cryoporometry results are in good agreement with each other and prove in a complementary manner that the original open and interconnected mesopore networks of the aerogels are conserved in water, because the nanoscale architectures of their hybrid skeletons are practically independent of hydration.

Localization of water in hydrated aerogels. The localization of water in the different chemical environments present in the hydrated aerogels was investigated using NMR relaxometry. [128]

In general, the sorption of water on amorphous silica surfaces starts with the formation of a 1-3 molecular layer thick film where the water molecules are strongly bound by H-bonds with surface silanol (Si-OH) groups. This primary water layer is termed in the literature as "strongly bound" or "non-freezing" surface water. Additional water forms a second layer atop the strongly bound molecules, which still displays restricted mobility and high molecular level order. Finally, bulk-like liquid forms on the ordered layers. [255,256]

Several studies investigated the formation of thin water film inside the nanoscale pores of silicas as the first step of the pore-filling process, and described the structure of confined water. By the combination of solid state and liquid phase NMR relaxometry, cryoporometry, differential scanning calorimetry (DSC), FT-IR spectroscopy and neutron diffraction analysis, a semi-ordered water layer was identified in the pores, which is distinct from the strongly bound water. [134,247,257-259] This secondary (termed also as "freezing") water layer was detected even when the pores of amorphous silicas were completely filled with water.

When the wetting (pore-filling) process of controlled-porous silicas was investigated using liquid-phase NMR relaxometry, a distinct relaxation domain was detected with characteristically low T_2 values, different from the liquid-like pore water even close to the saturation of the pores. [135,246,260-262] This domain was identified as the semi-ordered water layer atop of the strongly bound water. It was shown that this semi-ordered water layer is in slow exchange with the bulk-like pore water on the timescale of the relaxometry.

In the case of the cited examples of controlled-porous silicas, the presence of physically separated pores of well-defined sizes (e.g. separated micropores and mesopores) are not possible, thus, the fluid in each pore cannot be considered to be magnetically isolated [143,263]. Therefore, the separate relaxation domains arise not because of the difference in the geometrical confinement in the separate pore regions, but because of the different chemical environments of the water domains in the interconnected pores. Naturally, the situation is completely different in other material families (e.g. in concretes or natural minerals) due to the distinct chemical compositions and nanoscale morphologies [264,265]. This is the reason why purely geometry based generalization is not possible for the interpretation of relaxometry data, which is emphasized in the literature [143,263].

The general tendency in the wetting and pore-filling of silica based mesoporous aerogels is as follows. [126,127] The strongly bound water molecules in the primary layer on the solid aerogel skeleton are not detectable by the presented liquid-phase relaxometry approach, but the protons in the semi-ordered water layer atop the primary layer are detectable and have characteristically low T_2 relaxation times [95]. After the saturation of the semi-ordered layer at higher water contents, bulk-like water builds up forming droplets in the void spaces (pores) defined by the solid skeleton. The mean T_2 relaxation times in these droplets can be magnitudes higher than in the semi-ordered surface layer depending on shape and size. Generally, the signal amplitudes of the domains are proportional to the amounts of water localized in them. [129]

In the present study, two relaxation domains were identified at low water contents in BS. The T_2 values are 2 ± 1 ms and 12 ± 4 ms at 0.6 g/g water content, but the low hydrolytic stability of this material prevented its full scale investigation. The hydrated hybrid aerogels display three relaxation domains (**Fig. 23**). The T_2 relaxation times measured under the same conditions in related silica-based aerogels are also shown in **Fig. 23** for comparison. [125,129]

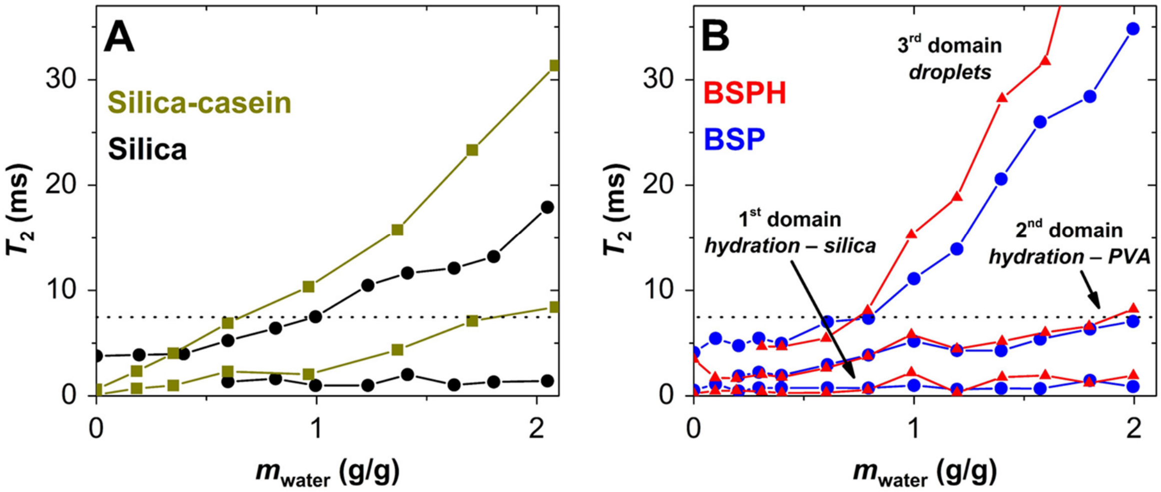

Figure 23. NMR relaxometry of hydrated aerogels. The T_2 relaxation times measured in hydrated silica and silica-casein aerogels (A), [125] and those measured in hydrated BSP and BSPH (B) as a function of their water contents. The *y*-axis scales are the same for better comparison. The data points shown are the average of two series of independent experiments. The difference between results from the repeated experiments was less than 10%.

The 1st relaxation domain with the lowest T_2 values is associated with the semi-ordered surface water layer on the aerogel skeleton. These water molecules form only a thin layer, which saturates already at low water contents. Therefore, the T_2 and the amplitude values of this domain are characteristically small, and remain constant even with the dramatic increase of the water contents of the aerogels. These features are typical of nanostructured porous silicas, including the pure silica aerogels (cf. **Fig. 23A**) [129,135,246,260-262].

The 3rd relaxation domain of BSP and BSPH with the highest T_2 values is associated with quasi-bulk water droplets filling the pore system. Both the T_2 values and the corresponding amplitudes of this domain increase systematically with the increase of the water contents of the aerogels. This is rational, because after the saturation of the semi-ordered water layer, all additional water is expected to accumulate in the droplets. In hydrophilic silicas, this is reflected in the steady growth of the droplet sizes until the complete filling of the pores, which causes the consequent increase of the associated T_2 values, as well as the amplitudes. One of the most frequently used theories in the case of silicas is based on the projection of the strong surface relaxation of water into the bulk of the pores by fast exchange. [137,142-144] The corresponding filling-factor ($1/T_2$ vs. $1/f^k$) plot gives the expected linear trend in the case of BSP when $k = 1$. However, the ca. $\lambda = 0.08$ nm value resulting from **eq. 2** based on this plot is physically not realistic. The same plot gives a large negative intercept in the case of BSPH.

This deviation from the geometry based theory is explained by the presence of an additional relaxation domain in the hybrid aerogels compared to the pure silica aerogel. The T_2 value of this new domain (denoted as 2nd domain) is 2 ms at low water contents that increases to 7 ms at high water contents. A relaxation domain with similar T_2 values has been observed in other hybrid silica-polymer aerogels (cf. **Fig. 23A**) [125,129]. Furthermore, this domain is also missing from the parent BS aerogel. Based on these observations, the new domain in BSP and BSPH is assigned to the secondary hydration sphere of the hybrid skeleton, which consists of water molecules bound mainly to the hydrophilic PVA polymer chains. Such a secondary hydration sphere grows in size with the increase of the water content of the aerogel due to the extensive hydration and partial dissolution of the polymer chains, explaining the increase of T_2 with increasing water content. This phenomenon has been identified in the case of the hybrid silica-gelatin and silica-casein aerogels, as well [125,129].

In the case of the hybrid borosilicate-PVA aerogels, the solid nanoscale architecture of the aerogels is practically intact even when completely hydrated, as shown by the SANS and NMR cryoporometry results. In spite of this, the wetting mechanism of the borosilicate-PVA hybrids is distinct from that of pure silica. The water molecules in the secondary hydration sphere (2nd domain) and those in the droplets (3rd domain) exchange with each other, but still yield mathematically separable decays. The amplitudes were estimated using a pre-set number of exponential functions for fitting, and were found to be commeasurable for the last two domains, showing that the amount of water is ca. the same in the secondary hydration sphere and in the droplets. Interestingly, despite the extensive hydration of the hybrid backbone, the semi-ordered water layer (1st relaxation domain) is still distinguishable in the borosilicate-PVA aerogels, similarly to pure silica aerogels [135].

Overall, the extensive hydration of the backbone accounts for the deviation of the operative pore-filling mechanism from the purely geometry based theory. The reason is, that such theories were laid down for nanostructured inorganic skeletons where hydration takes place only on the surface and water cannot penetrate the surface.

Unique hydration and wetting of silica-PVA aerogels. The conservation of the pore structures of the borosilicate-PVA aerogels resemble to that of pure silica, which was unexpected, because the pores of a number of biopolymer-silica hybrids (e.g. silica-gelatin) close in water due to the extensive hydration of the backbone. In the case of the present borosilicate-PVA aerogels, the polymer component develops an extensive hydration sphere starting at low water contents, which exists along the semi-ordered water layer that is characteristic to amorphous silicas. When the water content of the hybrid aerogel is increased, water droplets start to form on the hydrated skeleton. This naturally alters the pore-filling mechanism of the hybrid aerogels compared to pure silicas. Nevertheless, the nanoscale architectures and morphologies of the hybrid skeletons are not altered by this extensive hydration. These conclusions also apply even when nanosized hydroxyapatite particles are incorporated into the hybrid skeleton.

V-1.4. Detailed mechanism of hydration and hydration induced structural changes in an archetypical calcium alginate aerogel [P5]

Polysaccharide (celluloses, starch, alginate, chitosan) aerogels are advanced materials that are prepared by the controlled gelation and subsequent supercritical drying of solvated gels. [25,32,54,56,57,59,61,63,64,67,78] The key properties of advanced porous materials in practical applications are directly determined by their microstructures. [76,266-271] One of the most common conditions that can alter the microstructures of the highly hydrophilic aerogels is the hydration of their backbones, which is usually accompanied with significant structural changes that can cause volume reduction, stiffening, and, in extreme cases, the collapse of the pores. [266,272,273] These significant structural changes take place not only when the aerogels get in direct contact with liquid aqueous media, but also at a certain level of relative humidity in air. Our primary aim in this study is to understand and describe the intimate nature of the molecular level structural changes taking place upon the hydration of an archetypical polysaccharide aerogel, specifically calcium-alginate. Light microscopy images of as-prepared (dry) and hydrated Ca-alginate aerogel (CaAG) beads are shown in **Fig. 24**.

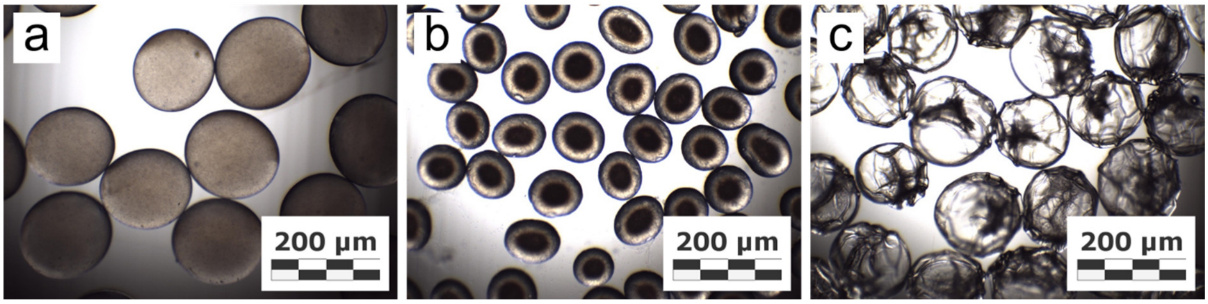

Figure 24. Microscopy images of Ca-alginate aerogel (CaAG) beads. a: Dry, as-prepared aerogel; b: Hydrated CaAG of 0.32 g/g water content; c: Hydrated CaAG of 2.0 g/g water content.

V-1.4.1. Characterization of the dry Ca-alginate aerogel

The molecular structure of the dry as-prepared CaAG was determined by magic angle spinning (MAS) NMR spectroscopy. Alginate is an anionic copolymer of β-D-mannuronate (M) and α-L-guluronate (G) units. The mole fraction of G is 0.48 in this copolymer. The solid backbone of CaAG is built from alginate polyanionic macromolecules bound together by ionotropic interactions with Ca^{2+} ions and hydrogen bonds. This structure is archetypical of metal ion cross-linked alginates at full degree of cross-linking. The Ca-alginate macromolecules are randomly ordered and immobile, and the aerogel backbone is amorphous.

The backbone of CaAG is built from fibrillar blocks that have a characteristic diameter of 25 ± 3 nm (**Fig. 25**). Very few macropores are visible in the SEM images. This morphology of CaAG is archetypical for metal ion crosslinked alginate aerogels. [274-276]

The N_2-sorption isotherms (**Fig. 26**) are characteristic for mesoporous materials, and indicate that there are practically no macropores in the aerogel. [14] The pore size distribution of CaAG calculated by the BJH method is narrow and symmetrical with a mean pore size of 42 nm (**Fig. 26B**). The structural parameters of CaAG are compiled in **Table 8**.

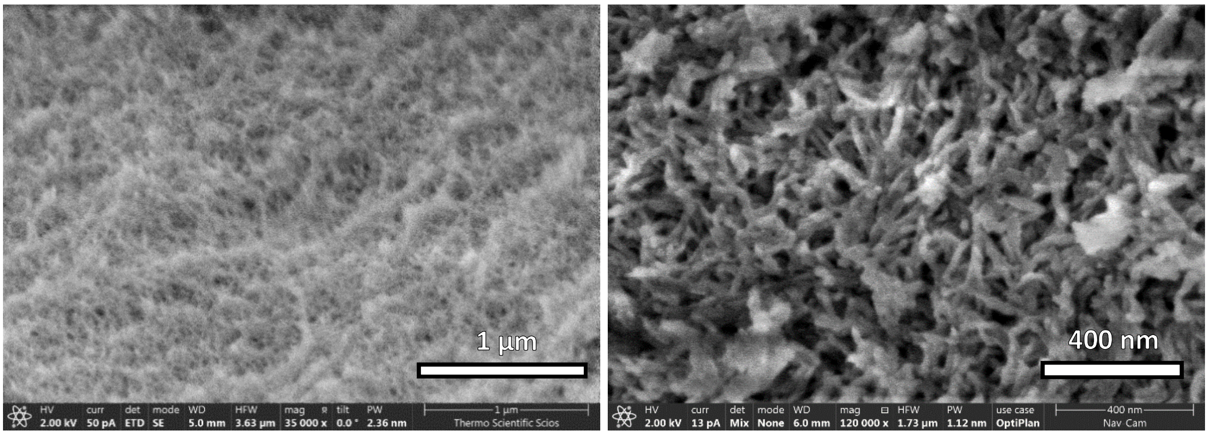

Figure 25. SEM images of dry as-prepared Ca-alginate aerogel (CaAG) at different magnifications.

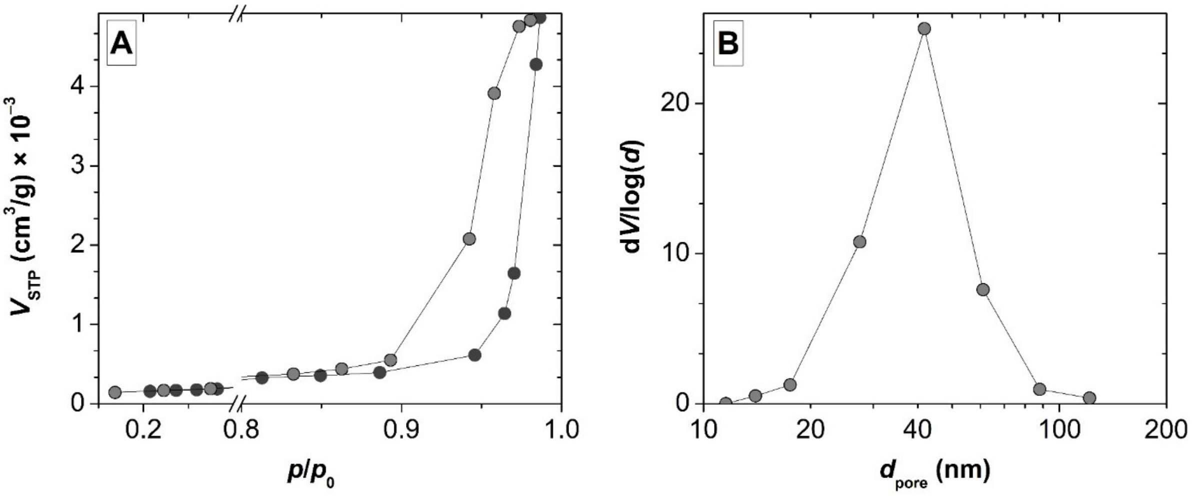

Figure 26. N_2 adsorption-desorption isotherms (A) and pore size distribution (B) calculated from the desorption isotherm using the BJH method.

Table 8. Structural parameters of as-prepared CaAG estimated by the BET and the BJH methods from N_2 adsorption-desorption porosimetry data (cf. **Fig. 26**).

Parameter	Value	Evaluation
Specific surface area	544 ± 70 m^2/g	BET
Pore diameter	42 ± 11 nm	BJH
Total pore volume (cm^3/g)	7.5 ± 0.2 cm^3/g	BJH

V-1.4.2. Morphology by small angle neutron scattering

Calcium alginate aerogel was gradually hydrated with D_2O in a stepwise manner up to a water content of 1.9 g/g. The shapes of the scattering curves change in a gradual manner with the increase of the hydration level of CaAG until reaching the water content of 0.6 g/g (**Fig. 27**). At this point, the additional uptake of even a small portion of water causes the dramatic transformation of the scattering curve. After this transition, the shape of the scattering curve changes again in a gradual manner when the water content is increased. The SANS curves of the samples of low hydration levels (< 0.6 g/g) can be fitted to the Beaucage model (**eq. 8**) reasonably well, yielding estimates for both the gyration radius (R_g) and the power exponent (p). The shape of the scattering curves changes at water contents of ca. 0.6 – 0.7 g/g in the investigated Q range. The shape changes from the Guinier type to the power-law type tendency, which is accompanied by the radical transformation of the Beaucage model variables. Another equivalent interpretation is that the Guinier feature is increasing in gyration radius, and shifting to lower Q outside the experimental range. Therefore, at water contents higher than 0.6 g/g, the power-law model was used for fitting SANS curves instead of the full Beaucage model, and only the values of the power exponent were estimated (**Fig. 27B**). Other models have been tested for data fitting, but only the Beaucage approximation is suitable to describe all the SANS curves, thus enabling the direct comparison of the estimated structural parameters for all hydration levels. [173,277,278]

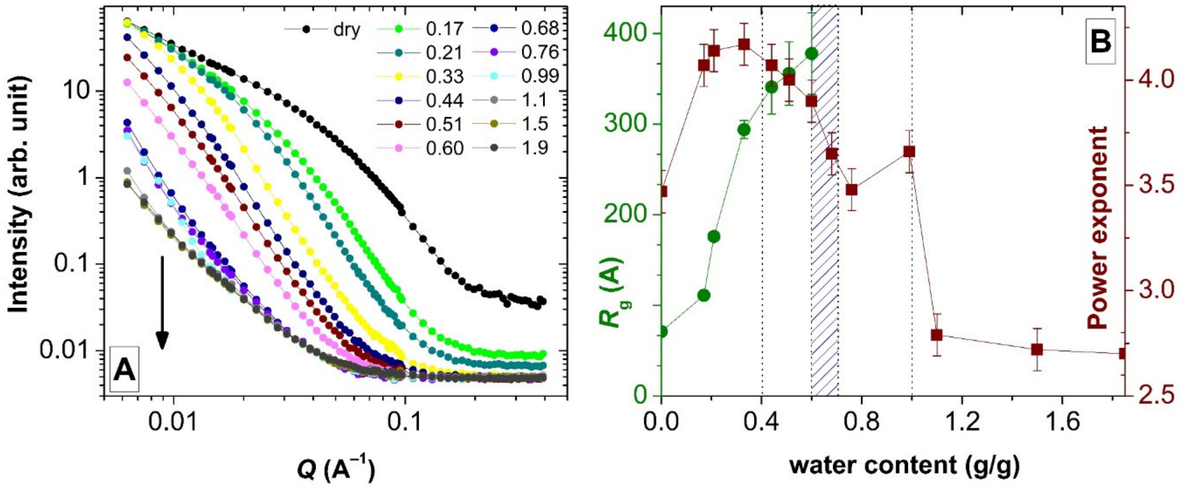

Figure 27. Panel A: SANS curves of CaAG samples of different water contents. The curves are offset for better visibility. The arrow shows the direction of the increase of the water content of the samples that are given in the legend in g/g unit. Panel B: The values of the power exponent (*p*) and the gyration radius (R_g) estimated by the Beaucage model. The dotted vertical lines indicate the approximate water contents where significant structural changes occur.

The gradual change of the shapes of the SANS curves together with the systematic variation of the encoded structural parameters are consistent with the gradual transformation of the aerogel structure with the increase of hydration until a critical water content of 0.6 g/g. [276] Complementary techniques (NMR relaxometry, cryoporometry, PGSTE NMR; *vide infra*) indicate as well the dramatic transformation of the aerogel structure at these conditions.

The as-prepared CaAG is a surface fractal ($p = 3.5$), but the 4.0 – 4.1 values of the power exponent at 0.2 – 0.5 g/g water contents indicate that there is a smooth border including a transition zone between the fluid component and the solid scattering objects of these samples. [221] The increase of the power exponent is accompanied by a significant increase of the gyration radius of the hydrated samples compared to that of the dry aerogel; from 81 Å (dry state) to 378 Å (at 0.6 g/g water content). This is most likely due to the hydration driven gradual modification of the tertiary and quaternary structures of the Ca-alginate macromolecules forming the aerogel backbone, which is detected by solid-state NMR (*vide infra*). As a consequence, the primary Ca-alginate fibrils rearrange into fibers or fascicles with the increasing hydration level of the aerogel that, in turn, results in the smoothing of the nanostructured surface, the increase of the fractal dimension of the system, the opening of the pore network and the significant increase of the pore sizes. [279] The proposed mechanism is visualized in **Scheme 6** in the context of the SANS measurements. However, this mechanism does not account for the marked change of the SANS curves due to the minor increase of water content in the 0.6 – 0.7 g/g region. Only significant structural modifications can account for these observations.

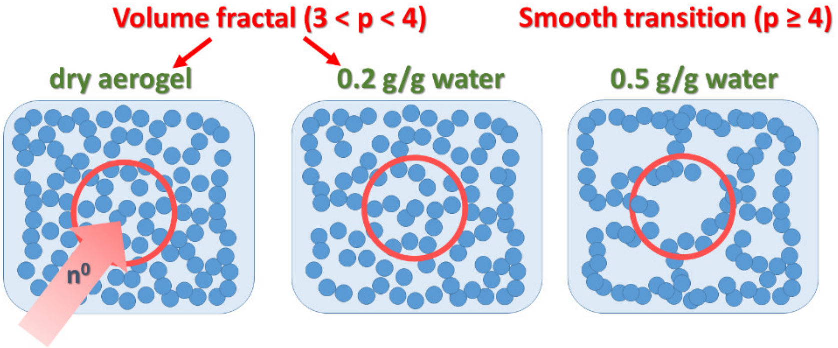

Scheme 6. The schematic representation of the structural changes that take place upon the hydration of CaAG up to a critical water content of 0.6 g/g. The filled circular markers represent the aerogel backbone. The red circle shows the theoretical observation window of the SANS technique. The structural changes induced by the increase of the hydration level are reflected in the increase of the values of both the power exponent and the gyration radius. (The intimate features of the hydration mechanism are given later in **Scheme 7** and in **Table 9**.)

The most reasonable explanation is the collapse of the pore structure of CaAG due to the formation of extensive well-hydrated structural regions at this critical level of water content. [276] The well-defined solid backbone ceases to exist as the previously separated Ca-alginate fibers get in close contact with one another and merge into a quasi-homogeneous, dense 3D network of hydrated Ca-alginate macromolecules of hydrogel-like characteristics. [280] These features explain the significant shifting of the Guinier-region and the sudden drop of the value of the power exponent of the SANS curves at 0.7 g/g water content and above.

By the additional uptake of water, the extension of the quasi homogeneous 3D network of the well-hydrated Ca-alginate macromolecules increases, and finally encompasses the whole amount of CaAG at ca. 1.0 g/g water content. From this point on, the morphology of hydrated CaAG does not change significantly, in analogy with a common hydrogel taking up additional water. Consequently, the shape of the SANS curve and the value of the power exponent changes only slightly with the increase of water content from 1.0 to 1.9 g/g.

It should be noted, that the macroscopic distribution of water can slightly be different among the aerogel beads in the sample holder, which causes an uncertainty in the scattered neutron intensities close to the critical hydration level, i.e. between 0.7 and 0.9 g/g.

V-1.4.3. Liquid phase and solid state NMR spectroscopy

A very meticulous interpretation of the NMR results is required, because adding more and more water to the aerogel not only alters the localization of water molecules in the porous matrix, but simultaneously causes extensive structural changes in the CaAG backbone. These structural changes in turn alter the immediate chemical environment of the water molecules localized in the different structural regions that changes their apparent physico-chemical properties (self-diffusion, rotational correlation times, melting point depression, etc.).

NMR relaxometry. Four different relaxation domains were identified during the gradual hydration of CaAG by the inverse Laplace transformation of the primary NMR data. Panels A and B of **Fig. 28** show the T_2 relaxation times of water protons in the individual relaxation domains (marked by different colors) as a function of water content. The data set is the same in these two panels, the only difference is the enlarged y-scale in panel B. Panel C of **Fig. 28** shows the water content of each domain calculated from the corresponding relaxation amplitudes. The different relaxation domains belong to water localized in different structural regions of hydrated CaAG. Fast chemical exchange does not take place between these micro-environments. The different domains appear and become saturated in a consecutive manner with increasing water content. The mechanism of hydration of CaAG and the hydration induced modification of the aerogel backbone manifest in the properties of these relaxation domains.

The amplitudes and the T_2 relaxation times of the domains generally increase with the increasing hydration level of CaAG. The T_2 values of the 1st domain (GREEN in **Fig. 28**) are very small (ca. 0.1 ms), and can only be measured with a relative standard deviation of ca. 30%. Still, the presence of this domain is unambiguously verified by the MERA algorithm. The T_2 of the 2nd domain (RED in **Fig. 28**) increases with the increasing hydration level and reaches a limiting high value (ca. 3 ms) at ca. 1.2 g/g water content. The T_2 of the 3rd domain (GRAY in **Fig. 28**) and that of the 4th domain (BLUE in **Fig. 28**) are high and increase steadily with increasing water content. The amount of water localized in the 1st relaxation domain increases with increasing water content, and reaches saturation at ca. 0.4 g/g (**Fig. 28C**). Simultaneously, the amount of water extensively increases in the 2nd domain and saturates only at a relatively high water content, at ca. 1.2 g/g. Most of the water in the aerogel sample is localized in the 2nd domain at water contents higher than 0.4 g/g. The 4th domain appears when an extensive amount of water is localized already in the 2nd domain, at water contents higher than 0.7 g/g. The filling of the 2nd, 3rd and 4th domains are quasi simultaneous.

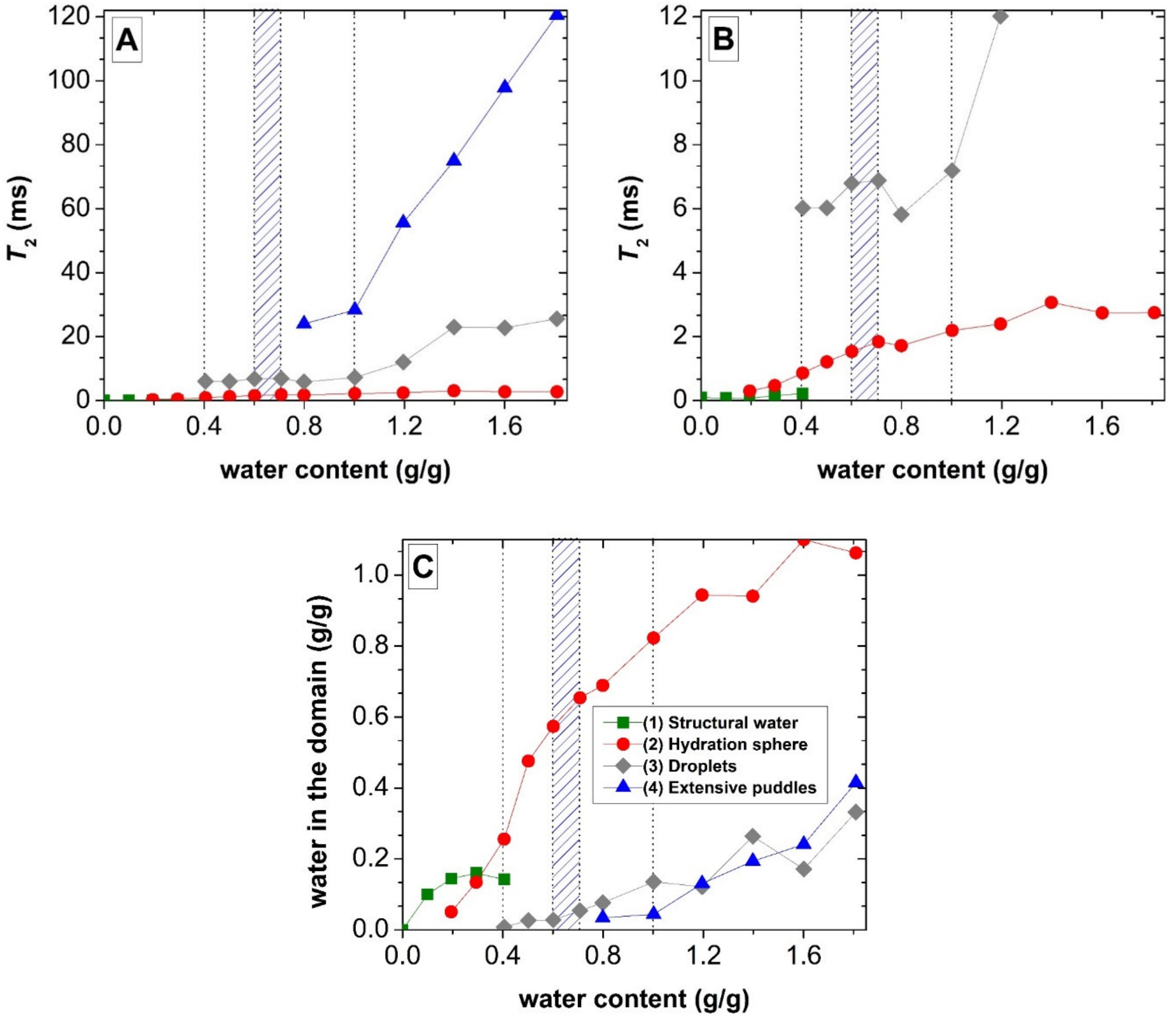

Figure 28. NMR relaxometry of hydrated CaAG. Four different relaxation domains are present in the hydrated aerogel as a function of its hydration level. The relaxation domains are numbered as they appear with increasing water content. (1) Green: structural water; (2) Red: primary hydration sphere; (3) Gray: droplets; (4) Blue: extensive puddles. Panels A and B: Observed T_2 relaxation times of the different domains as a function of water content. The data set is the same in these two panels, but the scales of the *y*-axes are different. Panel C: The water content of each domain as a function of the extent of hydration, calculated from the relaxation amplitudes.

The relaxation domains are assigned to the structural regions of hydrated CaAG by comparing the characteristics of the domains with those of previously investigated systems published in the literature, and by taking into account the SANS, the cryoporometry and the diffusiometry results (*vide infra*). [121,129,135] Based on these considerations, the 1st relaxation domain represents strongly bound structural water that is directly associated with the Ca-alginate macromolecules. The 2nd relaxation domain represents the primary, highly ordered hydration sphere of the Ca-alginate chains. The 3rd domain is loosely bound water that form droplets and puddles in the focal points of the fibrillar backbone. The 4th domain is quasi-bulk water filling the large cavities of the well-hydrated Ca-alginate network and the hydrogel-like matrix. The intimate hydration mechanism will be presented later in view of the compiled data.

NMR cryoporometry. Cryoporometry measurements were performed with CaAG samples of different water contents (**Fig. 29**). The correct interpretation of the NMR cryoporometry data is possible only by taking into account the structural information deduced from the SANS and the NMR relaxometry measurements. Importantly, hydrated CaAG retains its well-defined porous structure at 0.3 g/g water content. Based on the NMR relaxometry results, water can be localized in the aerogel in 3 different structural regions at this hydration level: *i*) structural water associated to Ca-alginate macromolecules (1st relaxation domain), *ii*) in the primary hydration sphere (2nd relaxation domain), and *iii*) in small droplets and puddles (3rd relaxation domain).

The T_2 relaxation time of the water molecules in the 1st domain is too small to pass the relaxation filter of the pulse sequence of the NMR cryoporometry measurements. Water in the 2nd relaxation domain has long enough T_2 to pass the relaxation filter, but ice formation is not feasible in the primary hydration sphere due to the strong interaction of water with the backbone. An important feature of the cryoporometry data is that the ^{1}H NMR signal intensity converges to a non-zero value at low temperature. This verifies that there is a substantial amount of water in the hydrated sample that does not freeze even at 256 K and has a long enough T_2 relaxation time to pass the relaxation filter of the pulse sequence. [148,149,237]

Water in droplets (3rd relaxation domain) confined in the focal points of the aerogel network freezes and melts between 256 K and 273 K, thus, the well-defined hysteresis of the ^{1}H NMR signal in **Fig. 29A** is assigned to the phase transformations of water in these droplets. The inflection points on the hysteresis curve define a 2:1 ratio of the depressions of the melting and the freezing temperatures of pore water (**Fig. 29A**). This indicates that water droplets undergo phase transitions in spherical confinement in the hydrated CaAG of 0.3 g/g water content. The size distribution of these droplets [149,237,238] are given in **Fig. 29B**. According to the SANS results, the pores of hydrated CaAG of 0.3 g/g water content are significantly larger than the original pores of the dry material. (R_g = 81 Å and 294 Å, which translates into d_{pore} = 210 and 760 Å for the dry and the hydrated aerogels, respectively.) Thus, the mean size of the water droplets (ca. 25 nm in **Fig. 29B**) confined in the focal points of the hydrated network are significantly smaller than the pores of the deformed backbone.

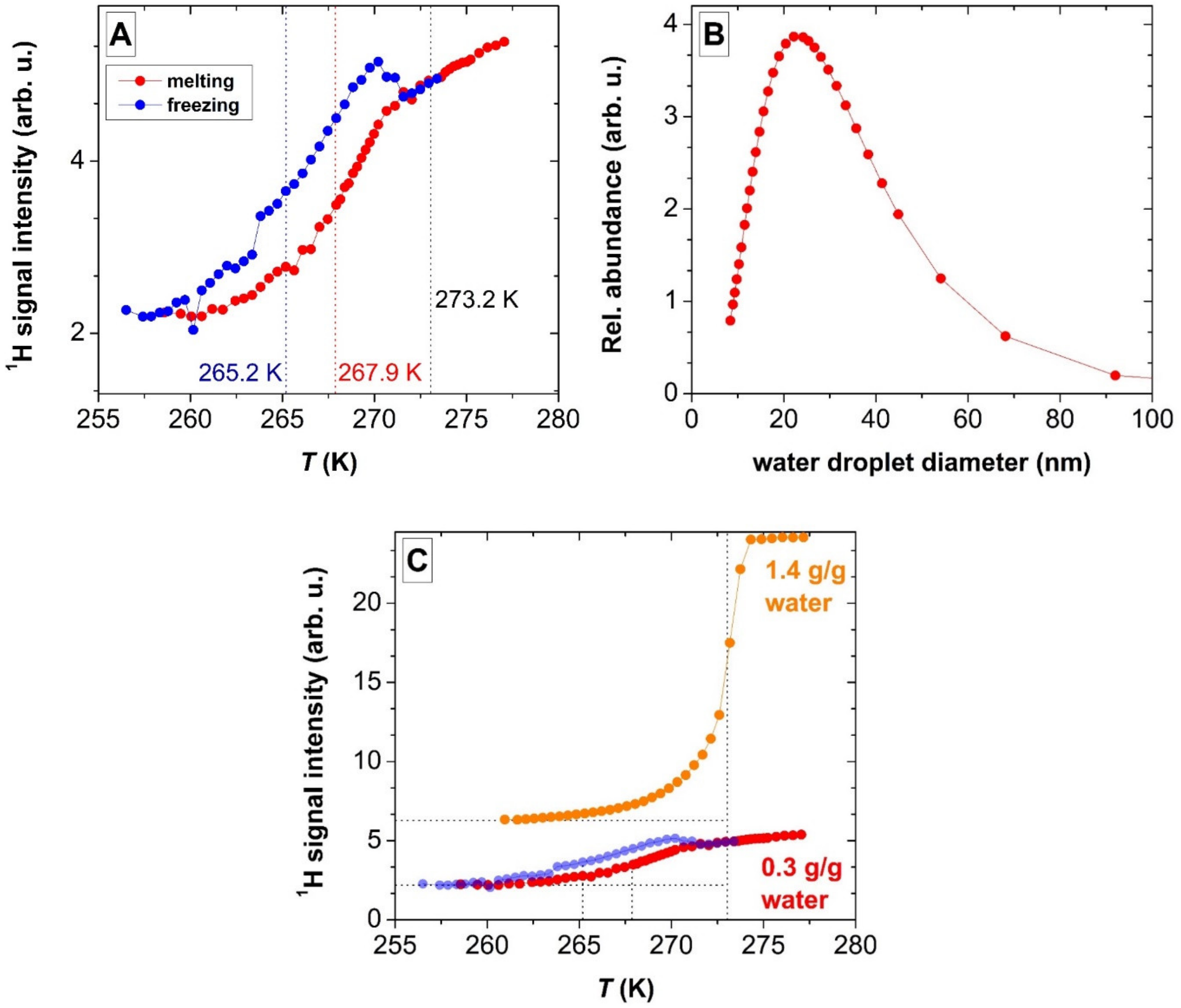

Figure 29. NMR cryoporometry characterization of hydrated CaAG samples. Panel A: The ^{1}H NMR signal intensity of the water protons as a function of the temperature at 0.3 g/g water content. Red markers: melting. Blue markers: freezing. The vertical lines show the phase transition temperatures. Panel B: Size distribution of the water droplets in hydrated CaAG of 0.3 g/g water content (reconstructed from the melting curve in Panel A). Panel C: NMR cryoporometry curves at different water contents. There is no well-expressed hysteresis curve in the case of the sample of 1.4 g/g water content. Horizontal lines indicate the limiting low ^{1}H NMR intensities.

The melting-freezing features significantly change by the increase of the hydration level of CaAG. In the case of the well-hydrated CaAG sample of 1.4 g/g water content, the ^{1}H NMR signal intensity does not show hysteresis as a function of temperature (**Fig. 29C**). Such cryoporometry data indicate that there are no confined, geometrically well-defined water droplets in the sample in the size range between 10 nm and 200 nm. [147,148] These findings are in good agreement with the structural information deduced from the SANS and the NMR relaxometry data, i.e. Ca-alginate aerogel of 1.4 g/g water content has hydrogel like characteristics. At this hydration level, water is dominantly localized in the primary hydration sphere of the Ca-alginate chains (2nd relaxation domain) and as quasi-bulk water (4th relaxation domains). Water in the primary hydration sphere does not form ice crystals even below 260 K, therefore, it is responsible for the non-zero intensity of the ^{1}H NMR signal at low temperatures (**Fig. 29C**). Quasi-bulk water in the hydrogel-like structure of the well-hydrated sample is practically free of confinement, therefore its phase transition cannot be differentiated by NMR.

NMR diffusiometry. It should be noted, that the results of the PGSTE measurements cannot be interpreted correctly using only the conventional approaches of data evaluation for NMR diffusiometry. This is evident by examining the NMR spectra of the hydrated CaAG samples. **Fig. 30** shows the ^{1}H NMR spectra of CaAG samples of different water contents next to their PGSTE NMR spectra recorded using δ = 2 ms gradient pulse length and Δ = 60 ms diffusion time. Two peaks can be identified in the ^{1}H NMR spectrum of CaAG of 0.2 g/g water content, and this is replaced by one dominant peak in the case of samples of higher hydration. The PGSTE NMR spectrum of the aerogel of 0.2 g/g water content also displays 2 peaks. Interestingly, the intensities of all PGSTE NMR peaks decrease significantly with the increase of the water content of the sample, and completely diminish at 0.4 g/g water content (**Fig. 30B**). When the water content of the sample is increased further, a new well-defined peak appears in the PGSTE NMR spectrum with a minor shoulder at lower chemical shift, which is persistent even in the case of the well-hydrated samples.

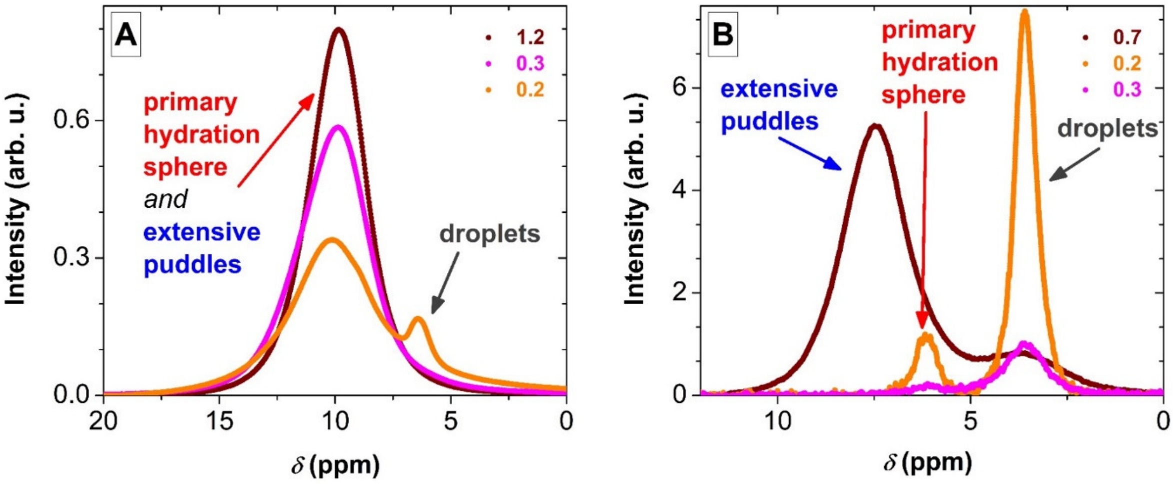

Figure 30. NMR spectra of hydrated CaAG recorded at different hydration levels, as given in the legend. The assignment of the signals is displayed on the figures using the same color code as in the case of NMR relaxometry (cf. **Fig. 28**). Panel A: ^{1}H NMR spectra. Panel B: PGSTE NMR spectra of diffusiometry experiments recorded using minimum gradient field strength, δ = 2 ms gradient pulse length and Δ = 60 ms diffusion time.

The key differences between the two types of NMR measurements are the total time of the experiment and the shifting of the magnetization of the sample. [155,281] The ^{1}H NMR spectrum is recorded in ca. 0.01 ms, while the PGSTE NMR spectrum is recorded in ca. 60 ms. In the PGSTE NMR experiment, the sample is magnetized in the transversal plane only during the length of the gradient pulse (δ = 2 ms), otherwise it is magnetized in the longitudinal plane. The information content and the difference of the ^{1}H NMR and PGSTE NMR spectra can be interpreted based on the results of the NMR relaxometry experiments. The major peak of the ^{1}H NMR spectra in **Fig. 30A** is assigned to water in the primary hydration sphere (2nd relaxation domain), because structural water built into the solid backbone (1st relaxation domain) barely gives a signal in liquid phase NMR spectroscopy. The minor peak at lower chemical shift in the ^{1}H NMR spectrum measured at 0.2 g/g water content is assigned to small water droplets that form in the focal points of the solid pore network (3rd relaxation domain). The peak at higher chemical shift is very small in the PGSTE NMR spectrum of the sample of 0.2 g/g water content (**Fig. 30B**). The reason is that the transversal relaxation of the protons of water in the primary hydration sphere (2nd relaxation domain) is almost complete in 2 ms. The relaxation of water is much slower in the droplets; thus these water molecules yield a signal in the PGSTE NMR spectrum at lower chemical shift. When the hydration level of CaAG increases, its ^{1}H NMR spectrum becomes unstructured, because the chemical shift values of the water molecules localized in the different structural regions are not significantly different. On the other hand, the PGSTE NMR spectrum remains structured even at high hydration levels, because the major signal of the water protons in the extensive primary hydration sphere is not present due to fast transversal relaxation (T_2 filtering effect). Importantly, the chemical exchange of water within the ca. 60 ms timeframe of the PGSTE NMR measurement has a significant effect on the spectra, and causes the disappearance of the signal when the water content of the sample is between 0.4 and 0.6 g/g. Two counteracting effects are operational. One effect is the increase of the signal intensity, and the other effect is the increase of the rate of exchange between low T_2 water in the primary hydration sphere and high T_2 water in the droplets. The exchange of water transfers the relaxation effect of the Ca-alginate backbone from the primary hydration sphere to the droplets and causes the diminishing of the corresponding PGSTE NMR signal (transfer of T_2 filtering effect). The increasing rate of water exchange and relaxation transfer overcompensate the increasing signal intensity by the addition water until ca. 0.6 g/g. At water contents higher than 0.7 g/g, the PGSTE NMR spectrum is dominated by the signal of water molecules forming a quasi-bulk phase in the hydrogel-like network (3rd and 4th relaxation domains). In this case, the effect of relaxation transfer is overcompensated by the increase of the T_2 values and the water contents of these domains. Thus, the intensity of the PGSTE NMR signal has a minimum as a function of the water content of CaAG (cf. **Fig. 30B** and **Fig. 31**).

The self-diffusion properties of water in hydrated CaAG were characterized as functions of the hydration level of the sample and the observation time of the diffusion measurement. [156,157,242] Only one diffusion domain is detectable in hydrated CaAG regardless of its water content (**Fig. 31**), because of the fast exchange of water among the structural regions in the timeframe of the experiment. [127,153] At low water contents, the size of the droplets where diffusion is detected increases with the hydration level of the aerogel, therefore, the value of D_{obs} increases. This increase continues even after the formation of the hydrogel with the dilution of the Ca-alginate macromolecule network that facilitates mass transport.

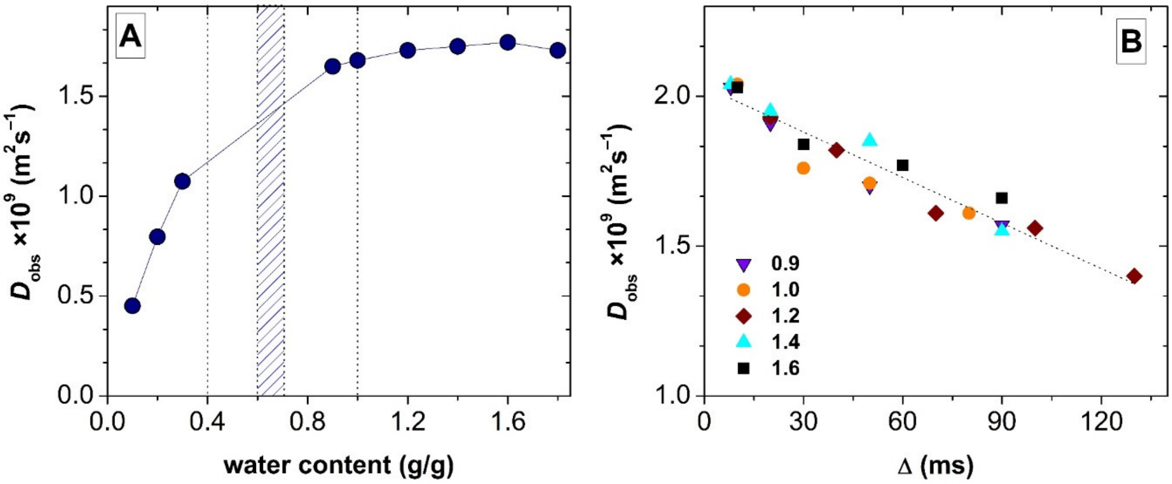

Figure 31. The self-diffusion properties of water in hydrated CaAG samples. Corresponding PGSTE NMR spectra are shown in **Fig. 30**. Panel A: The experimental self-diffusion coefficient of water (D_{obs}) as a function of the hydration level of the aerogel. Strong relaxation effects cause the diminishing of the PGSTE NMR signal between 0.4 and 0.7 g/g of water contents. Panel B: The value of D_{obs} as a function of the observation time of the diffusion experiment (Δ) recorded in samples of different water contents, as shown in the legend. The dashed line highlights the trend in the data points.

The value of D_{obs} is independent of the observation time of the diffusion experiment (Δ) when the water content of CaAG is below 0.7 g/g, but D_{obs} decreases with the increase of Δ at high water content (**Fig. 31B**). On the basis of this trend, it is possible to approximate the physical dimensions of the confinement of water molecules in the well-hydrated CaAG using the established theories of diffusiometry. [156,157] This boundary of confinement was found to be 220 µm in the case of CaAG of 1.2 g/g water content, which is in excellent agreement with the approximate diameter of the hydrated CaAG beads (cf. **Fig. 24**).

Magic angle spinning (MAS) NMR spectroscopy. The assignment of the ^{13}C CPMAS NMR resonance peaks (**Fig. 32**) was performed as described in earlier literature. [282,283]

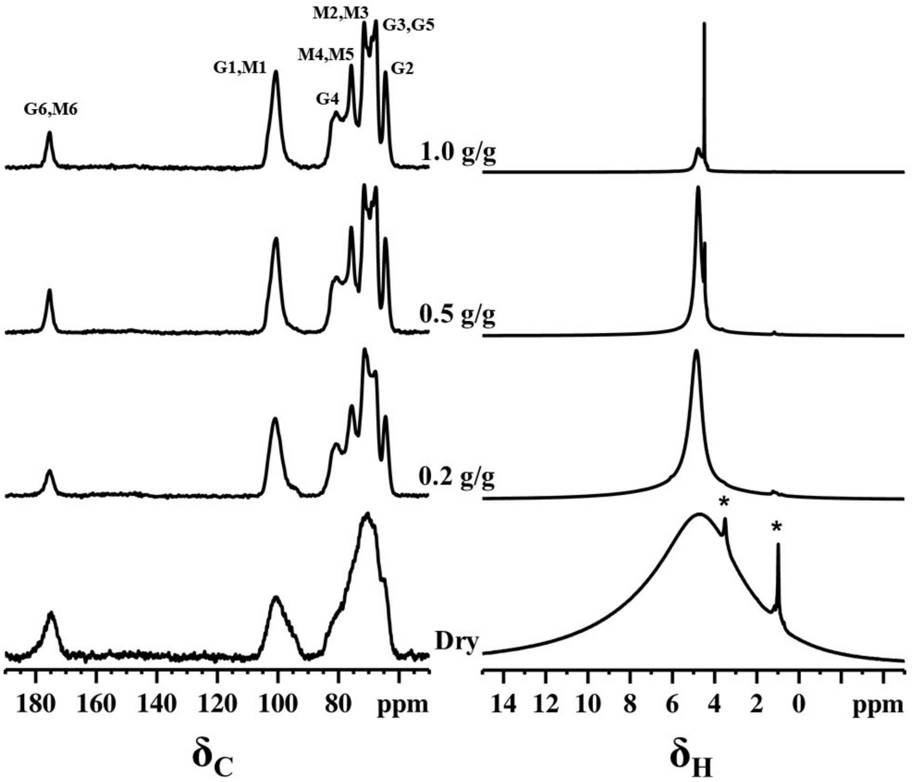

Figure 32. The ^{13}C CPMAS (left panel) and the ^{1}H MAS (right panel) NMR spectra of CaAG samples of different water contents (shown between the panels). The ^{13}C CPMAS spectra were recorded using a MAS rate of 10 kHz and a CP contact time of 0.5 ms while the MAS rate for ^{1}H MAS was 15 kHz. The asterisk (*) denotes peaks from traces of residual ethanol. Spectra are normalized to the highest intensity peak. (M = β-D-mannuronate unit, G = α-L-guluronate unit)

The ^{13}C resonance peaks are very broad in the spectrum of the dry CaAG. When the water content of the sample is increased to 0.2 g/g, the resolution of the resonance peaks improves, especially in the pyranose region (60 – 90 ppm). Further NMR line narrowing and the increase of the ^{13}C intensities take place with the increase of the water content to 0.5 g/g. Additional water does not affect the ^{13}C chemical shift values and the peak resolution. The mechanistic explanation for the increase of the peak resolution is as follows. In the dry aerogel, the Ca-alginate macromolecules exist in a generally amorphous state as a disordered interconnected network immobilized by intra- and inter-chain ionotropic and hydrogen bonds. This interconnected network constitutes of several randomly ordered 3D arrangements of Ca-alginate macromolecules, which leads to intrinsic structural heterogeneities and broad ^{13}C CPMAS NMR peaks. The hydration of the Ca-alginate chains enables a series of molecular level rearrangement processes, such as conformation changes, segmental chain motions, local rotational state transitions and hydrogen bonding rearrangements. Thus, it is reasonable to assume, that at low hydration level, the disordered network of the original dry backbone rearranges into a thermodynamically more favored semi-ordered structure by the change of the secondary to quaternary structures of the Ca-alginate macromolecules. [160-164] These changes are expressed in the NMR relaxometry results indicating that the first portions of water molecules added to the dry aerogel are incorporated into the fibers in the form of structural water (1st relaxation domain) in strong interaction with the Ca-alginate macromolecules. This, and the subsequent formation of the primary hydration sphere induces the alteration of the secondary to quaternary structures of the macromolecules. These molecular changes can very well cause the morphological changes detected by SANS up to ca. 0.5 g/g water content.

Proton MAS NMR spectroscopy complements the ^{13}C NMR data (**Fig. 32**). In the ^{1}H MAS NMR spectrum of the dry CaAG, there is only a single very broad band centered at 4.8 ppm, which is attributed to hydroxyl and CH protons. Water molecules forming hydrogen bonds with the macromolecules are in fast proton exchange with the hydroxyl groups in this timeframe, therefore their signals are incorporated into the main peak. A broad shoulder is also present in the spectrum down-field from the main peak in the range of 6 to 12 ppm, and it is assigned to species in hydrogen bonding, but not in proton exchange. [165]

The main resonance peak at ca. 5 ppm assigned to hydroxyl and CH protons becomes narrower with the increase of the hydration level of the aerogel. In-line with the above described hydration induced changes, we propose that a motion assisted line narrowing is responsible for the modulation of the proton-proton dipolar interactions. Thus, the ^{1}H MAS NMR data indicates that the hydrogen bonding network characteristic for the dry amorphous CaAG breaks up, and segmental chain motions and hydroxyl proton exchange with water start upon hydration. A new sharp resonance peak appears in the spectrum of the sample of 0.5 g/g water content at 4.5 ppm. This peak is assigned to a new proton environment in hydrated CaAG. Based on the sharpness of this resonance peak and the increase of its intensity with the increase of hydration level, it is assigned to water molecules that are not in close association with the Ca-alginate macromolecules. In agreement with the liquid phase NMR results, it is reasonable to assume that these water molecules are localized in droplets and puddles, and finally form a quasi-bulk phase in the hydrogel-like network of the Ca-alginate chains.

V-1.4.3. Hydration mechanism and corresponding structural changes

The hydration induced modification of the solid skeleton of CaAG adds a new level of complexity to the evaluation and interpretation of characterization data. Prior studies dealt only with the hydration of porous solids of rigid backbones (e.g. porous silicas, carbons, natural minerals) that are not modified during the course of hydration. In the present study, SANS data provide information on the morphological changes of CaAG as a function of its hydration level, while NMR data can advantageously be utilized as complementary sources of information for deducing the intimate mechanisms on the molecular level.

The hydration mechanism and the hydration induced structural changes of CaAG are visualized in **Scheme 7**. The characteristic structural elements of the hydrated aerogel as a function of its water content are listed in **Table 9**.

Upon gradual hydration, the first aliquots of water are bound by the hydroxyl and the carboxyl groups of the Ca-alginate macromolecules by H-bonds. These water molecules become part of the tertiary and quaternary structures of the Ca-alginate macromolecules, their relaxation is very fast (1st relaxation domain), and their exchange with other water molecules is slow. The sites for binding structural water saturate at ca. 0.4 g/g water content. Parallel to this, the primary hydration sphere of the Ca-alginate macromolecules builds up from several molecular layers of water. [239,240] Water molecules in the primary hydration sphere are in strong association with the Ca-alginate macromolecules of the aerogel backbone that results in fast transversal relaxation (2nd relaxation domain; low T_2) and slow exchange of water. [241] Due to the extremely hydrophilic character of calcium-alginate, its primary hydration sphere is extensive and most of the water in the aerogel is localized in the primary hydration sphere. The gradual increase of the T_2 of the 2nd domain indicates that the thickness of the primary hydration sphere gradually increases with the increasing level of hydration. [137] Hydration partially mobilizes the Ca-alginate macromolecules in the backbone, and enable conformational changes, i.e. the energetically favorable modification of the tertiary and quaternary structures. These structural changes induce the rearrangement of the primary Ca-alginate fibrils of the original dry aerogel backbone into fibers and fascicles resulting in the increase of pore size, the smoothing of the nanostructured surface and the increase of the fractal dimension.

In parallel to the filling of the primary hydration sphere, droplets form in the focal points of the aerogel backbone starting at ca. 0.3 g/g water content (3rd relaxation domain). These droplets are in connection with the primary hydration sphere, but the exchange is slow between these domains on the timescale of relaxometry. The relaxation of water is significantly slower in the droplets than in the primary hydration sphere. [121,135-138,154] Furthermore, water molecules in the primary hydration sphere of the Ca-alginate chains and in the droplets yield individual signals in the solution phase PGSTE NMR spectrum of hydrated CaAG at low water contents, but a T_2 relaxation filter effect cancels most of the signal of the hydration sphere (2nd relaxation domain) (cf. **Fig. 30**). Water molecules in droplets also yield a sharp ^{1}H MAS NMR peak (cf. **Fig. 32**). The size of the confined droplets is approximated by NMR cryoporometry to be 20 – 40 nm. This is much smaller than the size of the pores of hydrated CaAG at this hydration level (ca. 76 nm) according to SANS. The T_2 value of the droplets and puddles increases in a gradual manner with increasing water content, suggesting that their extension increases in a continuous manner in the fibrillar backbone.

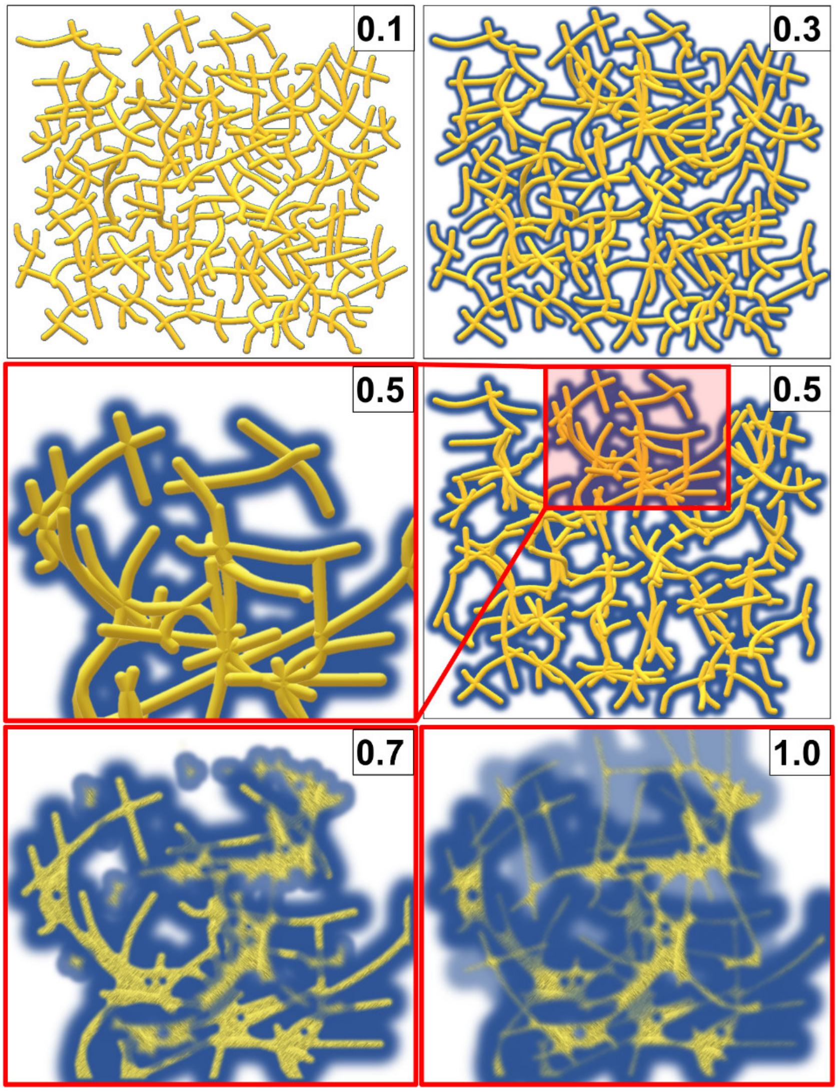

Scheme 7. Graphical representation of the hydration mechanism and the hydration induced structural changes of CaAG. The corresponding water content is given in the upper right corner of each panel in g/g units. The red frame indicates magnification. The well-defined porous aerogel structure is intact up to ca. 0.6 g/g water content. The formation of water droplets starts in the focal points of the aerogel network at ca. 0.3 g/g water content. The original Ca-alginate fibrils rearrange into fibers and fascicles that is well-expressed at 0.5 g/g water content. The formation of a hydrogel-like phase takes place at the critical water content of 0.6 – 0.7 g/g, where the well-hydrated Ca-alginate chains rearrange into a quasi-homogeneous 3D network. The characteristic structural elements of hydrated CaAG as a function of its water content are listed in **Table 9**.

The mechanism of hydration of CaAG up to a water content of 0.5 – 0.6 g/g is consistent with the hydration of a solid porous material that constitutes a strongly hydrophilic backbone that in turn changes upon hydration. [122,135] Up to this point, water is localized in association with the macromolecules, in the primary hydration sphere, and in droplets in the focal points of the modified porous structure defined by the newly formed Ca-alginate fibers and fascicles.

Table 9. Characteristic structural elements of CaAG as a function of its water content. The hydration mechanism and the hydration induced structural changes of CaAG are visualized in **Scheme 7**.

total water content (g/g)	**Ca-alginate backbone**	**localization of water**
0.1 – 0.4	solid backbone; bound Ca-alginate macromolecules; primary fibrils; mesopores	H-bonded structural water; primary hydration sphere; small droplets
0.4 – 0.6	solid backbone; re-oriented Ca-alginate macromolecules; fibers and fascicles; large pores	H-bonded structural water; extensive primary hydration sphere; droplets and puddles
0.6 – 0.7	formation of quasi-homogeneous 3D network of hydrated Ca-alginate chains	critical hydration level; formation of a hydrogel-like state
0.7 – 0.9	quasi-homogeneous 3D network of hydrated Ca-alginate chains; no solid backbone; no pores	extensive primary hydration sphere; extensive puddles; quasi-bulk water in the network; minor inhomogeneities in the gel network
1.0 – 1.8	quasi-homogeneous 3D network of hydrated Ca-alginate chains in loose connection; hydrogel	extensive primary hydration sphere; continuous phase of quasi-bulk water in the network

A critical level of hydration is reached at ca. 0.7 g/g. At this point, a new relaxation domain appears (4th relaxation domain). This new domain represents quasi-bulk regions of water, in agreement with the sharp transition of the SANS curves at ca. 0.7 g/g water content. The Ca-alginate fibers disintegrate into a well-hydrated but still entangled network of macromolecules with concentration gradients. Consequently, the pore structure collapses and the well-defined solid backbone ceases to exist. These structural changes manifest themselves in the steep increase of the T_2 of the 3rd relaxation domain and the marked expansion of the 4th domain starting at ca. 0.8 g/g water content. There is water exchange between the 3rd and 4th domains, which is generally characteristic for the hydrogel-like state. [240] The transformation of the aerogel into this hydrogel-like network is complete at ca. 1.0 g/g water content.

The further increase of the hydration level does not cause any sharp structural or morphological changes in the well-hydrated CaAG, but the hydrogel-like network gradually becomes less and less concentrated, which is reflected in the increase of the T_2 of the 4th domain and the value of D_{obs}. [226,228] Most of the water is localized in the extensive hydration sphere of the entangled Ca-alginate chains that is clearly shown by the relaxometry and cryoporometry results, and manifests in the restricted self-diffusion of water. Interestingly, the original CaAG beads keep their integrity even at a water content of 1.6 g/g (**Fig. 24**), which is reflected by the inability of water to diffuse from one hydrated bead to another.

V-1.4.4. Outlook and perspectives

In general, the presented methodology can guide the understanding of the alteration of the macroscopic properties of porous biomaterials in relation to both humid air and aqueous environments. Regarding CaAG, a complementary study pointed out that the stiffness and the compressive strength of hydrated CaAG significantly increase compared to its dry state properties. [266] Now, it is clear that the stiffening of the aerogel is due to the formation of new nanoscale superstructures in the hydrated backbone. The molecular level understanding of the hydration mechanism formed the basis of a subsequent study in which a constitutive model was developed that accurately accounts for the hydration induced changes of the mechanical properties of CaAG. [284] In another follow-up study, a multi-scale model was developed based on the SANS results presented here, to precisely quantify the hydration induced structural changes in CaAG both in the molecular level and in the nanoscale. [172]

V-1.5. Nanoscale structures of polyurea cross-linked Ca-alginate aerogels [P6]

An issue that has to be overcome for the practical application of bio-aerogels is the enhancement of their mechanical strength and water resistance. These issues are addressed for biopolymer aerogels by the development of polymer-crosslinking methods. In the case of the so called “X-biopolymer” aerogels, a triisocyanate is reacted with the biopolymer network post-gelation. The triisocyanate first reacts with the –OH or –NH_2 groups available on the surface of the biopolymer gel, and attaches to these through urethane or urea linkages. Subsequently, this new reactive moiety hydrolyzes with the (residual) water on the biopolymer, and reacts with a new triisocyanate forming a new polymer network. This results in the coating and crosslinking of the entire original biopolymer gel network with a thin polyurea structure (**Scheme 8**). [285]

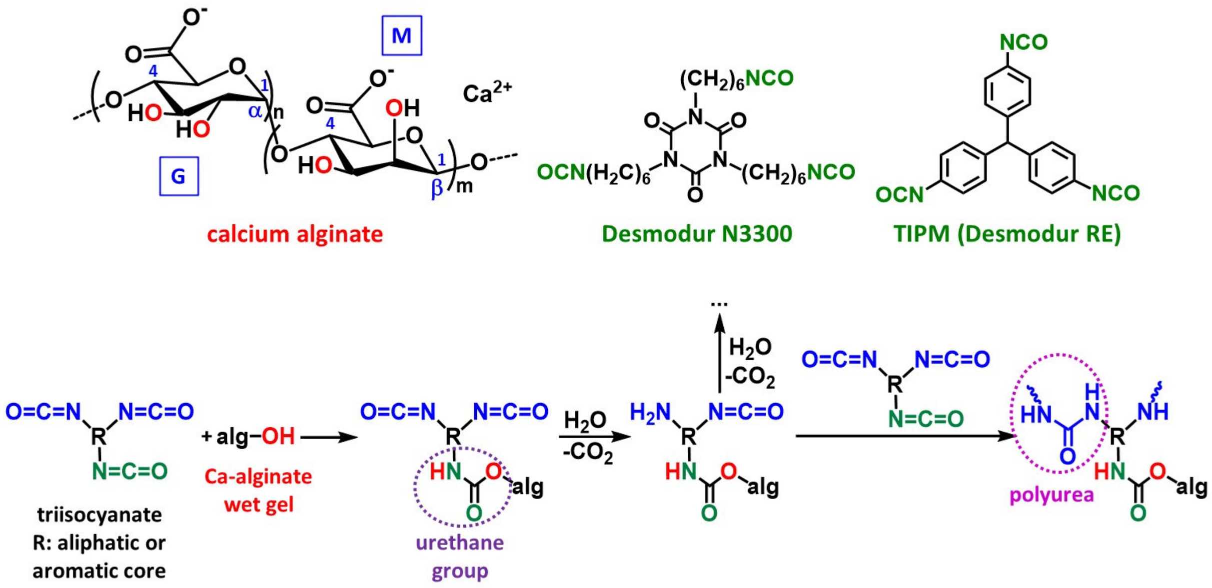

Scheme 8. Reaction scheme showing the crosslinking of Ca-alginate wet gels with the triisocyanates Desmodur N3300 (aliphatic) or Desmodur RE (aromatic). [285]

V-1.5.1. Morphological properties and nanoscale architectures of X-Ca-alginate aerogels

Representative material properties of native (Ca-alg) and crosslinked (X-Ca-alg-N3300 and X-Ca-alg-RE) aerogels are collected in **Table 10**. The polyurea content, calculated from the skeletal densities of native and crosslinked samples, is approximately the same: 56wt% for X-Ca-alg-N3300 and 60wt% for X-Ca-alg-RE. All the experimental N_2-sorption isotherms (**Fig. 33**) are characteristic for mixed meso- and macroporous materials. The pore size distribution curves show a maximum at 33–35 nm for all three materials, and otherwise broad distributions. The apparent BET specific surface area of the X-Ca-alginate aerogels is lower compared to that of the native Ca-alginate aerogel, suggesting that polyurea covered some fine morphological features along the original skeletal framework.

Representative SEM images are shown in **Fig. 34**. The general fibrous morphology of the modified aerogels is traced back to the native Ca-alginate aerogels. As seen in the SEM images, fiber entanglement creates macropores. The morphology of the crosslinked X-Ca-alginate aerogels is practically the same as that of the native Ca-alginate aerogels. Upon closer inspection, the fibrils that form the skeletal framework of all three materials have the same aspect ratio and consist of strings of tiny beads – presumably secondary particles. As indicated by the SANS study detailed below, the fibers of the native Ca-alginate aerogels are indeed built from secondary particles that in turn are mass-fractal aggregates of primary nanoparticles. The mesoporosity measured by N_2-sorption corresponds to the void space among these particles.

Table 10. Properties of native (Ca-alg) and crosslinked (X-Ca-alg-N3300, X-Ca-alg-RE) aerogels.

Sample	Envelope density (g cm^{-3})	Skeletal density (g cm^{-3})	Porosity (V/V%)	BET app. surf. area (m^2 g^{-1}) [micropore surf. area]	V_{Total} ($V_{1.7\text{-}300\text{nm}}$) (cm^3 g^{-1})	Mean pore diam. (nm)
Ca-alg	0.076±0.006	1.89±0.02	96	485 [81]	13 (1.9)	16 (104)
X-Ca-alg-N3300	0.19±0.02	1.43±0.01	87	265 [0]	4.6 (1.5)	23 (69)
X-Ca-alg-RE	0.18±0.02	1.44±0.01	88	425 [49]	4.9 (1.9)	19 (46)

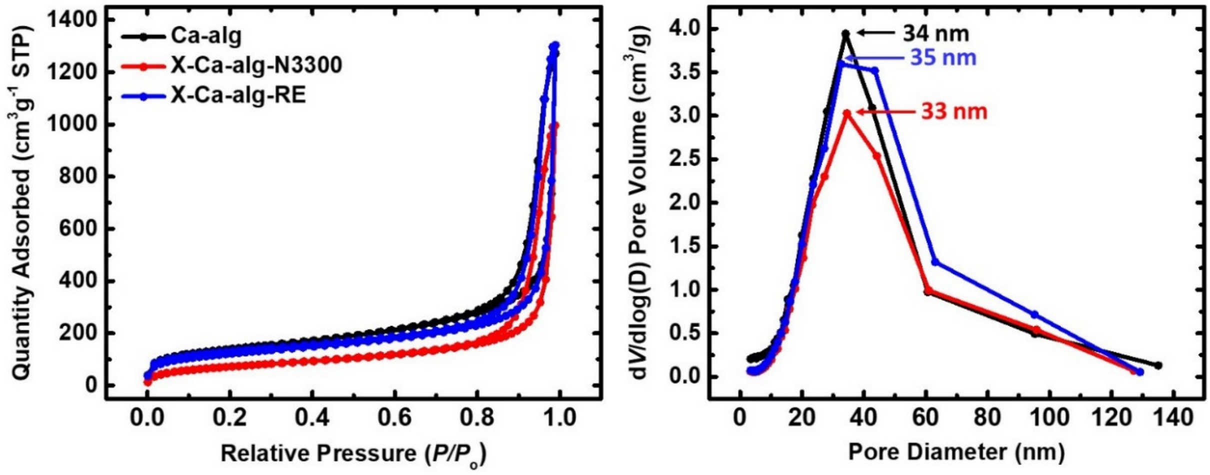

Figure 33. N_2-sorption isotherms (left) and pore size distributions calculated by the BJH method (right) of native (Ca-alg) and crosslinked (X-Ca-alg-N3300 and X-Ca-alg-RE) aerogels, as indicated.

The SANS curves of the three aerogels are shown in **Fig. 34**. For every one of the three materials, the scattering curves of the as-prepared aerogel and that of the same aerogel filled with a H_2O–D_2O mixture, as specified below, are overlaid. [236] The best fits using the Beaucage model are also displayed in **Fig. 34**, and the estimated structural parameters are given in **Table 11**. The scattering curves of the H_2O–D_2O–filled Ca-alg and X-Ca-alg-RE samples feature only power-law type scattering, and were fitted accordingly. The geometry of the primary scattering objects was approximated with spheres, and scattering particle radii (r_{particle}) were calculated from the estimated radii of gyration (R_g). The neutron scattering length density (SLD) of Ca-alginate aerogel is estimated based on its chemical formula [$(C_{12}H_{14}CaO_{12})_n$] and skeletal density (1.89 cm^3 g^{-1}; **Table 11**). Based on this, the SANS contrast of the Ca-alginate component is expected to be matched by completely filling the samples with the 46wt% H_2O – 54wt% D_2O liquid mixture. Indeed, the filled Ca-alg and X-Ca-alg-RE samples show very minor specific SANS scattering caused by nanosized objects (**Fig. 34**). Both SANS curves show a power law behavior characteristic to mass fractals. However, the fitted curves deviate slightly from the experimental points. This feature might indicate the somewhat incomplete filling of pores due to hydrophobic spots, or to a small number of closed micropores. The shape of the SANS curves of the pristine and the H_2O–D_2O–filled X-Ca-alg-N3300 samples are similar, which indicates that contrast matching was not realized in this case.

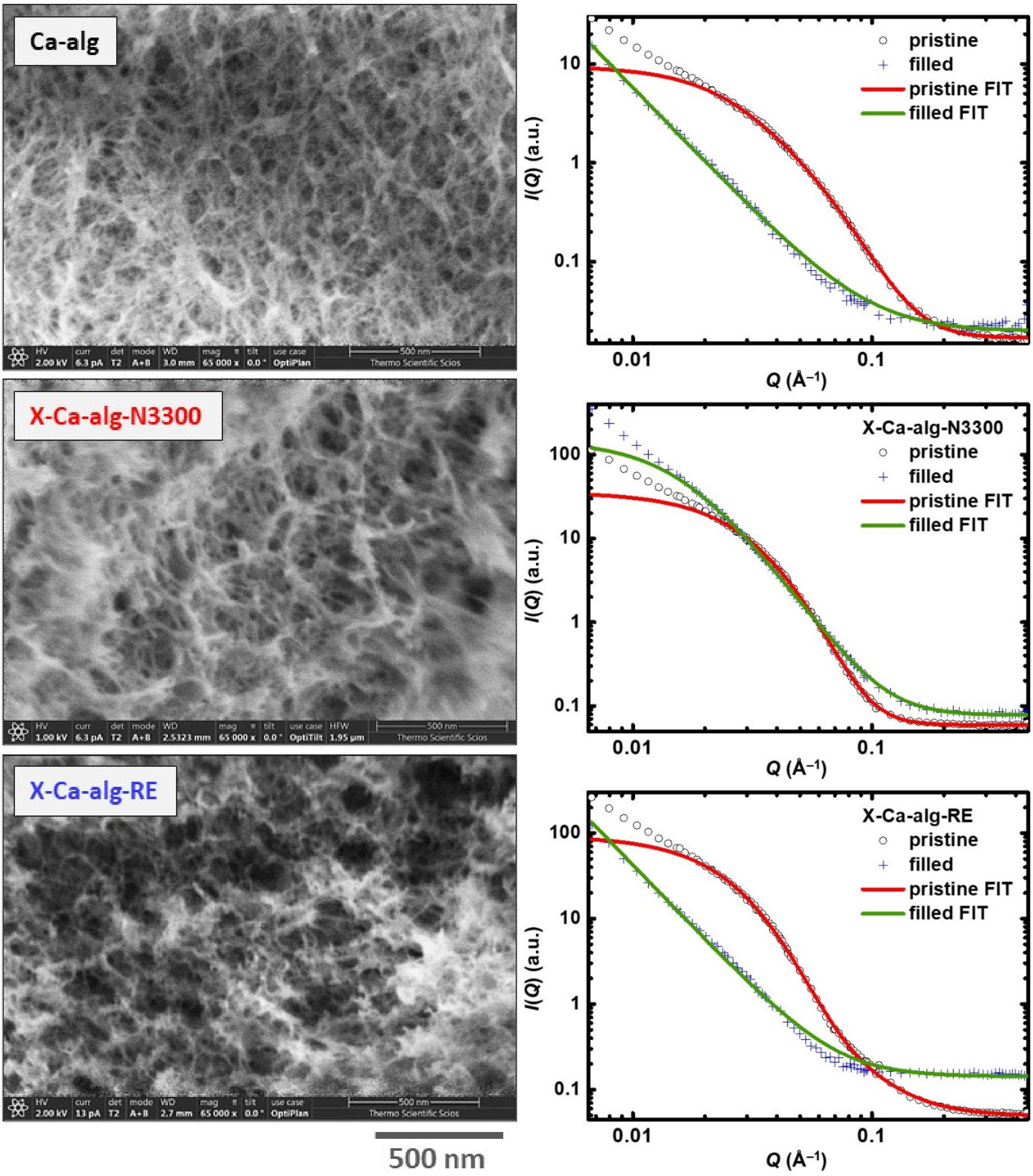

Figure 34. Left panel: Representative low-voltage SEM images of fresh-fracture surfaces of native (Ca-alg) and crosslinked (X-Ca-alg-N3300 and X-Ca-alg-RE) aerogels. Right panel: Small angle neutron scattering (SANS) curves of the same aerogels, as indicated. Pristine aerogels were measured first, and the same samples were filled with the H_2O–D_2O mixture. Continuous lines are results of non-linear model fitting. Estimated structural parameters are given in **Table 11**.

Table 11. Structural parameters estimated by fitting the SANS curves of the pristine and the filled native (Ca-alg) and crosslinked (X-Ca-alg-N3300 and X-Ca-alg-RE) aerogels. The SANS curves and the non-linear fits are shown in **Fig. 34**.

Sample	**Beaucage model R_g (Å)**	**$r_{particle}$ (nm)**	**Beaucage model p**	**Power-law model p**
Ca-alg *PRISTINE*	64 ± 1	8.3 ± 0.1	4.55 ± 0.03	
X-Ca-alg-N3300 *PRISTINE*	68 ± 1	8.8 ± 0.1	5.63 ± 0.17	
X-Ca-alg-RE *PRISTINE*	79 ± 1	10.0 ± 0.1	2.94 ± 0.03	
Ca-alg *FILLED*				2.49 ± 0.01
X-Ca-alg-N3300 *FILLED*	122 ± 4	16 ± 0.5	3.80 ± 0.03	
X-Ca-alg-RE *FILLED*				2.90 ± 0.01

The fundamental fibrous structure of native Ca-alginate aerogels is hierarchically constructed of primary and secondary nanoparticles. Fibrous aerogels consisting of such nano-structural elements have previously been reported in the cases of certain polyurea and polyimide aerogels, and have been described as the consequence of phase separation during the sol-gel process yielding solid primary nanoparticles that assemble with one another by diffusion-controlled cluster aggregation mechanism. [286,287] According to these considerations, the proposed nanoscale structure of native Ca-alginate aerogels and the illustration of the principal idea behind contrast matching in SANS are shown in **Scheme 9**.

It is reasonable to assume that the difference in the SANS contrast matching in the case of the two X-Ca-alginate aerogels indicates the different associations of the Ca-alginate and the polyurea structural elements in the two aerogel nanoscale architectures. [288] The matching of contrast in the case of X-Ca-alg-N3300 aerogels can be imperfect because the flexible aliphatic polyurea forms a more compact coating on the primary Ca-alginate nanoparticles. This tighter association and the interfacial covalent connectivity of the two polymers change the scattering length density of the X-Ca-alg-N3300 backbone compared to that of the native Ca-alginate, as seen in the case of the silica-gelatin and silica-casein hybrid aerogels (**Sections V-1.1. and V-1.2.**). [125,129] Interestingly, the p value for the pristine X-Ca-alg-N3300 aerogel is larger than 4, which indicates a gradual density change on the nano-interfaces of the crosslinked aerogel. This agrees with the fact that the nanoparticle network of the samples was formed first from Ca-alginate, and polyurea accumulated in the second step on the reactive surfaces of the nanoparticles of the biopolymer network by different mechanisms.

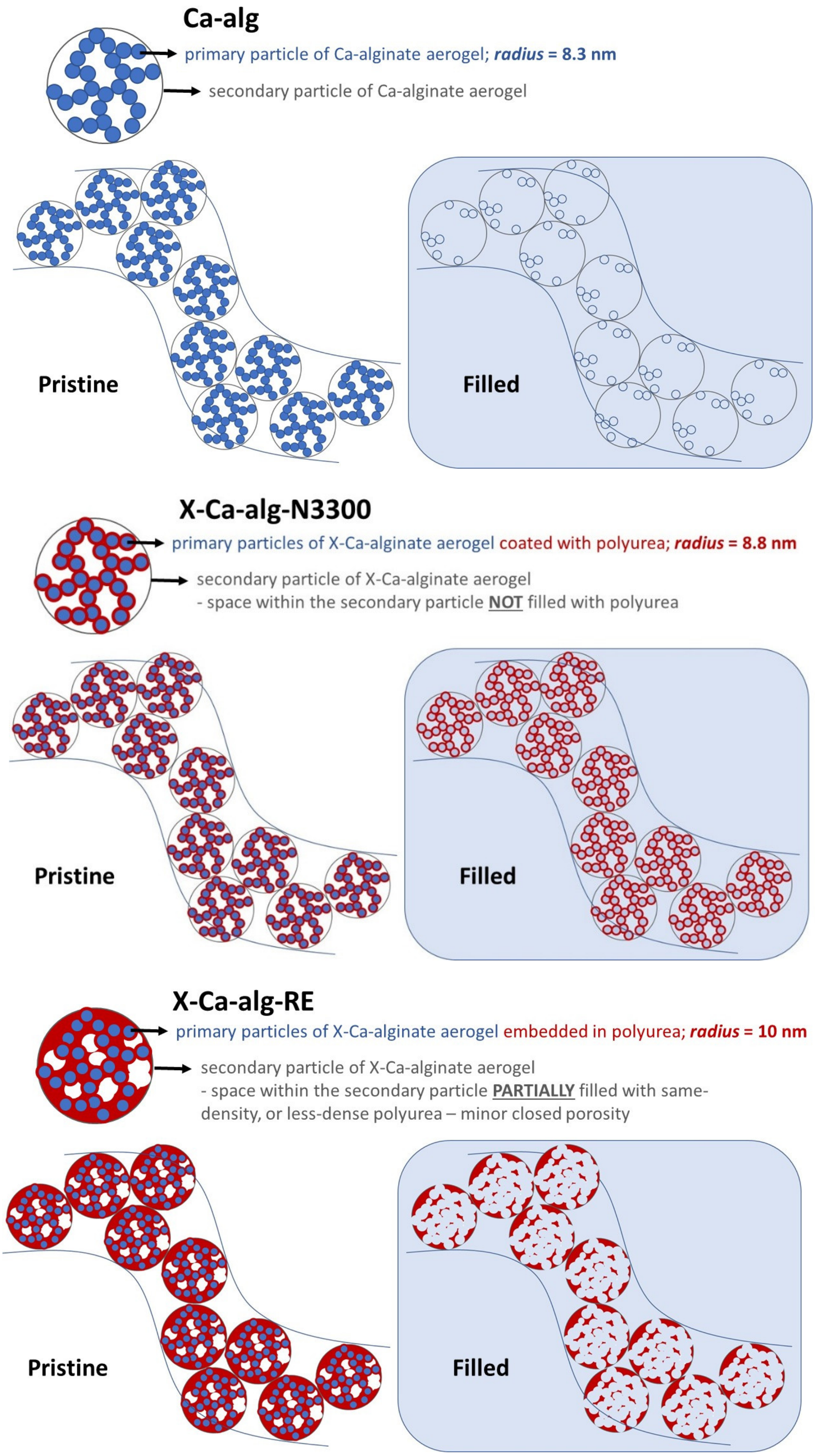

Scheme 9. The proposed nanoscale structures of native Ca-alginate (Ca-alg) aerogel, and crosslinked X-Ca-alg-N3300 and X-Ca-alg-RE aerogels. Panels labeled “Filled” denotes filling with the contrast matching H_2O–D_2O mixture in SANS. [285]

In the case of X-Ca-alg-RE aerogel, the observations can be interpreted by assuming that the rigid aromatic polyurea does not coat the original Ca-alginate nanoparticles as compactly as its flexible aliphatic counterpart, but loosely fills the space among the biopolymer particles. The proposed nanoscale structures of X-Ca-alg-N3300 and X-Ca-alg-RE aerogels are shown in **Scheme 9** using the same principles as for depicting the Ca-alginate aerogel.

As a summary, polyurea-crosslinked Ca-alginate (X-Ca-alginate) aerogels have distinct nanoscale morphologies depending on the crosslinking triisocyanate reagent. Crosslinking with the aliphatic triisocyanate Desmodur N3300 yields flexible aliphatic polyurea macromolecules in the final aerogel framework, while the aromatic triisocyanate Desmodur RE yields rigid aromatic polyurea macromolecules. Probing the different aerogels using contrast-variation SANS enabled the reconstruction of the nanoscale architectures. Native Ca-alginate aerogels are built of primary nanoparticles that aggregate in mass-fractal like secondary particles forming long fibers. Crosslinking with the flexible aliphatic triisocyanate leads to the formation of a compact polyurea layer over the primary nanoparticles following the contours of the native Ca-alginate skeletal framework. On the other hand, the rigid aromatic triisocyanate forms a randomly oriented polymer network that only loosely fills the empty space among the original biopolymer nanoparticles. Overall, both processes leave the original Ca-alginate gel structure practically intact, but increase the primary particle size, and reduce porosity and surface area.

V-1.6. Mechanism of hydration induced stiffening and subsequent plasticization of an archetypical polyamide aerogel [P7]

One constraint of the applications of advanced polyamide aerogels is the possibility of extensive structural changes upon the sorption of water vapor. The hydration of nanostructured biopolymers and polymers is accompanied by complicated changes both in their molecular conformation and in their nanoscale architecture. [289-291] The exact nature of these changes and the mechanism of the hydration of the backbone can be elucidated in fine details only by the combination of state-of-the-art characterization techniques that provide information on the molecular level structural changes, as well as the alteration of the nanoscale architecture. [95,123,129,241,292] Another complication is, that water is a Janus-type small molecular weight additive in polymer science; capable of both the plasticization and the anti-plasticization of the same polymer in a concentration dependent manner. [293-295]

A linear polyamide gel similar in chemical structure to Kevlar was synthesized, and a monolithic aerogel (polyamide aerogel: PAA – **Scheme 10**) was prepared from it by drying in supercritical CO_2 based on a published recipe. [211] The hydration of the monolithic PAA causes dramatic changes in its mechanical properties in a non-monotonic way. To understand the molecular basis of these alterations, the intimate mechanism of the hydration of the aerogel was investigated using solid state and liquid phase NMR methods in combination with SANS. No macroscopic swelling (or shrinkage) was observed when the aerogel was hydrated.

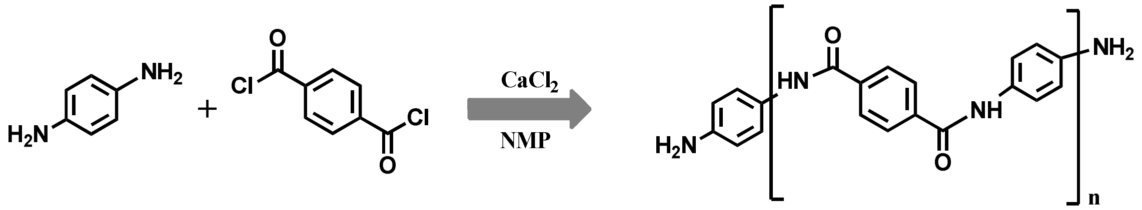

Scheme 10. The formation and the chemical structure of the linear polyamide (PA) macromolecules.

V-1.6.1. Morphology of the dry aerogel

The main structural elements dominating the nanoscale architecture of PAA are strut-like entangled and interconnected polymer fibrils (**Fig. 35**). [211] The thickness and the length of the fibrils vary to a large extent. Some of the fibrils are branched and some struts merge by the ends. The regions in the backbone where fibrils entangle or merge are termed "focal points". In this architecture "pores" are best defined as the void spaces among interweaved fibrils. Mesopores are evidently not visible in this magnification, but large macropores are. There are no geometrical elements that clearly separate these void spaces from each other, thus, the variation of the size and the shape of these voids are very high. Therefore, the interpretation of characterization data has to be very meticulous, because the classical geometrical models generally used for the calculations have limited validity in this case.

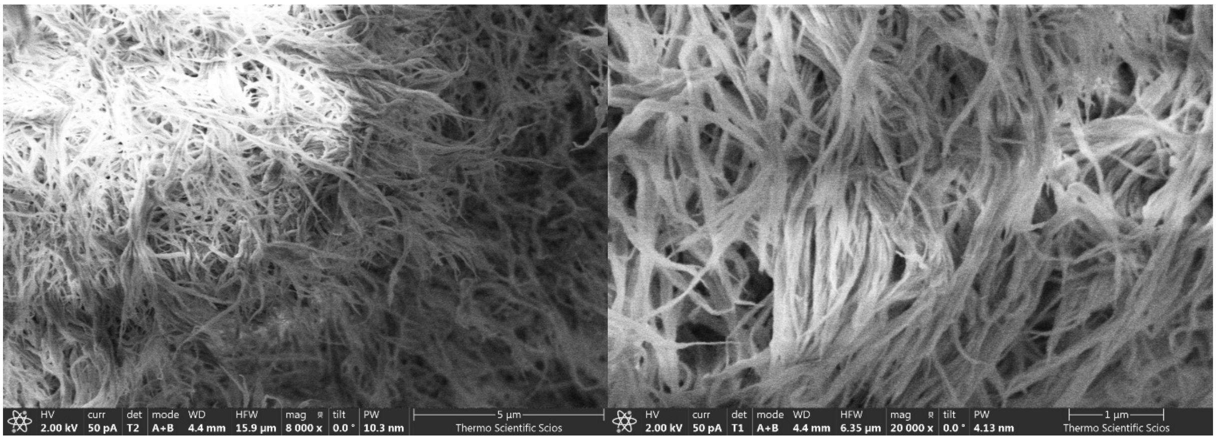

Figure 35. Representative LV-SEM images of the pristine polyamide aerogel (PAA).

The shape of the N_2-sorption isotherms (**Fig. 36**) fit into the IUPAC IV category with the H3 hysteresis loop, which is characteristic for mesoporous materials. The steep increase at the lowest relative pressures indicates the presence of micropores. Macropores are also present in PAA, as seen in the SEM images. The structural parameters calculated by the classical BET and BJH evaluation methods are shown in **Table 12**. The unique morphology of PAA should carefully be taken into account for assessing the calculated structural parameters. Specifically, the N_2-sorption method is not sensitive to large pores that cannot be filled by the condensed N_2, therefore, the macropores of PAA only partially contribute to the calculated pore volume and pore size distribution. This limitation of the method is extensively discussed in the literature. [12] The envelope density of PAA is 0.23 g $\mathrm{cm^{-3}}$, while the density of its polymer skeleton is 1.27 g $\mathrm{cm^{-3}}$. [211] The large difference between the calculated total pore volume (3.5 $\mathrm{cm^{-3}}$ g) and the measured mesopore volume (0.7 $\mathrm{cm^{-3}}$ g) reflects the extensive macroporosity of PAA.

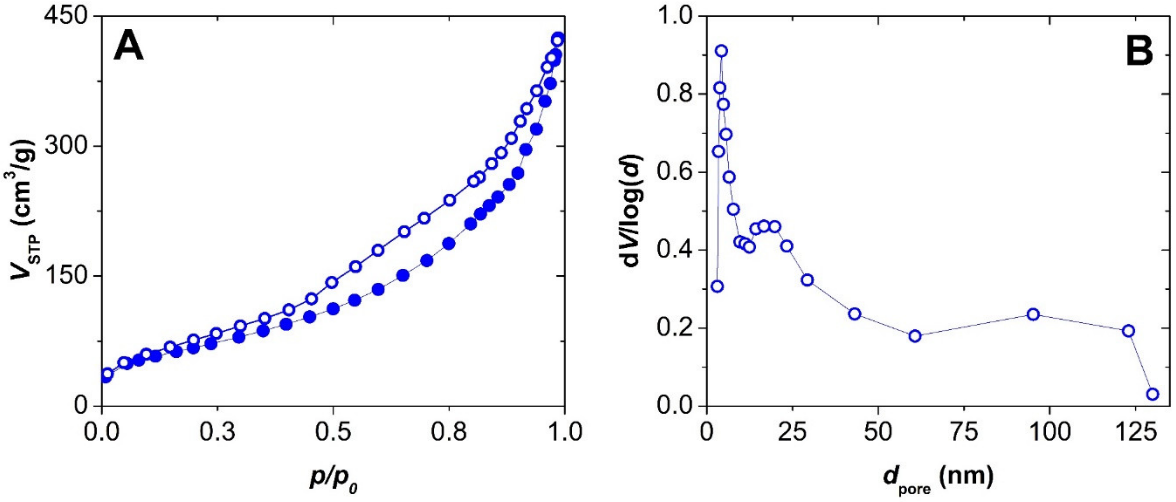

Figure 36. Panel A: Nitrogen adsorption-desorption isotherms of PAA. Panel B: Pore size distribution calculated from the desorption isotherm using the BJH method.

Table 12. Structural parameters of pristine PAA estimated by the BET and the BJH methods from the N_2 adsorption-desorption data (cf. **Fig. 36**).

Parameter	**PAA**	**Data evaluation**
***C*-constant**	59 ± 3	BET
Specific surface area (m^2/g)	251 ± 20	BET
Mesopore volume (cm^3/g)	0.7 ± 0.1	BJH

The BJH pore size distribution of PAA is apparently bimodal (**Fig. 36B**). However, the narrow peak around $d_{pore} \approx 4$ nm might not be real, because this feature arises from the deviation between the adsorption and desorption branches at low relative pressures. Such a deviation can result from morphological distortion of the PA fibers caused by solvation in the condensed N_2.

V-1.6.2. Mechanical properties as a function of hydration

The experimental compression strain-stress curves and the estimated Young's modulus values of monolithic PAA are shown in **Fig. 37** as a function of hydration. The full experimental strain-stress curves were mathematically fitted using the extended version of the standard linear solid (SLS) viscoelastic model. [296] Starting from the dry aerogel, the Young's modulus and the compressive strength of the monolithic PAA dramatically increase when its water content increases, and display a maximum when equilibrating with 50% relative humidity air (0.16 g/g water content). Importantly, the additional hydration of PAA under higher relative humidity causes a sharp decrease in these mechanical parameters.

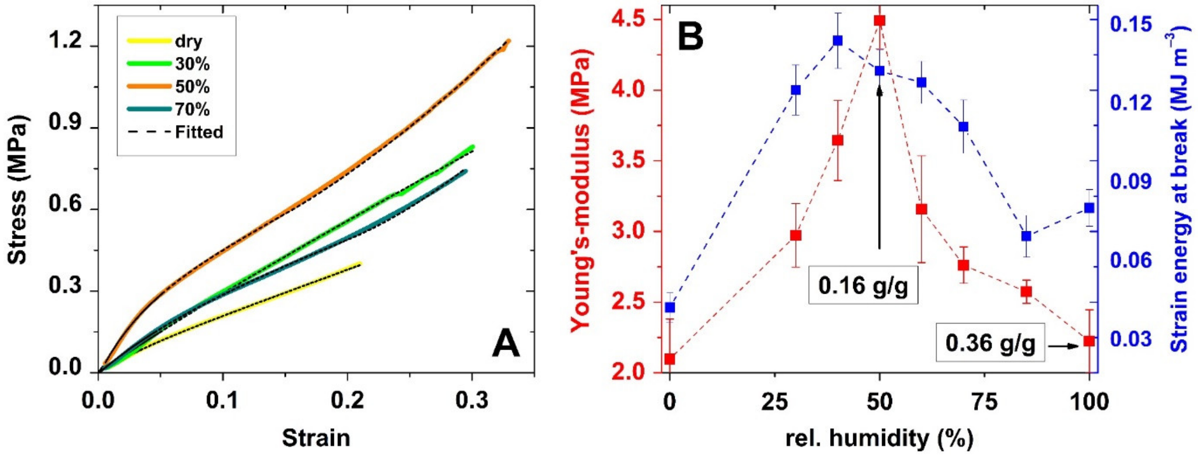

Figure 37. Panel A: Compression strain-stress curves of PA aerogel monoliths. The relative humidity of air used for conditioning the PAA monoliths is given in the legend. The black curves are results of mathematical fitting by the standard linear solid (SLS) viscoelastic model. Panel B: Estimated Young's modulus and compressive strength as a function of the aerogel conditioning. The water contents in g/g units are given in the legend. The error bars represent specimen-to-specimen standard deviation.

In order to give an explanation for this phenomenon, the hydration mechanism of PAA was studied in multiple scales. The molecular level processes were probed by various NMR methods, and the alterations in the nanostructure were investigated by SANS.

V-1.6.3. Characterization of hydrated PAA

SANS. The experimental scattering curves are shown in **Fig. 38A** together with the best fits. The Beaucage model is adequate for fitting the curves until 0.4 g/g water content. Above this water content, the Guinier regions of the SANS curves gradually shift towards the small Q values and out of the experimental range, as shown in **Fig. 38B**. The SANS curves are less structured at water contents higher than 1.8 g/g, and can only be fitted with the simple power-law model (Porod region). The estimated structural parameters are shown **Fig 38C**. Several other models were tested for fitting the scattering curves, but only the presented approach was found consistent for describing the full range of the investigated samples. [12,297]

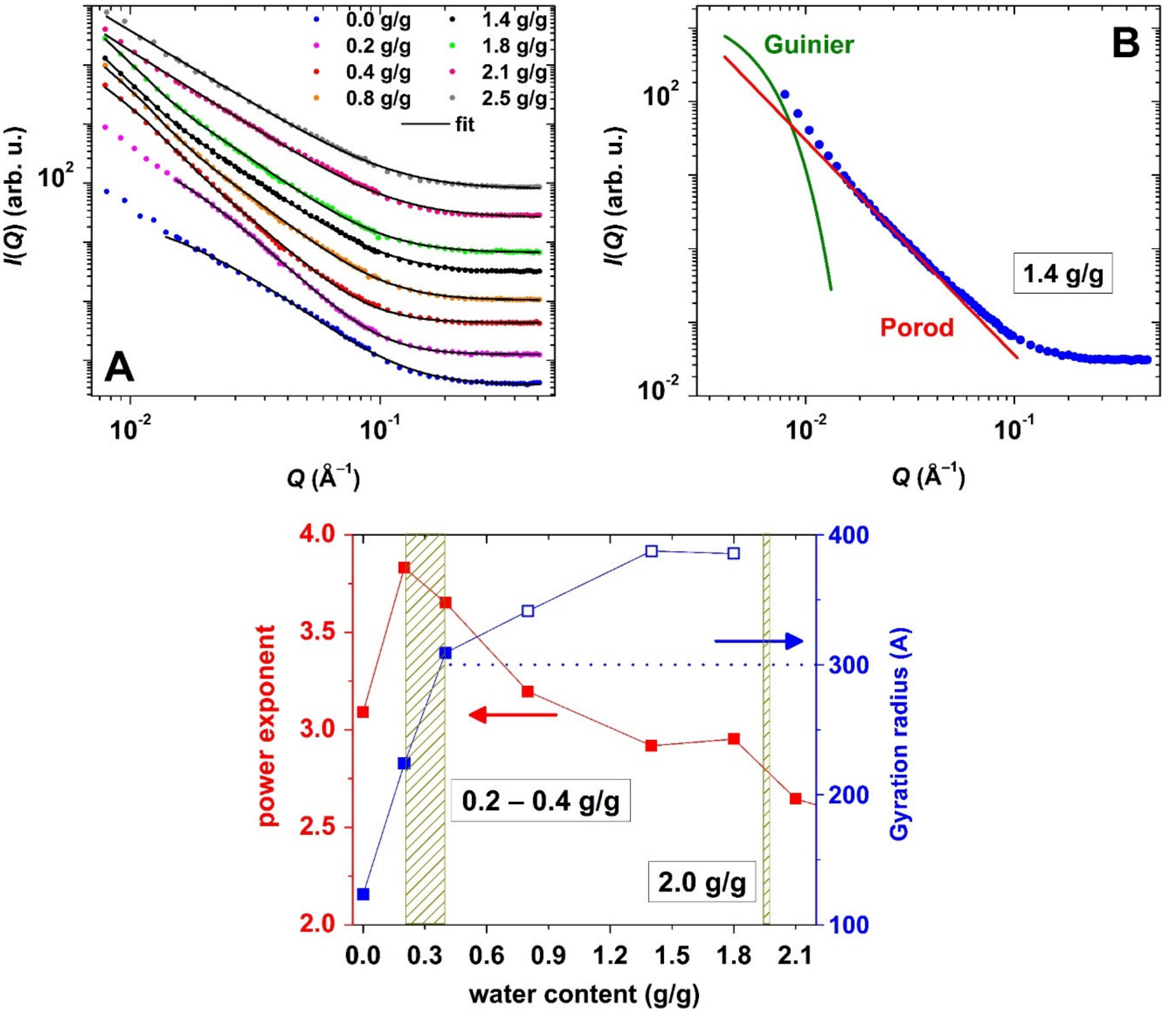

Figure 38. SANS characterization of partially hydrated PAA. Panel A: The experimental SANS curves (markers) together with the best fits (lines). The water (D_2O) contents of the PAA samples are given in the legend. Panel B: Contribution of the different model functions to the overall fit. Panel C: Estimated structural parameters as a function of the water (D_2O) content of PAA. (The deviation between duplicate measurements is ca. 10%.) The estimated R_g values are uncertain above 300 Å. The dashed vertical bars indicate water contents of special interest.

The R_g steeply increases with increasing water (D_2O) content up to ca. 0.4 g/g. At higher water contents, the increase of the R_g is approximately gradual. The p exponent has a maximum value at ca. 0.2 g/g water content ($p \approx 4$), and decreases from this point on in a gradual manner with increasing water content until $p < 3$. The SANS results demonstrate the dramatic change of the nanoscale morphology of the PA aerogel as a function of its water content. [12,297] The increase of R_g is associated with the increase of the size of the pores, which is naturally accompanied by the initial smoothening of the surface of the pore walls as shown by the $p \approx 4$

value at 0.2 g/g water. Above this water content, the size of the pores still increases, although, the roughness of the pore walls also increase. The *p* value is between 3 and 4 in this region of hydration, which indicates surface fractal-like structures and points out that the smooth surface becomes rough again as a consequence of additional hydration. The explanation is the partial dissolution of the fibers of the solid backbone that is accompanied by the increased segmental motion the PA macromolecules. [289,298] Evidence for these molecular level changes is supported by the solid state and the liquid state NMR results that are discussed in the next sections. At water contents higher than 2 g/g, the *p* exponent is lower than 3 indicating the presence of mass-fractals in the hydrated aerogel. This is attributed to the formation of nano-sized water (D_2O) droplets in the focal points of the hydrated aerogel backbone, which is strongly supported by the NMR relaxometry and cryoporometry results (*vide infra*).

The formation of a hydrogel at high water contents can be ruled out due to the absence of sharp changes in the *p* exponent. This is in contrast to the features of biopolymer aerogels. [95] According to the SANS data, marked structural changes take place in the PA aerogel when reaching the critical water content of ca. 0.2 g/g, and subsequently when reaching 2 g/g. The nature of these marked structural changes is further elucidated in the next sections.

Solid state NMR. The high resolution of the ^{13}C CPMAS peaks allowed the unambiguous assignation of the five aromatic resonances (**Fig. 39**). [211] The 3D organization of the PA macromolecules in the fibrous aerogel backbone is similar to those in bulk Kevlar materials. [299,300] The high intensity shoulder at ca. 10 ppm in the ^{1}H MAS spectrum of the dry PAA indicates the presence of several intermolecular H-bonds among the macromolecules generally characteristic for linear polyamides. Hydrating PAA does not alter the ^{13}C chemical shifts, or the peak widths and resolution, yet cause marked changes in the relative peak intensities, which becomes expressed at around 0.5 g/g water content. This indicates the significant reorientation of the macromolecules. The accompanying marked decrease in the ^{13}C CPMAS intensities is attributed to the increased segmental motion of the polymer chains when reaching this critical hydration level, which lowers the effectiveness of the magnetic cross-polarization. [289,298] In-line with this, the ^{1}H MAS spectra of the partially hydrated samples show that the extensive intermolecular H-bonding network of the linear PA macromolecules is gradually disrupted with increasing hydration. [301] The ratio of the aromatic protons to the ones participating in strong intermolecular H-bonds between the PA molecules was derived from the quantitative ^{1}H MAS NMR (Ar/H-bond values in **Fig. 39**). This value is 1.3 for the dry aerogel; and it increases to 3.9 at 1.0 g/g water content indicating a significant decrease in the number of intermolecular

H-bonds in the partially hydrated PA macromolecular network. [302] The effects of other non-covalent interactions, such as π-stacking, were not detected in the solid state NMR data.

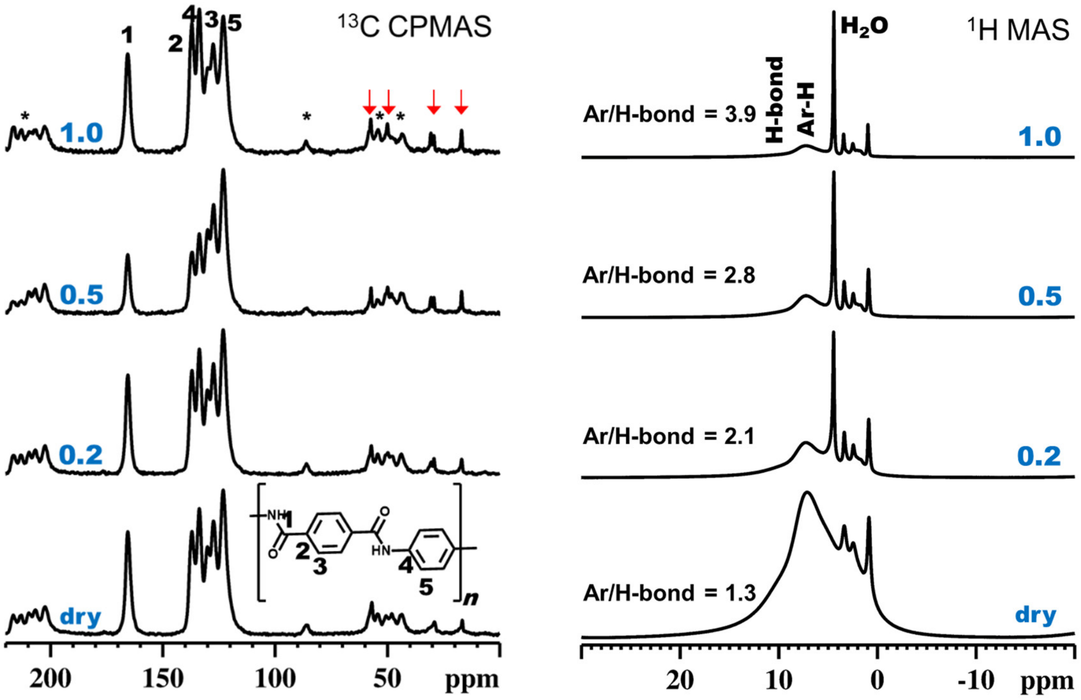

Figure 39. The mass-loading normalized ^{13}C CPMAS (left panel) and ^{1}H MAS (right panel) NMR spectra of the PAA at different water contents, as shown in the panels in g/g units. Peak assignments are given in the panels. The explanation of the spectral changes is given in the main text. The ^{13}C CPMAS spectra were recorded using a MAS rate of 10 kHz and a CP contact time of 0.5 ms. The MAS rate was 15 kHz for the ^{1}H MAS. Spectra are normalized to the highest peak intensity. The peaks of residual solvents are marked by red arrows, and the spinning sidebands by asterisks.

NMR relaxometry. As-prepared PAA was gradually hydrated, and the measured T_2 relaxation times represent the equilibrium sates of the partially hydrated PAA samples (**Fig. 40**). The saturation of the pores by water is reached at a water content of ca. 3 g/g. At the lowest water contents, there is only one relaxation domain detectable with very small T_2 values. This domain corresponds to water molecules in strong interaction with the PA macromolecules. [301] The 2nd domain appears at ca. 0.19 g/g water content with significantly higher T_2 values. However, these T_2 values are not high enough to indicate the formation of well-defined water droplets in the pores at this hydration level. Accordingly, the 2nd domain corresponds to water molecules still in strong interaction with the PA backbone. The amplitudes associated with the decay signals of the first two domains are in correlation with each other even at small water contents indicating the exchange of water between these domains. Based on the approximate equivalence of the amplitude values (not shown), the amount of water associated with the two domains is approximately the same at low overall water contents.

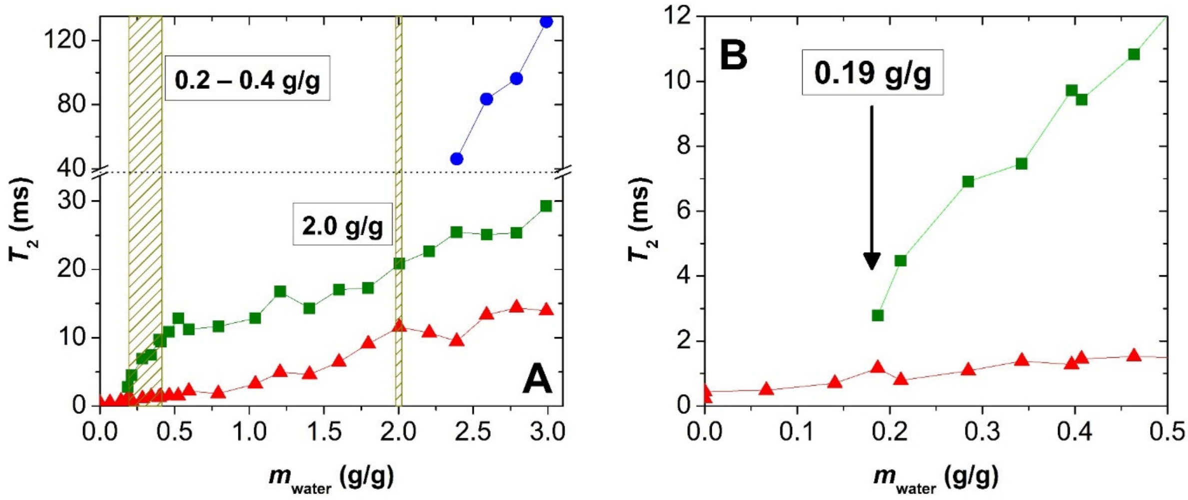

Figure 40. NMR-relaxometry of partially hydrated PAA. Both panels show the values of the spin-spin relaxation times (T_2) as the function of the water content of PAA. Panel B is a magnification of Panel A; the data points are the same. (The deviation between duplicate measurements is ca. 10%.) Three relaxation domains (marked with red triangles, green squares and blue circles) were observed at the different hydration levels until the saturation of pores of the aerogel by water at ca. 3 g/g. The dashed vertical bars indicate water contents of special interest.

The difference in the chemical environments of the water molecules of the 1st and the 2nd domains can be elucidated based on the ssNMR results. The first water molecules form H-bonds with the PA macromolecules on the surface of the fibers and build into the existing network of intermolecular H-bonds, as depicted in **Scheme 11**. This assumption is corroborated by previous studies. [303-306] Such a binding mode of water does not cause dramatic changes in the solid state ^{13}C CPMAS NMR spectrum. When the vacant H-bonding sites are saturated at ca. 0.19 g/g water content, the additional water molecules enter into the fibers, insert in-between the PA macromolecules and disrupt their intermolecular H-bonding network present in the dry aerogel (**Scheme 11**). [306,307] This becomes expressed in the ^{13}C CPMAS spectrum at ca. 0.5 g/g water content. The segmental motion of the PA macromolecules increases, and their original molecular orientations are altered in parallel to the formation of the 2nd relaxation domain. This process is the beginning of the partial dissolution of the PA fibers, which alters the morphology of the aerogel backbone. The nanoscale level morphological changes are well-expressed in the alteration of the SANS curves measured until ca. 0.4 g/g water content (cf. **Section V-1.6.3**). The presented mechanistic theory for the hydration of PAA is in good agreement with the observed sharp decrease of the Young's modulus value of the partially hydrated aerogel starting above ca. 0.16 g/g water content (cf. **Section V-1.6.2**), because this is concerted with the appearance of the 2nd NMR relaxation domain, as well as, the dramatic change of the nanoscale morphology reflected in the SANS results. [306,307]

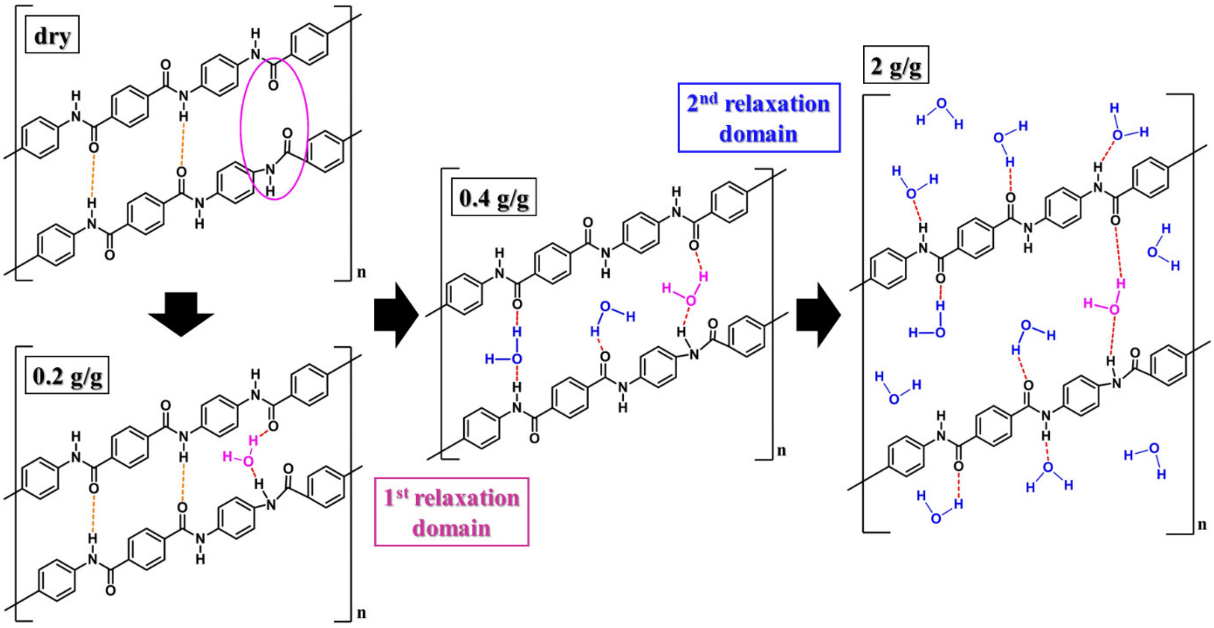

Scheme 11. Schematic representation of the interaction of water with the PA macromolecules as a function of the water content of the aerogel (displayed in the legend). The first portion of water molecules (1st relaxation domain) occupy the empty H-binding sites in the intermolecular H-bonding network of the linear PA macromolecules. Additional hydration results in the insertion of water molecules (2nd relaxation domain) between the macromolecules, which eventually results in the partial dissolution of the PA fibers at high water contents.

The additional increase of the water content above 0.5 g/g results in the extensive hydration and partial dissolution of the solid PA fibers. Water molecules are in less and less constraint in the well-hydrated fibers, therefore, the T_2 values of the first two relaxation domains increase. Evidently, water molecules in the different regions of the PA backbone exchange with one another. Finally, a third relaxation domain appears at ca. 2.0 g/g water. The T_2 values of the 3rd domain are significantly higher than those of the first two domains that corresponds to the formation of water droplets in the focal points of the entangled fibers. The sharp increase of the T_2 values of the 3rd domain with increasing water content indicates the dramatic increase of the size of the droplets. An important observation is that the appearance of the 3rd domain does not alter the gradual increase of the T_2 values of the 2nd domain. Because the T_2 values of the 2nd domain are characteristic for water inside the hydrated polymer fibers, this finding suggests the conservation of the fibrous structure of the aerogel even when it is saturated with water. This argument is further strengthened by the absence of a sharp decrease of the SANS power exponent at high water contents, which would be indicative for the transformation of the solid backbone into a quasi-homogeneous hydrogel. Despite the morphological changes, the backbone remains well-defined even when flooded by water, and the material does not form a hydrogel. For comparison, hydrogel formation is characteristic for biopolymer aerogels, which causes dramatic, yet concerted changes in the NMR relaxometry and the SANS data. [95]

NMR diffusiometry. Two variables were changed in the NMR diffusiometry measurements: *i*) the water content of the PA aerogel, and *ii*) the observation time of the experiments (**Fig. 41**). The self-diffusion of water is not detectable below ca. 0.5 g/g water content, as the dislocation of the water molecules bound to the PA macromolecules in the 1st NMR relaxation domain is very limited. [301,308] Furthermore, the T_2 values of these water protons are very small, and thus, the PGSTE sequence filters out the signal of these protons. [95] At higher water contents, two diffusion domains were detected. These were assigned based on the numerical values of D_{obs}, and taking into account the structural data collected by the other techniques.

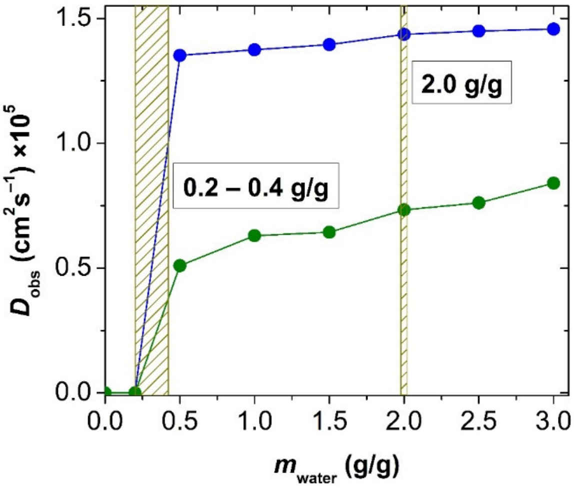

Figure 41. The observed self-diffusion coefficients (D_{obs}) of water as a function of the water content of the partially hydrated PAA. (The deviation between duplicate measurements is ca. 10%.) The self-diffusion of water is not detectable below 0.5 g/g water content. Two diffusion domains are present at higher water contents. For comparison, $D = 2.30\times10^{-5}$ cm^{2}s^{-1} in the pure phase of bulk water. [227] The dashed vertical bars indicate water contents of special interest.

The appearance of the diffusion signal at ca. 0.5 g/g water content is coincident with the sharp increase of the T_2 of the 2nd relaxation domain (cf. **Fig. 40**). The first diffusion domain ($D_{\mathrm{obs}} \approx 0.6\times10^{-5}$ cm^{2}s^{-1}) represents water molecules diffusing inside the hydrated PA fibers, which is naturally hindered. [308,309] In comparison, water molecules forming droplets and puddles are more mobile, and yield a second diffusion domain ($D_{\mathrm{obs}} \approx 1.4\times10^{-5}$ cm^{2}s^{-1}). The signals of the two diffusion domains are mathematically separable, however, water molecules exchange between these domains on the timescale of the diffusion experiments (ca. 100 ms), which is significantly longer than the timescale of the relaxation experiments (ca. 1 ms). [310] Consequently, the 2nd diffusion domain appears at a lower water content than the 3rd relaxation domain associated with the same droplets in the focal points in the backbone. The proportion of water in these droplets is too small for detection by relaxometry at around 0.5 g/g water.

The slight increase of the D_{obs} values of the domains with the increasing water content of the aerogel is due to the increasing amount and mobility of water in the partially dissolved fibers, and due to the size increase of the water droplets in the pores.

The D_{obs} values of both domains are independent of the observation time of the diffusion experiment, suggesting that the structural regions where the water molecules translocate are continuous in the hundreds of nanometers scale. This is further evidence for the preservation of the highly interconnected fibrillar backbone of the aerogel even at high water contents.

NMR cryoporometry. The relaxation filter of the CPMG sequence was optimized to remove the proton signal of ice, but this necessarily filters out the fast-relaxing 1st and 2nd domains of water (cf. **Fig. 40**). Therefore, the partially hydrated PA aerogel displays a meaningful liquid phase ^{1}H NMR signal only at water contents higher than 1 g/g (**Fig. 42**). The low intensity hysteresis loop detected in the cryoporometry curves at 1.0 g/g water content suggest that minor but mobile ”freezing” water bodies are present in the system even before the detection of the 3rd relaxation domain. [311] Thus, the NMR cryoporometry and diffusiometry results support each other, since the existence of such mobile (freezing) water accounts for the presence of the faster diffusion domain even at low water contents (cf. **Fig. 41**).

Owing to the relaxation transfer arising from the exchange between the domains, the CPMG signal is regarded quantitative only at water contents higher than 2 g/g, which is the start of the formation of distinct droplets giving rise to the 3rd relaxation domain. At 2.5 g/g water content, the shape of the well-defined melting-freezing hysteresis loop follows the approximate $\Delta T_{\mathrm{f}}/\Delta T_{\mathrm{m}}$ ratio of 3:2. This indicates that the majority of the confined water bodies are spherical. The corresponding droplet sizes are larger than the original mesopore sizes of the dry aerogel (cf. **Fig. 36)** that is in agreement with the significant increase of the SANS gyration radius by the hydration of PAA (cf. **Fig. 38**). These results are strong indication that the pore sizes of PAA dramatically increase with its hydration. Cryoporometry measurements conducted at 3.4 g/g water content indicate that the confined water bodies in the hydrated aerogel take the geometry of extensive slabs, because there is no detectable melting point depression ($\Delta T_{\mathrm{m}} = 0$ K) accompanying the freezing point decrease (**Fig. 42B**). The width of the slabs (continuous water bodies) confined by the solid skeleton is in good agreement with the previously measured size of the water droplets at 2.5 g/g water content (**Fig. 42C**). This is possible, if the void spaces (pores) of hydrated PAA are only partially filled with water at 2.5 g/g water content, and these separated water bodies merge and fill the available slit-like voids at 3.4 g/g without significantly changing the backbone architecture. This is further evidence for the conservation of the solid aerogel backbone even at its complete hydration.

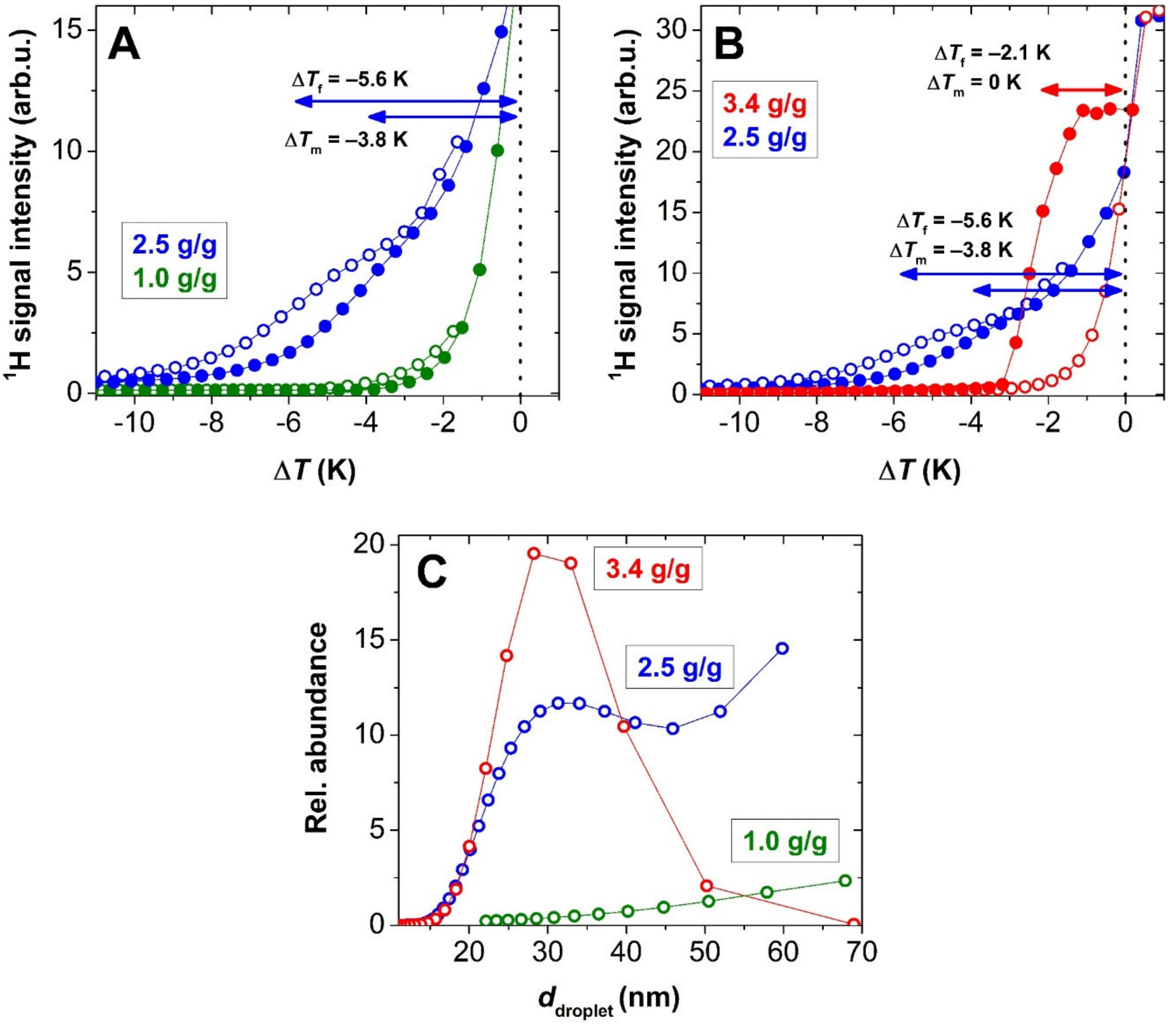

Figure 42. NMR cryoporometry data of hydrated PAA samples. The water content of PAA is given in the legend. Panels A and B: Normalized melting-freezing curves measured at different water contents. The arrows indicate the temperature depressions in the hysteresis curves. Panel C: Size distribution of the water droplets and puddles reconstructed from the freezing curves. (The deviation between duplicate samples is less than 15%.) The values at 1.0 g/g are strongly biased by relaxation effects.

V-1.6.4. Multi-scale hydration mechanism

Based on the compiled results of ssNMR, liquid phase NMR and SANS, the major steps of the hydration of the PAA are summarized graphically in **Scheme 12**. The molecular events and the alteration of the nanoscale architecture are concerted. These multi-scale structural changes are definite in governing the macroscopic properties of the aerogel, and account for even such a complicated phenomenon as the non-monotonic change of the compressive strength of the monolithic aerogel as a function of its hydration level.

The first water molecules fill the vacancies in the intermolecular H-bonding network of the PA macromolecules. [303-305] Water molecules bound in the fibers in this manner form the first 1st relaxation domain and regarded to be practically immobile structural water. These water molecules strengthen the H-bonding network stabilizing the solid PA fibers, which causes the slight rearrangement of the nanostructure, [312] as detected by SANS. The strengthening of the fibers and their rearrangement are together responsible for the increasing stiffness of the monolithic aerogel. As indicated by several techniques, the primary sites are saturated at ca. 0.2 g/g water content. Additional hydration causes dramatic structural changes.

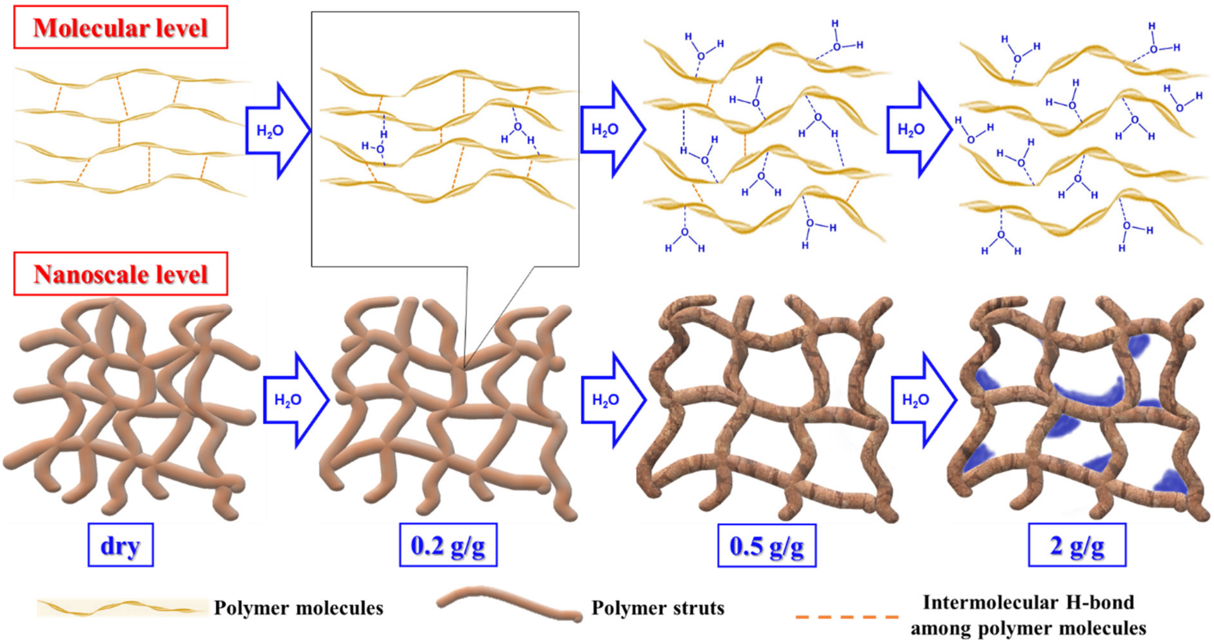

Scheme 12. Graphical representation of the different stages of the hydration of the PA aerogel. The concerted molecular level events and nanoscale rearrangements are depicted in respective panels. The detailed description of the hydration mechanism is given in the text.

From ca. 0.2 g/g, water molecules enter into the bulk of the PA fibers, insert in-between the macromolecules and occupy some of their H-bonding sites. This disrupts the intermolecular H-bonding network characteristic for the dry aerogel. As a consequence, the conformation of the macromolecules changes and their segmental motion increases. This causes the macroscopic plasticization of the monolithic aerogel. [293,294,307] The insertion of water molecules and the disruption of the original H-bonding network is complete at ca. 0.4 g/g water content.

Additional hydration causes the partial dissolution of the fibers, which further increases the pore sizes and the surface roughness of the partially dissolved PA fibers. The combined results of NMR diffusiometry and cryoporometry suggest that a small portion of water forms a mobile layer on the surface of the fibers above ca. 0.5 g/g water. Nevertheless, most of the water is absorbed in the hydrated PA fibers at this stage, which causes their partial dissolution. Several water droplets form above ca. 2 g/g water content that merge at ca. 3 g/g to extensive slabs fully saturating the pores. The experimental data show that the well-defined fibrous structure of the aerogel is preserved even above 3 g/g of water, and no hydrogel formation takes place.

V-2. Aerogels as drug delivery systems [P8-P12, R1]

V-2.1. Fe(III)-alginate aerogels for redox responsive drug delivery [P8]

Metal ion crosslinked alginate aerogels are versatile biomaterials that have recently been introduced into the field of drug delivery research and development. [96,313-319]

The timeframe of the dissolution of loaded drugs from metal-alginate aerogel carriers heavily depends on the hydration, swelling and erosion of the matrix. Metal-alginate gels readily dissolve in neutral or slightly acidic ($pH > 5$) solutions where the concentration of the cross-linking metal ion is low. In this case, the coordination bonds break, metal ions leach from the gel, and the alginate chains are hydrated. [96,97] Importantly, the kinetics of drug release can be fine-tuned by altering the rate of swelling and erosion of the alginate matrix.

A promising strategy to produce redox responsive gels is to crosslink alginate by a redox active metal ion that changes its affinity towards alginate when its oxidation state changes. For example, iron(III) interacts strongly with alginate, [320,321] while Fe(II) is does not crosslink the macromolecules in aqueous solution. [322-324] Thus, by the in situ reduction of Fe(III) to Fe(II), the degradation of the ionically crosslinked gel is triggered.

We showed that the drug delivery properties of Fe(III)-alginate aerogels can be tuned by incorporating ascorbic acid into the formulations. Fe(III)-alginate aerogels were synthesized by the sol-gel method in the form of spherical particles ($d = 3 – 5$ mm) and loaded with the model drug ibuprofen in supercritical CO_2. Some of the ibuprofen impregnated Fe(III)-alginate aerogels were co-impregnated with ascorbic acid. Finally, in vitro dissolution experiments were performed to show that the rate of drug release is significantly faster in the case of the latter system, where ascorbic acid in situ reduces Fe(III) to Fe(II) upon the hydration of the aerogels.

V-2.1.1. Preparation of ibuprofen loaded Fe(III)-alginate aerogels

Spherical Fe(III)-alginate beads (3.0 – 4.5 mm) were synthesized by dropping 2 w/w% aqueous solution of either low G (LG) or high G (HG) alginate into 0.05 M $FeCl_3$ solution from fixed height. [325] The samples were subjected to solvent exchange to ethanol, and dried with supercritical CO_2 in cooperation with Prof. Pavel Gurikov at TUHH. [78] Four different aerogel samples were produced (**Table 13**).

Table 13. Properties of the different Fe(III)-alginate aerogel samples (S = small, B = big). S_{BET} denotes the specific surface area determined by N_2 adsorption-desorption porosimetry. The standard deviation was calculated from parallel measurements (*n* = 3, for porosimetry *n* = 2).

Sample	G content (w/w%)	Fe(III) content (w/w%)	bead diameter (mm)	S_{BET} (m^2/g)	Total pore volume (cm^3/g)
S-LG	30	8.56 ± 0.04	3.0 ± 0.2	420 ± 19	1.2 ± 0.2
B-LG	30	8.08 ± 0.03	4.5 ± 0.3	406 ± 18	1.8 ± 0.2
S-HG	70	6.99 ± 0.05	3.3 ± 0.2	442 ± 25	1.8 ± 0.2
B-HG	70	6.82 ± 0.02	4.5 ± 0.3	316 ± 19	1.2 ± 0.2

In one set of experiments the Fe(III)-alginate aerogel beads were impregnated with ibuprofen alone, in another set of experiments the beads were simultaneously impregnated with ibuprofen and ascorbic acid by adsorptive deposition from supercritical CO_2 at TUHH. [83] The loadings of the samples are summarized in **Table 14**.

Table 14. Drug loading of the different Fe(III)-alginate aerogel samples (I = loaded with ibuprofen only, IA = loaded with ibuprofen and ascorbic acid). Properties of the pristine aerogel samples are given in **Table 13**. The error bars were calculated from parallel measurements (*n* = 3).

Sample	Ibuprofen mass content (w/w%)	Ascorbic acid mass content (w/w%)	Specific loading (mg *ibuprofen* / m^2 *aerogel*)
S-LG-I	41 ± 4	–	1.5 ± 0.1
B-LG-I	37.9 ± 0.2	–	1.50 ± 0.01
S-HG-I	36.4 ± 0.9	–	1.30 ± 0.02
B-HG-I	37 ± 2	–	1.8 ± 0.1
S-LG-IA	34 ± 5	4.0 ± 0.4	1.2 ± 0.1
B-LG-IA	35 ± 2	4.3 ± 0.7	1.32 ± 0.05
S-HG-IA	33.6 ± 0.9	3.4 ± 0.4	1.14 ± 0.02
B-HG-IA	34 ± 3	3.4 ± 0.4	1.6 ± 0.1

V-2.1.2. Redox responsive drug release

The release of ibuprofen was measured at pH = 2.0 in HCl and at pH = 7.4 in PBS. All of the different Fe(III)-alginate matrices dissolved (at least partially) in both media in the timeframe of the experiments (**Fig. 43**). The beads completely dissolved in 2 h in PBS, but not in HCl. Earlier studies with Ca(II)-alginate aerogels concluded that alginate particles form a macroscopic semi-permeable outer membrane in HCl. [96,97] This layer is composed of alginic acid gel, which has a low solubility in water. The alginic acid layer never dissolves completely, as it is replenished immediately from alginate in contact with HCl, limiting the overall rate of dissolution in HCl. This mechanism is practically independent of the alginate bead size and the composition of the polymer, thus assumed to be operative also in the case of the Fe(III)-alginate aerogels (cf. **Fig. 43A**). In PBS, the particles readily dissolved, and the rate was much faster in the case of the smaller beads. It is also worth to note that the kinetics was significantly different in the case of low G and high G samples, besides the size effect.

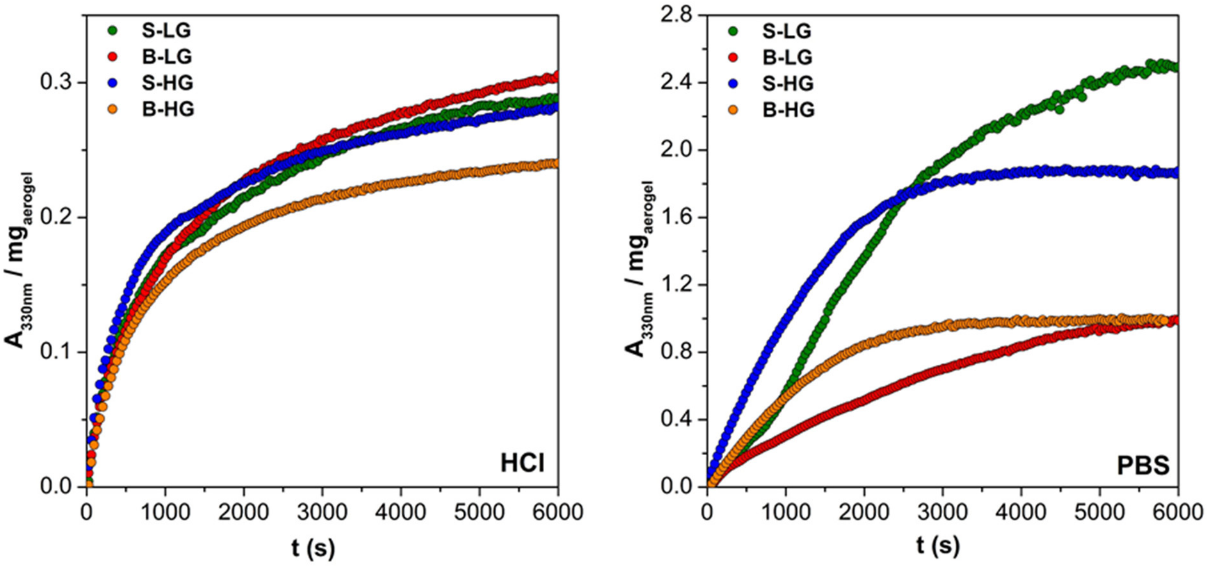

Figure 43. Dissolution of pristine Fe(III)-alginate aerogel samples at pH = 2.0 in HCl (left) and at pH = 7.4 in PBS (right). Every 3rd point is shown for clarity.

The aerogel formulations containing only the drug (coded: I) did not display any difference in drug release in HCl, where sink conditions did not apply (**Fig. 44**). The kinetics was also indifferent to the weight of the loaded aerogel in the cuvette. This suggest that the factor limiting the rate of drug release is the mass transport through the alginic acid layer on the surface of the dissolving particles. Incorporation of ascorbic acid (code: IA) slightly accelerated the release of ibuprofen in all samples. This proves that the in situ chemical reduction of the crosslinking metal ion accelerates the rate of drug release even in highly acidic media.

The release of ibuprofen was much faster in PBS than in HCl (**Fig. 44**). The experiments in PBS were run under sink conditions. As seen above, the dissolution of the Fe(III)-alginate matrices are much faster in this medium. Surprisingly, in the case of the high G samples loaded with ibuprofen alone (S-HG-I and B-HG-I) the rate of drug release dropped to near zero at reaching ca. 50% ibuprofen dissolution. Nevertheless, ascorbic acid significantly increased both the rate and the extent of drug release in all samples. This effect was much more pronounced in PBS than in HCl, which can be accounted for by the following. The aerogel beads take up more solvent and effectively swell in PBS, while this process is hindered in HCl. The in situ reduction of the crosslinking Fe(III) is faster in a swollen hydrogel matrix, thus the accelerating effect is stronger in PBS. Another important observation is that the effect of ascorbic acid is more pronounced in the case of the high G samples. The explanation can be the different hydration and dissolution characteristics of the different alginate backbones.

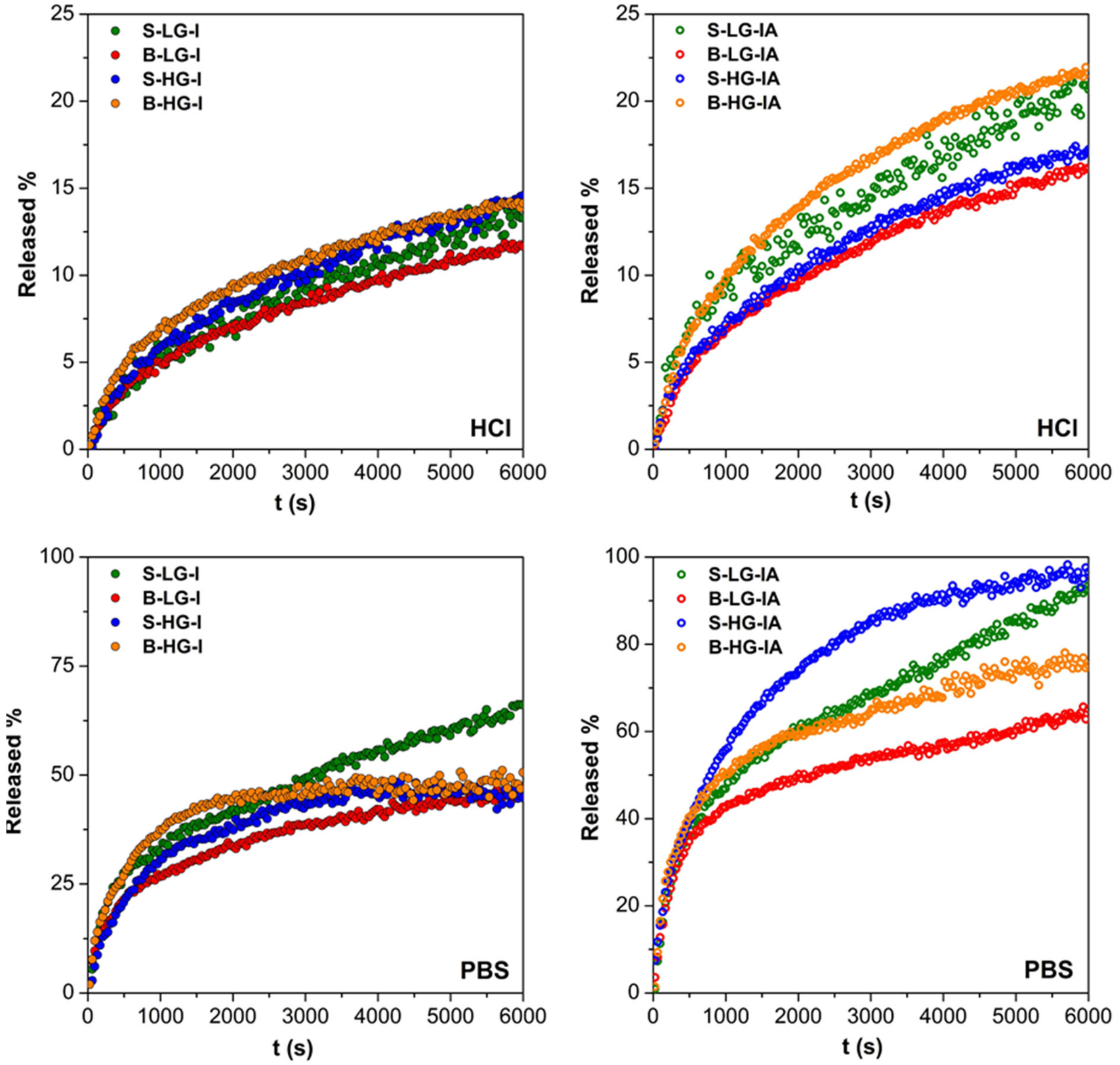

Figure 44. The release of ibuprofen from different Fe(III)-alginate aerogel formulations in pH = 2.0 HCl (upper panels) and in pH = 7.4 PBS (lower panels). Some aerogel samples were impregnated with ibuprofen only (code: I; left panels), and some were co-impregnated with ibuprofen and ascorbic acid (code: IA; right panels) in order to accelerate drug release.

All release curves were mathematically fitted using the Peppas and the Hopfenberg semi empirical models for drug release. [92] In HCl release medium, the shapes of the release curves approximately followed the Peppas model with *n* between 0.40 and 0.44. However, the curves recorded in PBS could not successfully be fitted with either of these release models.

As a summary, it can be concluded that the size of the aerogel beads and the G/M ratio of the Fe(III)-alginate backbone have only minor effects on the rate of drug release. The slight increase of the release rate with smaller bead size and higher G content can be observed. More importantly, the significant acceleration of the rate of drug release is achieved by incorporating ascorbic acid into the Fe(III)-alginate aerogel preparations in all cases.

V-2.2. Calcium alginate aerogel microparticles for pulmonary drug delivery [P9]

Aerogels made of calcium alginate are biocompatible and biodegradable, and their mucoadhesive properties can be exploited for the delivery of drugs directly to mucosal tissues. [59,326] Alginate aerogels for pulmonary administration should have suitable aerodynamic size in the 1-5 μm range, low bulk density, low cohesive forces and high flowability as a powder. [58,327-329] Calcium alginate is not yet approved for dry powder inhaler formulations yet, but clinical trials have demonstrated its safety in humans (FDA clinical trial NCT02157922). [330]

Calcium alginate aerogel microparticles were prepared in cooperation with Prof. Carlos A. García González at USC for pulmonary delivery applications using compressed air-assisted prilling gelation, solvent exchange, and drying by supercritical CO_2. The anti-inflammatory drug beclomethasone dipropionate (BDP) used for asthma treatment was impregnated into these alginate aerogel particles under supercritical CO_2 assisted conditions. *In vitro* drug release experiments were performed to assess the solubilization of the drug from this carrier, and NMR relaxometry was utilized to correlate drug release and hydration features of the aerogel carriers. Finally, *in vitro* cytotoxicity tests in fibroblasts and *ex vivo* permeability tests in porcine bronchial tissues were conducted at USC. These biological tests confirmed the absence of toxic effects of the aerogel formulations, and demonstrated the efficient deposition of BDP from the porous alginate aerogel carrier in porcine bronchial tissues.

V-2.2.1. General characteristics of Ca-alginate aerogel microparticles

The obtained aerogel particles have high specific surface areas, and the pores are mainly in the mesoporous range (**Table 15**). Both the pristine and the BDP-impregnated particles had spherical shapes with high surface roughness (**Fig. 45**). The most promising aerogel formulation impregnated for 9 h in the supercritical CO_2 assisted process contains 6.7wt% BDP. Powder XRD measurements performed on the BDP-loaded aerogel formulations confirmed that BDP was deposited in its amorphous state.

Table 15. Specific surface area (A_{BET}), pore volume ($V_{\mathrm{p,BJH}}$) and mean pore diameter ($d_{\mathrm{p,BJH}}$) of the Ca-alginate aerogel, the and BDP-loaded Ca-alginate aerogel obtained after 9 h of scCO$_2$ impregnation.

Formulation	A_{BET} (m^2/g)	$V_{\mathrm{pore,\,BJH}}$ (cm^3/g)	$d_{\mathrm{pore,\,BJH}}$ (nm)
pristine Ca-alginate aerogel	351 ± 17	3.6 ± 0.2	37.0 ± 1.8
BDP-loaded aerogel (impregnated 9 h)	299 ± 15	3.1 ± 0.2	31.0 ± 1.6

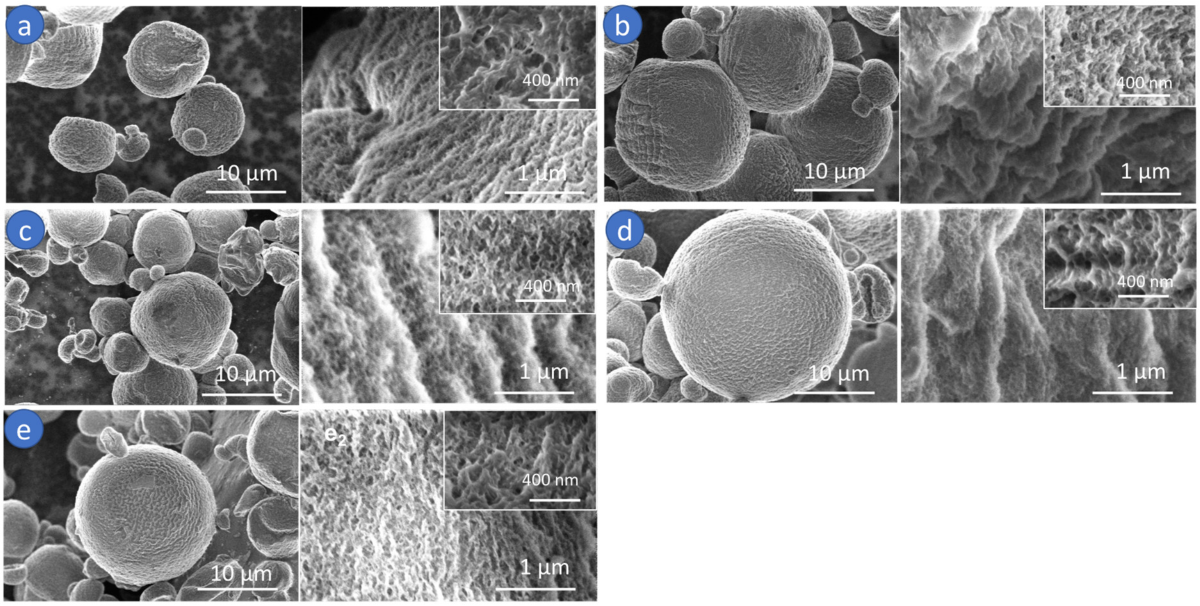

Figure 45. SEM images in different magnifications of (a) the pristine alginate aerogels and BDP-loaded alginate aerogels obtained using different contact times in impregnation: (b) 1, (c) 2, (d) 6, and (e) 9 h.

V-2.2.2. In vitro drug release studies of BDP-loaded alginate aerogels

Drug release results obtained by the classical dialysis method [331] are shown in **Fig. 46a**. The BDP-loaded alginate aerogels exhibit a release pattern characterized by two distinct phases. First, a sudden (burst) release of BDP takes place during the initial 10 min, followed by a slow and sustained release. The process is controlled by the limited solubility of the drug, which was measured to be 4.3 µg/mL in the release medium (PBS of pH = 7.4 with 20V/V% methanol) at 37 °C. Sink conditions did not apply in this experiment. The aerogel carrier formed a hydrogel in the longer term, which did not dissolve during the 48 h test.

The observed burst in the first phase of the release kinetics can be explained by the fast and facile hydration of the porous alginate carrier in the aqueous medium, which instantly repels the lipophilic BDP initially covering the surface of alginate aerogel backbone. [31] However, the instantaneously released drug precipitates from the release medium, and can also bind to the dialysis membrane. Furthermore, the highly hydrophilic nature of the alginate aerogels leads to microscopic swelling that ultimately collapses the pore structure of the aerogel. As a result, some of the BDP can be trapped or re-absorbed in the formed dense hydrogel. In the longer term, these effects ultimately limit the amount of the dissolved drug in the release medium.

Fast kinetics experiments were conducted to study the first part of the drug release process. Typical release curves measured by this method are shown in **Fig. 46b**. The applied on-line time resolved UV-vis spectrophotometric method unambiguously confirmed the prompt appearance of high concentrations of BDP in the release medium. The maximum concentration of dissolved BDP was 45 μM. This concentration is ca. 10 times higher than the solubility of crystalline BDP (4.6 μM) under the applied conditions. The observed maximum concentration was reached in ca. 1 min and maintained for an additional ca. 3 min. The drug concentration then decreased because of the recrystallization and precipitation of BDP from the supersaturated solution. Overall, the alginate aerogel particles proved to be effective solubilizing aids for the low water solubility drug under the applied non-sink conditions. [89,90,332]

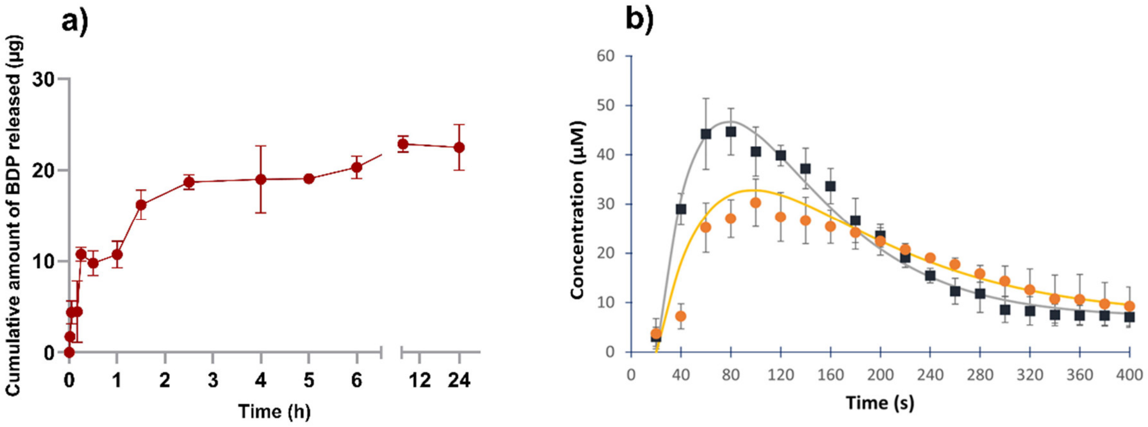

Figure 46. (a) *In vitro* release profile (n=3) of BDP from alginate aerogel carriers in PBS pH = 7.4 with 20V/V% methanol (37 °C, 100 rpm) measured by the classical dialysis method. (b) Drug release profiles (n=3) of different amounts of BDP-loaded alginate aerogels in the same medium measured by on-line UV-vis spectrophotometry. Curved lines correspond to the simulated drug release profiles based on the kinetic model developed by Hirai et.al. [91] Symbols: black squares and gray line: experimental and simulated data of 1.5 mg BDP-loaded alginate aerogel, respectively; orange circles and yellow line: the same for 1.0 mg BDP-loaded alginate aerogel, respectively.

The enhanced solubilization and the special drug release profiles can be explained by the amorphization of BDP deposited on the pore walls of the alginate aerogels in the adsorptive precipitation in the supercritical fluid-assisted impregnation. [83-85] The hydration of the alginate and the repulsion of the amorphous drug from the alginate backbone is faster than the recrystallization of BDP, which leads to a temporally supersaturated solution. [89,90] This kinetic phenomenon is termed as the "spring effect" in the literature. A mathematical model was developed by Hirai et.al. to describe such release profiles. [91] This model was adequate to fit the release curves with a single data set for the kinetic and solubility parameters, and varying the starting amount of the BDP-loaded aerogel carrier (**Fig. 46b**). The successful modeling further corroborates the above proposed mechanistic considerations.

V-2.2.3. Hydration properties of pristine and BDP-loaded alginate aerogels

The hydration properties of the pristine and the BDP-loaded Ca-alginate aerogels were evaluated via NMR relaxometry to gain further insights into the drug release mechanism based on our experience with similar aerogels. Three relaxation domains were detected (**Fig. 47**). The lowest T_2 values (1st relaxation domain) represent strongly bound water inside the Ca-alginate fibers, as discussed in **Section V-1.4**. [95] The evolution of the primary hydration sphere (2nd relaxation domain), as well as the amount of quasi-bulk water in droplets and puddles (3rd relaxation domain) give information on the hydration and the wetting of the alginate aerogels. It is noteworthy to compare the hydration profile of the present pristine alginate aerogel with the archetypical alginate aerogel. [95] There are major differences in the hydration, namely the third domain representing water droplets appear at a much lower hydration level in the present alginate aerogel discussed in **Section V-1.4**. This indicates that water forms droplets on the alginate fibers instead of penetrating into the fibers. Thus, the backbone of the present particular alginate aerogel is less prone to hydrogel formation. These hydration features are beneficial carrier properties for drug solubilization, because the chance of trapping the drug in a hydrogel during release is lower.

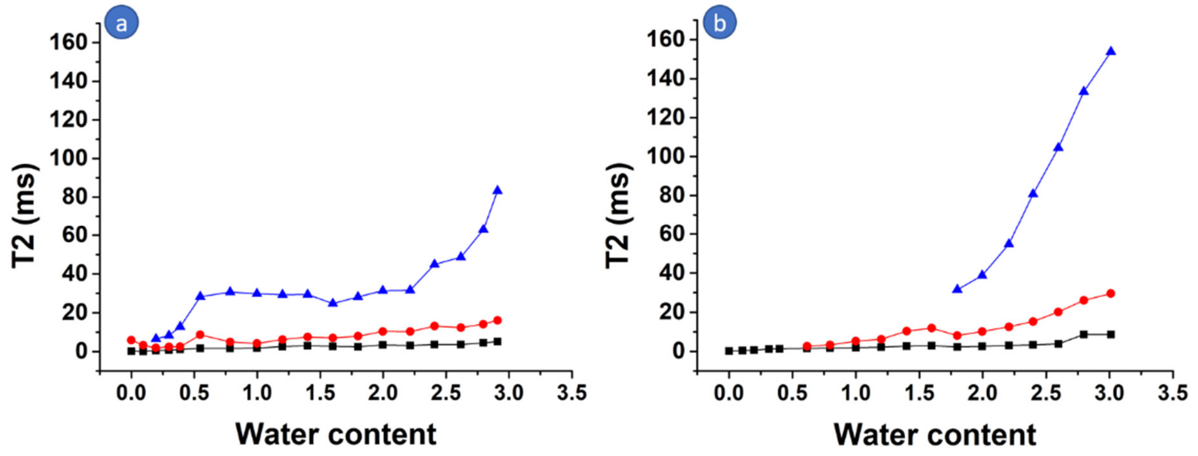

Figure 47. NMR relaxometry of partially hydrated (a) pristine and (b) BDP-loaded Ca-alginate aerogels (first domain: black square, second domain: red circle, third domain: blue triangle).

The explanation for the special hydration properties of the present alginate aerogel is attributed to the single step solvent exchange of water to absolute ethanol in its preparation, whereas the reference alginate aerogel was prepared by multi-step gradual exchange of water to ethanol. [95] The difference in the hydration profiles are due to the molecular level and the nanoscale changes of the gel structures during the different solvent exchange procedures. Such phenomena are discussed in a recent paper. [333] The one-step solvent exchange process could have increased the resistance of the resulting alginate gel against dissolution by water, which is beneficial for the fast release of the loaded drug from the surface of the pores.

Comparing the hydration profiles of the pristine and the loaded alginate aerogels, the 2nd domain (red circle) representing the primary hydration sphere appear at a significantly later stage of hydration in the BDP-loaded aerogel. This is also true for the third domain of the water droplets, suggesting that the solid alginate backbone of the BDP-loaded aerogel is somewhat masked by the deposited drug, and thus, less susceptible for hydrogel formation.

V-2.3. Covalently labeled florescent silica-gelatin aerogel microparticles for *in vitro* and *in vivo* biocompatibility and biodistribution experiments [P10, P11]

The lack of the biodegradability of silica aerogel raised an ever-growing interest in fully biobased and hybrid materials in order to broaden the area of use and ensure safe applications. Besides oral and nasal delivery, subcutaneous, intraperitoneal and other administration routes gained significance. Using aerogels as DDS in these routes also requires the monitoring of the particles in the living system. Tracking the movement and possible accumulation of aerogel particles in different organs are crucial to ensure their safety and to gather more information for developing targeted delivery. The most convenient monitoring technique in animal studies is fluorescence imaging. [203,334] For biocompatibility investigations, a potential method is the *in vitro* time-lapse video-microscopy, which enables long-term dynamical observations. [335] A good labeling technique should not alter either the aerogel matrix or the fluorescence properties of the dye to obtain representative results in subsequent biological experiments. To reach this goal, we investigated the feasibility of two strategies for the labeling of hybrid silica-gelatin aerogel by covalently binding fluorescein isothiocyanate either to the amino groups of gelatin molecules, or to amine-functionalized silica prior to sol-gel condensation.

V-2.3.1. Fluorescence spectroscopy characterization of labelled aerogels

The shapes of the absorption and the emission peaks of both the homogeneously labeled and the selectively labeled aerogels are identical to those of hydrated fluorescein (**Fig. 48**).

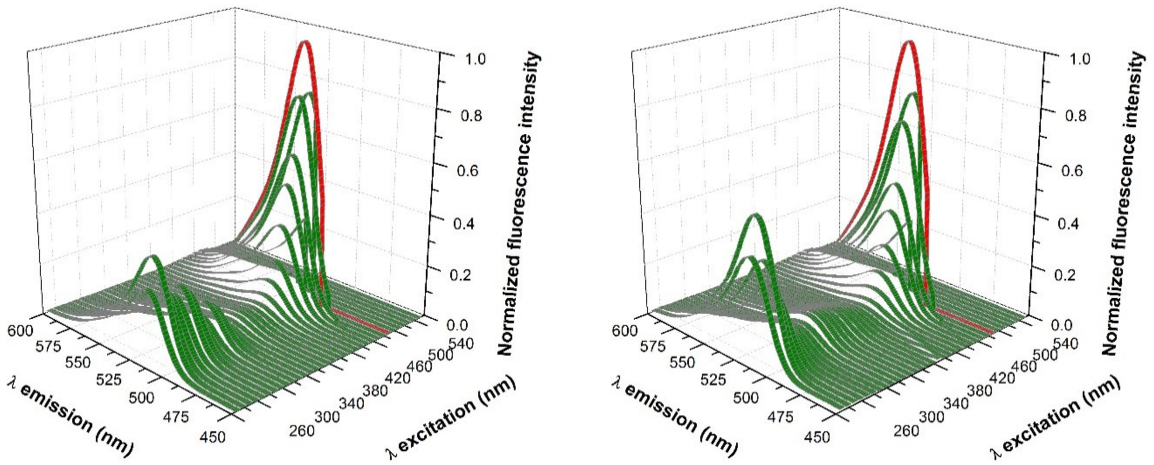

Figure 48. Normalized 3D fluorescence spectra of hydrated fluorescein (aqueous solution) (left) and selectively labeled aerogel dispersed in phosphate buffer (right). Maximum fluorescence intensities were obtained at λ_{ex} = 490 nm (red). T = 25 °C, PBS, pH = 7.0.

The time-resolved fluorescence properties of the samples were measured by a laser-flash instrument using different excitation wavelengths (**Table 16**). At λ_{ex} = 532 nm, only the fluorescein moieties are excited, thus the unlabeled aerogel and dissolved gelatin does not give any fluorescence signal. At λ_{ex} = 355 nm dissolved gelatin displays characteristic fluorescence, resulting in a broad emission peak with a maximum around 400 – 410 nm. At λ_{ex} = 266 nm, a new emission peak of gelatin appears at around 305 nm. [336] As a conclusion, the covalent links do not alter the photophysical properties of the dye, regardless of the labeling strategy.

Table 16. Fluorescence lifetimes at different excitation and emission wavelengths measured by a laser flash instrument. Stable aerogel suspensions were studied.

	fluorescence lifetime (ns)			
	λ_{ex}=532 nm	λ_{ex}= 355 nm	λ_{ex}= 266 nm	λ_{ex}=266 nm
	λ_{em}= 560nm			**λ_{em}= 305nm**
dissolved gelatin	–	3.8 ± 0.6	–	1.8 ± 0.3
unlabeled aerogel	–	–	–	–
dissolved fluorescein	4.6 ± 0.1	4.6 ± 0.2	4.7 ± 0.2	–
homogeneously labeled aerogel	4.3 ± 0.2	4.0 ± 0.2	4.1 ± 0.2	–
selectively labeled aerogel	4.4 ± 0.5	4.2 ± 0.4	4.0 ± 0.8	–

V-2.3.2. Biocompatibility and biodistribution of silica-gelatin aerogel microparticles

It was proved via *in vitro* experiments with SCC-VII cells that silica-gelatin aerogel is non-toxic and displays good biocompatibility. Time-lapse microscopy imaging scans showed no signs of apoptosis, or necrosis, or any harmful effect at the different phases of the cell cycle. The surface of the aerogel microparticles proved to be suitable for the adhesion of the cells. In addition, the cells had a more directed and faster movement towards the aerogel microparticles then their motion in the control culture, probably due to the collagen content of the particles.

The biodistribution pathways and the physiological effects of fluorescein-labeled silica-gelatin aerogel microparticles (FSGM) were investigated by injecting their suspension into the peritoneum (abdominal cavity) of healthy C3H mice. In general, the injected FSGM were well tolerated over the 3-week-long acute toxicity experiments. No reduction was observed in food intake, no physiological defects or dysfunctions were detected, and all mice were healthy at the end of the experiments. The autopsy revealed the important finding that the FSGM were not present at the site of injection in the abdominal cavity of the animals at the end of the experiment. The histological study of abdominal organs (liver, spleen, kidneys, thymus) and lymphatic tissues showed no signs of toxicity. The localization of the FSGM was studied by fluorescence microscopy. Aerogel microparticles were not detected in any of the abdominal organs, but they were clearly visible in the cortical part of the parathymic lymph nodes, where they accumulated. The accumulation of the aerogel microparticles in the parathymic lymph nodes in combination with their absence in the reticuloendothelial system organs, such as the liver or spleen, suggests that FSGM entered the lymphatic circulation. A similar biodistribution pathway was observed before for dry ink particles injected into the abdominal cavity of mice. [337] The entrance of silica–gelatin aerogel microparticles into the lymphatic circulation can be exploited to design passive targeting drug delivery systems for flooding metastatic pathways of abdominal cancers that spread via the lymphatic circulation.

V-2.4. Methotrexate functionalized silica-gelatin aerogel microparticles [P12, R1]

Methotrexate (MTX) is one of the most widely used agents in the treatment of cancer and autoimmune diseases such as rheumatoid arthritis and Crohn's disease. [338-341] MTX is an effective anti-tumor drug [342-344], but its application has several disadvantages. Since the absorption of MTX in the gastrointestinal tract follows saturation type kinetics with increasing concentration, its bioavailability is dose dependent. [345] This results in a short plasma half-life (5–8 h) and low drug concentrations in the target tissues. [346-348] Several drug delivery approaches have been developed to overcome the shortcomings of conventional MTX therapy, including pro-drug approaches using bioconjugates with gelatin. [104,111-115]

Silica-gelatin hybrid aerogels are excellent candidates for controlled drug delivery, because various cell lines tend to closely interact with silica-gelatin aerogel microparticles. [206,349] Thus, the objective of this study was to prepare MTX functionalized silica-gelatin hybrid aerogel microparticles and investigate their cytotoxicity against some widely used solid tumor (SCC VII), leukemic (HL-60) and immortalized (HaCaT) cell lines.

Gelatin-methotrexate conjugate was prepared following the synthesis route developed by Kosasih et.al. [113] Silica-gelatin-MTX hybrid aerogels (SGM) were prepared from the bioconjugate by co-gelation with TMOS, solvent exchange and drying by supercritical CO_2.

V-2.4.1. Methotrexate release from the functionalized aerogel

Soaking SGM particles for 72 h in 0.01 M HCl solution, in pH = 5.0 acetate buffer or in pH = 7.4 PBS yielded MTX concentrations below this quantification limit (**Table 17**). Similarly, practically no MTX dissolution was detected in the supplemented DMEM-HAM'S F12 medium, regardless of its FBS content. Incubating SGM particles with SCC VII cell cultures for 72 h resulted in 9% of the total MTX dissolved in the culture supernatant. When only the supernatant of SCC VII cell culture was used as a dissolution medium, 12% MTX was released in 72 h. In experiments where SCC cell growth was induced by a gelatin coating, an MTX release of 9% was measured in the SCC lysate, and 12% in the culture supernatant. Incubation of functionalized hybrid aerogel (SGM) particles with CAT-B enzyme resulted in the release of 5% of the total conjugated MTX. [114]

Table 17. The release of methotrexate (MTX) from the aerogel in 72 h under various conditions.

Medium & conditions	Released MTX
Buffer (pH = 2.0; 5.0; 7.4)	< 3 %
DMEM-HAM'S F12	< 3 %
SCC VII cell culture	8.6 ± 1.9 %
Cell culture supernatant	11.8 ± 2.0 %
Induced cell culture lysate	8.7 ± 1.2 %
Induced cell culture supernatant	11.6 ± 1.4 %
Cathepsin B in PBS	4.6 ± 0.9 %

V-2.4.2. HaCaT, SCC VII and HL-60 cell growth inhibition

The growth inhibitory effect of the SGM microparticles was assessed on 2 cancerous cell lines (SCC VII, HL-60) and on an epithelial cell line (HaCaT). The SGM particles inhibited the growth of every cell line at every SGM concentrations after at least 24 h incubation (**Fig. 49**). The MTX content of 2.0 mg/mL SGM is approximately equivalent to 0.2 mg/mL free MTX (control experiment No.2), because the MTX content of SGM is ca. 6wt% by the dry weight. The dose dependent cytotoxic effect of SGM was the most pronounced in HL-60 cells. The inhibition of growth of the SCC cells was also pronounced at every SGM concentration, but only after 48 h incubation. The HaCaT cultures were tolerant towards 0.5 mg/mL SGM, but the viability decreased significantly when applying 1.0 and 2.0 mg/mL SGM concentrations.

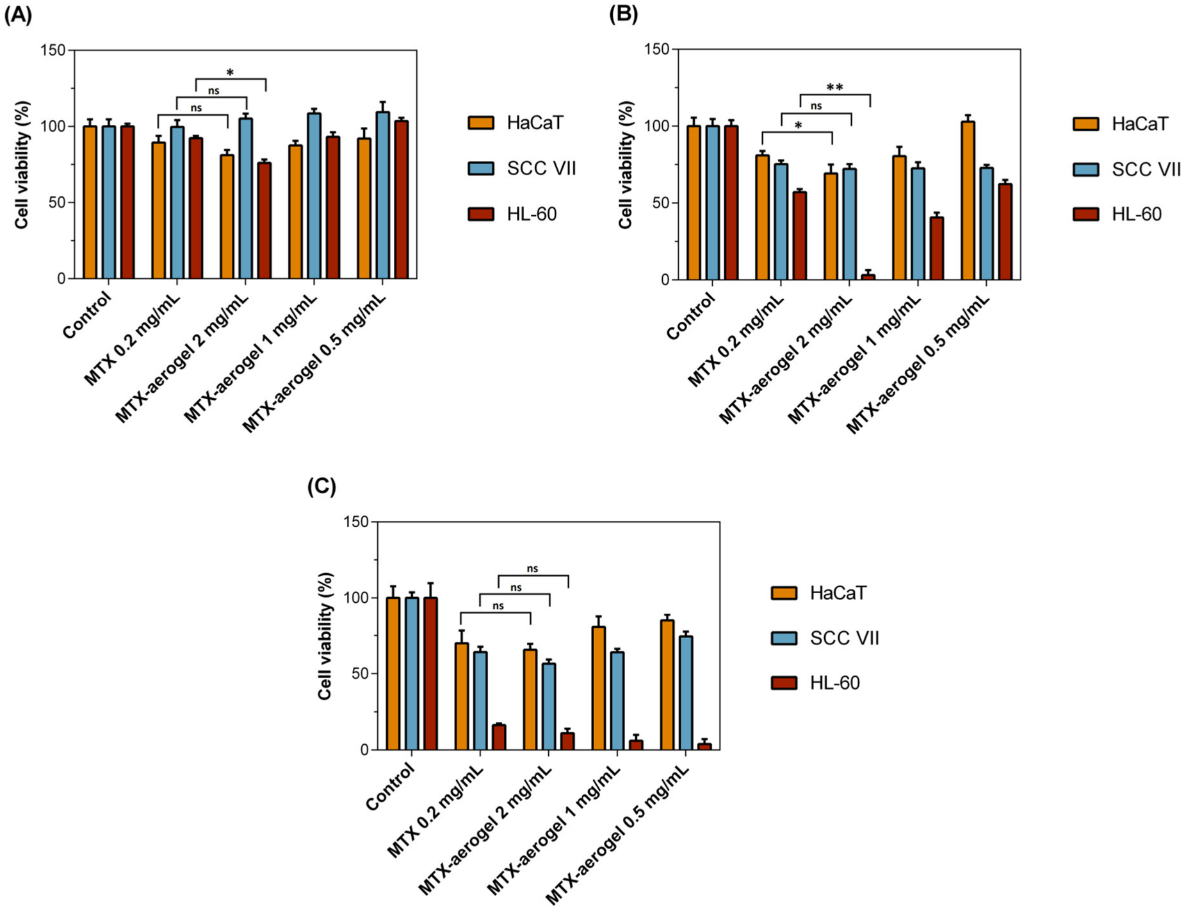

Figure 49. Summary of MTX functionalized silica-gelatin hybrid aerogel (SGM) growth inhibition tests conducted with HaCaT, SCC VII and HL-60 cell lines for 24 h (A), 48 h (B) and 72 h (C) of treatment. The bars show the percentages of growth relative to control cell cultures measured by the MTT assay. All experiments were run in triplicates. Significance levels at *: $p < 0.05$ and **: $p < 0.01$.

The various drug dissolution tests proved, that the covalently attached MTX is not released from SGM without the interplay of living cells, because the amide-bond linking MTX to the aerogel backbone does not hydrolyze in cell free buffers, and can only be partially cleaved by the collagenase enzyme Cathepsin B. In contrast to this, the incubation of the SGM particles with cell containing medium and cell culture supernatant caused the release of MTX. A feasible explanation is that the collagen coating on the flasks triggered the collagenase production in the cells, and in turn, the treatment of SGM with the induced lysate and media caused the release of MTX. In summary, the complex collagenase activity of cells can liberate MTX from SGM. The applied cell lines have different collagenase activities due to their different biological functions. Collagenase activity is required for HaCaT cells to support their migration on the collagen matrix [350], and the enhanced collagenase activity of tumor cells is needed for the degradation of the extracellular matrix. [115] Thus, it is reasonable to assume that the main difference in the cytotoxicity of SGM against the tested cells lines is related to the difference in their collagenase activities. It is also noteworthy, that the quantitative growth inhibitory effect of SGM is equivalent to that of an equal dose of free (aqueous) MTX.

V-2.4.3. Future outlook

The MTX bioconjugate aerogel microparticle drug formulation does not target oral administration, but could advantageously be applied e.g. as a post-operative treatment in a body cavity. The size of the aerogel delivery vehicle is similar to the size of cancer cells. The importance of this lies in the fact that the metastatic pathways of the tumor cells can be flooded with such micronized particles carrying antimetabolites. A high local concentration can be reached in lymphatic and/or extracellular focal points and in sentinel lymph nodes, as shown in preliminary studies. [349] Thus, these microparticles can particularly be useful in the treatment of diffuse tumors. Furthermore, the application of the hybrid aerogel microparticles could meet the requirements of postoperative treatment and metastatic prophylaxis.

V-3. Mechanisms of interfacial processes in aerogels [P13-P17]

V-3.1. Sorption of methylene blue from aqueous solution on silica aerogels [P13]

In recent years, functionalized mesoporous silica aerogels have gained significance in various applications. This generated increasing demand for the thorough understanding of the mechanisms of aqueous phase sorption processes on these advanced materials. The evaluation of the experimental data on fast sorption processes is often simplified, because the system cannot be followed with sufficiently high time resolution. In order to overcome this limitation, we designed a set of kinetic experiments to explore the intimate nature of the aqueous phase sorption properties of mesoporous hydrophilic aerogel particles. The common cationic dye methylene blue (MB) was selected to be the model compound for the mechanistic studies, solely, because it is still widely applied in sorption and other heterogeneous benchmark studies. [351,352] We developed an on-line UV-Vis spectrophotometric method to follow the sorption of MB with 1 s time resolution, and show that sophisticated spectrophotometry is suitable to provide reliable and reproducible kinetic data in a heterogeneous system. Finally, we construct an advanced mechanistic model based on Langmuir-type sorption models [353-357] for the interpretation of the kinetic and thermodynamic results.

V-3.1.1. Kinetic and sorption experiments

The kinetics of the sorption of MB on aerogel particles was followed by injecting an aqueous MB solution into an aerogel suspension under continuous stirring in a cuvette and following the spectral change on-line by a UV-Vis spectrophotometer. When the MB solution is injected, ca. 8 s is needed for the dispersion of the dye. [358] After this initial period, a steady decrease in absorbance was detected with biphasic kinetic characteristics (**Fig. 50**). During the sorption experiments, the aerogel particles became visibly colored and aggregated to large (even ca. 0.5 mm) blocks that settled from the suspension even under continuous stirring.

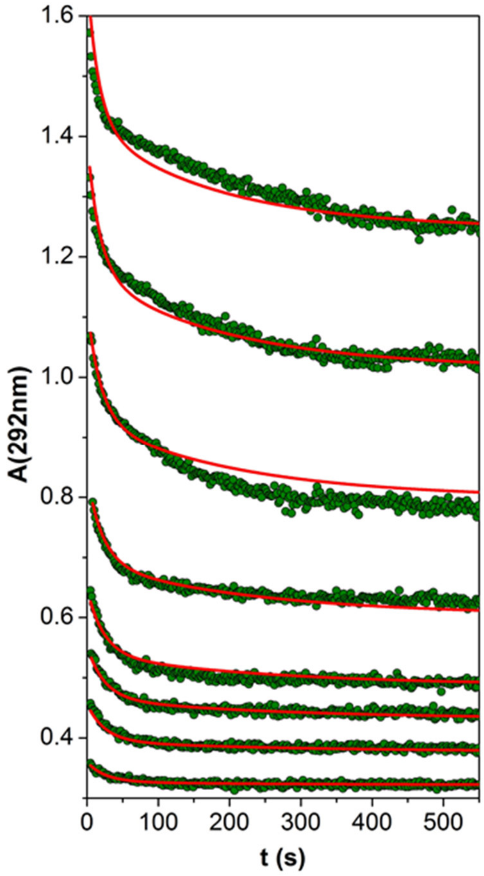

Figure 50. Kinetic curves detected after injecting an MB solution into an aerogel suspension. The initial concentration of the aerogel was constant (340 µg/mL), and the initial concentrations of MB were 2.5, 7.4, 9.9, 14.8, 22.0, 29.1 and 36.1 µM. Kinetic curves are shown from 8 s after injection. Green dots are experimental data points. Continuous red lines are the results of global data fitting to the kinetic model given in **Scheme 13**. $c(NaH_2PO_4+Na_2HPO_4)$ = 50 mM; pH = 6.93; 25 °C; 1000 rpm stirring.

Sorption isotherm. The aerogel was centrifuged after reaching equilibrium at the end of each kinetic experiment, and the concentration of the remaining dissolved MB was quantified by spectrophotometry (**Fig. 51**). As expected, the amount of adsorbed MB calculated from the absorbance of the centrifuged solution is the same as given by the total absorbance change during a kinetic experiment. The experimental isotherm was fitted with the Langmuir model:

$$\mathbf{MB} + \mathbf{S} \rightleftharpoons \mathbf{SMB} \tag{13}$$

$$K_{\text{ads}} = \frac{\theta_{\text{SMB}}}{[\text{MB}]_{\text{Eq}}\,\theta_{\text{S}}} \qquad c_{\text{MB}} = [\text{MB}]_{\text{Eq}} + c_{\text{gel}}s\theta_{\text{SMB}} \qquad 1 = \theta_{\text{S}} + \theta_{\text{SMB}} \tag{14}$$

$$\Delta A = \varepsilon l c_{\text{gel}} s \theta_{\text{SMB}} = \frac{\varepsilon l}{2}\left\{\left(c_{\text{gel}}s + c_{\text{MB}} + \frac{1}{K_{\text{ads}}}\right) - \sqrt{\left(c_{\text{gel}}s + c_{\text{MB}} + \frac{1}{K_{\text{ads}}}\right)^2 - 4c_{\text{MB}}c_{\text{gel}}s}\right\} \approx$$

$$\approx \varepsilon l \frac{K_{\text{ads}}c_{\text{MB}}c_{\text{gel}}s}{1 + K_{\text{ads}}c_{\text{MB}}} \tag{15}$$

where MB is dissolved methylene blue, S represents an unoccupied adsorption site on the aerogel and SMB is the adsorbed dye occupying an adsorption site. K_{ads} is the Langmuir equilibrium constant. The total concentration of MB is c_{MB}. The total concentration of the aerogel is c_{gel} in g/L units. The number of adsorption sites on the aerogel particles is s in mol/g units. θ_{S} and θ_{SMB} represent the surface coverage of free and occupied sites, respectively. The absorbance change is ΔA. The experimental isotherm of **Fig. 51** was fitted with **eq. 15**; and the following parameters were estimated: $K_{\text{ads}} = (1.8 \pm 0.2) \times 10^5\ \text{M}^{-1}$, $s = 48 \pm 5$ μmol/g.

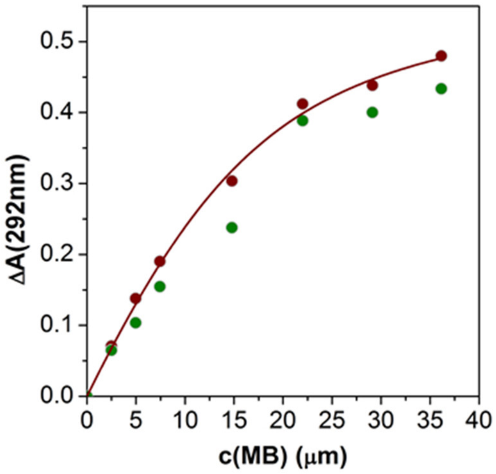

Figure 51. The experimental isotherm of the adsorption of MB. The *y* axis displays the absorbance change accompanying the depletion of the dye from solution due to adsorption. Brown dots: measured by the centrifugation method. Green dots: determined from the kinetic experiments. Brown line: best fit by **eq. 15**. c(gel) = 340 μg/mL; c(NaH_2PO_4+Na_2HPO_4) = 50 mM; pH = 6.93; 25 °C; 1000 rpm stirring.

Validity of Beer's law. The measured absorbance of the suspension containing MB is the superposition of two components: the absorbance of dissolved MB and the apparent absorbance of the aerogel particles due to extinction. The additivity of the absorbances of the heterogeneous and homogeneous components has been tested in several systems earlier. The results confirm that the absorbances of the components are additive in a limited concentration range. [178,179,359] In **Fig. 52A**, we present the spectrum of a well stirred aerogel suspension, the spectrum recorded immediately after the addition of MB to this suspension, the difference spectrum of these two and, finally, the spectrum of a pure MB solution. The difference spectrum and the spectrum of the pure MB solution are practically identical confirming that the apparent absorbance arising from the extinction of the suspension and the absorbance of dissolved MB are additive in the studied wavelength range. The absorbance vs. c_{gel} plot is linear with zero intercept (**Fig. 52B**). Accordingly, any absorbance change observed in this system is solely due to physico-chemical processes associated with the specific interactions of MB and the aerogel.

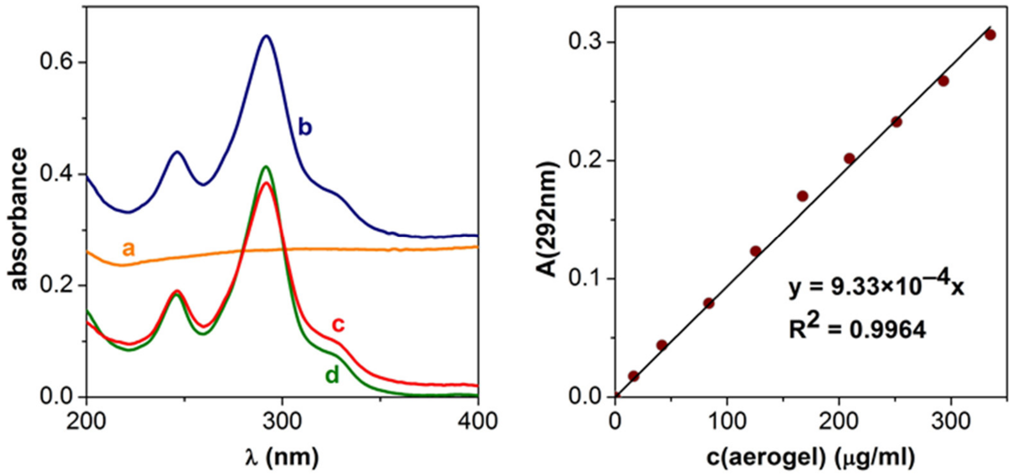

Figure 52. Left: a) The UV-vis spectrum of a well stirred aerogel suspension (331 μg/mL), b) the spectrum recorded immediately after the addition of MB to this suspension, c) the difference spectrum of these two, d) the spectrum of the MB solution (10.2 μM). Right: Absorbance versus concentration plot of the aerogel suspension. $c(\mathrm{NaH_2PO_4{+}Na_2HPO_4}) = 50$ mM; pH = 6.91; 25 °C; 1000 rpm stirring.

V-3.1.2. Detailed kinetic model

The concentration of dissolved MB decreases in time after MB is added to the aerogel suspension. The apparent absorbance of the aerogel caused by light scattering also decreases, because a portion of the particles covered by MB aggregate into large blocks (0.5 – 1 mm), and some of these aggregates settle down in the stirred suspension being removed from the light path of the photometer. The aggregation of the aerogel particles is induced by the adsorption of MB, because the cationic dye masks the negative surface charge of the particles that diminishes particle-particle repulsion.

The initial rate of absorbance change is proportional to both the initial MB concertation (c_{MB}) and the initial aerogel concentration (c_{gel}). This indicates that the simplest kinetic model, i.e. the Langmuir model, [353,356,357] can be applied to describe the reversible adsorption of MB on aerogel particles in the applied concentration range. In order to adequately interpret the observed biphasic kinetics (cf. **Fig. 50**), the adsorption facilitated aggregation of aerogel particles also needs to be taken into account. For the sake of simplicity, the aggregation is assumed to be a second order kinetic process with respect to the particles covered by MB. The kinetic model incorporating both of these reversible steps is given in **Scheme 13**.

R1) **MB + S ⟶ SMB** $k_1 = (1.09 \pm 0.03) \times 10^{3}\ \mathrm{M^{-1}\ s^{-1}}$

R2) **SMB ⟶ MB + S** $k_2 = (2.0 \pm 0.1) \times 10^{-2}\ \mathrm{s^{-1}}$

R3) 2 **SMB ⟶ aggregate** $k_3 = (1.4 \pm 0.1) \times 10^{2}\ \mathrm{M^{-1}\ s^{-1}}$

R4) **aggregate ⟶** 2 **SMB** $k_4 = (3.1 \pm 0.1) \times 10^{-3}\ \mathrm{s^{-1}}$

$$\frac{d[\mathrm{MB}]}{dt} = -k_1[\mathrm{MB}][\mathrm{S}] + k_2[\mathrm{SMB}] \tag{16}$$

$$\frac{d[\mathrm{S}]}{dt} = -k_1[\mathrm{MB}][\mathrm{S}] + k_2[\mathrm{SMB}] \tag{17}$$

$$\frac{d[\mathrm{SMB}]}{dt} = +k_1[\mathrm{MB}][\mathrm{S}] - k_2[\mathrm{SMB}] - 2k_3[\mathrm{SMB}]^2 + 2k_4[\mathrm{aggr}] \tag{18}$$

$$\frac{d[\mathrm{aggr}]}{dt} = +k_3[\mathrm{SMB}]^2 - k_4[\mathrm{aggr}] \tag{19}$$

$$\theta_{\mathrm{S}} c_{\mathrm{gel}} s = [\mathrm{S}] \tag{20}$$

$$\theta_{\mathrm{SMB}} c_{\mathrm{gel}} s = [\mathrm{SMB}] + 2[\mathrm{aggr}] \tag{21}$$

$$c_{\mathrm{MB}} = [\mathrm{MB}] + \theta_{\mathrm{SMB}} c_{\mathrm{gel}} s \qquad \theta_{\mathrm{S}} + \theta_{\mathrm{SMB}} = 1 \qquad (\text{cf. eq. } 14)$$

Scheme 13. Kinetic model detailing the adsorption of methylene blue (MB) on aerogel particles. A free adsorption site on the aerogel is symbolized by S, and an occupied site by SMB. The first process (R1 and R2) is the reversible adsorption of the dye, and the second process (R3 and R4) is the reversible aggregation of those aerogel particles that are covered by MB. The time-dependent concentrations of dissolved MB, free and covered aerogel particles and aggregates are [MB], [S], [SMB] and [aggr], respectively. The initial (total) concentrations of MB and the aerogel are c_{MB} and c_{gel}, respectively. Time-dependent surface coverage is θ. The adsorptive capacity of the aerogel is $s = 48$ μmol/g.

The contribution of these species to the measured absorbance signal at time *t* is given by:

$$A^t = \{\varepsilon_{\mathrm{MB}}[\mathrm{MB}] + \varepsilon_{\mathrm{gel}}[\mathrm{S}] + \varepsilon^*{}_{\mathrm{gel}}[\mathrm{SMB}] + \varepsilon_{\mathrm{aggr}}[\mathrm{aggr}]\}l \tag{22}$$

where A^t is the measured absorbance, and ε denotes the molar absorbance of each species. Integrating the ordinary differential equation system of **Scheme 13** gives A^t as a function of time. Using this method, the kinetic curves in **Fig. 50** were fitted simultaneously by minimizing the difference between the measured and calculated absorbance values. The fit is reasonably good at every c_{MB}. The estimated constants are given in **Scheme 13**. The estimated value of $\varepsilon^*{}_{\mathrm{gel}}$ is the same as the independently determined $\varepsilon_{\mathrm{gel}}$, implying that the adsorption of MB on the aerogel does not affect the apparent absorbance (extinction) of these particles. The estimated value of $\varepsilon_{\mathrm{aggr}}$ is zero within the experimental error, meaning that the contribution of the aggregates to the absorbance is practically zero. This is not unexpected because the aggregates are removed from the detection light path via sedimentation.

Another model to describe biphasic kinetics could be constructed by assuming that MB adsorbs on the aerogel particles on multiple different sorption sites with different rates, e.g. inside smaller and larger pores. [360] However, the multi-site adsorption of MB can be ruled out considering that NMR diffusiometry showed that small molecules can enter and exit the pore system of the aerogel in a practically uninhibited manner in a few milliseconds timescale.

V-3.2. Adsorption of methylene blue from aqueous solution on quartz [P14]

Methylene blue (MB) is often a model compound in sorption studies. Due to its planar structure with 14 delocalized electrons, this compound is easily involved in molecular stacking interactions. Consequently, MB readily forms dimers and higher level aggregates in solution even at micro-molar analytical concentrations. [361-364] The thermodynamic and UV-Vis spectroscopic characteristics of MB adsorbed on silica surface are well understood. [180-183] There seems to be a consensus in the literature that MB forms a monolayer on silica when adsorbed from solutions of high micro-molar concentrations at short contact times. The UV-Vis spectrum of adsorbed MB shows a blue shift at around 600 nm, which has been attributed to dimer formation on the surface, similar to solvated dimers. [184]

The introduction of an aqueous solution of MB into a standard spectrophotometric quartz cuvette is always followed by a 1–3% decay in the absorbance signal of MB in the first few minutes. We have conducted a rigorous mechanistic study to account for this phenomenon and connect it with the sorption of MB on the inner surface of the quartz cuvette.

V-3.2.1. Experimental procedures and considerations

The most convenient way to study the adsorption of MB on the inner surface of a quartz cuvette is by simply injecting an aqueous MB solution into an empty cuvette and following the spectral change on-line by a UV-vis spectrophotometer under continuous stirring. However, we experienced better reproducibility and robustness when the MB solution was not directly injected into the empty cuvette, but into an aqueous buffer already stirred inside the cuvette. The moment of injection can clearly be identified in the recorded kinetic traces (**Fig. 53**). A steady absorbance decay was detected, which was attributed exclusively to the depletion of the dye from solution due to adsorption on the quartz surface.

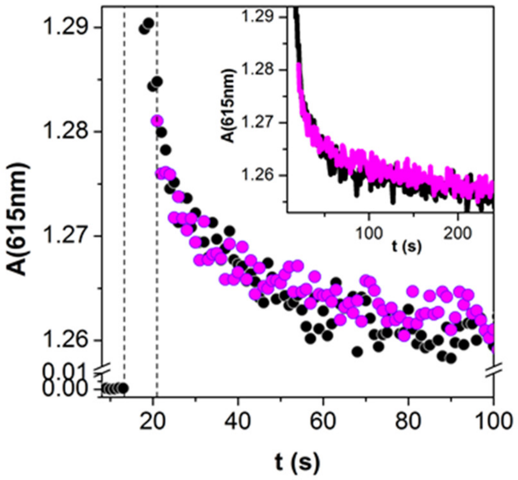

Figure 53. Absorbance change detected after injecting a methylene blue (MB) solution into a quartz cuvette. The black curve was recorded by injecting 70 µL of a 1.00 mM MB solution into 2.00 mL buffer stirred in a cuvette. Some time is required for homogenization. The magenta curve was recorded after injecting 2.00 mL of a 33.8 µM MB solution into an empty dry cuvette containing only a stirrer. The first vertical dotted line at 13 s indicates the time of injection of the dye in the first experiment. The second dotted line at 21 s indicates the time of injection in the second experiment. The time shift between the two kinetic curves gives the time needed for homogenization in the first experiment (8 s). The inset shows the same two kinetic curves on a longer time scale. c_0(MB) = 33.8 µM; c(NaH_2PO_4+Na_2HPO_4) = 50 mM; pH = 6.84; 25 °C; 1000 rpm mixing.

Solution phase dimerization of methylene blue. The UV-Vis spectra of aqueous MB solutions were recorded in the concentration range from 1.00 µM to 1.00 mM. The absorbance *versus* c(MB) plots are non-linear at various wavelengths, which is unambiguously attributed to the solution phase dimerization of MB. [363] The dimerization equilibrium constant of MB (phosphate buffer; pH = 6.9; I = 0.10) was estimated to be log(K_f) = 3.9 ± 0.1, which is in good agreement with literature data reporting log(K_f) of 3.5–3.9 under different conditions. [362,363]

Kinetics of adsorption of methylene blue. After injecting a MB solution into a buffer solution, a steady decrease in absorbance was detected at all wavelengths (**Fig. 54**) with biphasic kinetic characteristics (**Fig. 55**). The number of the light absorbing components in a time-resolved UV-Vis spectral series was estimated to be 2 by the singular value decomposition of the data. [365,366] The results are consistent with the presence of the main absorbing species (hydrated MB) and an additional weakly absorbing component (presumably the absorbed MB). Plotting absorbance values recorded in the same experiment at different wavelengths *versus* each other gives a straight line regardless of the chosen wavelength pairs. This proportionality means that the data obtained at different wavelengths carry exactly the same information.

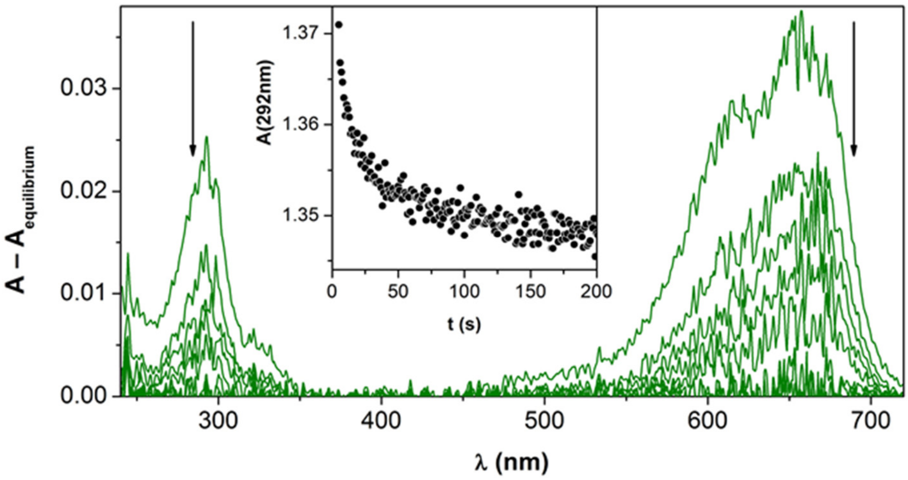

Figure 54. Time resolved difference spectra obtained after injecting 70 µL of a 1.00 mM methylene blue (MB) solution into 2.00 mL buffer stirred in a quartz cuvette. The spectra were calculated by subtracting the final spectrum (the spectrum recorded when the adsorption process was complete) from the spectrum recorded at a given reaction time. Inset: the corresponding kinetic curve at 292 nm. c_0(MB) = 33.8 µM; c(NaH_2PO_4+Na_2HPO_4) = 50 mM; pH = 6.89; 25 °C; 1000 rpm mixing.

The UV-Vis spectrum of MB adsorbed on the wall of the cuvette was recorded by equilibrating the cuvette for 15 min with a MB solution, then discarding it. The spectrum of this pre-treated cuvette represents the UV-Vis spectrum of MB adsorbed on its quartz wall. This experiment was performed at several MB concentrations, and we found that the spectrum of adsorbed MB does not show any blue shift compared to its solution phase spectrum when 10 – 50 µM solutions were used for equilibration. (**Fig. 56**). The similarity of the spectra of adsorbed and solution phase MB at low concentrations indicates that MB forms a monolayer on the quartz surface in the applied concentration range. Aggregates are not formed when the cuvette is treated with dilute MB solutions, and the dimerization of MB is not favored on quartz. Apparently, dimerization on the surface takes place only when the surface is in contact with 100 – 1000 µM MB solutions, which already contain MB dimers.

The kinetic curves and the spectral change attributed to MB adsorption from 1:1 ethanol are almost identical to those recorded in water. The lack of any significant solvent effects means that the adsorption of MB on quartz is not influenced by its solution phase dimerization, as this is suppressed in ethanol. [367] It also follows that it is not the dimer which promotes monolayer formation on the surface. Furthermore, the excellent reproducibility of the adsorption studies in 1:1 ethanol-water rules out any possible side effects (e.g. ion-pair formation) arising from the use of phosphate buffer in the kinetic experiments.

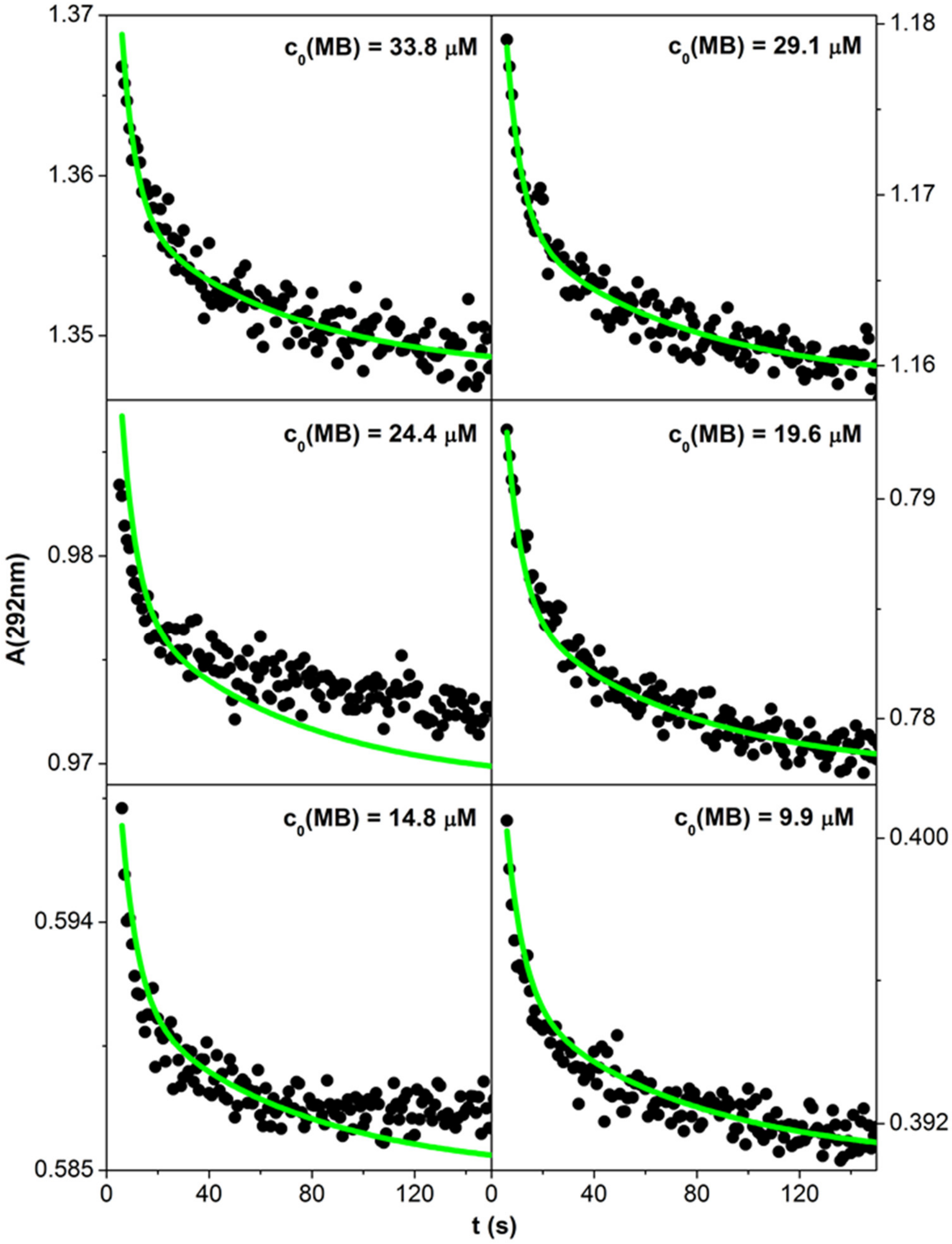

Figure 55. Kinetic curves detected after injecting 10 – 70 µL of a 1.00 mM MB solution into 2.00 mL buffer solution stirred in a quartz cuvette. Kinetic curves are shown from 8 s after injection. Black dots are experimental data points. Continuous green lines are the results of global data fitting to the kinetic model given in **Scheme 14**. c(NaH_2PO_4+Na_2HPO_4) = 50 mM; pH = 6.89; 25 °C; 1000 rpm mixing.

Experimental observations indicate that the protolytic equilibria involving the quartz surface, as well as, the stirring rate of the solution have profound effects on the adsorption process. Under acidic conditions, the quartz surface and, to some extent, MB (pK_a = 1.69 [361]) are protonated, thus, the attractive Coulomb interaction between them diminishes. This leads to limited adsorption of the dye. Basic pH enhances the negative surface charge of silica, thus, facilitates the adsorption. Stirring provides an efficient way for transporting MB to the surface, but the rate of the adsorption becomes independent of stirring at sufficiently high stirring rates.

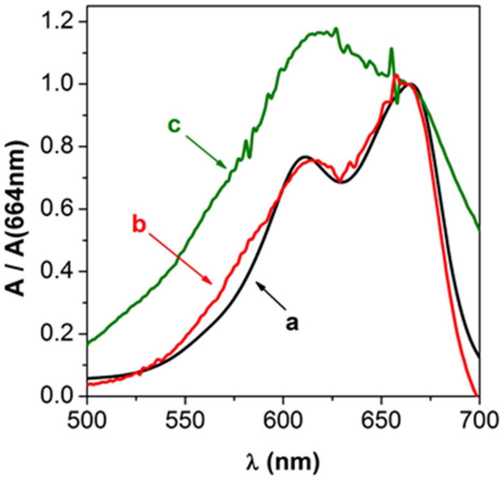

Figure 56. a) UV-Vis spectrum of 50 µM aqueous MB solution. b) UV-Vis spectrum of an empty quartz cuvette equilibrated with the 50 µM MB solution. This spectrum represents the transmission UV-Vis spectrum of MB adsorbed on quartz. c) The same as b), but in this case a 1.0 mM MB solution was used. All spectra are normalized to the absorbance measured at 664 nm. This transformation magnifies spectra b) and c) ca. 10-times compared to spectrum a). The absorption peak of the MB monomer at 664 nm dominates spectra a) and b), and the peak at 612 nm is characteristic for the MB dimer in spectrum c).

V-3.2.2. Adsorption isotherm

The characteristic isotherm for the adsorption of MB on quartz was constructed by plotting the amplitude of the absorbance change in the kinetic experiments (cf. **Fig. 55**) as a function of the MB concentration (**Fig. 57**). None of our experimental results suggest a deviation from monolayer adsorption, thus the isotherm was fitted to the Langmuir. The extent of dimerization of MB in aqueous solution is small in the applied concentration range, and negligible in the context of the model.

$$\mathbf{MB} + \mathbf{S} \rightleftharpoons \mathbf{SMB} \tag{23}$$

$$K_{\mathrm{ads}} = \frac{\theta_{\mathrm{SMB}}}{[\mathrm{MB}]\theta_{\mathrm{S}}} \qquad c = [\mathrm{MB}] + s\theta_{\mathrm{SMB}}/V \qquad 1 = \theta_{\mathrm{S}} + \theta_{\mathrm{SMB}} \tag{24}$$

where MB is hydrated methylene blue, S represents an unoccupied site on the surface and SMB is the adsorbed dye occupying a site. K_{ads} is the equilibrium constant of monolayer adsorption, V is the volume of the solution in the cuvette. The total concentration of MB is c and the number of moles of adsorption sites on the quartz cuvette is *s*. Square brackets denote equilibrium concentrations. θ_S and θ_{SMB} represent the surface coverage of free and occupied sites, respectively. The absorbance change associated with the adsorption of MB on quartz (ΔA) is due to the lower apparent molar absorptivity of adsorbed MB compared to hydrated MB. On the basis of Beer's law, ΔA is given as follows:

$$\Delta A = \varepsilon_{\mathrm{sol}} l_{\mathrm{sol}} c - (\varepsilon_{\mathrm{sol}} l_{\mathrm{sol}}[\mathrm{MB}] + \varepsilon_{\mathrm{ads}} l_{\mathrm{ads}}[\mathrm{SMB}]) = (\varepsilon_{\mathrm{sol}} l_{\mathrm{sol}} - \varepsilon_{\mathrm{ads}} l_{\mathrm{ads}})[\mathrm{SMB}] = \\ = E[\mathrm{SMB}] \quad (25)$$

Here $\varepsilon_{\mathrm{sol}}$ and $\varepsilon_{\mathrm{ads}}$ are the molar absorbances of hydrated and adsorbed MB, respectively; while l_{sol} and l_{ads} are the optical pathlengths. *E* is the difference between the molar absorptivity of hydrated and adsorbed MB. The molar absorbance of hydrated MB is well known and $l_{\mathrm{sol}} = 1.0$ cm in our experiments. In principle, l_{ads} could be calculated from the thickness of the adsorption layer on the surface, but the uncertainty associated with estimating the thickness makes any effort to separate $\varepsilon_{\mathrm{ads}}$ and l_{ads} pointless.

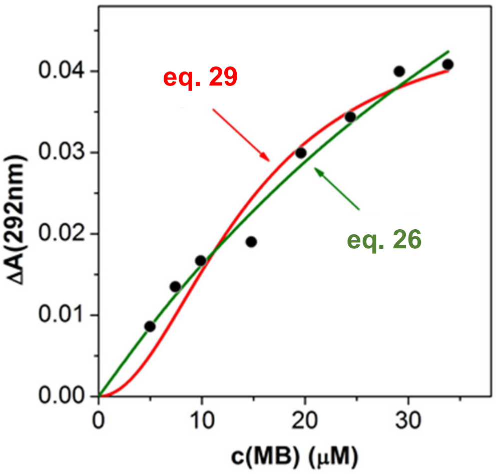

Figure 57. Experimental isotherm describing the adsorption of methylene blue (MB) on the surface of a quartz cuvette. Black points: difference between measured initial and equilibrium absorbance values (i.e., amplitude of spectral change, ΔA) as a function of the analytical concentration of MB (*c*(MB)). The corresponding experimental kinetic curves are shown in **Fig. 55**. Green line: best non-linear least squares fit to the Langmuir isotherm, assuming that only MB monomers adsorb to the surface (**eq. 26**). Red line: best non-linear least squares fit assuming that only MB dimers adsorb to the surface (**eq. 29**). (NaH_2PO_4+Na_2HPO_4) = 50 mM; pH = 6.89; 25 °C; 1000 rpm mixing.

According to earlier studies, the absorbance of adsorbed MB drops to ca. 10 % compared to that of in solution. [180,368] Our observations are in line with such a difference, thus *E* is fixed at 90 % of $\varepsilon_{\mathrm{sol}} \times l_{\mathrm{sol}}$ in the calculations. ΔA can be given by combining **eq. 24** and **eq. 25**:

$$\Delta A = \frac{Es\theta_{\mathrm{SMB}}}{V} = E\frac{1}{2}\left\{\left(\frac{s}{V} + c + \frac{1}{K_{\mathrm{ads}}}\right) - \sqrt{\left(\frac{s}{V} + c + \frac{1}{K_{\mathrm{ads}}}\right)^2 - \frac{4sc}{V}}\right\} \approx$$

$$\approx E\frac{K_{\mathrm{ads}}c}{1 + K_{\mathrm{ads}}c}s/V \tag{26}$$

As shown in **Fig. 57**, equation 4 fits the experimental data reasonably well. The non-linear least squares fitting yields the following estimates for the parameters: $K_{\mathrm{ads}} = (1.5 \pm 0.5) \times 10^4$ M^{-1} and $s = (7.0 \pm 1.8)$ nmol (equivalent to 3.5 μM MB in 2.0 mL solution). The volume of the MB solution is 2.0 cm^3 and the surface of the cuvette covered by this solution is 9.0 cm^2. This translates into 7.8×10^{-10} mol adsorbed MB per cm^2 quartz. Therefore, the area per adsorbed MB molecule is 21 Å^2 (21×10^{-20} m^2). This is in good agreement with the area requirement of MB measured previously under conditions when a monolayer forms, and MB molecules bind roughly perpendicularly to the surface. [364,369]

The amount of adsorption sites is 7.0 nmol, and the amount of MB present in solution was 60 nmol (2.0 mL of a 30 μM solution) at most. The small difference in the amount of available sites and MB predicts that the outer hydration sphere of the sites is never saturated with MB. This is in agreement with the adsorption of MB being faster with increasing MB concentration (cf. **Fig. 55**). The rate of adsorption does not level off, as would be expected if it was controlled by the amount of dye in the outer hydration sphere of quartz. On the contrary, MB is rapidly adsorbed, and effective mixing was needed to replenish it near the surface.

The visible total reflection spectrum of adsorbed MB on quartz is reported to show a blue shift in the 600 – 700 nm wavelength range. A similar blue shift is also associated with the formation of the hydrated MB dimer. [180,184] In the case of the formation of a monolayer exclusively from the dimers on the surface when $c \gg [(\mathrm{MB})_2] + [\mathrm{S(MB)_2}]$, the following expressions can be derived using the simplest, Langmuir-type adsorption model:

$$2\,\mathbf{MB} \rightleftharpoons \mathbf{(MB)_2} \qquad \mathbf{(MB)_2} + \mathbf{S} \rightleftharpoons \mathbf{S(MB)_2} \tag{27}$$

$$K_{\mathrm{f}} = \frac{[(\mathrm{MB})_2]}{[\mathrm{MB}]^2} \qquad K_{\mathrm{ads2}} = \frac{\theta_{\mathrm{SMB2}}}{[\mathrm{MB}_2]\theta_{\mathrm{S}}} \qquad c = [\mathrm{MB}] + 2[(\mathrm{MB})_2] + \frac{2s\theta_{\mathrm{SMB2}}}{V}$$

$$1 = \theta_{\mathrm{S}} + \theta_{\mathrm{SMB2}} \tag{28}$$

$$\Delta A = 2E\theta_{\mathrm{SMB2}}s/V = 2E\frac{K_{\mathrm{ads2}}K_{\mathrm{f}}c^2}{1 + K_{\mathrm{ads2}}K_{\mathrm{f}}c^2}s/V \tag{29}$$

Here, K_f is the dimerization constant of hydrated MB and K_{ads2} is the equilibrium constant describing the monolayer adsorption of the MB dimers. Other symbols were defined earlier. The comparison of the data sets (**Fig. 57**) clearly shows that the characteristic sigmoid profile of the calculated curve is absent from the experimental data.

The results confirm that the quartz surface does not facilitate the dimerization of MB in the adsorption layer. This conclusion is also supported by the noted similarity between the UV-Vis spectra of adsorbed and solution phase MB recorded after equilibrating the quartz surface with relatively low concentration MB solution (**Fig. 56**).

V-3.2.3. Kinetics and mechanism of adsorption

The biphasic shape of the kinetic curves is invariant to the ratio of the *in situ* dilution of MB (**Fig. 55**). If solution phase dimerization were slow and had significant contribution to the measured absorbance decay, the kinetics should depend on dilution. Thus, a kinetic model was developed based on the following considerations: *i*) the absorbance change is solely caused by the adsorption of MB; *ii*) in line with the analysis of the isotherm, only monolayer adsorption occurs; *iii*) the observed biphasic kinetics can be consistent with dimerization on the surface, but the molar fraction of the adsorbed dimers cannot exceed that of hydrated dimers, as discussed in connection with the transmission UV-Vis spectrum of adsorbed MB (cf. **Fig. 56**); *iv*) on a longer time scale, the isomerization of the binding of MB can take place. [370] The simplest model to give biphasic kinetics and include the adsorption of both dimers and monomers is practically the consecutive adsorption of two MB molecules to the same surface site. [371] However, this model is inadequate to describe the experimental kinetic data. An alternative kinetic model is the relatively fast reversible adsorption of MB on the surface in the first step, and a slower isomerization of the binding mode of the adsorbed species in a second reversible step (**Scheme 14**).

The monolayer capacity of quartz was set to be 7.0 nmol. The resulting fit is good at every initial concentration (**Fig. 55**). The observed spectral changes can also be successfully reconstructed using the model of **Scheme 14**. The calculated spectra of MB present in different binding modes on quartz are reasonable, and the calculation, as expected, is not sensitive to c(MB), as seen in **Fig. 58**. It is interesting to note that no blue shift can be observed in these reconstructed spectra, which is in good agreement with the measured transmission UV-Vis spectra of adsorbed MB (**Fig. 56**). The assumption that the molar absorbance of hydrated MB decreases by ca. 90% upon adsorption on quartz is also strengthened by these results.

R5) **MB + S ⟶ SMB** $k_5 = (1.36 \pm 0.03) \times 10^{-3}\ \mu\mathrm{M}^{-1}\ \mathrm{s}^{-1}$

R6) **SMB ⟶ MB + S** $k_6 = (1.29 \pm 0.03) \times 10^{-1}\ \mathrm{s}^{-1}$

R7) **SMB ⟶ $\mathbf{SMB^{I}}$** $k_7 = (5.3 \pm 0.4) \times 10^{-3}\ \mathrm{s}^{-1}$

R8) **$\mathbf{SMB^{I}}$ ⟶ SMB** $k_8 = (1.46 \pm 0.06) \times 10^{-2}\ \mathrm{s}^{-1}$

$$\frac{d[\mathrm{MB}]}{dt} = -k_1[\mathrm{MB}]\theta_{\mathrm{S}}s/V + k_2\theta_{\mathrm{SMB}}s/V \tag{30}$$

$$\frac{d\theta_{\mathrm{SMB}}}{dt} = +k_1[\mathrm{MB}]\theta_{\mathrm{S}} - k_2\theta_{\mathrm{SMB}} - k_3\theta_{\mathrm{SMB}} + k_4\theta_{\mathrm{SMBI}} \tag{31}$$

$$\frac{d\theta_{\mathrm{SMBI}}}{dt} = +k_3\theta_{\mathrm{SMB}} - k_4\theta_{\mathrm{SMBI}} \tag{33}$$

$$\frac{d\theta_{\mathrm{SMB}}}{dt} = -k_1[\mathrm{MB}]\theta_{\mathrm{S}} + k_2\theta_{\mathrm{SMB}} \tag{34}$$

Scheme 14. Kinetic model detailing the adsorption of a methylene blue (MB) to a surface site on quartz. The first process (reactions R5 and R6) is the reversible monolayer adsorption of the dye, and the second process (reactions R7 and R8) is an isomerization in the mode of binding on the surface. Square brackets indicate time-dependent actual concentrations, and k_i represent rate constants. θ is time-dependent surface coverage. Further details are given in the text and in **Fig. 58**.

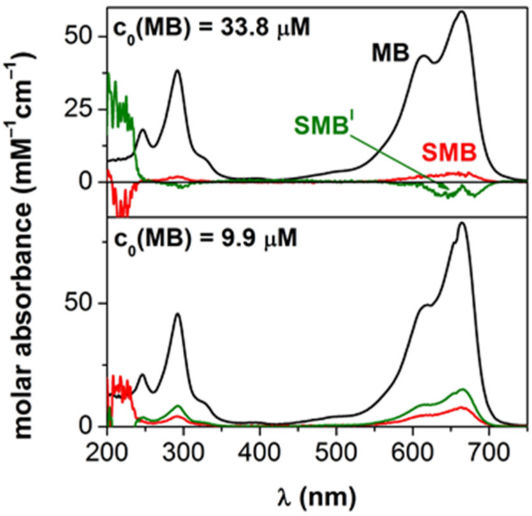

Figure 58. Calculated UV-Vis spectra of hydrated MB and MB monomers adsorbed on quartz in different binding modes. SMB is the primary product of adsorption, and $\mathrm{SMB^{I}}$ forms on a longer time scale. The calculation was based on the kinetic model of **Scheme 14**.

V-3.3. Adsorption of aqueous bovine serum albumin on silica aerogel particles [P15]

Silica-based aerogels have considerable innovation potential in biotechnology and medicine as enzyme and drug carriers, and tissue scaffolds. [31,61,372-374] These applications generate a demand for understanding the interactions of these nanostructured materials with biomolecules and living organism. [116,193] Serum albumins are widely used model proteins in interface research. [185,375,376] BSA is a soft protein, thus its aqueous tertiary structure is significantly influenced by the pH. [185-187] Protein sorption on solid surfaces usually displays complex mechanisms sensitive to the physico-chemical environment (temperature, pH, ionic strength, etc.), as well as, the chemical structure and morphology of the sorbent. [188-191] Two-state models are generally accepted for describing the binding of proteins. Two alternatives are proposed: 1) Initially, the protein binds via weak interactions, and subsequently undergo a transformation into a strongly bound state on the surface. 2) The formation of weakly bound and strongly bound forms of proteins on the surface are parallel processes depending on available sorption sites. [192-195] In this study, the interaction of BSA and an archetypical mesoporous silica aerogel was investigated in aqueous media using on-line time-resolved UV-vis spectrophotometry and turbidimetry. The pH-dependent binding of BSA on aerogel microparticles was elucidated based on a global kinetic analysis.

V-3.3.1. Zeta potentials of BSA and suspended silica aerogel particles

The ζ-potentials of aqueous BSA and silica aerogel microparticles were measured as a function of pH in the presence of acetate and phosphate electrolytes at the same ionic strength ($I = 0.10$ M; **Fig. 59**). The isoelectric point of BSA is between pH = 4.5 and 5.0 in both media, which agrees with literature data. [185] The ζ-potential values at a given pH are different depending whether acetate or phosphate is present both in the case of BSA and silica aerogel microparticles, which indicates the specific interactions of these with acetate and phosphate ions in accordance with the Hofmeister series theory. [377-379] The generally negative ζ-potential of silica aerogel strengthens the idea of the specific sorption of anions form the corresponding electrolytes. In the absence of these anions, the isoelectric point of amorphous silica particles is reported to be at pH = 3.5. [223]

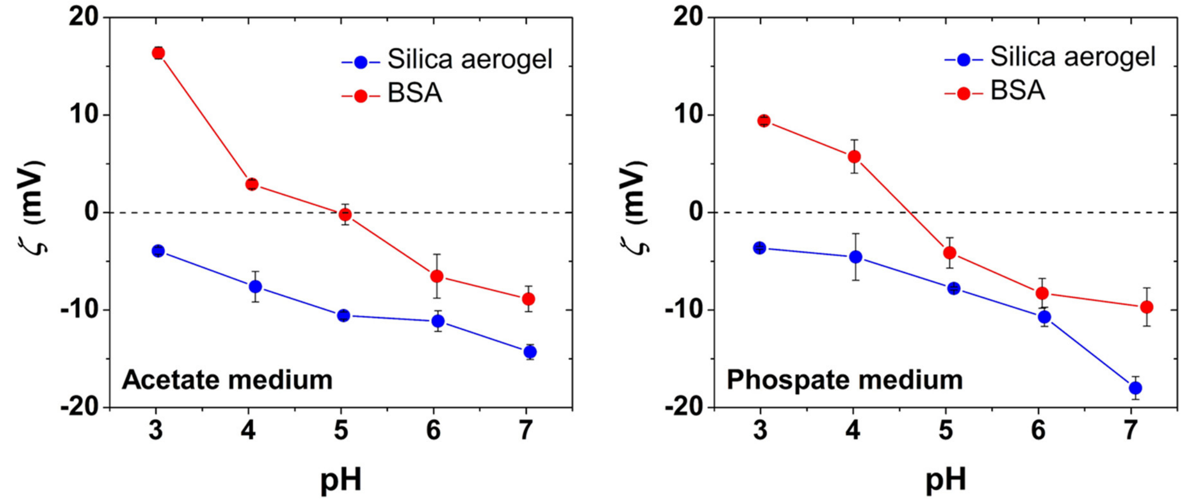

Figure 59. Zeta potentials (ζ) of aqueous BSA and silica aerogel microparticles as a function of pH in the presence of 0.01 M acetate (a), or phosphate (b) electrolytes at constant ionic strength (I = 0.10 M).

V-3.3.2. Sorption of BSA on silica aerogel microparticles

When aqueous BSA is injected into a stable aerogel suspension, a rapid increase in turbidity is immediately visible, which is well-aligned with the corresponding UV-vis spectral change (**Fig. 60**). The initial concentrations of BSA and silica aerogel were varied in a series of kinetic experiments at pH = 4.6 in acetate buffer, and at pH =6.4 in phosphate buffer (**Fig. 61**). Two well-separated steps are present in all the experimental kinetic curves regardless of the pH and concentration conditions.

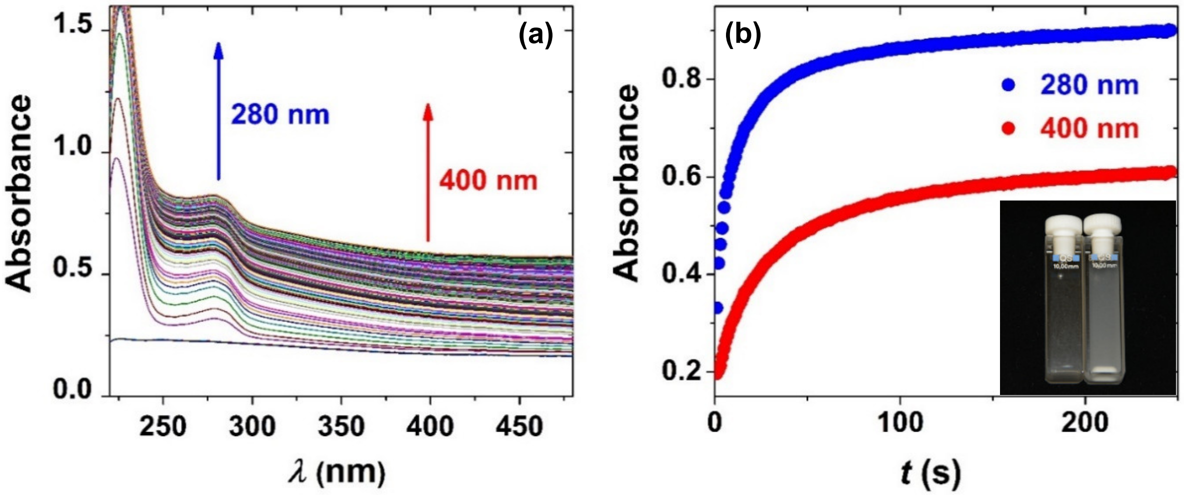

Figure 60. (a) Time-resolved UV-vis spectral change following the mixing of aqueous BSA to a stable silica aerogel suspension. (b) The corresponding kinetic curves at 280 nm and 400 nm. Inset: photograph of the aerogel suspension in a cuvette before adding BSA and 5 min after mixing. [c_0(aero) = 100 µg/mL; c_0(BSA) = 300 µg/mL; pH = 4.6 acetate buffer; 800 rpm stirring; 25.0 °C].

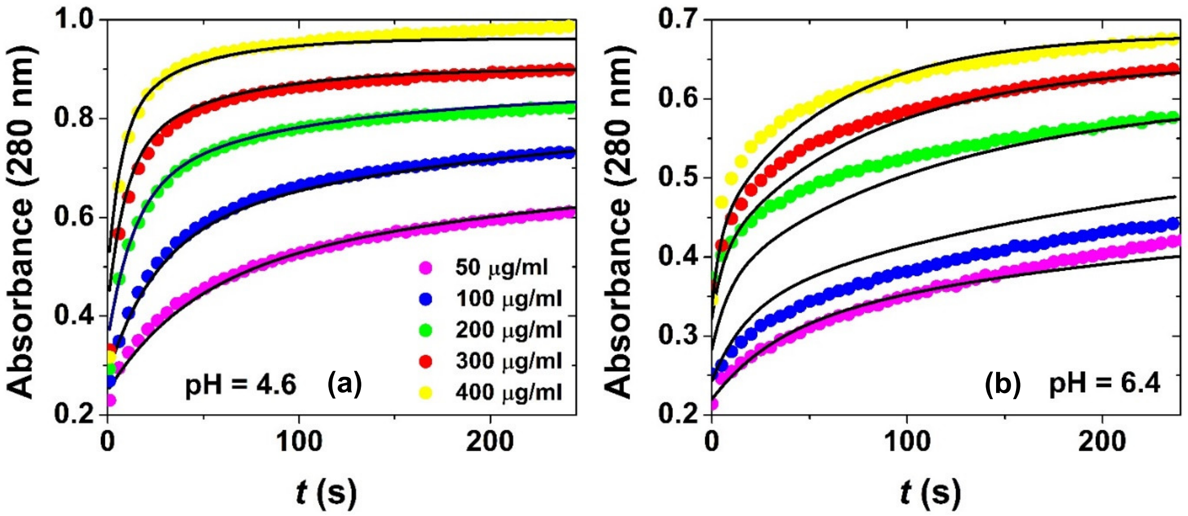

Figure 61. Series of kinetic experiments using different initial concentrations of BSA at pH = 4.6 in acetate buffer (a) and at pH = 6.4 in phosphate buffer (b). The markers are experimental data points and the continuous lines are the results of global data fitting using the model in **Scheme 15**. Some of the corresponding simulated time-dependent concentration profiles are shown in **Fig. 62**. [c_0(aero) = 100 μg/mL; c_0(BSA) = 50 – 400 μg/mL; 800 rpm stirring; 25.0 °C].

Kinetic model construction. A kinetic model is proposed in **Scheme 15**, which consists of two reversible processes denoted as reactions R9/R10 and R11/R12.

R9 BSA + AERO ⟶ PROD k_9 (adsorption of BSA)

R10 PROD ⟶ BSA + AERO k_{10} (desorption of BSA)

R11 BSA + PROD ⟶ AGGR k_{11} (aggregation)

R12 AGGR ⟶ PROD + BSA k_{12} (disaggregation)

$$\frac{\mathrm{d[BSA]}}{\mathrm{dt}} = -\,k_9\times[\mathrm{BSA}]\times[\mathrm{AERO}] + k_{10}\times[\mathrm{PROD}] - k_{11}\times[\mathrm{BSA}]\times[\mathrm{PROD}] + \\ +k_{12}\times[\mathrm{AGGR}] \tag{35}$$

$$\frac{\mathrm{d[AERO]}}{\mathrm{dt}} = -\,k_9\times[\mathrm{BSA}]\times[\mathrm{AERO}] + k_{10}\times[\mathrm{PROD}] \tag{36}$$

$$\frac{\mathrm{d[PROD]}}{\mathrm{dt}} = +\,k_9\times[\mathrm{BSA}]\times[\mathrm{AERO}] - k_{10}\times[\mathrm{PROD}] - k_{11}\times[\mathrm{BSA}]\times[\mathrm{PROD}] + \\ +k_{12}\times[\mathrm{AGGR}] \tag{37}$$

$$\frac{\mathrm{d[AGGR]}}{\mathrm{dt}} = +\,k_{11}\times[\mathrm{BSA}]\times[\mathrm{PROD}] - k_{12}\times[\mathrm{AGGR}] \tag{38}$$

Scheme 15. Kinetic model for the sorption of BSA on aerogel particles. Four species are defined: aerogel particles (AERO), bovine serum albumin (BSA), bovine serum covered aerogel (PROD) and aggregate (AGGR). The k parameters are the rates constants. The differential equation system describing the time-dependent concentration of each species ([BSA], [AERO], [PROD], [AGGR]) is given below the reaction steps. Fitted kinetic curves are shown in **Fig. 61**. The estimated kinetic parameters are given in **Table 18**. Simulated time-dependent concentration profiles are shown in **Fig. 62**.

First, BSA is adsorbed on the aerogel particles (AERO) yielding protein covered particles (PROD) in R9. Desorption takes place in R10. Second, the subsequent sorption of additional BSA results in the aggregation of the covered aerogel particles (AGGR) in R11. The physico-chemical rationale is that the extensive sorption of BSA alters the electrical double layer of the aerogel particles, and thus, destabilizes the colloid system. [190] Disaggregation takes place in R12. Similar models proposing two stages of protein binding have successfully been used earlier to describe the interaction of BSA with different silica surfaces. [190,193]

The kinetic model of **Scheme 15** was used for global data fitting on the basis of quantitative UV-vis spectrophotometry, as follows. The baseline of the recorded UV-vis spectra is elevated in the full studied wavelength range, because of the extinction (apparent absorbance) of the aerogel particles. The light absorption (absorbance) of BSA is superimposed onto this baseline (cf. **Fig. 60**). As experimentally validated, the total measured absorbance follows Beer's law for the absorption of BSA and the extinction of the suspended aerogel particles. This is summarized in **eq. 39** and **eq. 40**. [127,178,217,380]

$$A^{t} = A^{t}_{\mathrm{BSA}} + A^{t}_{\mathrm{AERO}} + A^{t}_{\mathrm{PROD}} + A^{t}_{\mathrm{AGGR}} \qquad (39)$$

$$A^{t} = (\varepsilon_{\mathrm{BSA}}[\mathrm{BSA}] + \varepsilon_{\mathrm{AERO}}[\mathrm{AERO}] + \varepsilon_{\mathrm{PROD}}[\mathrm{PROD}] + \varepsilon_{\mathrm{AGGR}}[\mathrm{AGGR}])l \qquad (40)$$

In these equations, A^{t} is the time-dependent measured absorbance and the A^{t}_{SPECIES} are the absorbances of BSA and the different aerogel particles. In **eq. 40**, the absorbances are expressed for each species as the products of their molar absorbances or extinction coefficients ($\varepsilon_{\mathrm{SPECIES}}$) and their time-dependent concentrations (l is the optical length). The final (equilibrium) BSA concentrations after the establishment of the equilibrium in the colloid system were determined experimentally by analyzing the clear supernatants. These equilibrium BSA concentrations were used as fixed input data in the global fitting. Additional fixed input data were the molar absorbance of BSA and the extinction coefficient of AERO that were measured independently. All other parameters were estimated by simultaneously fitting all experimental kinetic curves at two wavelengths (280 and 400 nm) using the GEAR algorithm with the ZiTa software. [381,382] The goodness of fit is exceptional in the case of the experiments in acetate buffer (cf. **Fig. 61** and **Table 18**). Simulated time dependent concentration profiles are shown in **Fig. 62**.

Table 18. Kinetic parameters for the model of **Scheme 15** estimated by global fitting. The corresponding fitted curves are shown in **Fig. 61**.

	k_9 [$\mu g^{-1} L s^{-1}$]	k_{10} [$\mu g^{-1} L s^{-1}$]	k_{11} [$\mu g^{-1} L s^{-1}$]	k_{12} [$\mu g^{-1} L s^{-1}$]
acetate	$(7.5 \pm 0.1) \times 10^{-5}$	$(7.2 \pm 0.1) \times 10^{-4}$	$(3.6 \pm 0.1) \times 10^{-4}$	$(1.4 \pm 0.1) \times 10^{-3}$
phosphate	$(4.4 \pm 0.2) \times 10^{-5}$	$(8.0 \pm 1.0) \times 10^{-4}$	$(5.9 \pm 0.4) \times 10^{-4}$	$(1.4 \pm 0.3) \times 10^{-3}$

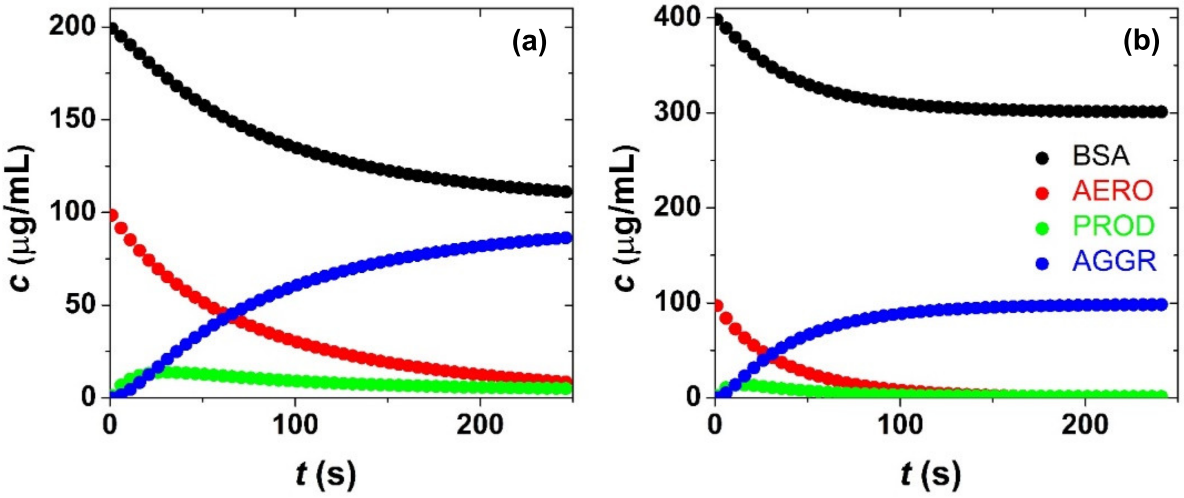

Figure 62. Simulated time dependent concentrations of aerogel particles (AERO), bovine serum albumin (BSA), BSA covered aerogel (PROD) and aggregate (AGGR) calculated at two different initial BSA concentrations of c_0(BSA) = 200 μg/mL (a) and c_0(BSA) = 400 μg/mL (b) at pH = 4.6 in acetate buffer [cf. **Fig. 61a**; c_0(aero) = 100 μg/mL; 800 rpm stirring; 25.0 °C]. The simulation is based on the kinetic model of **Scheme 15** using the parameters in **Table 18**. The color code is given in the legend.

V-3.3.3. Sorption isotherm and mechanism of sorption

The sorption isotherm measured in acetate buffer is shown in **Fig. 63**. The classical isotherm models (Langmuir, Temkin, etc.) are evidently not adequate to describe a two-stage sorption process, because of the fundamental differences in the underlying mechanisms. [193,383] However, the model in **Scheme 15** is adequate to give the final (equilibrium) concentrations of the different species in the aerogel-BSA system. The measured maximum sorption capacity is 0.96 ± 0.10 μg BSA per 1 μg of silica aerogel in acetate buffer at pH = 4.6, which is reasonable in the case of multilayer sorption of proteins. The sorption capacity is significantly less, 0.52 ± 0.10 μg BSA per 1 μg of silica aerogel in phosphate buffer at pH = 6.4. The difference is due to the alteration of the Zeta potentials of BSA and silica as a function of pH (cf. **Fig. 59**). Both the sorption of BSA and the subsequent aggregation of the aerogel particles is more extensive at pH =4.6 in acetate buffer where the Zeta potential of BSA is close to zero, yet still positive, and that of the aerogel is negative.

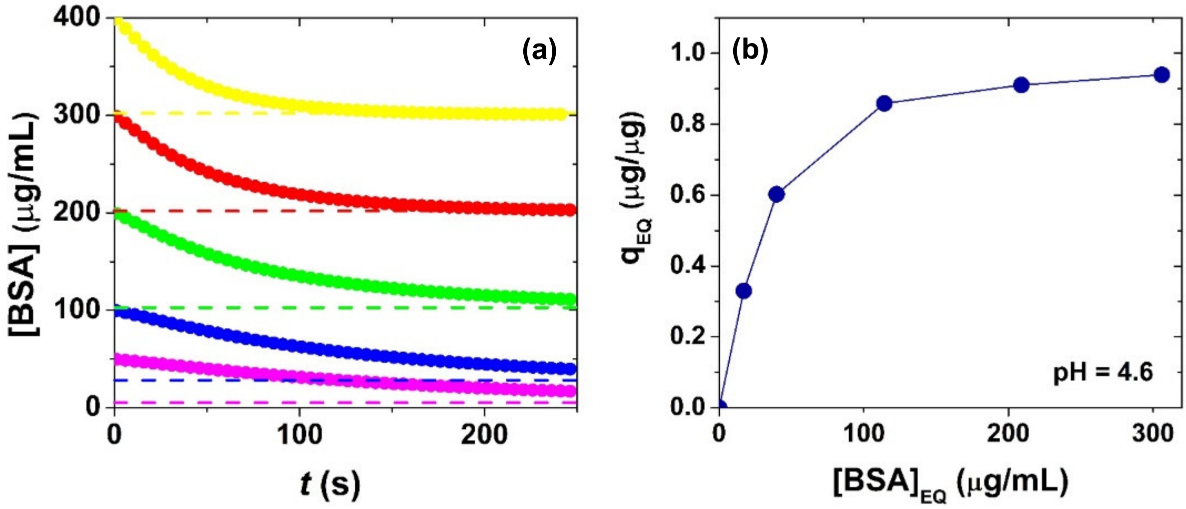

Figure 63. Panel (a): Time dependent concentration of bovine serum albumin ([BSA]) in experiments of different initial BSA concentrations (c_0(BSA) = 50, 100, 200, 300, 400 μg/mL) at pH = 4.6 in acetate buffer. Dotted lines show the final (equilibrium) BSA concentrations. [cf. **Fig. 61**; c_0(aero) = 100 μg/mL; 800 rpm stirring; 25.0 °C]. Panel (b): Sorption isotherm showing the mass of bound BSA per 1 μg of silica aerogel (q_{EQ}) as a function of the equilibrium concentration of aqueous BSA ($[BSA]_{EQ}$) following the completion of the aggregation process.

Importantly, the electrostatic protein–protein repulsion is nearly minimal at pH = 4.6, which results in the high packing density of the protein on the aerogel surface. [190,193] The highly compact structure of BSA under these conditions ensures maximum sorption capacity and the formation of a highly packed protein layer (also termed as corona) on the silica aerogel particles. This BSA layer has an effective charge close to zero, meaning no stabilizing Coulomb repulsion between the covered aerogel particles, which evidently facilitates their aggregation. [190,195]

V-3.4. Reactivities of Cu(II)-cyclen and Cu(II)-cyclam functionalized aerogels [P16, P17]

We realized the covalent immobilization of copper(II) 1,4,7,10-tetraazacyclo-dodecane ($[Cu(II)\text{-cyclen}]^{2+}$) and Cu(II) 1,4,8,11-tetraazacyclotetradecane ($[Cu(II)\text{-cyclam}]^{2+}$) in silica aerogels. These Cu(II)-complexes were chosen because of their high catalytic activities in redox reactions including H_2O_2 activation and biological antioxidant processes. [212,384,385] Both complexes show high thermodynamic stability and kinetic inertness. The half-lives of the dissociations are 0.87 days for $[Cu(II)\text{-cyclen}]^{2+}$ in 2.0 M $HClO_4$ (25°C) and 2.7 days for $[Cu(II)\text{-cyclam}]^{2+}$ in 1.0 M HCl (30°C). [386,387] The functionalized aerogels were thoroughly characterized, and their reactivities were quantitatively compared to those of their aqueous counterparts in two catalytic systems. The alteration of the catalytic activities were accounted for by the complementary structural information on the functionalized aerogels (**Scheme 16**).

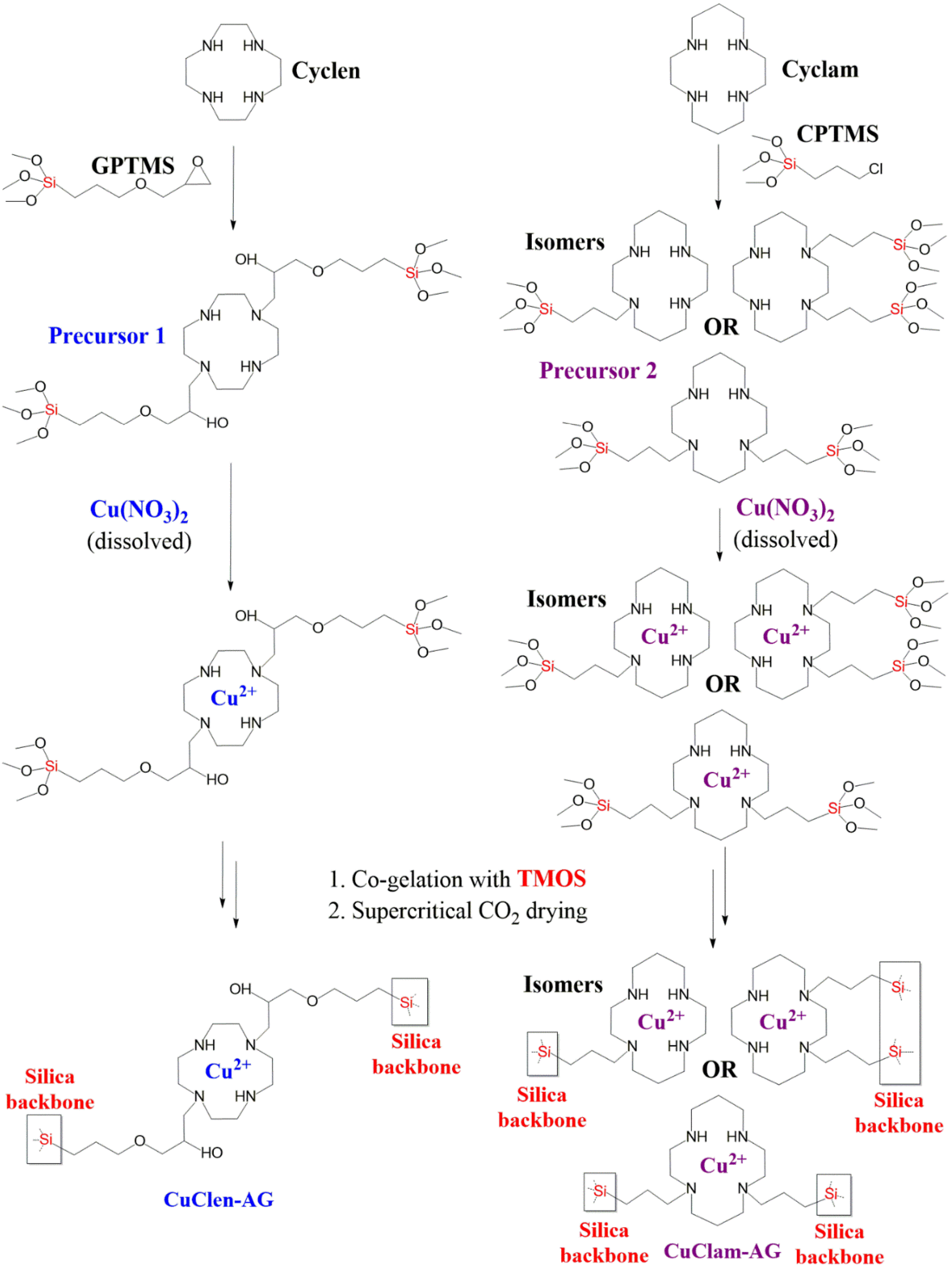

Scheme 16. The preparation steps and the chemical structures of the Cu(II)-cyclen and Cu(II)-cyclam functionalized aerogels based on the combined MS and NMR [^{1}H-NMR, ^{1}H-^{1}H COSY, ^{1}H-^{1}H TOCSY and (^{1}H,^{13}C)-HSQC] characterization of the synthetic precursors. The coordination modes of Cu(II) in the functionalized aerogels were studied by EPR as detailed in the main text. In the case of CuClen-AG, the macrocycle is attached to the silica backbone via two linkers in *trans* position. In the case of the CuClam-AG, the majority of the macrocycle is attached via two linkers in the form the two *cis* position isomers. A minor portion of the cyclam macrocycle can be present in attachment via one linker.

V-3.4.1. Chemical structures and morphologies of functionalized aerogels

The covalent attachment of the macrocyclic ligands to the organosilica moieties were verified before gelation by NMR and MS techniques, and further verified by the FT-IR study of the as-prepared functionalized aerogels (**Scheme 16**).

The copper-contents of the Cu(II)-cyclen containing aerogel (Cu-Clen-AG) is 1.59wt%, and that of the Cu(II)-cyclam containing aerogel (Cu-Clam-AG) is 1.13wt%. No leaching of copper was detected from the functionalized aerogels at basic and neutral pH in 8 h at 37 °C. In slightly acidic buffers, max. 11% of the copper content of CuClen-AG and max. 26% of that of CuClam-AG was released at pH = 4.0 in 8 h at 37 °C. The corresponding UV-Vis spectra of the supernatants clearly show that the liberated Cu(II) species are the respective macrocyclic complexes in both cases, and not free (aqueous) Cu(II).

Contrast variation SANS measurements verified that the immobilized Cu(II)-complexes are distributed evenly in the solid aerogel backbones and do not form nanosized clusters.

Nitrogen-sorption measurements show that CuClam-AG is a typical mesoporous silica aerogel with a high apparent specific surface area and narrow pore size distribution. However, the apparent surface area and cumulative pore volume of CuClen-AG are significantly lower (**Table 19**). The N_2-adsortpion-desorption isotherms and the SEM images are indicative for the presence of a large number of macropores in CuClen-AG. These morphological differences are well-related to the application of different base catalysts for the sol-gel preparation of the different functionalized gels.

Table 19. Structural parameters of CuClen-AG and CuClam-AG estimated by the classical BET and BJH methods from N_2 adsorption-desorption data.

	CuClam-AG	**CuClen-AG**
Specific surface area ($m^2\ g^{-1}$)	874 ± 69	464 ± 33
Pore volume ($cm^3\ g^{-1}$)	3.9 ± 0.4	1.7 ± 0.1
Mean pore size (nm)	43 ± 3	45 ± 2

Electron paramagnetic resonance spectroscopy (EPR) results verify the presence of the expected Cu(II) complexes in both of the as-prepared aerogels. The measured spin-Hamiltonian parameters confirm that the Cu(II) ions are bound to the respective macrocyclic cavities, and the EPR parameters correspond well to those obtained for the original $[Cu(II)\text{-cyclam}]^{2+}$ and $[Cu(II)\text{-cyclen}]^{2+}$ complexes in frozen solution. [388] The EPR spectrum of the as-prepared CuClam-AG supports that the Cu(II) complexes are not close enough to each other to cause an antiferromagnetic coupling. Both the dry powder and the frozen suspension spectra of CuClen-AG suggest that the immobilization of Cu(II)-cyclen in the aerogel leads to the formation of a new Cu(II) complex species next to the complex that is well related to the free Cu(II)-cyclen. In this new complex, most probably one of the nitrogen atoms is not involved in the binding of Cu(II), and replaced by the hydroxyl group of the linker side chain. The same scenario is not operational for the CuClam-AG, thus, it is reasonable to assume that the coordination sphere of Cu(II)-cyclam is not altered upon immobilization.

The Zeta potential of the functionalized aerogel particles is positive in acidic media and close to zero around neutral pH (**Fig. 64A**). The isoelectric points of the functionalized aerogels are at significantly higher pH values than that of the parent silica aerogel (pH ≈ 4) due to the presence of the cationic Cu(II)-complexes. The functionalized aerogels erode in aqueous media similarly to pristine silica aerogels, and yield stable suspensions of microparticles (**Fig. 64B**).

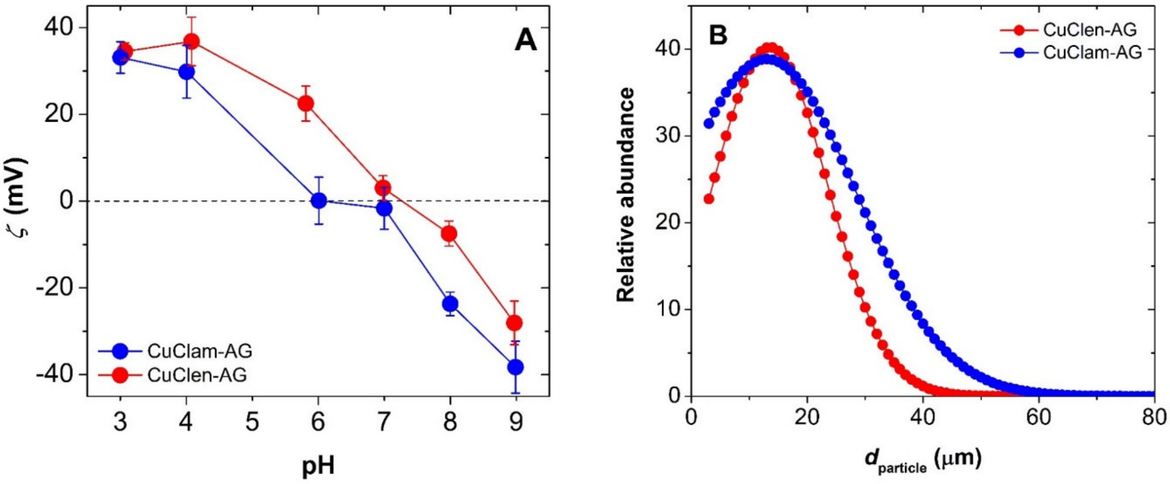

Figure 64. Panel A: The Zeta potentials of the hydrated CuClen-AG (red) and CuClam-AG (blue) microparticles as a function of pH. Panel B: Size distribution of the hydrated aerogel microparticles.

V-3.4.2. Catalytic oxidation of phenol by H_2O_2 in the presence of CuClen-AG

V-3.4.2.1. Reaction intermediates

Phenol was oxidized by H_2O_2 in aqueous media in the presence of either dissolved $[Cu(II)\text{-cyclen}]^{2+}$ or suspended CuClen-AG in an equivalent amount regarding the metal complex. Both the homogeneous and the heterogeneous reactions were followed on-line by UV-vis spectrophotometry (**Fig. 65**), and off-line by capillary electrophoresis (CE). The spectral changes correspond to the depletion of phenol, the concerted formation of multiple UV-vis absorbing reaction intermediates, and finally, the depletion of these intermediates. Four intermediates were identified in both of the reaction systems using CE: 1,2-dihydroxybenzene (*1,2*-DH); 1,4-dihydroxybenzene (*1,4*-DH); 1,2-benzoquinone (*1,2*-BQ) and 1,4-benzoquinone

(*1,4*-BQ). [212] The on-line recorded time resolved UV-vis spectra of the reaction mixtures are also characteristic for these intermediates (**Fig. 65B**).

The pH values of the reaction mixtures change during the reaction due to the formation of dicarboxylic acid products. The starting pH is between 4.4 and 5.6 depending on the initial concentrations of phenol and H_2O_2. The final pH after the oxidation of the DH and BQ intermediates is between 3.1 and 3.3, depending on the conditions of the kinetic experiments.

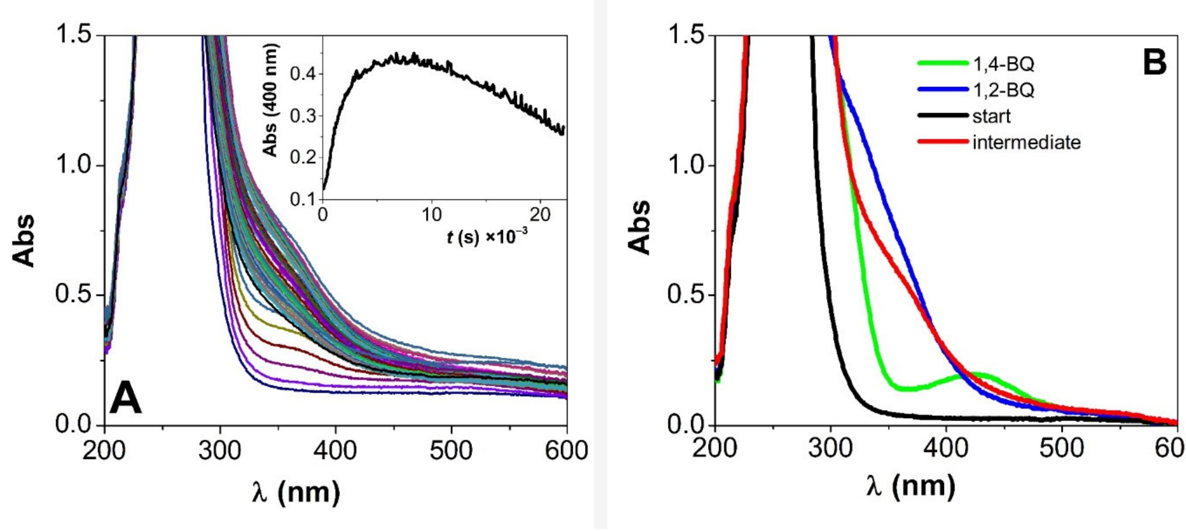

Figure 65. Panel A: Time resolved UV-vis spectra recorded during the oxidation of phenol by H_2O_2 in the presence of CuClen-AG. Inset: kinetic curve at 400 nm (c_0(phenol) = 4.3 mM; $c_0(H_2O_2)$ = 300 mM; $c_{catalyst}$ = 0.027 mM; 70 °C). Panel B: UV-vis spectra of *1,2*-BQ (blue) and *1,4*-BQ (green) superimposed on the baseline corrected spectrum of the mixed reactants (black) and the spectrum of the reaction mixture when the intermediates are present at maximum concentration levels (red).

V-3.4.2.2. Kinetic model

In the heterogeneous experiments, light scattering from the aerogel caused a slight elevation in baseline of the UV-vis spectra. This effect was corrected by the subtraction of the apparent absorbance (extinction) of the aerogel at each reaction time point. [178,217] At 400 nm, only the *1,2*-BQ and *1,4*-BQ intermediates absorb light. Thus, the kinetic curves start at zero absorbance, and return to zero absorbance by the oxidation of these intermediates (**Fig. 66**). A semi-quantitative observation is that the oxidation of phenol, thus the formation of the intermediates are faster when using CuClen-AG, but the subsequent oxidation of these intermediates is significantly faster in the presence of dissolved Cu(II)-cyclen.

The simplest kinetic model found to adequately describe both reaction systems is given in **Scheme 17**. The proposed reaction steps (R13–R24) are the same for the homogeneous and the heterogeneous systems, and all are kinetically second order.

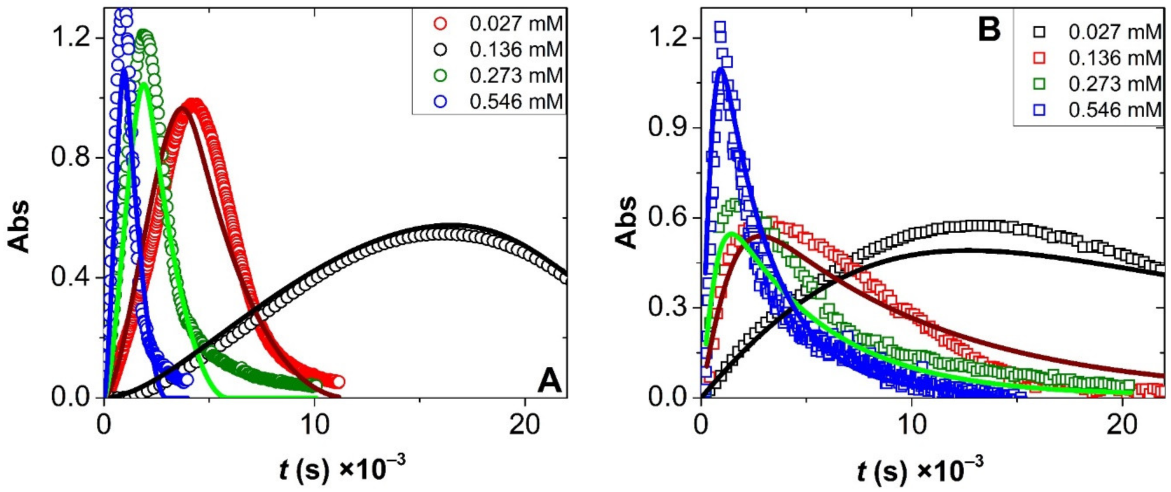

Figure 66. Kinetic curves recorded at different catalyst concentrations in the homogeneous (A) and heterogeneous (B) reactions. Markers: measured data. Lines: results of global fitting using the kinetic model of **Scheme 17**. c_0(phenol) = 4.3 mM; $c_0(H_2O_2)$ = 300 mM; $c_{catalyst}$ = 0.027 – 0.546 mM; 70 °C.

			Heterogeneous	**Homogeneous**
R13	2 CuCat + $H_2O_2 \rightarrow$ 2 CuCat*	$\boldsymbol{k}_{13}$ ($M^{-1}s^{-1}$)	$(7.4 \pm 0.4)\times10^{-2}$	$(2.3 \pm 0.1)\times10^{-2}$
R14	2 CuCat* + $H_2O_2 \rightarrow$ 2 CuCat + O_2	$\boldsymbol{k}_{14}$ ($M^{-1}s^{-1}$)	$< 10^{-5}$	$< 10^{-5}$
R15	CuCat* + Phe → *1,2*-DH + CuCat	$\boldsymbol{k}_{15}$ ($M^{-1}s^{-1}$)	$(1.1 \pm 0.2)\times10^{0}$	$(7.1 \pm 0.7)\times10^{3}$
R16	CuCat* + Phe → *1,4*-DH + CuCat	$\boldsymbol{k}_{16}$ ($M^{-1}s^{-1}$)	$(9.1 \pm 0.3)\times10^{0}$	$(2.6 \pm 0.2)\times10^{4}$
R17	*1,2*-DH +$H_2O_2 \rightarrow$ *1,2*-BQ	$\boldsymbol{k}_{17}$ ($M^{-1}s^{-1}$)	$< 10^{-5}$	
R18	*1,4*-DH + $H_2O_2 \rightarrow$ *1,4*-BQ	$\boldsymbol{k}_{18}$ ($M^{-1}s^{-1}$)	$< 10^{-5}$	
R19	*1,2*-DH + 2 CuCat* → *1,2*-BQ + 2 CuCat	$\boldsymbol{k}_{19}$ ($M^{-1}s^{-1}$)	$> 10^{4}$	$> 10^{4}$
R20	*1,4*-DH + 2 CuCat* → *1,4*-BQ + 2 CuCat	$\boldsymbol{k}_{20}$ ($M^{-1}s^{-1}$)	$< 10^{1}$	$< 10^{1}$
R21	*1,2*-BQ + $H_2O_2 \rightarrow$ $Prod_1$	$\boldsymbol{k}_{21}$ ($M^{-1}s^{-1}$)	$< 10^{-4}$	
R22	*1,4*-BQ + $H_2O_2 \rightarrow$ $Prod_2$	$\boldsymbol{k}_{22}$ ($M^{-1}s^{-1}$)	$< 10^{-5}$	
R23	*1,2*-BQ + 2 CuCat* → $Prod_1$ + 2 CuCat	$\boldsymbol{k}_{23}$ ($M^{-1}s^{-1}$)	$(6.7 \pm 0.2)\times10^{0}$	$(2.0 \pm 0.5)\times10^{3}$
R24	*1,4*-BQ + 2 CuCat* → $Prod_2$ + 2 CuCat	$\boldsymbol{k}_{24}$ ($M^{-1}s^{-1}$)	$> 10^{0}$	$> 10^{3}$

Scheme 17. Kinetic model for the catalytic oxidation of phenol. All reaction steps are second order, and the rate constants are in the unit of M^{-1} s^{-1}. The rate constants were estimated by global data ($c_{catalyst}$ = 0.027 – 0.546 mM; c_0(phenol) = 1.0 – 5.7 mM; $c_0(H_2O_2)$ = 200 – 500 mM). Calculated kinetic curves are shown in **Figs. 66 and 67**. [CuCat: catalyst, CuCat*: activated catalyst, Phe: phenol, Prod: product]

The first step (R13) is the direct reaction of H_2O_2 with Cu(II)-cyclen producing the intermediate CuCat*. Based on previously published studies, we propose that the reactive CuCat* intermediate is a Cu(II)-hydroperoxide complex of Cu(II)-cyclen. [389-391] This elementary reaction step is of key importance in the kinetic model, because this is naturally the first step in the catalytic cycle. Once formed, CuCat* reacts rapidly with phenol, and its stepwise oxidation products. The direct oxidations of these dihydroxybenzenes (R17 and R18) and quinones (R21 and R22) by H_2O_2 are also considered, together with the direct oxidation of H2O2 by CuCat* (R14), as a side reaction. [392] A general nature of multistep reaction systems is that the absolute rate of a reaction step that consumes an intermediate cannot be higher than the rate of the step producing this intermediate, because the concentration of the intermediate would otherwise drop to very small values rapidly halting the reaction. CuCat* is a steady-state intermediate under both heterogeneous and homogeneous conditions, and the rate of Phe degradation is determined by the interplay of several kinetically coupled reaction steps. Therefore, we refrained from using any approximations and applied the approach of global kinetic data fitting and simulation. [393] The differential equations were solved and the kinetic curves were globally fitted using the program package ZiTa. [382] The molar absorbances were determined independently and were fixed during fitting.

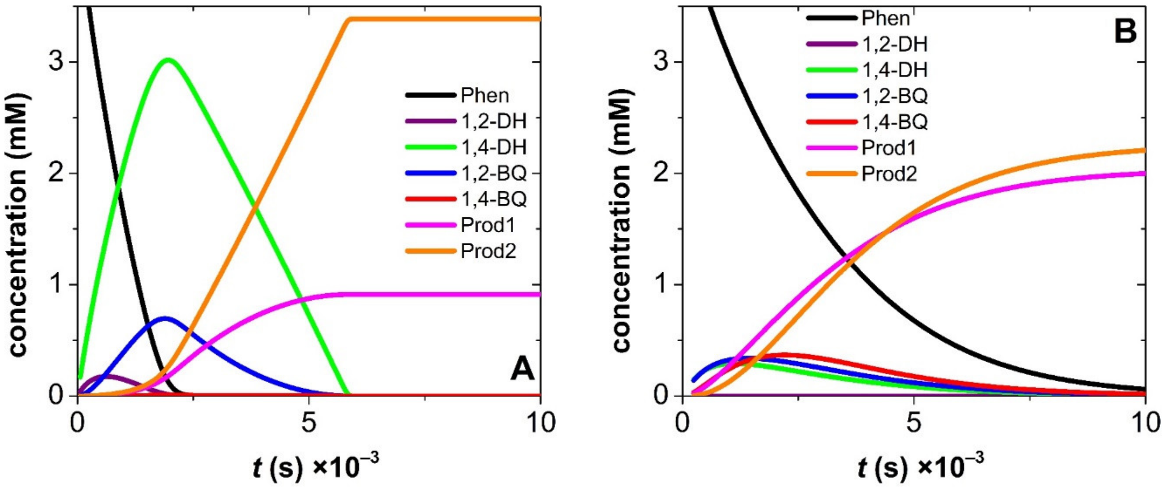

Figure 67. Calculated concentrations of phenol, the intermediates and the oxidation products as function of reaction time using the same initial concentrations of the reactants in the homogeneous (A) and heterogeneous (B) systems. The calculations are based on the results of global fitting using the kinetic model of **Scheme 2**. The experimental and the fitted UV-vis kinetic curves are shown in **Fig. 66** (green markers and lines). c_0(phenol) = 4.3 mM; $c_0(H_2O_2)$ = 300 mM; c_{catalyst} = 0.273 mM; 70 °C.

Satisfactory fitting results were obtained in the selected range of initial concentrations as shown in **Fig. 66**. The estimated rate constants are given in **Scheme 17**, while **Fig. 67** shows the calculated concentration profiles of phenol, the intermediates and the oxidation products as function of reaction time. In general, the oxidation of phenol and the intermediates display very distinctive kinetics in the heterogeneous and the homogeneous systems. Most of the catalytic reactions are faster in the presence of the homogeneous catalyst, but some trends are similar in the rate constants of the analogous reactions. The oxidation of phenol to *1,4*-DH (R16) is significantly faster than the formation of *1,2*-DH (R15) in both the heterogeneous and the homogeneous systems. However, the subsequent oxidation of *1,4*-DH to *1,4*-BQ (R20) is significantly slower than the oxidation of *1,2*-DH to *1,2*-BQ (R19). Finally, the overoxidation of *1,4*-BQ (R24) is faster than that of *1,2*-BQ (R23) in both systems.

Earlier reports indicate that *1,2*-DH could reduce Cu(II) compounds to Cu(I) and induce Fenton-like reactions. [394] We introduced such reaction steps in the kinetic model, but the global fitting was sensitive to these in either reaction systems. The explanation can be that the reductions of Cu(II)-complexes are preferred only under highly acidic solutions. [394]

V-3.4.2.3. Mechanistic considerations

The kinetic properties of the heterogeneous reaction system are the consequence of multiple kinetic and mass transport effects. The mass transport (diffusion) of H_2O_2 is practically unhindered in the pores of silica aerogel, similar to that of water. [127] However, the diffusion of phenol and its oxidation products are assumed to be hindered in the pores, which is reflected in the low rate constants of reactions R15, R16, R23, R24.

Interestingly, the activation of the catalyst in reaction R13 is faster in the case of the CuCy-AG compared to the dissolved Cu-cyclen. One effect can be the separation of the copper centers as shown by SANS and EPR, which might inhibit the unwanted interactions of the catalytic centers. Furthermore, the local concentration of H_2O_2 can be elevated inside the pores, which can also cause the increase of the effective rate constant of the activation. In addition, the EPR studies showed the presence of another Cu(II) species in the aerogel. Here, either the binding of an apical hydroxyl group, or a partially occupied equatorial plane is expected. On the basis of earlier studies, the equatorial plane of the Cu(II) is expected to contain a displaced water molecule. [389,390] This probably provides an easier attack for the H_2O_2 and readily yields the active form of the catalyst, i.e. the Cu(II)-hydroperoxide complex. In contrast, the homogenous system unambiguously possesses one exclusive Cu(II) species, wherein all the four equatorial places of Cu(II) are accommodated by the nitrogen atoms of the cyclen moiety. Consequently, the formation of the active form of the catalyst by H_2O_2 (R13) requires the rearrangement of the coordination sphere, and results in a lower rate of the activation.

V-3.4.3. Superoxide dismutase (SOD) catalytic activities of functionalized aerogels

The SOD activity of the suspended aerogels were tested using the indirect xanthine / xanthine oxidase / NBT assay. Several control experiments were performed. It was confirmed that suspended pristine silica aerogel does not exhibit any SOD activity. The occurrence of side reactions between the reactants and the functionalized aerogels were ruled out. The aerogels do not inhibit the production of the superoxide anion by xanthine oxidase. It was also confirmed that the NBT detector molecule is not reacting with the functionalized aerogels.

The IC50 values that are inversely proportional to SOD activities, were determined by the classical xanthine / xanthine oxidase / NBT assay under different conditions (**Table 20**). The first important observation is that the aqueous [Cu(II)-cyclen]$^{2+}$ complex does not exhibit any SOD activity. Consequently, the SOD activity of the CuClen-AG microparticles certainly arises due to the immobilization of Cu(II)-cyclen. Furthermore, the results clearly demonstrate that the functionalized aerogel microparticles show excellent performance in the dismutation of superoxide anion. This effect is more pronounced at pH 6.45, however, it is important to note that the rate of the non-catalyzed disproportionation of superoxide also increases by decreasing the pH. When benchmarked against several previously reported aqueous Cu(II) complexes and immobilized Cu(II) species, the present aerogels display good performance. [198,395-397]

Table 20. The IC_{50} (μM) values of dissolved and immobilized SOD mimetic systems determined by the classical xanthine / xanthine oxidase / NBT assay.

pH	**pH = 7.60**		**pH = 6.45**
T	**37 °C**	**25 °C**	**37 °C**
[Cu(II)-cyclam]$^{2+}$	0.8 ± 0.1	26.1 ± 0.8	0.42 ± 0.08
[Cu(II)-cyclen]$^{2+}$	N.A.	N.A.	N.A.
CuClam-AG	0.20 ± 0.07	1.7 ± 0.1	0.09 ± 0.01
CuClen-AG	4 ± 1	2.1 ± 0.2	0.61 ± 0.01

V-3.4.3.1. Reactivities of covalently immobilized Cu(II) complexes

The IC_{50} of the CuClam-AG is one order of magnitude smaller than that of dissolved [Cu(II)-cyclam]$^{2+}$, demonstrating a significant increase in the SOD activity due to the covalent immobilization. In order to account for this, several factors have to be considered. First, the chemical surroundings of Cu(II) is different in the aerogel due to the covalent linkers, however, new coordination modes were not detected by EPR. Second, the Cu(II)-cyclam moieties are molecularly dispersed in the highly permeable aerogel skeleton, as shown by SANS and EPR.

This ensures the accessibility of the catalytic sites, while the nanoscale curved pore walls exert a confinement effect. [212,398] Third, on the basis of coordination chemical considerations, immobilization stabilizes the activated form of the complex produced by reacting with superoxide, and inhibits intermolecular side. Finally, the Zeta potential of the CuClam-AG particles is only slightly negative at the pH of the SOD activity experiments, which does not hinder the transport and sorption of superoxide anion.

The increase of the SOD activity as a result of the covalent immobilization is even more profound in the case of CuClen-AG. In this aerogel, the covalent linkers alter the molecular environment of Cu(II). Here, the EPR data unambiguously show that covalent immobilization directly leads to the alteration of the coordination geometry of Cu(II). The logical assumption is that the new species with a somewhat distorted coordination geometry is the catalytically active component in the functionalized aerogel, because the hydrated [Cu(II)-cyclen]$^{2+}$ does not exhibit any SOD activity. [396] Apparently, the noted structural feature is strong enough under the applied conditions to compensate for the slightly negative Zeta potential of the particles.

Consequently, the most important factors responsible for the altered reactivities of the immobilized complexes compared to the aqueous ones are as follows. *i*) The formation of new chemical environments, i.e., new catalytically active complex species due to the covalent immobilization. *ii*) The effective separation of the active Cu(II) centers. *iii*) The confinement effect operative in the nanoporous network.

VI. SUMMARY AND OUTLOOK

In this dissertation, I collected some of the most interesting results we obtained between 2015 and 2025 while investigating the structures and applications of aerogels. Our research interest is driven by the desire to understand the relationships among the chemical structures, nanoscale architectures and physico-chemical properties of this unique family of materials. Aerogels are dry solid gels that display low envelope densities (even below 0.1 g/cm^3) with porosities as high as 99%. Their open nanostructured solid skeleton can have an accessible specific surface area as high as 1300 m^2/g. The size of the characteristic nanoscale structural elements is from a few nanometers to a few hundreds of nanometers. Aerogels can be fabricated from a wide range of materials including, but not limited to inorganic oxides, carbon, metals, biopolymers and synthetic polymers. The wide range of base materials combined with the large variety of unique nanoscale morphologies enable advanced applications, such as superior thermal and electrical insulation and shielding, molecular level separation and purification, stimuli responsive drug delivery, tissue engineering, advanced electrochemistry and catalysis.

First, we explored the intimate mechanism of hydration and the consequent structural changes in silica-gelatin, silica-casein and borosilicate-PVA hybrid aerogels. Implications were put forward for exploiting the tunable hydration properties in oral drug delivery applications. We also gave and explanation to the hydration induced macroscopic changes observed in Ca-alginate and Kevlar aerogels by constructing multi-scale mechanistic models.

Novel drug delivery systems were also developed mainly for oral, local and pulmonary administration. We have shown that our Fe(III)-alginate aerogels are versatile redox-responsive delivery systems. We formulated Ca-alginate into microparticles of limited hydrophilicity that yielded an unprecedentedly high solubilization effect for a very hydrophobic commercial drug. Silica-gelatin aerogels were administered in the form of suspension to cell cultures and into the abdominal cavity of mice to explore their biological response and biodistribution.

Finally, we explored the intimate mechanisms of interfacial processes on aerogels. We constructed mechanistic models for the adsorption of a model dye and a model protein on suspended silica aerogel microparticles. We have shown that macrocyclic Cu(II) complexes display elevated reactivities in selected redox reactions when immobilized in silica aerogel. We have systematically explored the kinetics and the mechanism of these catalytic reactions.

With these results we hope to contribute to the molecular level of structure-property-function relationships in functional aerogels. We have specifically chosen the above detailed aerogel systems, because we believe that these are the closest to be designed systematically and translated to industrial scale standardized manufacturing needed for commercialization.

VII. ÖSSZEFOGLALÁS ÉS KITENKINTÉS

Ebben a disszertációban az aerogélek szerkezetének és alkalmazásainak vizsgálata során elért legérdekesebb eredményeinket gyűjtöttem össze a 2015. és 2025. közötti évekből. Kutatási érdeklődésünket főként az a törekvés vezéreli, hogy megértsük ezen egyedülálló anyagcsalád kémiai szerkezete, nanoszerkezete és a fizikai-kémiai tulajdonsági közötti kapcsolatokat.

Az aerogélek kicsi (akár 0,1 g/cm³ alatti) sűrűségű, 95-98% porozitású szilárd gélek. Nyitott, nanoszerkezetű szilárd vázuk akár 1300 m²/g hozzáférhető fajlagos felületet is biztosít. A jellemző nanoszerkezeti elemek mérete a néhány nanométertől a néhány száz nanométerig terjed. Az aerogélek sokféle szerkezeti anyagból állíthatók elő, beleértve, de nem kizárólagosan a szervetlen oxidokat, a szenet, a fémeket, a biopolimereket és a szintetikus polimereket. Az alapanyagok széles köre és a nanoszerkezeti morfológia sokfélesége fejlett alkalmazásokat tesz lehetővé, mint például kiváló hő- és elektromos szigetelés, molekuláris szintű szeparáció és kinyerés, ingerre reagáló gyógyszeradagolás, szövetpótlás, elektrokémia és katalízis.

Elsőként szilika-zselatin, szilika-kazein és boroszilikát-PVA hibrid aerogélek hidratációjának molekuláris szintű mechanizmusát és az ezzel összefüggő szerkezeti változásokat vizsgáltuk. Javaslatokat tettünk a hibridek összetételével szabályozható hidratációs tulajdonságok kiaknázására orális gyógyszeradagolási alkalmazásokban. Magyarázatot adtunk továbbá a hidratáció hatására megfigyelt makroszkopikus változásokra Ca-alginát és Kevlár aerogélek esetében több méretskálán átívelő mechanisztikus modellek felállításával.

Új gyógyszerhordozó rendszereket fejlesztettünk, elsősorban orális, lokális és pulmonális alkalmazásokra. Redoxi környezetre érzékeny hordozórendszereket fejlesztettünk Fe(III)-alginát aerogélekből. Olyan korlátozottan hidrofil aerogél mikrorészecskéket formuláltunk Ca-alginátból, amelyek példátlanul nagy oldékonyságnövelő hatást eredményeztek egy erősen hidrofób pulmonálisan adagolt gyógyszerhatóanyag esetében. Szilika-zselatin aerogélek biokompatibilitását és biodisztribúcióját vizsgáltuk sejtes kísérletekben és élő állatok segítségével.

Mechanisztikus modelleket dolgoztunk ki egy modellfesték és egy modellfehérje adszorpciójára szuszpendált szilika aerogél mikrorészecskéken. Kimutattuk, hogy egyes makrociklusos Cu(II)-komplexek fokozott reakcióképességet mutatnak bizonyos redoxireakciókban, ha szilika aerogélben immobilizáljuk őket. Részletesen kinetikai modelleket állítottunk fel.

Eredményeinkkel a modern aerogélekre jellemző szerkezet–tulajdonság–funkció összefüggések molekuláris szintű megértéséhez kívánunk főként hozzájárulni. A disszertációmban bemutatott aerogél rendszereket kifejezetten azért választottuk, mert úgy véljük, ezek állnak legközelebb ahhoz, hogy szisztematikusan tervezhetők és ipari méretekben, szabványosított gyártási folyamatok mellett kereskedelmi forgalomba hozhatók legyenek.

PUBLICATIONS COVERED IN THE THESIS

The following is the list of our own publications that are the basis of my present thesis. These publications are referenced in the section titles in the ***Results and Discussion*** chapter.

All the texts and the graphics in the thesis are my own work and were reproduced from my final manuscript drafts before acceptance, copy-editing and publication in a journal.

V-1. Hydration induced structural changes in aerogels

[P1] Veres, Péter ; Kéri, Mónika ; Bányai, István ; Lázár, István ; Fábián, István ; Domingo, Concepción ; Kalmár, József ✉
Mechanism of drug release from silica - gelatin aerogel – Relationship between matrix structure and release kinetics
COLLOIDS AND SURFACES B: BIOINTERFACES 152 pp. 229-237. , 9 p. (2017)

[P2] Kéri, Mónika ; Forgács, Attila ; Papp, Vanda ; Bányai, István ; Veres, Péter ; Len, Adél ; Dudás, Zoltán ; Fábián, István ; Kalmár, József ✉
Gelatin content governs hydration induced structural changes in silica-gelatin hybrid aerogels – Implications in drug delivery
ACTA BIOMATERIALIA 105 pp. 131-145. , 15 p. (2020)

[P3] Lázár, István ; Forgács, Attila ; Horváth, Anita ; Király, Gábor ; Nagy, Gábor ; Len, Adél ; Dudás, Zoltán ; Papp, Vanda ; Balogh, Zoltán ; Moldován, Krisztián ; Juhász, Laura ; Cserháti, Csaba ; Szántó, Zsuzsanna ; Fábián, István ; Kalmár, József ✉
Mechanism of hydration of biocompatible silica-casein aerogels probed by NMR and SANS reveal backbone rigidity
APPLIED SURFACE SCIENCE 531 Paper: 147232 , 13 p. (2020)

[P4] Ecsédi, Bertold ; Forgács, Attila ; Balogh, Zoltán ; Fábián, István ; Kalmár, József ✉
Hydration and wetting mechanism of borosilicate – Polyvinyl alcohol (PVA) hybrid aerogels of potential bioactivity
JOURNAL OF MOLECULAR LIQUIDS 401 Paper: 124605 , 8 p. (2024)

[P5] Forgács, Attila ; Papp, Vanda ; Paul, Geo ; Marchese, Leonardo ; Len, Adél ; Dudás, Zoltán ; Fábián, István ; Gurikov, Pavel ; Kalmár, József ✉
Mechanism of Hydration and Hydration Induced Structural Changes of Calcium Alginate Aerogel
ACS APPLIED MATERIALS & INTERFACES 13 : 2 pp. 2997-3010. , 14 p. (2021)

[P6] Paraskevopoulou, Patrina ✉ ; Raptopoulos, Grigorios ; Len, Adél ; Dudás, Zoltán ; Fábián, István ; Kalmár, József ✉

Fundamental Skeletal Nanostructure of Nanoporous Polymer-Cross-Linked Alginate Aerogels and Its Relevance to Environmental Remediation
ACS APPLIED NANO MATERIALS 4 : 10 pp. 10575-10583. , 9 p. (2021)

[P7] Moldován, Krisztián ; Forgács, Attila ; Paul, Geo ; Marchese, Leonardo ; Len, Adél ; Dudás, Zoltán ; Kéki, Sándor ; Fábián, István ; Kalmár, József ✉
Mechanism of Hydration Induced Stiffening and Subsequent Plasticization of Polyamide Aerogel
ADVANCED MATERIALS INTERFACES 10 : 17 Paper: 202300109 , 15 p. (2023)

V-2. Aerogels as drug delivery systems

[P8] Veres, Péter ; Sebők, Dániel ; Dékány, Imre ; Gurikov, Pavel ; Smirnova, Irina ; Fábián, István ; Kalmár, József ✉
A redox strategy to tailor the release properties of Fe(III)-alginate aerogels for oral drug delivery
CARBOHYDRATE POLYMERS 188 pp. 159-167. , 9 p. (2018)

[P9] Duong, Thoa ; Vivero-Lopez, Maria ; Ardao, Inés ; Alvarez-Lorenzo, Carmen ; Forgács, Attila ; Kalmár, József ✉ ; García-González, Carlos A. ✉
Alginate aerogels by spray gelation for enhanced pulmonary delivery and solubilization of beclomethasone dipropionate
CHEMICAL ENGINEERING JOURNAL 485 Paper: 149849 , 15 p. (2024)

[P10] Veres, Péter ; Király, Gábor ; Nagy, Gábor ; Lázár, István ; Fábián, István ; Kalmár, József ✉
Biocompatible silica-gelatin hybrid aerogels covalently labeled with fluorescein
JOURNAL OF NON-CRYSTALLINE SOLIDS 473 pp. 17-25. , 9 p. (2017)

[P11] Király, Gábor ; Egu, John Chinonso ; Hargitai, Zoltán ; Kovács, Ilona ; Fábián, István ; Kalmár, József ✉ ; Nagy, Gábor
Mesoporous Aerogel Microparticles Injected into the Abdominal Cavity of Mice Accumulate in Parathymic Lymph Nodes
INTERNATIONAL JOURNAL OF MOLECULAR SCIENCES 22 : 18 Paper: 9756 , 14 p. (2021)

[P12] Nagy, Gábor ✉ ; Király, Gábor ; Veres, Péter ; Lázár, István ; Fábián, István ; Bánfalvi, Gáspár ; Juhász, István ; Kalmár, József ✉
Controlled release of methotrexate from functionalized silica-gelatin aerogel microparticles applied against tumor cell growth
INTERNATIONAL JOURNAL OF PHARMACEUTICS 558 pp. 396-403. , 8 p. (2019)

[R1] García-González, Carlos A. ; Sosnik, Alejandro ; Kalmár, József ; De Marco, Iolanda ; Erkey, Can ; Concheiro, Angel ; Alvarez-Lorenzo, Carmen ✉
Aerogels in drug delivery: From design to application [Review Article]
JOURNAL OF CONTROLLED RELEASE 332 pp. 40-63. , 24 p. (2021)

V-3. Mechanisms of interfacial processes in aerogels

[P13] Kalmár, József ✉ ; Kéri, Mónika ; Erdei, Zsolt ; Bányai, István ; Lázár, István ; Lente, Gábor ; Fábián, István
The Pore Network and the Adsorption Characteristics of Mesoporous Silica Aerogel: Adsorption Kinetics on a Timescale of Seconds
RSC ADVANCES 5 : 130 pp. 107237-107246. , 10 p. (2015)

[P14] Kalmár, József ✉ ; Lente, Gábor ; Fábián, István
Kinetics and mechanism of the adsorption of methylene blue from aqueous solution on the surface of a quartz cuvette by on-line UV-Vis spectrophotometry
DYES AND PIGMENTS 127 pp. 170-178. , 9 p. (2016)

[P15] Forgács, Attila ; Ranga, Madalina ; Fábián, István ; Kalmár, József ✉
Interaction of Aqueous Bovine Serum Albumin with Silica Aerogel Microparticles: Sorption Induced Aggregation
INTERNATIONAL JOURNAL OF MOLECULAR SCIENCES 23 : 5 Paper: 2816 , 11 p. (2022)

[P16] Forgács, Attila ; Balogh, Zoltán ; Andrási, Melinda ; Len, Adél ; Dudás, Zoltán ; May, Nóra V ; Herman, Petra ; Juhász, Laura ; Fábián, István ; Lihi, Norbert ✉ ; Kalmár, József ✉
Mechanistic Explanation for Differences Between Catalytic Activities of Dissolved and Aerogel Immobilized Cu(II) Cyclen
APPLIED SURFACE SCIENCE 579 Paper: 152210 , 11 p. (2022)

[P17] Lihi, Norbert ✉ ; Balogh, Zoltán ; Diószegi, Róbert ; Forgács, Attila ; Moldován, Krisztián ; May, Nóra Veronika ; Herman, Petra ; Fábián, István ; Kalmár, József ✉
Functionalizing Aerogels with Tetraazamacrocyclic Copper(II) Complexes: Nanoenzymes with Superoxide Dismutase Activity
APPLIED SURFACE SCIENCE 611 Paper: 155622 , 12 p. (2023)

REFERENCES

[1] N. Hüsing, U. Schubert, Aerogels–Airy Materials: Chemistry, Structure, and Properties, Angew. Chem. Int. Ed. 37(1-2) (1998) 22-45.

[2] T. Taghvaee, S. Donthula, P.M. Rewatkar, H. Majedi Far, C. Sotiriou-Leventis, N. Leventis, K-Index: A Descriptor, Predictor, and Correlator of Complex Nanomorphology to Other Material Properties, ACS Nano 13(3) (2019) 3677-3690.

[3] L. Juhasz, K. Moldovan, P. Gurikov, F. Liebner, I. Fabian, J. Kalmar, C. Cserhati, False Morphology of Aerogels Caused by Gold Coating for SEM Imaging, Polymers 13(4) (2021) 588.

[4] C. Ziegler, A. Wolf, W. Liu, A.K. Herrmann, N. Gaponik, A. Eychmuller, Modern Inorganic Aerogels, Angew. Chem. Int. Ed. 56(43) (2017) 13200-13221.

[5] D. Zambo, A. Schlosser, P. Rusch, F. Lubkemann, J. Koch, H. Pfnur, N.C. Bigall, A Versatile Route to Assemble Semiconductor Nanoparticles into Functional Aerogels by Means of Trivalent Cations, Small 16(16) (2020) e1906934.

[6] P.N. Depta, P. Gurikov, B. Schroeter, A. Forgacs, J. Kalmar, G. Paul, L. Marchese, S. Heinrich, M. Dosta, DEM-Based Approach for the Modeling of Gelation and Its Application to Alginate, J. Chem. Inf. Model. 62(1) (2022) 49-70.

[7] J.M. Gac, B. Nowak, N.H. Borzęcka, Cellular Automata Coupled with Two-Phase Lattice Boltzmann Model for Modeling of Kinetics of Formation and Structure of Silica-Based Sol–Gel Materials, Adv. Eng. Mater. 27(13) (2024) 2400756.

[8] Z. Balogh, M. Tátrai, Z. Dudás, G. Vecsei, C. Cserháti, A. Csík, I. Csarnovics, I. Fábián, J. Kalmár, Morphological features control drug release from nanostructured borosilicate – alginate aerogels and xerogels, Colloids Surfaces A 727 (2025) 138320.

[9] P. Gurikov, S.P. Raman, J.S. Griffin, S.A. Steiner, I. Smimova, Solvent Exchange in the Processing of Biopolymer Aerogels: Current Status and Open Questions, Ind. Eng. Chem. Res. 58(40) (2019) 18590-18600.

[10] I. Lázár, I. Fábián, A Continuous Extraction and Pumpless Supercritical CO2 Drying System for Laboratory-Scale Aerogel Production, Gels 2(4) (2016) 26.

[11] A.E. Lebedev, A.M. Katalevich, N.V. Menshutina, Modeling and scale-up of supercritical fluid processes. Part I: Supercritical drying, J. Supercrit. Fluid. 106 (2015) 122-132.

[12] G. Reichenauer, Structural Characterization of Aerogels, in: M.A. Aegerter, N. Leventis, M. Koebel, S.A. Steiner Iii (Eds.), Springer Handbook of Aerogels, Springer International Publishing, Cham, 2023, pp. 151-195.

[13] J. Landers, G.Y. Gor, A.V. Neimark, Density functional theory methods for characterization of porous materials, Colloid Surface A 437 (2013) 3-32.

[14] M. Thommes, K. Kaneko, A.V. Neimark, J.P. Olivier, F. Rodriguez-Reinoso, J. Rouquerol, K.S.W. Sing, Physisorption of gases, with special reference to the evaluation of surface area and pore size distribution (IUPAC Technical Report), Pure Appl. Chem. 87(9-10) (2015) 1051-1069.

[15] W.J. Malfait, H.P. Ebert, S. Brunner, J. Wernery, S. Galmarini, S. Zhao, G. Reichenauer, The poor reliability of thermal conductivity data in the aerogel literature: a call to action!, J. Sol-Gel Sci. Technol. 109(2) (2024) 569-579.

[16] J. Kröner, D. Platzer, B. Milow, M. Schwan, Electrical conductivity of monolithic and powdered carbon aerogels and their composites, Mater. Adv. 5(20) (2024) 8042-8052.

[17] T. Budtova, T. Lokki, S. Malakooti, A. Rege, H.B. Lu, B. Milow, J. Vapaavuori, S.L. Vivod, Acoustic Properties of Aerogels: Current Status and Prospects, Adv. Eng. Mater. 25(6) (2023) 2201137.

[18] E. Başaran, T. Alp Arıcı, A. Özcan, Ö. Gök, A.S. Özcan, Effects of different parameters on the synthesis of silica aerogel microspheres in supercritical CO2 and their potential use as an adsorbent, J. Sol-Gel Sci. Techn. 89(2) (2019) 458-472.

[19] P. Leroy, N. Devau, A. Revil, M. Bizi, Influence of surface conductivity on the apparent zeta potential of amorphous silica nanoparticles, J. Colloid Interface Sci. 410 (2013) 81-93.

[20] A.C. Pierre, G.M. Pajonk, Chemistry of aerogels and their applications, Chem. Rev. 102(11) (2002) 4243-4265.

[21] C. Scherdel, G. Reichenauer, S. Vidi, E. Wolfrath, Variation of structural properties of silica aerogels over more than one order of magnitude-opportunities, challenges and limits, J. Porous Mater. 31(6) (2024) 2083-2090.

[22] J.L. Gurav, I.K. Jung, H.H. Park, E.S. Kang, D.Y. Nadargi, Silica Aerogel: Synthesis and Applications, J. Nanomater. 2010(1) (2010) 409310.

[23] J.H. Lee, S.J. Park, Recent advances in preparations and applications of carbon aerogels: A review, Carbon 163 (2020) 1-18.

[24] C.Z. Zhu, D. Du, A. Eychmüller, Y.H. Lin, Engineering Ordered and Nonordered Porous Noble Metal Nanostructures: Synthesis, Assembly, and Their Applications in Electrochemistry, Chem. Rev. 115(16) (2015) 8896-8943.

[25] S. Zhao, W.J. Malfait, N. Guerrero-Alburquerque, M.M. Koebel, G. Nystrom, Biopolymer Aerogels and Foams: Chemistry, Properties, and Applications, Angew. Chem. Int. Ed. 57(26) (2018) 7580-7608.

[26] N. Leventis, Polyurea Aerogels: Synthesis, Material Properties, and Applications, Polymers 14(5) (2022) 969.

[27] B. Merillas, C.A. García-González, T.E.G. Álvarez-Arenas, M.A. Rodríguez-Pérez, Towards the Optimization of Polyurethane Aerogel Properties by Densification: Exploring the Structure–Properties Relationship, Small Struct. 5(10) (2024) 2400120.

[28] M.A.B. Meador, S.L. Vivod, B.A. Nguyen, H. Guo, R.P. Viggiano, Aerogels from Engineering Polymers: Polyimide and Polyamide Aerogels, in: M.A. Aegerter, N. Leventis, M. Koebel, S.A. Steiner Iii (Eds.), Springer Handbook of Aerogels, Springer International Publishing, Cham, 2023, pp. 567-594.

[29] V.G. Parale, T. Kim, H. Choi, V.D. Phadtare, R.P. Dhavale, K. Kanamori, H.H. Park, Mechanically Strengthened Aerogels through Multiscale, Multicompositional, and Multidimensional Approaches: A Review, Adv. Mater. 36(18) (2024) e2307772.

[30] R.A. Collins, S. Zhao, J. Wang, J.S. Griffin, S.A. Steiner, The Aerogel Industry, in: M.A. Aegerter, N. Leventis, M. Koebel, S.A. Steiner Iii (Eds.), Springer Handbook of Aerogels, Springer International Publishing, Cham, 2023, pp. 1583-1640.

[31] C.A. Garcia-Gonzalez, A. Sosnik, J. Kalmar, I. De Marco, C. Erkey, A. Concheiro, C. Alvarez-Lorenzo, Aerogels in drug delivery: From design to application, J. Control. Release 332 (2021) 40-63.

[32] Z. Ulker, C. Erkey, An emerging platform for drug delivery: aerogel based systems, J. Control. Release 177 (2014) 51-63.

[33] H. Maleki, L. Duraes, C.A. Garcia-Gonzalez, P. Del Gaudio, A. Portugal, M. Mahmoudi, Synthesis and biomedical applications of aerogels: Possibilities and challenges, Adv. Colloid Interface Sci. 236 (2016) 1-27.

[34] H. Maleki, Recent advances in aerogels for environmental remediation applications: A review, Chem. Eng. J. 300 (2016) 98-118.

[35] H. Maleki, N. Hüsing, Current status, opportunities and challenges in catalytic and photocatalytic applications of aerogels: Environmental protection aspects, Appl. Catal. B 221 (2018) 530-555.

[36] Y.F. Shen, J.B. Yang, Progress in the synthesis of carbon aerogels for advanced energy storage applications, Green Chem. 26(16) (2024) 8969-9004.

[37] P.Z. Gu, L.L. Lu, X. Yang, Z.Y. Hu, X.Y. Zhang, Z.J. Sun, X. Liang, M.X. Liu, Q. Sun, J. Huang, G.Q. Zu, Highly Stretchable Semiconducting Aerogel Films for High-Performance Flexible Electronics, Adv. Funct. Mater. 34(33) (2024) 2400589.

[38] P. Liu, X. Chen, Y. Li, P. Cheng, Z. Tang, J. Lv, W. Aftab, G. Wang, Aerogels Meet Phase Change Materials: Fundamentals, Advances, and Beyond, ACS Nano 16(10) (2022) 15586-15626.

[39] J.M. Sun, T.T. Wu, H. Wu, W. Li, L. Li, S.X. Liu, J. Wang, W.J. Malfait, S.Y. Zhao, Aerogel-based solar-powered water production from atmosphere and ocean: A review, Mat. Sci. Eng. R 154 (2023) 100735.

[40] C.A. García-González, Review and perspectives on the sustainability of organic aerogels, ACS Sus. Chem. Eng. 13(18) (2025) 6469-6492.

[41] I. Turhan Kara, B. Kiyak, N. Colak Gunes, S. Yucel, Life cycle assessment of aerogels: a critical review, J. Sol-Gel Sci. Technol. 111(2) (2024) 618-649.

[42] S. Zhao, G. Siqueira, S. Drdova, D. Norris, C. Ubert, A. Bonnin, S. Galmarini, M. Ganobjak, Z. Pan, S. Brunner, G. Nystrom, J. Wang, M.M. Koebel, W.J. Malfait, Additive manufacturing of silica aerogels, Nature 584(7821) (2020) 387-392.

[43] I. Michaloudis, A.V. Rao, K. Kanamori, Sky-mimesis, a path from nanotechnology to visual arts: A review of art applications of aerogels, Micro Nano Eng. 23 (2024) 100248.

[44] I. Michaloudis, Aer( )sculpture: A Free-Dimensional Space Art, in: M.A. Aegerter, N. Leventis, M. Koebel, S.A. Steiner Iii (Eds.), Springer Handbook of Aerogels, Springer International Publishing, Cham, 2023, pp. 1555-1579.

[45] A. Tzur-Balter, J.M. Young, L.M. Bonanno-Young, E. Segal, Mathematical modeling of drug release from nanostructured porous Si: combining carrier erosion and hindered drug diffusion for predicting release kinetics, Acta Biomater. 9(9) (2013) 8346-53.

[46] D. Palmer, M. Levina, D. Douroumis, M. Maniruzzaman, D.J. Morgan, T.P. Farrell, A.R. Rajabi-Siahboomi, A. Nokhodchi, Mechanism of synergistic interactions and its influence on drug release from extended release matrices manufactured using binary mixtures of polyethylene oxide and sodium carboxymethylcellulose, Colloid. Surface. B 104 (2013) 174-80.

[47] T. Ukmar, U. Maver, O. Planinsek, V. Kaucic, M. Gaberscek, A. Godec, Understanding controlled drug release from mesoporous silicates: theory and experiment, J. Control. Release 155(3) (2011) 409-17.

[48] V. Uskokovic, Mechanism of formation governs the mechanism of release of antibiotics from calcium phosphate nanopowders and cements in a drug-dependent manner, J. Mater. Chem. B 7(25) (2019) 3982-3992.

[49] M.L. Parello, R. Rojas, C.E. Giacomelli, Dissolution kinetics and mechanism of Mg-Al layered double hydroxides: a simple approach to describe drug release in acid media, J. Colloid Interface Sci. 351(1) (2010) 134-9.

[50] T.J. Wooster, S. Acquistapace, C. Mettraux, L. Donato, B.L. Dekkers, Hierarchically structured phase separated biopolymer hydrogels create tailorable delayed burst release during gastrointestinal digestion, J. Colloid Interface Sci. 553 (2019) 308-319.

[51] C.A. Garcia-Gonzalez, A. Sosnik, J. Kalmar, I. De Marco, C. Erkey, A. Concheiro, C. Alvarez-Lorenzo, Aerogels in drug delivery: From design to application, J Control Release 332 (2021) 40-63.

[52] C. Lopez-Iglesias, J. Barros, I. Ardao, F.J. Monteiro, C. Alvarez-Lorenzo, J.L. Gomez-Amoza, C.A. Garcia-Gonzalez, Vancomycin-loaded chitosan aerogel particles for chronic wound applications, Carbohydr. Polym. 204 (2019) 223-231.

[53] T. Budtova, Cellulose II aerogels: a review, Cellulose 26(1) (2019) 81-121.

[54] P. Veres, D. Sebok, I. Dekany, P. Gurikov, I. Smirnova, I. Fabian, J. Kalmar, A redox strategy to tailor the release properties of Fe(III)-alginate aerogels for oral drug delivery, Carbohydr. Polym. 188 (2018) 159-167.

[55] S. Groult, T. Budtova, Tuning structure and properties of pectin aerogels, Eur. Polym. J. 108 (2018) 250-261.

[56] C.A. García-González, C. López-Iglesias, A. Concheiro, C. Alvarez-Lorenzo, Biomedical Applications of Polysaccharide and Protein Based Aerogels, Biobased Aerogels2018, pp. 295-323.

[57] K. Ganesan, T. Budtova, L. Ratke, P. Gurikov, V. Baudron, I. Preibisch, P. Niemeyer, I. Smirnova, B. Milow, Review on the Production of Polysaccharide Aerogel Particles, Materials 11(11) (2018) 2144.

[58] C. Lopez-Iglesias, A.M. Casielles, A. Altay, R. Bettini, C. Alvarez-Lorenzo, C.A. Garcia-Gonzalez, From the printer to the lungs: Inkjet-printed aerogel particles for pulmonary delivery, Chem. Eng. J. 357 (2019) 559-566.

[59] T. Athamneh, A. Amin, E. Benke, R. Ambrus, C.S. Leopold, P. Gurikov, I. Smirnova, Alginate and hybrid alginate-hyaluronic acid aerogel microspheres as potential carrier for pulmonary drug delivery, J. Supercrit. Fluid. 150 (2019) 49-55.

[60] T.A. Esquivel-Castro, M.C. Ibarra-Alonso, J. Oliva, A. Martinez-Luevanos, Porous aerogel and core/shell nanoparticles for controlled drug delivery: A review, Mater. Sci. Eng. C 96 (2019) 915-940.

[61] C.A. García-González, T. Budtova, L. Durães, C. Erkey, P. Del Gaudio, P. Gurikov, M. Koebel, F. Liebner, M. Neagu, I. Smirnova, An Opinion Paper on Aerogels for Biomedical and Environmental Applications, Molecules 24(9) (2019) 1815.

[62] G. Vasvari, J. Kalmar, P. Veres, M. Vecsernyes, I. Bacskay, P. Feher, Z. Ujhelyi, A. Haimhoffer, A. Rusznyak, F. Fenyvesi, J. Varadi, Matrix systems for oral drug delivery: Formulations and drug release, Drug. Discov. Today Technol. 27 (2018) 71-80.

[63] I. Smirnova, P. Gurikov, Aerogel production: Current status, research directions, and future opportunities, J. Supercrit. Fluid. 134 (2018) 228-233.

[64] J. Stergar, U. Maver, Review of aerogel-based materials in biomedical applications, J. Sol-Gel Sci. Technol. 77(3) (2016) 738-752.

[65] S. Zhang, M. Xing, B. Li, Recent advances in musculoskeletal local drug delivery, Acta Biomater. 93 (2019) 135-151.

[66] C. Lopez-Iglesias, J. Barros, I. Ardao, P. Gurikov, F.J. Monteiro, I. Smirnova, C. Alvarez-Lorenzo, C.A. Garcia-Gonzalez, Jet Cutting Technique for the Production of Chitosan Aerogel Microparticles Loaded with Vancomycin, Polymers 12(2) (2020).

[67] S.P. Raman, C. Keil, P. Dieringer, C. Hubner, A. Bueno, P. Gurikov, J. Nissen, M. Holtkamp, U. Karst, H. Haase, I. Smirnova, Alginate aerogels carrying calcium, zinc and silver cations for wound care: Fabrication and metal detection, J. Supercrit. Fluid. 153 (2019) 104545.

[68] H. Maleki, N. Huesing, Silica-silk fibroin hybrid (bio) aerogels: two-step versus one-step hybridization, J. Sol-Gel Sci. Technol. (2019) 1-9.

[69] H. Sugihara, L.S. Taylor, Evaluation of Pazopanib Phase Behavior Following pH-Induced Supersaturation, Mol Pharm 15(4) (2018) 1690-1699.

[70] C. Lopez-Iglesias, J. Barros, I. Ardao, F.J. Monteiro, C. Alvarez-Lorenzo, J.L. Gomez-Amoza, C.A. Garcia-Gonzalez, Vancomycin-loaded chitosan aerogel particles for chronic wound applications, Carbohydr Polym 204 (2019) 223-231.

[71] A.N. Kovacs, N. Varga, A. Juhasz, E. Csapo, Serum protein-hyaluronic acid complex nanocarriers: Structural characterisation and encapsulation possibilities, Carbohydr Polym 251 (2021) 117047.

[72] C. Kleemann, R. Schuster, E. Rosenecker, I. Selmer, I. Smirnova, U. Kulozik, In-vitro-digestion and swelling kinetics of whey protein, egg white protein and sodium caseinate aerogels, Food Hydrocolloid 101 (2020) 105534.

[73] C.A. Bugnone, S. Ronchetti, L. Manna, M. Banchero, An emulsification/internal setting technique for the preparation of coated and uncoated hybrid silica/alginate aerogel beads for controlled drug delivery, J. Supercrit. Fluid. 142 (2018) 1-9.

[74] Z. Ulker, C. Erkey, A novel hybrid material: an inorganic silica aerogel core encapsulated with a tunable organic alginate aerogel layer, RSC Adv. 4(107) (2014) 62362-62366.

[75] M. Alnaief, S. Antonyuk, C.M. Hentzschel, C.S. Leopold, S. Heinrich, I. Smirnova, A novel process for coating of silica aerogel microspheres for controlled drug release applications, Micropor. Mesopor. Mat. 160 (2012) 167-173.

[76] H. Maleki, M.A. Shahbazi, S. Montes, S.H. Hosseini, M.R. Eskandari, S. Zaunschirm, T. Verwanger, S. Mathur, B. Milow, B. Krammer, N. Husing, Mechanically Strong Silica-Silk Fibroin Bioaerogel: A Hybrid Scaffold with Ordered Honeycomb Micromorphology and Multiscale Porosity for Bone Regeneration, ACS Appl. Mater. Interfaces 11(19) (2019) 17256-17269.

[77] L. Goimil, M.E.M. Braga, A.M.A. Dias, J.L. Gomez-Amoza, A. Concheiro, C. Alvarez-Lorenzo, H.C. de Sousa, C.A. García-González, Supercritical processing of starch aerogels and aerogel-loaded poly (ε-caprolactone) scaffolds for sustained release of ketoprofen for bone regeneration, J. CO2 Util. 18 (2017) 237-249.

[78] V.S.S. Goncalves, P. Gurikov, J. Poejo, A.A. Matias, S. Heinrich, C.M.M. Duarte, I. Smirnova, Alginate-based hybrid aerogel microparticles for mucosal drug delivery, Eur. J. Pharm. Biopharm. 107 (2016) 160-170.

[79] S. Zhuo, F. Zhang, J. Yu, X. Zhang, G. Yang, X. Liu, pH-Sensitive Biomaterials for Drug Delivery, Molecules 25(23) (2020) 5649.

[80] C. Nemeth, B. Gyarmati, T. Abdullin, K. Laszlo, A. Szilagyi, Poly(aspartic acid) with adjustable pH-dependent solubility, Acta Biomater 49 (2017) 486-494.

[81] N.Z. Nagy, Z. Varga, J. Mihály, G. Kasza, B. Iván, É. Kiss, Highly efficient encapsulation of curcumin into and pH-controlled drug release from poly (ε-caprolactone) nanoparticles stabilized with a novel amphiphilic hyperbranched polyglycerol, Express Polymer Letters 14(1) (2020) 90-101.

[82] Ž. Knez, Z. Novak, M. Pantić, Incorporation of Drugs and Metals into Aerogels Using Supercritical Fluids, Supercritical and Other High-pressure Solvent Systems2018, pp. 374-394.

[83] P. Gurikov, I. Smirnova, Amorphization of drugs by adsorptive precipitation from supercritical solutions: A review, J. Supercrit. Fluid. 132 (2018) 105-125.

[84] M. Pantic, Z. Knez, Z. Novak, Supercritical impregnation as a feasible technique for entrapment of fat-soluble vitamins into alginate aerogels, J. Non-Cryst. Solids 432 (2016) 519-526.

[85] W. Li-Hong, C. Xin, X. Hui, Z. Li-Li, H. Jing, Z. Mei-Juan, L. Jie, L. Yi, L. Jin-Wen, Z. Wei, C. Gang, A novel strategy to design sustained-release poorly water-soluble drug mesoporous silica microparticles based on supercritical fluid technique, Int. J. Pharm. 454(1) (2013) 135-42.

[86] M. Champeau, J.M. Thomassin, T. Tassaing, C. Jerome, Drug loading of polymer implants by supercritical CO2 assisted impregnation: A review, J. Control. Release 209 (2015) 248-59.

[87] K. Matsuyama, N. Hayashi, M. Yokomizo, T. Kato, K. Ohara, T. Okuyama, Supercritical carbon dioxide-assisted drug loading and release from biocompatible porous metal–organic frameworks, J. Mater. Chem. B 2(43) (2014) 7551-7558.

[88] I. De Marco, E. Reverchon, Starch aerogel loaded with poorly water-soluble vitamins through supercritical CO2 adsorption, Chem. Eng. Res. Des. 119 (2017) 221-230.

[89] Y.F. Wei, L. Zhang, N.N. Wang, P.Y. Shen, H.T. Dou, K. Ma, Y. Gao, J.J. Zhang, S. Qian, Mechanistic Study on Complexation-Induced Dissolution Behavior of Ibuprofen-Nicotinamide Cocrystal, Cryst. Growth. Des. 18(12) (2018) 7343-7355.

[90] M. Fujita, T. Tsuchida, H. Kataoka, C. Tsunoda, K. Moritake, S. Goto, Spring and parachute approach for piroxicam dissolution; its phenomenological model on the thermodynamics of irreversible processes, Int. J. Pharm. 667(Pt A) (2024) 124886.

[91] D. Hirai, Y. Iwao, S.I. Kimura, S. Noguchi, S. Itai, Mathematical model to analyze the dissolution behavior of metastable crystals or amorphous drug accompanied with a solid-liquid interface reaction, Int. J. Pharm. 522(1-2) (2017) 58-65.

[92] J. Siepmann, F. Siepmann, Mathematical modeling of drug delivery, Int. J. Pharm. 364(2) (2008) 328-43.

[93] J. Siepmann, F. Siepmann, Modeling of diffusion controlled drug delivery, J. Control. Release 161(2) (2012) 351-62.

[94] Y. Fu, W.J. Kao, Drug release kinetics and transport mechanisms of non-degradable and degradable polymeric delivery systems, Expert Opin. Drug Deliv. 7(4) (2010) 429-44.

[95] A. Forgacs, V. Papp, G. Paul, L. Marchese, A. Len, Z. Dudas, I. Fabian, P. Gurikov, J. Kalmar, Mechanism of Hydration and Hydration Induced Structural Changes of Calcium Alginate Aerogel, ACS Appl. Mater. Interfaces 13(2) (2021) 2997-3010.

[96] A. Veronovski, Z. Novak, Z. Knez, Synthesis and Use of Organic Biodegradable Aerogels as Drug Carriers, J Biomat Sci-Polym E 23(7) (2012) 873-886.

[97] P. Sriamornsak, N. Thirawong, K. Korkerd, Swelling, erosion and release behavior of alginate-based matrix tablets, Eur J Pharm Biopharm 66(3) (2007) 435-50.

[98] O. Koniev, A. Wagner, Developments and recent advancements in the field of endogenous amino acid selective bond forming reactions for bioconjugation, Chem Soc Rev 44(15) (2015) 5495-551.

[99] J.M. Shin, S.H. Kim, T. Thambi, D.G. You, J. Jeon, J.O. Lee, B.Y. Chung, D.G. Jo, J.H. Park, A hyaluronic acid-methotrexate conjugate for targeted therapy of rheumatoid arthritis, Chem Commun (Camb) 50(57) (2014) 7632-5.

[100] D.C. Wu, C.R. Cammarata, H.J. Park, B.T. Rhodes, C.M. Ofner, 3rd, Preparation, drug release, and cell growth inhibition of a gelatin: doxorubicin conjugate, Pharm Res 30(8) (2013) 2087-96.

[101] G. Choi, T.H. Kim, J.M. Oh, J.H. Choy, Emerging nanomaterials with advanced drug delivery functions; focused on methotrexate delivery, Coordin. Chem. Rev. 359 (2018) 32-51.

[102] Z.A. Khan, R. Tripathi, B. Mishra, Methotrexate: a detailed review on drug delivery and clinical aspects, Expert Opin. Drug Deliv. 9(2) (2012) 151-69.

[103] D. Devineni, C.D. Blanton, J.M. Gallo, Preparation and in vitro evaluation of magnetic microsphere-methotrexate conjugate drug delivery systems, Bioconjug. Chem. 6(2) (1995) 203-210.

[104] R. Narayani, K.P. Rao, Biodegradable microspheres using two different gelatin drug conjugates for the controlled delivery of methotrexate, Int. J. Pharm. 128(1-2) (1996) 261-268.

[105] U.V. Singh, N. Udupa, In vitro characterization of methotrexate loaded poly(lactic-co-glycolic) acid microspheres and antitumor efficacy in Sarcoma-180 mice bearing tumor, Pharm. Acta Helv. 72(3) (1997) 165-173.

[106] K. Affleck, M.J. Embleton, Monoclonal antibody targeting of methotrexate (MTX) against MTX-resistant tumour cell lines, Br. J. Cancer 65(6) (1992) 838-844.

[107] J. Boratynski, A. Opolski, J. Wietrzyk, A. Gorski, C. Radzikowski, Cytotoxic and antitumor effect of fibrinogen-methotrexate conjugate, Cancer Lett. 148(2) (2000) 189-195.

[108] N. Endo, Y. Kato, Y. Takeda, M. Saito, N. Umemoto, K. Kishida, T. Hara, In vitro cytotoxicity of a human serum albumin-mediated conjugate of methotrexate with anti-MM46 monoclonal antibody, Cancer Res. 47(4) (1987) 1076-1080.

[109] F. Hudecz, J.A. Clegg, J. Kajtar, M.J. Embleton, M.V. Pimm, M. Szekerke, R.W. Baldwin, Influence of carrier on biodistribution and in vitro cytotoxicity of methotrexate-branched polypeptide conjugates, Bioconjug. Chem. 4(1) (1993) 25-33.

[110] Z. Wu, A. Shah, N. Patel, X. Yuan, Development of methotrexate proline prodrug to overcome resistance by MDA-MB-231 cells, Bioorg. Med. Chem. Lett. 20(17) (2010) 5108-5112.

[111] R. Narayani, K.P. Rao, Preparation, Characterization and in-Vitro Stability of Hydrophilic Gelatin Microspheres Using a Gelatin-Methotrexate Conjugate, Int. J. Pharm. 95(1-3) (1993) 85-91.

[112] R. Narayani, K.P. Rao, Gelatin microsphere cocktails of different sizes for the controlled release of anticancer drugs, Int. J. Pharm. 143(2) (1996) 255-258.

[113] A. Kosasih, B.J. Bowman, R.J. Wigent, C.M. Ofner, Characterization and in vitro release of methotrexate from gelatin/methotrexate conjugates formed using different preparation variables, Int. J. Pharm. 204(1-2) (2000) 81-89.

[114] C.M. Ofner III, K. Pica, B.J. Bowman, C.S. Chen, Growth inhibition, drug load, and degradation studies of gelatin/methotrexate conjugates, Int. J. Pharm. 308(1-2) (2006) 90-99.

[115] K. Pica, R. Tchao, C.M. Ofner, Gelatin-methotrexate conjugate microspheres as a potential drug delivery system, J. Pharm. Sci. 95(9) (2006) 1896-1908.

[116] J.P. Vareda, C.A. Garcia-Gonzalez, A.J.M. Valente, R. Simon-Vazquez, M. Stipetic, L. Duraes, Insights on toxicity, safe handling and disposal of silica aerogels and amorphous nanoparticles, Environ. Sci. Nano 8(5) (2021) 1177-1195.

[117] N.S. Sani, N.A.N.N. Malek, K. Jemon, M.R.A. Kadir, H. Hamdan, In vitro bioactivity and osteoblast cell viability studies of hydroxyapatite-incorporated silica aerogel, J. Sol-Gel Sci. Techn. 96(1) (2020) 166-177.

[118] D.D. Lovskaya, A.E. Lebedev, N.V. Menshutina, Aerogels as drug delivery systems: In vitro and in vivo evaluations, J. Supercrit. Fluid. 106 (2015) 115-121.

[119] M.A.A. Al-Najjar, T. Athamneh, R. AbuTayeh, I. Basheti, C. Leopold, P. Gurikov, I. Smirnova, Evaluation of the orally administered calcium alginate aerogel on the changes of gut microbiota and hepatic and renal function of Wistar rats, PLoS One 16(4) (2021) e0247633.

[120] F. Sabri, M.E. Sebelik, R. Meacham, J.D. Boughter, Jr., M.J. Challis, N. Leventis, In vivo ultrasonic detection of polyurea crosslinked silica aerogel implants, PLoS One 8(6) (2013) e66348.

[121] T. Asakura, K. Isobe, S. Kametani, O.T. Ukpebor, M.C. Silverstein, G.S. Boutis, Characterization of water in hydrated Bombyx mori silk fibroin fiber and films by (2)H NMR relaxation and (13)C solid state NMR, Acta Biomater. 50 (2017) 322-333.

[122] F. Gallego-Gomez, C. Cadar, C. Lopez, I. Ardelean, Microporosity Quantification via NMR Relaxometry, J. Phys. Chem. C 123(50) (2019) 30486-30491.

[123] Y. Kharbanda, M. Urbanczyk, O. Laitinen, K. Kling, S. Pallaspuro, S. Komulainen, H. Liimatainen, V.V. Telkki, Comprehensive NMR Analysis of Pore Structures in Superabsorbing Cellulose Nanofiber Aerogels, J. Phys. Chem. C 123(51) (2019) 30986-30995.

[124] A. Forgacs, V. Papp, G. Paul, L. Marchese, A. Len, Z. Dudas, I. Fabian, P. Gurikov, J. Kalmar, Mechanism of Hydration and Hydration Induced Structural Changes of Calcium Alginate Aerogel, ACS Appl Mater Interfaces 13(2) (2021) 2997-3010.

[125] I. Lázár, A. Forgács, A. Horváth, G. Király, G. Nagy, A. Len, Z. Dudás, V. Papp, Z. Balogh, K. Moldován, L. Juhász, C. Cserháti, Z. Szántó, I. Fábián, J. Kalmár, Mechanism of hydration of biocompatible silica-casein aerogels probed by NMR and SANS reveal backbone rigidity, Appl. Surf. Sci. 531 (2020) 147232.

[126] P. Veres, M. Keri, I. Banyai, I. Lazar, I. Fabian, C. Domingo, J. Kalmar, Mechanism of drug release from silica-gelatin aerogel-Relationship between matrix structure and release kinetics, Colloid. Surface. B 152 (2017) 229-237.

[127] J. Kalmar, M. Keri, Z. Erdei, I. Banyai, I. Lazar, G. Lente, I. Fabian, The pore network and the adsorption characteristics of mesoporous silica aerogel: adsorption kinetics on a timescale of seconds, RSC Adv. 5(130) (2015) 107237-107246.

[128] M. Kéri, D. Nyul, K. László, L. Novák, I. Bányai, Interaction of resorcinol-formaldehyde carbon aerogels with water: A comprehensive NMR study, Carbon 189 (2022) 57-70.

[129] M. Kéri, A. Forgács, V. Papp, I. Bányai, P. Veres, A. Len, Z. Dudás, I. Fábián, J. Kalmár, Gelatin content governs hydration induced structural changes in silica-gelatin hybrid aerogels– Implications in drug delivery, Acta Biomater. 105 (2020) 131-145.

[130] J.E. Mangold, C.M. Park, H.M. Liljestrand, L.E. Katz, Surface complexation modeling of Hg(II) adsorption at the goethite/water interface using the charge distribution multi-site complexation (CD-MUSIC) model, J. Colloid Interface Sci. 418 (2014) 147-161.

[131] C.S. Johnson Jr, Diffusion ordered nuclear magnetic resonance spectroscopy: principles and applications, Prog. Nucl. Magn. Res. Spect. 34(3-4) (1999) 203-256.

[132] P.J. Barrie, Characterization of porous media using NMR methods, Annu. Rep. NMR Spectro. 41 (2000) 265-316.

[133] O.V. Petrov, I. Furo, NMR cryoporometry: Principles, applications and potential, Prog. Nucl. Magn. Res. Spect. 54(2) (2009) 97-122.

[134] J.B.W. Webber, Studies of nano-structured liquids in confined geometries and at surfaces, Prog. Nucl. Magn. Reson. Spectrosc. 56(1) (2010) 78-93.

[135] S.G. Allen, P.C.L. Stephenson, J.H. Strange, Morphology of porous media studied by nuclear magnetic resonance, J. Chem. Phys. 106(18) (1997) 7802-7809.

[136] I. Bardenhagen, W. Dreher, D. Fenske, A. Wittstock, M. Bäumer, Fluid distribution and pore wettability of monolithic carbon xerogels measured by 1H NMR relaxation, Carbon 68 (2014) 542-552.

[137] M. Simina, R. Nechifor, I. Ardelean, Saturation-dependent nuclear magnetic resonance relaxation of fluids confined inside porous media with micrometer-sized pores, Magn. Reson. Chem. 49(6) (2011) 314-9.

[138] P.J. Barrie, Characterization of porous media using NMR methods, Annu. Rep. NMR Spectr. 41 (2000) 265-316.

[139] B. Maillet, R. Sidi-Boulenouar, P. Coussot, Dynamic NMR Relaxometry as a Simple Tool for Measuring Liquid Transfers and Characterizing Surface and Structure Evolution in Porous Media, Langmuir 38(49) (2022) 15009-15025.

[140] J.R. Zimmerman, W.E. Brittin, Nuclear magnetic resonance studies in multiple phase systems: lifetime of a water molecule in an adsorbing phase on silica gel, J. Phys. Chem. 61(10) (1957) 1328-1333.

[141] P.S. Belton, B.P. Hills, E.R. Raimbaud, The effects of morphology and exchange on proton N.M.R. relaxation in agarose gels, Molecular Physics 63(5) (2006) 825-842.

[142] F. Gallego-Gómez, C. Cadar, C. López, I. Ardelean, Imbibition and dewetting of silica colloidal crystals: An NMR relaxometry study, J. Colloid Interface Sci. 561 (2020) 741-748.

[143] C. Schlumberger, L. Sandner, A. Michalowski, M. Thommes, Reliable Surface Area Assessment of Wet and Dry Nonporous and Nanoporous Particles: Nuclear Magnetic Resonance Relaxometry and Gas Physisorption, Langmuir 39(13) (2023) 4611-4621.

[144] U. Baig, M. Faizan, M.A. Dastageer, Polyimide based super-wettable membranes/materials for high performance oil/water mixture and emulsion separation: A review, Adv. Colloid Interface Sci. 297 (2021) 102525.

[145] G. Vigil, Z. Xu, S. Steinberg, J. Israelachvili, Interactions of Silica Surfaces, J. Colloid Interface Sci. 165(2) (1994) 367-385.

[146] S.G. Allen, P.C.L. Stephenson, J.H. Strange, Internal surfaces of porous media studied by nuclear magnetic resonance cryoporometry, J. Chem. Phys. 108(19) (1998) 8195-8198.

[147] N. Gopinathan, B. Yang, J.P. Lowe, K.J. Edler, S.P. Rigby, NMR cryoporometry characterisation studies of the relation between drug release profile and pore structural evolution of polymeric nanoparticles, Int. J. Pharm. 469(1) (2014) 146-58.

[148] V.M. Gun'ko, V.V. Turov, R. Leboda, V.I. Zarko, J. Skubiszewska-Zieba, B. Charmas, Comparative analysis of heterogeneous solid and soft materials by adsorption, NMR and thermally stimulated depolarisation current methods, Appl. Surf. Sci. 253(13) (2007) 5640-5644.

[149] T.J. Rottreau, G.E. Parkes, M. Schirru, J.L. Harries, M.G. Mesa, P.D. Topham, R. Evans, NMR cryoporometry of polymers: Cross-linking, porosity and the importance of probe liquid, Colloid. Surface. A 575 (2019) 256-263.

[150] J.C. Dore, J.B.W. Webber, J.H. Strange, Characterisation of porous solids using small-angle scattering and NMR cryoporometry, Colloid. Surface. A 241(1-3) (2004) 191-200.

[151] V.M. Gun'ko, V.V. Turov, E.M. Pakhlov, T.V. Krupska, B. Charmas, Effect of water content on the characteristics of hydro-compacted nanosilica, Appl. Surf. Sci. 459 (2018) 171-178.

[152] T.J. Rottreau, C.M.A. Parlett, A.F. Lee, R. Evans, Diffusion NMR Characterization of Catalytic Silica Supports: A Tortuous Path, J. Phys. Chem. C 121(30) (2017) 16250-16256.

[153] D. Benjamini, J.J. Elsner, M. Zilberman, U. Nevo, Pore size distribution of bioresorbable films using a 3-D diffusion NMR method, Acta Biomater. 10(6) (2014) 2762-8.

[154] J. Götz, R. Hinrichs, Diffusion and relaxation in gels, Modern magnetic resonance, Springer2008, pp. 1713-1719.

[155] Y. Cohen, L. Avram, L. Frish, Diffusion NMR spectroscopy in supramolecular and combinatorial chemistry: an old parameter--new insights, Angew. Chem. Int. Ed. 44(4) (2005) 520-54.

[156] C.H. Cho, Y.S. Hong, K. Kang, V.I. Volkov, V. Skirda, C.Y. Lee, C.H. Lee, Water self-diffusion in Chlorella sp. studied by pulse field gradient NMR, Magn. Reson. Imaging 21(9) (2003) 1009-17.

[157] R. Valiullin, V. Skirda, Time dependent self-diffusion coefficient of molecules in porous media, J. Chem. Phys. 114(1) (2001) 452-458.

[158] M. Keri, Z. Nagy, L. Novak, E. Szarvas, L.P. Balogh, I. Banyai, Beware of phosphate: evidence of specific dendrimer-phosphate interactions, Phys. Chem. Chem. Phys. 19(18) (2017) 11540-11548.

[159] M. Keri, C. Peng, X. Shi, I. Banyai, NMR characterization of PAMAM_G5.NH2 entrapped atomic and molecular assemblies, J. Phys. Chem. B 119(7) (2015) 3312-9.

[160] G. Mollica, F. Ziarelli, S. Lack, F. Brunel, S. Viel, Characterization of insoluble calcium alginates by solid-state NMR, Carbohydr. Polym. 87(1) (2012) 383-391.

[161] G. Paul, C. Bisio, I. Braschi, M. Cossi, G. Gatti, E. Gianotti, L. Marchese, Combined solid-state NMR, FT-IR and computational studies on layered and porous materials, Chemical Society Reviews 47(15) (2018) 5684-5739.

[162] T. Salomonsen, H.M. Jensen, F.H. Larsen, S. Steuernagel, S.B. Engelsen, Alginate monomer composition studied by solution- and solid-state NMR – A comparative chemometric study, Food Hydrocoll. 23(6) (2009) 1579-1586.

[163] D.M. Sperger, S. Fu, L.H. Block, E.J. Munson, Analysis of composition, molecular weight, and water content variations in sodium alginate using solid-state NMR spectroscopy, J. Pharm. Sci. 100(8) (2011) 3441-3452.

[164] H. Maleki, S. Montes, N. Hayati-Roodbari, F. Putz, N. Huesing, Compressible, Thermally Insulating, and Fire Retardant Aerogels through Self-Assembling Silk Fibroin Biopolymers Inside a Silica Structure-An Approach towards 3D Printing of Aerogels, ACS Appl. Mater. Interfaces 10(26) (2018) 22718-22730.

[165] M. Diener, J. Adamcik, A. Sanchez-Ferrer, F. Jaedig, L. Schefer, R. Mezzenga, Primary, Secondary, Tertiary and Quaternary Structure Levels in Linear Polysaccharides: From Random Coil, to Single Helix to Supramolecular Assembly, Biomacromolecules 20(4) (2019) 1731-1739.

[166] L. Almásy, New Measurement Control Software on the Yellow Submarine SANS Instrument at the Budapest Neutron Centre, J. Surf. Investig. 15(3) (2021) 527-531.

[167] C.I. Merzbacher, J.G. Barker, K.E. Swider, D.R. Rolison, Effect of re-wetting on silica aerogel structure: a SANS study, J. Non-Cryst. Solids 224(1) (1998) 92-96.

[168] G. Beaucage, Approximations leading to a unified exponential power-law approach to small-angle scattering, J. Appl. Crystallogr. 28(6) (1995) 717-728.

[169] S.M. King, Small-angle Neutron Scattering (in Modern techniques for polymer characterisation), John Wiley & Sons Ltd1999.

[170] H. Porritt, A. Chalard, J. Fitremann, J. Mata, J. Malmstrom, Small and ultra small angle neutron scattering on pure and supramolecular composite GelMA hydrogels, J. Colloid Interface Sci. 700(Pt 2) (2025) 138443.

[171] A. Fanova, K. Sotiropoulos, A. Radulescu, A. Papagiannopoulos, Advances in Small Angle Neutron Scattering on Polysaccharide Materials, Polymers 16(4) (2024) 490.

[172] Z. Balogh, J. Kalmár, C.J. Gommes, Wetting of alginate aerogels, from mesoporous solids to hydrogels: a small-angle scattering analysis, J. Appl. Crystallogr. 57(2) (2024) 369-379.

[173] B. Hammouda, Analysis of the Beaucage model, J. Appl. Crystallogr. 43(6) (2010) 1474-1478.

[174] J.T. Hu, D.L. Yang, Q. Kang, D.Z. Shen, Estimation the kinetics parameters for non-specific adsorption of fibrinogen on quartz surface from the response of an electrode-separated piezoelectric sensor, Sensor Actuat B-Chem 96(1-2) (2003) 390-398.

[175] C. Tamerler, E.E. Oren, M. Duman, E. Venkatasubramanian, M. Sarikaya, Adsorption kinetics of an engineered gold binding Peptide by surface plasmon resonance spectroscopy and a quartz crystal microbalance, Langmuir 22(18) (2006) 7712-8.

[176] F. Lacour, R. Torresi, C. Gabrielli, A. Caprani, Comparison of the Quartz-Crystal Microbalance and the Double-Layer Capacitance Methods for Measuring the Kinetics of the Adsorption of Bovine Serum-Albumin onto a Gold Electrode, J Electrochem Soc 139(6) (1992) 1619-1622.

[177] A.L. Mifflin, K.A. Gerth, F.M. Geiger, Kinetics of chromate adsorption and desorption at fused quartz/water interfaces studied by second harmonic generation, J Phys Chem A 107(45) (2003) 9620-9627.

[178] H. Liu, J.Y. Zhu, X.S. Chai, In situ, rapid, and temporally resolved measurements of cellulase adsorption onto lignocellulosic substrates by UV-vis spectrophotometry, Langmuir 27(1) (2011) 272-8.

[179] Q.Q. Wang, J.Y. Zhu, C.G. Hunt, H.Y. Zhan, Kinetics of adsorption, desorption, and re-adsorption of a commercial endoglucanase in lignocellulosic suspensions, Biotechnol. Bioeng. 109(8) (2012) 1965-75.

[180] D.A. Higgins, S.K. Byerly, M.B. Abrams, R.M. Corn, Second harmonic generation studies of methylene blue orientation at silica surfaces, J. Phys. Chem. 95(18) (1991) 6984-6990.

[181] K. Tsunoda, T. Umemura, H. Ueno, E. Okuno, H. Akaiwa, Adsorption of methylene blue onto silylated silica surfaces, studied using visible attenuated total reflection spectroscopy with a slab optical waveguide, Appl. Spectrosc. 57(10) (2003) 1273-7.

[182] S. Chakrabarti, B.K. Dutta, On the adsorption and diffusion of Methylene Blue in glass fibers, J. Colloid Interface Sci. 286(2) (2005) 807-11.

[183] B.J.C. Deboux, E. Lewis, P.J. Scully, R. Edwards, A Novel Technique for Optical-Fiber Ph Sensing Based on Methylene-Blue Adsorption, J. Lightwave Technol. 13(7) (1995) 1407-1414.

[184] K. Bergmann, C.T. O'konski, A spectroscopic study of methylene blue monomer, dimer, and complexes with montmorillonite, J. Phys. Chem. 67(10) (1963) 2169-2177.

[185] T. Peters, 2 - The Albumin Molecule: Its Structure and Chemical Properties, in: T. Peters (Ed.), All About Albumin, Academic Press, San Diego, 1995, pp. 9-75.

[186] R. Li, Z. Wu, Y. Wangb, L. Ding, Y. Wang, Role of pH-induced structural change in protein aggregation in foam fractionation of bovine serum albumin, Biotechnol. Rep. 9 (2016) 46-52.

[187] E. Csapo, A. Juhasz, N. Varga, D. Sebok, V. Hornok, L. Janovak, I. Dekany, Thermodynamic and kinetic characterization of pH-dependent interactions between bovine serum albumin and ibuprofen in 2D and 3D systems, Colloid. Surface. A 504 (2016) 471-478.

[188] K. Kubiak-Ossowska, K. Tokarczyk, B. Jachimska, P.A. Mulheran, Bovine Serum Albumin Adsorption at a Silica Surface Explored by Simulation and Experiment, J. Phys. Chem. B 121(16) (2017) 3975-3986.

[189] J.R. Sharpe, R.L. Sammons, P.M. Marquis, Effect of pH on protein adsorption to hydroxyapatite and tricalcium phosphate ceramics, Biomaterials 18(6) (1997) 471-476.

[190] M. Wiśniewska, K. Szewczuk-Karpisz, D. Sternik, Adsorption and thermal properties of the bovine serum albumin–silicon dioxide system, J. Therm. Anal. Calorim. 120(2) (2015) 1355-1364.

[191] J.J. Ramsden, J.E. Prenosil, Effect of Ionic-Strength on Protein Adsorption-Kinetics, J. Phys. Chem. 98(20) (1994) 5376-5381.

[192] J. Mcguire, M.C. Wahlgren, T. Arnebrant, Structural Stability Effects on the Adsorption and Dodecyltrimethylammonium Bromide-Mediated Elutability of Bacteriophage-T4 Lysozyme at Silica Surfaces, J. Colloid Interf. Sci. 170(1) (1995) 182-192.

[193] M. Rabe, D. Verdes, S. Seeger, Understanding protein adsorption phenomena at solid surfaces, Adv. Colloid Interface Sci. 162(1-2) (2011) 87-106.

[194] P. Schaaf, J.C. Voegel, B. Senger, From random sequential adsorption to ballistic deposition: A general view of irreversible deposition processes, J. Phys. Chem. B 104(10) (2000) 2204-2214.

[195] F. Felsovalyi, P. Mangiagalli, C. Bureau, S.K. Kumar, S. Banta, Reversibility of the adsorption of lysozyme on silica, Langmuir 27(19) (2011) 11873-82.

[196] S. Nath, C.S. Patrickios, T.A. Hatton, Turbidimetric Titration Study of the Interaction of Proteins with Acrylic Polyampholytes, Biotechnol. Progr. 11(1) (1995) 99-103.

[197] C.-H. Lee, H.-C. Lin, S.-H. Cheng, T.-S. Lin, C.-Y. Mou, Hydroxo-Bridged Dinuclear Cupric Complexes Encapsulated in Various Mesoporous Silicas to Mimic the Catalytic Activity of Catechol Oxidases: Reactivity and Selectivity Study, J. Phys. Chem. C 113(36) (2009) 16058-16069.

[198] Y.-C. Fang, H.-C. Lin, I.J. Hsu, T.-S. Lin, C.-Y. Mou, Bioinspired Design of a Cu–Zn–Imidazolate Mesoporous Silica Catalyst System for Superoxide Dismutation, J. Phys. Chem. C 115(42) (2011) 20639-20652.

[199] E.G. Derouane, Shape Selectivity in Catalysis by Zeolites - the Nest Effect, J. Catal. 100(2) (1986) 541-544.

[200] E.G. Derouane, J.M. Andre, A.A. Lucas, Surface Curvature Effects in Physisorption and Catalysis by Microporous Solids and Molecular-Sieves, J. Catal. 110(1) (1988) 58-73.

[201] V. Mouarrawis, R. Plessius, J.I. van der Vlugt, J.N.H. Reek, Confinement Effects in Catalysis Using Well-Defined Materials and Cages, Front. Chem. 6 (2018) 623.

[202] P. Veres, A.M. Lopez-Periago, I. Lazar, J. Saurina, C. Domingo, Hybrid aerogel preparations as drug delivery matrices for low water-solubility drugs, Int. J. Pharm. 496(2) (2015) 360-70.

[203] J. Lu, M. Liong, Z. Li, J.I. Zink, F. Tamanoi, Biocompatibility, biodistribution, and drug-delivery efficiency of mesoporous silica nanoparticles for cancer therapy in animals, Small 6(16) (2010) 1794-805.

[204] E. Hummert, U. Henniges, A. Potthast, Fluorescence labeling of gelatin and methylcellulose: monitoring their penetration behavior into paper, Cellulose 20(2) (2013) 919-931.

[205] P. Veres, A.M. Lopez-Periago, I. Lazar, J. Saurina, C. Domingo, Hybrid aerogel preparations as drug delivery matrices for low water-solubility drugs, Int. J. Pharm. 496(2) (2015) 360-370.

[206] P. Veres, G. Kiraly, G. Nagy, I. Lazar, I. Fabian, J. Kalmar, Biocompatible silica-gelatin hybrid aerogels covalently labeled with fluorescein, J. Non-Cryst. Solids 473 (2017) 17-25.

[207] Z. Balogh, A. Len, V. Baksa, A. Krajnc, P. Herman, G. Szemán-Nagy, Z. Czigány, I. Fábián, J. Kalmár, Z. Dudás, Nanoscale structural characteristics and in vitro bioactivity of borosilicate – polyvinyl alcohol (PVA) hybrid aerogels for bone regeneration, ACS Appl. Nano Mater. 7(4) (2024) 4092-4102.

[208] I. Preibisch, P. Niemeyer, Y. Yusufoglu, P. Gurikov, B. Milow, I. Smirnova, Polysaccharide-Based Aerogel Bead Production via Jet Cutting Method, Materials 11(8) (2018) 1287.

[209] P. Paraskevopoulou, I. Smirnova, T. Athamneh, M. Papastergiou, D. Chriti, G. Mali, T. Cendak, G. Raptopoulos, P. Gurikov, Polyurea-crosslinked biopolymer aerogel beads, RSC Adv. 10(67) (2020) 40843-40852.

[210] G. Raptopoulos, M. Papastergiou, D. Chriti, E. Effraimopoulou, T. Cendax, N. Samartzis, G. Mali, T. Ioannides, P. Gurikov, I. Smirnova, P. Paraskevopoulou, Metal-doped carbons from polyurea-crosslinked alginate aerogel beads†, Mater. Adv. 2(8) (2021) 2684-2699.

[211] J.C. Williams, B.N. Nguyen, L. McCorkle, D. Scheiman, J.S. Griffin, S.A. Steiner, M.A. Meador, Highly Porous, Rigid-Rod Polyamide Aerogels with Superior Mechanical Properties and Unusually High Thermal Conductivity, ACS Appl. Mater. Interfaces 9(2) (2017) 1801-1809.

[212] H.F. Bereczki, L. Darózi, I. Fábián, I. Lázár, Sol-gel synthesis, characterization and catalytic activity of silica aerogels functionalized with copper(II) complexes of cyclen and cyclam, Micropor. Mesopor. Mat. 234 (2016) 392-400.

[213] L.B. Rockland, Saturated Salt Solutions for Static Control of Relative Humidity between 5° and 40° C, Anal. Chem. 32(10) (1960) 1375-1376.

[214] C. Ammann, P. Meier, A. Merbach, A simple multinuclear NMR thermometer, J. Magn. Reson. 46(2) (1982) 319-321.

[215] D.H. Wu, A.D. Chen, C.S. Johnson, An Improved Diffusion-Ordered Spectroscopy Experiment Incorporating Bipolar-Gradient Pulses, J. Magn. Reson. Ser. A 115(2) (1995) 260-264.

[216] G. Paul, C. Bisio, I. Braschi, M. Cossi, G. Gatti, E. Gianotti, L. Marchese, Combined solid-state NMR, FT-IR and computational studies on layered and porous materials, Chem. Soc. Rev. 47(15) (2018) 5684-5739.

[217] Q.Q. Wang, J.Y. Zhu, C.G. Hunt, H.Y. Zhan, Kinetics of adsorption, desorption, and re-adsorption of a commercial endoglucanase in lignocellulosic suspensions, Biotechnol. Bioeng. 109(8) (2012) 1965-75.

[218] A. Gurikov, A. Kolnoochenko, M. Golubchikov, N. Menshutina, I. Smirnova, A synchronous cellular automaton model of mass transport in porous media, Comput. Chem. Eng. 84 (2016) 446-457.

[219] R. Mellaerts, E.J. Fayad, G. Van den Mooter, P. Augustijns, M. Rivallan, F. Thibault-Starzyk, J.A. Martens, In situ FT-IR investigation of etravirine speciation in pores of SBA-15 ordered mesoporous silica material upon contact with water, Mol. Pharm. 10(2) (2013) 567-73.

[220] C.J. Gommes, A.P. Roberts, Stochastic analysis of capillary condensation in disordered mesopores, Phys. Chem. Chem. Phys. 20(19) (2018) 13646-13659.

[221] P.W. Schmidt, Small-Angle Scattering Studies of Disordered, Porous and Fractal Systems, J. Appl. Crystallogr. 24(5) (1991) 414-435.

[222] J. Zaloga, A. Feoktystov, V.M. Garamus, W. Karawacka, A. Ioffe, T. Bruckel, R. Tietze, C. Alexiou, S. Lyer, Studies on the adsorption and desorption of mitoxantrone to lauric acid/albumin coated iron oxide nanoparticles, Colloid. Surface. B 161 (2018) 18-26.

[223] G.V. Franks, Zeta potentials and yield stresses of silica suspensions in concentrated monovalent electrolytes: isoelectric point shift and additional attraction, J. Colloid Interface Sci. 249(1) (2002) 44-51.

[224] D.J. Burgess, J.E. Carless, Microelectrophoretic Studies of Gelatin and Acacia for the Prediction of Complex Coacervation, J. Colloid Interface Sci. 98(1) (1984) 1-8.

[225] M. Vorob'ev, Bound water measurements for aqueous protein solutions and food gels, Colloid. Surface. B 31(1-4) (2003) 133-140.

[226] D. Noferini, A. Faraone, M. Rossi, E. Mamontov, E. Fratini, P. Baglioni, Disentangling Polymer Network and Hydration Water Dynamics in Polyhydroxyethyl Methacrylate Physical and Chemical Hydrogels, J. Phys. Chem. C 123(31) (2019) 19183-19194.

[227] M. Holz, S.R. Heil, A. Sacco, Temperature-dependent self-diffusion coefficients of water and six selected molecular liquids for calibration in accurate 1H NMR PFG measurements, Phys. Chem. Chem. Phys. 2(20) (2000) 4740-4742.

[228] F. Vaca Chavez, E. Hellstrand, B. Halle, Hydrogen exchange and hydration dynamics in gelatin gels, J. Phys. Chem. B 110(43) (2006) 21551-9.

[229] A. Luk, N.S. Murthy, W. Wang, R. Rojas, J. Kohn, Study of nanoscale structures in hydrated biomaterials using small-angle neutron scattering, Acta Biomater. 8(4) (2012) 1459-68.

[230] P.L. Ritger, N.A. Peppas, A simple equation for description of solute release II. Fickian and anomalous release from swellable devices, J. Control. Release 5(1) (1987) 37-42.

[231] P.L. Ritger, N.A. Peppas, A simple equation for description of solute release I. Fickian and non-fickian release from non-swellable devices in the form of slabs, spheres, cylinders or discs, J. Control. Release 5(1) (1987) 23-36.

[232] X. Zhao, Z. Wang, A pH-sensitive microemulsion-filled gellan gum hydrogel encapsulated apigenin: Characterization and in vitro release kinetics, Colloid. Surface. B 178 (2019) 245-252.

[233] A.V. Reis, M.R. Guilherme, A.F. Rubira, E.C. Muniz, Mathematical model for the prediction of the overall profile of in vitro solute release from polymer networks, J. Colloid Interface Sci. 310(1) (2007) 128-35.

[234] T. Benselfelt, L. Wagberg, Unidirectional Swelling of Dynamic Cellulose Nanofibril Networks: A Platform for Tunable Hydrogels and Aerogels with 3D Shapeability, Biomacromolecules 20(6) (2019) 2406-2412.

[235] C.G. de Kruif, T. Huppertz, V.S. Urban, A.V. Petukhov, Casein micelles and their internal structure, Adv. Colloid Interface Sci. 171-172 (2012) 36-52.

[236] A. Otsuki, L. de Campo, C.J. Garvey, C. Rehm, H2O/D2O Contrast Variation for Ultra-Small-Angle Neutron Scattering to Minimize Multiple Scattering Effects of Colloidal Particle Suspensions, Colloid Interfac. 2(3) (2018) 37.

[237] J. Wang, H. Xue, B. Zhou, Y.F. Yao, E.W. Hansen, Interfacial water in mesopores and its implications to the surface features – A solid state NMR study, Appl. Surf. Sci. 484 (2019) 1154-1160.

[238] V.M. Gun'ko, Composite materials: Textural characteristics, Appl. Surf. Sci. 307 (2014) 444-454.

[239] B.T. Nguyen, G. Balakrishnan, B. Jacquette, T. Nicolai, C. Chassenieux, C. Schmitt, L. Bovetto, Inhibition and Promotion of Heat-Induced Gelation of Whey Proteins in the Presence of Calcium by Addition of Sodium Caseinate, Biomacromolecules 17(11) (2016) 3800-3807.

[240] C. Rondeau-Mouro, D. Defer, E. Leboeuf, M. Lahaye, Assessment of cell wall porosity in Arabidopsis thaliana by NMR spectroscopy, Int. J. Biol. Macromol. 42(2) (2008) 83-92.

[241] P.M. Kekkonen, A. Ylisassi, V.V. Telkki, Absorption of Water in Thermally Modified Pine Wood As Studied by Nuclear Magnetic Resonance, J. Phys. Chem. C 118(4) (2014) 2146-2153.

[242] M.A. Gagnon, M. Lafleur, Comparison of the structure and the transport properties of low-set and high-set curdlan hydrogels, J. Colloid Interface Sci. 357(2) (2011) 419-427.

[243] F. Elwinger, P. Pourmand, I. Furo, Diffusive Transport in Pores. Tortuosity and Molecular Interaction with the Pore Wall, J. Phys. Chem. C 121(25) (2017) 13757-13764.

[244] F.S. Jahed, S. Hamidi, M. Zamani-Kalajahi, M. Siahi-Shadbad, Biomedical applications of silica-based aerogels: A comprehensive review, Macromol. Res. (2023) 1-20.

[245] S. Montes, H. Maleki, Aerogels and their applications, Colloidal Metal Oxide Nanoparticles, Elsevier2020, pp. 337-399.

[246] A.T. Krzyżak, I. Habina, Low field 1 H NMR characterization of mesoporous silica MCM-41 and SBA-15 filled with different amount of water, Micropor. Mesopor. Mat. 231 (2016) 230-239.

[247] J. Seyed-Yazdi, J.C. Dore, J.B.W. Webber, H. Farman, Structural characterization of water and ice in mesoporous SBA-15 silicas IV: partially filled cases for 86 A pore diameter, J. Phys. Condens. Matter 25(46) (2013) 465105.

[248] A. Irwin, J. Holmgren, J. Jonas, Solid state 29Si and 11B NMR studies of sol-gel derived borosilicates, J. Non-Cryst. Solids 101(2-3) (1988) 249-254.

[249] A.D. Irwin, J.S. Holmgren, T.W. Zerda, J. Jonas, Spectroscopic Investigations of Borosiloxane Bond Formation in the Sol-Gel Process, J. Non-Cryst. Solids 89(1-2) (1987) 191-205.

[250] P. Debye, A.M. Bueche, Scattering by an inhomogeneous solid, J. Appl. Phys. 20(6) (1949) 518-525.

[251] G. Porod, Die Röntgenkleinwinkelstreuung von dichtgepackten kolloiden Systemen: I. Teil, Kolloid-Z. 124(2) (1951) 83-114.

[252] L. Ludescher, R. Morak, C. Balzer, A.M. Waag, S. Braxmeier, F. Putz, S. Busch, G.Y. Gor, A.V. Neimark, N. Hüsing, G. Reichenauer, O. Paris, In Situ Small-Angle Neutron Scattering Investigation of Adsorption-Induced Deformation in Silica with Hierarchical Porosity, Langmuir 35(35) (2019) 11590-11600.

[253] R. Morak, S. Braxmeier, L. Ludescher, F. Putz, S. Busch, N. Husing, G. Reichenauer, O. Paris, Quantifying adsorption-induced deformation of nanoporous materials on different length scales, J. Appl. Crystallogr. 50(5) (2017) 1404-1410.

[254] J. Mitchell, J.B.W. Webber, J.H. Strange, Nuclear magnetic resonance cryoporometry, Phys. Rep. 461(1) (2008) 1-36.

[255] D.B. Asay, S.H. Kim, Evolution of the adsorbed water layer structure on silicon oxide at room temperature, J. Phys. Chem. B 109(35) (2005) 16760-16763.

[256] G.E. Ewing, Thin Film Water, J. Phys. Chem. B 108(41) (2004) 15953-15961.

[257] G. Buntkowsky, H. Breitzke, A. Adamczyk, F. Roelofs, T. Emmler, E. Gedat, B. Grunberg, Y. Xu, H.H. Limbach, I. Shenderovich, A. Vyalikh, G. Findenegg, Structural and dynamical properties of guest molecules confined in mesoporous silica materials revealed by NMR, Phys. Chem. Chem. Phys. 9(35) (2007) 4843-4853.

[258] B. Grunberg, T. Emmler, E. Gedat, I. Shenderovich, G.H. Findenegg, H.H. Limbach, G. Buntkowsky, Hydrogen bonding of water confined in mesoporous silica MCM-41 and SBA-15 studied by 1H solid-state NMR, Chem. Eur. J. 10(22) (2004) 5689-5696.

[259] A. Vyalikh, T. Emmler, B. Grünberg, Y. Xu, I. Shenderovich, G.H. Findenegg, H.H. Limbach, G. Buntkowsky, Hydrogen Bonding of Water Confined in Controlled-Pore Glass 10-75 Studied by 1H-Solid State NMR, Z. Phys. Chem. 221(1) (2007) 155-168.

[260] A.T. Krzyzak, W. Mazur, J. Matyszkiewicz, A. Kochman, Identification of Proton Populations in Cherts as Natural Analogues of Pure Silica Materials by Means of Low Field NMR, J. Phys. Chem. C 124(9) (2020) 5225-5240.

[261] W.E. Troyer, R. Holly, H. Peemoeller, M.M. Pintar, Proton spin-spin relaxation study of hydration of a model nanopore, Solid State Nucl. Magn. Reson. 28(2-4) (2005) 238-243.

[262] J.R. Zimmerman, B.G. Holmes, J.A. Lasater, A Study of Adsorbed Wateron Silica Gel by Nuclear Resonance Techniques, J. Phys. Chem. 60(9) (1956) 1157-1161.

[263] S. Davies, K.J. Packer, D.R. Roberts, F.O. Zelaya, Pore-size distributions from NMR spin-lattice relaxation data, Magn. Reson. Imaging 9(5) (1991) 681-685.

[264] M.A. Javed, S. Komulainen, H. Daigle, B. Zhang, J. Vaara, B. Zhou, V.-V. Telkki, Determination of pore structures and dynamics of fluids in hydrated cements and natural shales by various 1H and 129Xe NMR methods, Micropor. Mesopor. Mat. 281 (2019) 66-74.

[265] J. Li, S. Mailhiot, A.M. Kantola, H. Niu, H. Sreenivasan, V.-V. Telkki, P. Kinnunen, Longitudinal single-sided NMR study: Silica-to-alumina ratio changes the reaction mechanism of geopolymer, Cem. Concr. Res. 160 (2022) 106921.

[266] A. Rege, L. Ratke, I.D. Kulcu, P. Gurikov, Stiffening of biopolymer aerogel networks upon wetting: A model-based study, J. Non-Cryst. Solids 531 (2020) 119859.

[267] M. Dosta, K. Jarolin, P. Gurikov, Modelling of Mechanical Behavior of Biopolymer Alginate Aerogels Using the Bonded-Particle Model, Molecules 24(14) (2019).

[268] A. Rege, I. Preibisch, M. Schestakow, K. Ganesan, P. Gurikov, B. Milow, I. Smirnova, M. Itskov, Correlating Synthesis Parameters to Morphological Entities: Predictive Modeling of Biopolymer Aerogels, Materials 11(9) (2018).

[269] N. Guerrero-Alburquerque, S. Zhao, N. Adilien, M.M. Koebel, M. Lattuada, W.J. Malfait, Strong, Machinable, and Insulating Chitosan-Urea Aerogels: Toward Ambient Pressure Drying of Biopolymer Aerogel Monoliths, ACS Appl. Mater. Interfaces 12(19) (2020) 22037-22049.

[270] Z. Zhu, G. Snellings, M.M. Koebel, W.J. Malfait, Superinsulating Polyisocyanate Based Aerogels: A Targeted Search for the Optimum Solvent System, ACS Appl. Mater. Interfaces 9(21) (2017) 18222-18230.

[271] S.J. Talley, S.L. Vivod, B.A. Nguyen, M.A.B. Meador, A. Radulescu, R.B. Moore, Hierarchical Morphology of Poly(ether ether ketone) Aerogels, ACS Appl. Mater. Interfaces 11(34) (2019) 31508-31519.

[272] H. Maleki, L. Whitmore, N. Husing, Novel multifunctional polymethylsilsesquioxane-silk fibroin aerogel hybrids for environmental and thermal insulation applications, J. Mater. Chem. A 6(26) (2018) 12598-12612.

[273] J. Wang, X.C. Wang, X.T. Zhang, Cyclic molecule aerogels: a robust cyclodextrin monolith with hierarchically porous structures for removal of micropollutants from water, J. Mater. Chem. A 5(9) (2017) 4308-4313.

[274] C.A. García-González, M. Alnaief, I. Smirnova, Polysaccharide-based aerogels-Promising biodegradable carriers for drug delivery systems, Carbohydr. Polym. 86(4) (2011) 1425-1438.

[275] F. Quignard, R. Valentin, F. Di Renzo, Aerogel materials from marine polysaccharides, New J. Chem. 32(8) (2008) 1300-1310.

[276] P. Agulhon, M. Robitzer, L. David, F. Quignard, Structural regime identification in ionotropic alginate gels: influence of the cation nature and alginate structure, Biomacromolecules 13(1) (2012) 215-20.

[277] H.J. Martin, B.K. Hughes, W.A. Braunecker, T. Gennett, M.D. Dadmun, The impact of radical loading and oxidation on the conformation of organic radical polymers by small angle neutron scattering, J. Mater. Chem. A 6(32) (2018) 15659-15667.

[278] S.J. Rinehart, B.N. Nguyen, R.P. Viggiano, M.A.B. Meador, M.D. Dadmun, Quantitative Evaluation of the Hierarchical Porosity in Polyimide Aerogels and Corresponding Solvated Gels, ACS Appl. Mater. Interfaces 12(27) (2020) 30457-30465.

[279] A.E. Danks, M.J. Hollamby, B. Hammouda, D.C. Fletcher, F. Johnston-Banks, S.E. Rogers, Z. Schnepp, Mechanistic insights into the formation of porous carbons from gelatin, J. Mater. Chem. A 5(23) (2017) 11644-11651.

[280] Y. Maki, K. Ito, N. Hosoya, C. Yoneyama, K. Furusawa, T. Yamamoto, T. Dobashi, Y. Sugimoto, K. Wakabayashi, Anisotropic structure of calcium-induced alginate gels by optical and small-angle X-ray scattering measurements, Biomacromolecules 12(6) (2011) 2145-52.

[281] M.A. Isaacs, N. Robinson, B. Barbero, L.J. Durndell, J.C. Manayil, C.M.A. Parlett, C. D'Agostino, K. Wilson, A.F. Lee, Unravelling mass transport in hierarchically porous catalysts, J. Mater. Chem. A 7(19) (2019) 11814-11825.

[282] J. Brus, M. Urbanova, J. Czernek, M. Pavelkova, K. Kubova, J. Vyslouzil, S. Abbrent, R. Konefal, J. Horsky, D. Vetchy, J. Vyslouzil, P. Kulich, Structure and Dynamics of Alginate Gels Cross-Linked by Polyvalent Ions Probed via Solid State NMR Spectroscopy, Biomacromolecules 18(8) (2017) 2478-2488.

[283] H. Grasdalen, B. Larsen, O. Smisrod, 13C-n.m.r. studies of monomeric composition and sequence in alginate, Carbohydr. Res. 89(2) (1981) 179-191.

[284] I.D. Kulcu, A. Rege, Physics-informed constitutive modelling of hydrated biopolymer aerogel networks, Soft Matter 17(21) (2021) 5278-5283.

[285] P. Paraskevopoulou, G. Raptopoulos, A. Len, Z. Dudás, I. Fábián, J. Kalmár, Fundamental Skeletal Nanostructure of Nanoporous Polymer-Cross-Linked Alginate Aerogels and Its Relevance To Environmental Remediation, ACS Appl. Nano Mater. 4(10) (2021) 10575-10583.

[286] N. Leventis, C. Sotiriou-Leventis, N. Chandrasekaran, S. Mulik, Z.J. Larimore, H.B. Lu, G. Churu, J.T. Mang, Multifunctional polyurea aerogels from isocyanates and water. A structure−property case study, Chem. Mater. 22(24) (2010) 6692-6710.

[287] C. Chidambareswarapattar, L. Xu, C. Sotiriou-Leventis, N. Leventis, Robust monolithic multiscale nanoporous polyimides and conversion to isomorphic carbons, RSC Adv. 3(48) (2013) 26459-26469.

[288] C.M. Jeffries, M.A. Graewert, C.E. Blanchet, D.B. Langley, A.E. Whitten, D.I. Svergun, Preparing monodisperse macromolecular samples for successful biological small-angle X-ray and neutron-scattering experiments, Nat. Protoc. 11(11) (2016) 2122-2153.

[289] M.J. Ariza, J. Benavente, E. Rodriguez-Castellon, L. Palacio, Effect of hydration of polyamide membranes on the surface electrokinetic parameters: surface characterization by x-ray photoelectronic spectroscopy and atomic force microscopy, J. Colloid Interface Sci. 247(1) (2002) 149-58.

[290] N. Hu, L. Lin, E. Metwalli, L. Bießmann, M. Philipp, V. Hildebrand, A. Laschewsky, C.M. Papadakis, R. Cubitt, Q. Zhong, P. Müller-Buschbaum, Kinetics of Water Transfer Between the LCST

and UCST Thermoresponsive Blocks in Diblock Copolymer Thin Films Monitored by In Situ Neutron Reflectivity, Adv. Mater. Interfaces 10(3) (2022) 2201913.

[291] P. Bettotti, C.A. Maestri, R. Guider, I. Mancini, E. Nativ-Roth, Y. Golan, M. Scarpa, Dynamics of Hydration of Nanocellulose Films, Adv. Mater. Interfaces 3(5) (2016) 1500415.

[292] R. Digaitis, P. Falkman, V. Oltner, L.E. Briggner, V. Kocherbitov, Hydration and dehydration induced changes in porosity of starch microspheres, Carbohydr. Polym. 291 (2022) 119542.

[293] Y.P. Chang, P.B. Cheah, C.C. Seow, Plasticizing-Antiplasticizing Effects of Water on Physical Properties of Tapioca Starch Films in the Glassy State, J. Food Sci. 65(3) (2000) 445-451.

[294] L. Mascia, Y. Kouparitsas, D. Nocita, X. Bao, Antiplasticization of Polymer Materials: Structural Aspects and Effects on Mechanical and Diffusion-Controlled Properties, Polymers 12(4) (2020) 769.

[295] J.S. Vrentas, J.L. Duda, H.C. Ling, Antiplasticization and Volumetric Behavior in Glassy-Polymers, Macromolecules 21(5) (1988) 1470-1475.

[296] L. Nagy, M. Nagy, B. Vadkerti, L. Daroczi, G. Deak, M. Zsuga, S. Keki, Designed Polyurethanes for Potential Biomedical and Pharmaceutical Applications: Novel Synthetic Strategy for Preparing Sucrose Containing Biocompatible and Biodegradable Polyurethane Networks, Polymers 11(5) (2019) 825.

[297] A. Emmerling, J. Fricke, Small angle scattering and the structure of aerogels, J. Non-Cryst. Solids 145 (1992) 113-120.

[298] S. Goudeau, M. Charlot, F. Muller-Plathe, Mobility enhancement in amorphous polyamide 6,6 induced by water sorption: A molecular dynamics simulation study, J. Phys. Chem. B 108(48) (2004) 18779-18788.

[299] A.D. English, Solution and solid-state NMR characterization of poly(p-phenylene terephthalamide), J. Polym. Sci. B Pol. Phys. 24(4) (1986) 805-815.

[300] J.O. Brauckmann, P. Zolfaghari, R. Verhoef, E.A. Klop, G.A. de Wijs, A.P.M. Kentgens, Structural Studies of Polyaramid Fibers: Solid-State NMR and First-Principles Modeling, Macromolecules 49(15) (2016) 5548-5560.

[301] H. Kitano, K. Ichikawa, M. Fukuda, A. Mochizuki, M. Tanaka, The structure of water sorbed to polymethoxyethylacrylate film as examined by FT-IR spectroscopy, J. Colloid Interface Sci. 242(1) (2001) 133-140.

[302] G. Paul, S. Steuernagel, H. Koller, Non-covalent interactions of a drug molecule encapsulated in a hybrid silica gel, Chem. Commun. (48) (2007) 5194-6.

[303] M. Fukuda, M. Ochi, M. Miyagawa, H. Kawai, Moisture Sorption Mechanism of Aromatic Polyamide Fibers: Stoichiometry of the Water Sorbed in Poly(para-phenylene Terephthalamide) Fibers1, Textile Res. J. 61(11) (1991) 668-680.

[304] N. Chaupart, G. Serpe, Water accessibility in aliphatic polyamides by NIR and FT-IR spectroscopies, J. Near Infrared Spectrosc. 6(1) (1998) 307-316.

[305] R. Iwamoto, H. Murase, Infrared spectroscopic study of the interactions of nylon-6 with water, J. Polym. Sci. Pol. Phys. 41(14) (2003) 1722-1729.

[306] N.S. Murthy, M. Stamm, J.P. Sibilia, S. Krimm, Structural-Changes Accompanying Hydration in Nylon-6, Macromolecules 22(3) (1989) 1261-1267.

[307] Y.S. Hu, S. Mehta, D.A. Schiraldi, A. Hiltner, E. Baer, Effect of water sorption on oxygen-barrier properties of aromatic polyamides, J. Polym. Sci. Pol. Phys. 43(11) (2005) 1365-1381.

[308] R.J. Pace, A. Datyner, Statistical Mechanical Model of Sorption and Diffusion of Simple Penetrants in Polymers, Polym. Eng. Sci. 20(1) (1980) 51-58.

[309] M. Laurati, P. Sotta, D.R. Long, L.A. Fillot, A. Arbe, A. Alegria, J.P. Embs, T. Unruh, G.J. Schneider, J. Colmenero, Dynamics of Water Absorbed in Polyamides, Macromolecules 45(3) (2012) 1676-1687.

[310] S. Hwang, J. Haase, E. Miersemann, J. Kärger, Diffusion Analysis in Pore Hierarchies by the Two-Region Model, Adv. Mater. Interfaces 8(4) (2020) 2000749.

[311] T. Maeda, K. Yamamoto, T. Aoyagi, Importance of bound water in hydration-dehydration behavior of hydroxylated poly(N-isopropylacrylamide), J. Colloid Interface Sci. 302(2) (2006) 467-74.

[312] S. Bjorklund, V. Kocherbitov, Water vapor sorption-desorption hysteresis in glassy surface films of mucins investigated by humidity scanning QCM-D, J. Colloid Interface Sci. 545 (2019) 289-300.

[313] G. Tkalec, R. Kranvogl, A.P. Uzunalic, Z. Knez, Z. Novak, Optimisation of critical parameters during alginate aerogels' production, J Non-Cryst Solids 443 (2016) 112-117.

[314] F. Quignard, R. Valentin, F. Di Renzo, Aerogel materials from marine polysaccharides, New J Chem 32(8) (2008) 1300-1310.

[315] I. Smirnova, P. Gurikov, Aerogels in Chemical Engineering: Strategies Toward Tailor-Made Aerogels, Annu Rev Chem Biomol Eng 8(0) (2017) 307-334.

[316] R. Subrahmanyam, P. Gurikov, P. Dieringer, M. Sun, I. Smirnova, On the Road to Biopolymer Aerogels—Dealing with the Solvent, Gels 1(2) (2015) 291-313.

[317] T. Mehling, I. Smirnova, U. Guenther, R.H.H. Neubert, Polysaccharide-based aerogels as drug carriers, J Non-Cryst Solids 355(50-51) (2009) 2472-2479.

[318] V.S. Goncalves, P. Gurikov, J. Poejo, A.A. Matias, S. Heinrich, C.M. Duarte, I. Smirnova, Alginate-based hybrid aerogel microparticles for mucosal drug delivery, Eur J Pharm Biopharm 107 (2016) 160-70.

[319] M. Pantic, Z. Knez, Z. Novak, Supercritical impregnation as a feasible technique for entrapment of fat-soluble vitamins into alginate aerogels, J Non-Cryst Solids 432 (2016) 519-526.

[320] Y.C. Dong, W.J. Dong, Y.N. Cao, Z.B. Han, Z.Z. Ding, Preparation and catalytic activity of Fe alginate gel beads for oxidative degradation of azo dyes under visible light irradiation, Catal Today 175(1) (2011) 346-355.

[321] B.-J. Lee, G.-H. Min, T.-W. Kim, Preparation andin vitro release of melatonin-loaded multivalent cationic alginate beads, Archives of Pharmacal Research 19(4) (1996) 280.

[322] Z. Jin, G. Guven, V. Bocharova, J. Halamek, I. Tokarev, S. Minko, A. Melman, D. Mandler, E. Katz, Electrochemically controlled drug-mimicking protein release from iron-alginate thin-films associated with an electrode, ACS Appl Mater Interfaces 4(1) (2012) 466-75.

[323] G.E. Giammanco, C.T. Sosnofsky, A.D. Ostrowski, Light-responsive iron(III)-polysaccharide coordination hydrogels for controlled delivery, ACS Appl Mater Interfaces 7(5) (2015) 3068-76.

[324] M. Bruchet, A. Melman, Fabrication of patterned calcium cross-linked alginate hydrogel films and coatings through reductive cation exchange, Carbohydrate Polymers 131 (2015) 57-64.

[325] A. Veronovski, Z. Knez, Z. Novak, Preparation of multi-membrane alginate aerogels used for drug delivery, J Supercrit Fluid 79 (2013) 209-215.

[326] M.F. Aldawsari, M.M. Ahmed, F. Fatima, M.K. Anwer, P. Katakam, A. Khan, Development and Characterization of Calcium-Alginate Beads of Apigenin: In Vitro Antitumor, Antibacterial, and Antioxidant Activities, Mar. Drugs 19(8) (2021) 467.

[327] T. Duong, C. Lopez-Iglesias, P.K. Szewczyk, U. Stachewicz, J. Barros, C. Alvarez-Lorenzo, M. Alnaief, C.A. Garcia-Gonzalez, A Pathway From Porous Particle Technology Toward Tailoring Aerogels for Pulmonary Drug Administration, Front. Bioeng. Biotechnol. 9 (2021) 671381.

[328] M. Alnaief, R.M. Obaidat, M.M. Alsmadi, Preparation of Hybrid Alginate-Chitosan Aerogel as Potential Carriers for Pulmonary Drug Delivery, Polymers 12(10) (2020) 2223.

[329] T. Athamneh, A. Amin, E. Benke, R. Ambrus, P. Gurikov, I. Smirnova, C.S. Leopold, Pulmonary drug delivery with aerogels: engineering of alginate and alginate-hyaluronic acid microspheres, Pharm. Dev. Technol. 26(5) (2021) 509-521.

[330] S. van Koningsbruggen-Rietschel, J.C. Davies, T. Pressler, R. Fischer, G. MacGregor, S.H. Donaldson, K. Smerud, N. Meland, J. Mortensen, M.O. Fosbol, D.G. Downey, A.H. Myrset, H. Flaten, P.D. Rye, Inhaled dry powder alginate oligosaccharide in cystic fibrosis: a randomised, double-blind, placebo-controlled, crossover phase 2b study, ERJ Open Res. 6(4) (2020) 00132-2020.

[331] B.B. Eedara, R. Bastola, S.C. Das, Dissolution and Absorption of Inhaled Drug Particles in the Lungs, Pharmaceutics 14(12) (2022) 2667.

[332] D.E. Alonzo, Y. Gao, D. Zhou, H. Mo, G.G.Z. Zhang, L.S. Taylor, Dissolution and precipitation behavior of amorphous solid dispersions, J. Pharm. Sci. 100(8) (2011) 3316-3331.

[333] A. Hajnal, M.L. Aiyelari, M. Dirauf, P. Gurikov, Investigation of the Uniformity of Gel Shrinkage by Imaging Tracer Particles Using X-Ray Microtomography, Adv. Eng. Mater. 27(13) (2025) 2301423.

[334] X. Chen, Z. Liu, A pH-Responsive Hydrogel Based on a Tumor-Targeting Mesoporous Silica Nanocomposite for Sustained Cancer Labeling and Therapy, Macromol. Rapid Commun. 37(18) (2016) 1533-9.

[335] J. Soukup, P. Cisar, F. Sroubek, Segmentation Method of Time-Lapse Microscopy Images with the Focus on Biocompatibility Assessment, Microsc. Microanal. 22(3) (2016) 497-506.

[336] F.L. Mi, Synthesis and characterization of a novel chitosan-gelatin bioconjugate with fluorescence emission, Biomacromolecules 6(2) (2005) 975-87.

[337] G. Kiraly, Z. Hargitai, I. Kovacs, G. Szeman-Nagy, I. Juhasz, G. Banfalvi, Metastatic Spread from Abdominal Tumor Cells to Parathymic Lymph Nodes, Pathol. Oncol. Res. 25(2) (2019) 625-633.

[338] W.A. Bleyer, The clinical pharmacology of methotrexate: new applications of an old drug, Cancer 41(1) (1978) 36-51.

[339] J. Grim, J. Chladek, J. Martinkova, Pharmacokinetics and pharmacodynamics of methotrexate in non-neoplastic diseases, Clin. Pharmacokinet. 42(2) (2003) 139-151.

[340] G. Kiraly, A.S. Simonyi, M. Turani, I. Juhasz, G. Nagy, G. Banfalvi, Micronucleus formation during chromatin condensation and under apoptotic conditions, Apoptosis 22(2) (2017) 207-219.

[341] W.T. Purcell, D.S. Ettinger, Novel antifolate drugs, Curr. Oncol. Rep. 5(2) (2003) 114-125.

[342] C.C. Huang, P.C. Hsu, Y.C. Hung, Y.F. Liao, C.C. Liu, C.T. Hour, M.C. Kao, G.J. Tsay, H.C. Hung, G.Y. Liu, Ornithine decarboxylase prevents methotrexate-induced apoptosis by reducing intracellular reactive oxygen species production, Apoptosis 10(4) (2005) 895-907.

[343] E.W.B. Jeffes III, J.L. McCullough, M.R. Pittelkow, A. McCormick, J. Almanzor, G.Y. Liu, M. Dang, K. Voss, J. Voss, A. Schlotzhauer, Methotrexate therapy of psoriasis: differential sensitivity of proliferating lymphoid and epithelial cells to the cytotoxic and growth-inhibitory effects of methotrexate, J. Investig. Dermatol. 104(2) (1995) 183-188.

[344] J.E. Wright, M. Pardo, A. Tretyakov, W.L. Alperin, D. Trites, A. Rosowsky, Pharmacokinetics, antifolate activity and tissue distribution of PT523 in SCC VII tumor-bearing mice, Cancer. Chemother. Pharmacol. 42(4) (1998) 300-306.

[345] R.M. Bremnes, L. Slordal, E. Wist, J. Aarbakke, Dose-dependent pharmacokinetics of methotrexate and 7-hydroxymethotrexate in the rat in vivo, Cancer Res. 49(22) (1989) 6359-6364.

[346] W.A. Bleyer, J.A. Nelson, B.A. Kamen, Accumulation of methotrexate in systemic tissues after intrathecal administration, J. Pediatr. Hematol. Oncol. 19(6) (1997) 530-532.

[347] P.J. Creaven, H.H. Hansen, D.A. Alford, L.M. Allen, Methotrexate in liver and bile after intravenous dosage in man, Br. J. Cancer 28(6) (1973) 589-591.

[348] M.P. Iqbal, Accumulation of methotrexate in human tissues following high-dose methotrexate therapy, J. Pak. Med. Assoc. 48(11) (1998) 341-343.

[349] G. Kiraly, J.C. Egu, Z. Hargitai, I. Kovacs, I. Fabian, J. Kalmar, G. Szeman-Nagy, Mesoporous Aerogel Microparticles Injected into the Abdominal Cavity of Mice Accumulate in Parathymic Lymph Nodes, Int. J. Mol. Sci. 22(18) (2021) 9756.

[350] B.K. Pilcher, J.A. Dumin, B.D. Sudbeck, S.M. Krane, H.G. Welgus, W.C. Parks, The activity of collagenase-1 is required for keratinocyte migration on a type I collagen matrix, J. Cell Biol. 137(6) (1997) 1445-1457.

[351] M. Pudukudy, Z. Yaakob, R. Rajendran, T. Kandaramath, Photodegradation of methylene blue over novel 3D ZnO microflowers with hexagonal pyramid-like petals, React Kinet Mech Cat 112(2) (2014) 527-542.

[352] Y.M.H. Zhou, W.J.H. Hu, J.G. Yu, F.P. Jiao, Effective photocatalytic degradation of methylene blue by Cu2O/MgAl layered double hydroxides, React Kinet Mech Cat 115(2) (2015) 581-596.

[353] S. Azizian, H. Bashiri, Adsorption kinetics at the solid/solution interface: statistical rate theory at initial times of adsorption and close to equilibrium, Langmuir 24(20) (2008) 11669-76.

[354] Y. Liu, L. Shen, From Langmuir kinetics to first- and second-order rate equations for adsorption, Langmuir 24(20) (2008) 11625-30.

[355] W. Rudzinski, T. Panczyk, The langmuirian adsorption kinetics revised: A farewell to the XXth century theories ?, Adsorption 8(1) (2002) 23-34.

[356] M. Wahlgren, T. Arnebrant, I. Lundstrom, The Adsorption of Lysozyme to Hydrophilic Silicon-Oxide Surfaces - Comparison between Experimental-Data and Models for Adsorption-Kinetics, J Colloid Interf Sci 175(2) (1995) 506-514.

[357] M. Wahlgren, U. Elofsson, Simple models for adsorption kinetics and their correlation to the adsorption of beta-lactoglobulin A and B, J Colloid Interf Sci 188(1) (1997) 121-129.

[358] J. Kalmár, G. Lente, I. Fábián, Kinetics and mechanism of the adsorption of methylene blue from aqueous solution onto the surface of a quartz cuvette., (2015).

[359] K. Razi Naqvi, Screening hypochromism (sieve effect) in red blood cells: a quantitative analysis, Biomedical optics express 5(4) (2014) 1290-5.

[360] S. Azizian, A novel and simple method for finding the heterogeneity of adsorbents on the basis of adsorption kinetic data, J Colloid Interface Sci 302(1) (2006) 76-81.

[361] A.K. Ghosh, Study of the self-association of methylene blue from protonation equilibriums, J. Am. Chem. Soc. 92(22) (1970) 6415-6418.

[362] P. Mukerjee, A.K. Ghosh, Thermodynamic aspects of the self-association and hydrophobic bonding of methylene blue. Model system for stacking interactions, J. Am. Chem. Soc. 92(22) (1970) 6419-6424.

[363] K. Patil, R. Pawar, P. Talap, Self-aggregation of methylene blue in aqueous medium and aqueous solutions of Bu4NBr and urea, Phys. Chem. Chem. Phys. 2(19) (2000) 4313-4317.

[364] M.M. Allingham, J.M. Cullen, C.H. Giles, S.K. Jain, J.S. Woods, Adsorption at inorganic surfaces. II. Adsorption of dyes and related compounds by silica, Journal of Applied Chemistry 8(2) (1958) 108-116.

[365] G. Peintler, I. Nagypal, A. Jancso, I.R. Epstein, K. Kustin, Extracting experimental information from large matrixes .1. A new algorithm for the application of matrix rank analysis, J. Phys. Chem. A 101(43) (1997) 8013-8020.

[366] J. Kalmár, S.B. Ellis, M.T. Ashby, R.L. Halterman, Kinetics of Formation of the Host–Guest Complex of a Viologen with Cucurbit [7] uril, Org. Lett. 14(13) (2012) 3248-3251.

[367] S.L. Fornili, G. Sgroi, V. Izzo, Effects of Solvent on Stacking Interactions - a Spectrophotometric Study of Methylene-Blue Dimerization in Aqueous-Solutions of Some Monohydric Alcohols, J. Chem. Soc. Farad. T. 79(5) (1983) 1085-1090.

[368] Y.M. Yan, M.N. Zhang, K.P. Gong, L. Su, Z.X. Guo, L.Q. Mao, Adsorption of methylene blue dye onto carbon nanotubes: A route to an electrochemically functional nanostructure and its layer-by-layer assembled nanocomposite, Chem. Mater. 17(13) (2005) 3457-3463.

[369] K. Adachi, T. Mita, T. Yamate, S. Yamazaki, H. Takechi, H. Watarai, Controllable adsorption and ideal H-aggregation behaviors of phenothiazine dyes on the tungsten oxide nanocolloid surface, Langmuir 26(1) (2010) 117-25.

[370] S. Garoff, R.B. Stephens, C.D. Hanson, G.K. Sorenson, Surface Interactions of Adsorbed Molecules as Probed by Their Optical-Properties, Opt. Commun. 41(4) (1982) 257-262.

[371] Z.M. Qi, N. Matsuda, A. Takatsu, K. Kato, In situ investigation of coadsorption of myoglobin and methylene blue to hydrophilic glass by broadband time-resolved optical waveguide spectroscopy, Langmuir 20(3) (2004) 778-84.

[372] N. Carlsson, H. Gustafsson, C. Thorn, L. Olsson, K. Holmberg, B. Akerman, Enzymes immobilized in mesoporous silica: a physical-chemical perspective, Adv. Colloid Interface Sci. 205 (2014) 339-60.

[373] H.R. Luckarift, J.C. Spain, R.R. Naik, M.O. Stone, Enzyme immobilization in a biomimetic silica support, Nat. Biotechnol. 22(2) (2004) 211-3.

[374] I. Smirnova, J. Mamic, W. Arlt, Adsorption of drugs on silica aerogels, Langmuir 19(20) (2003) 8521-8525.

[375] T. Peters, 7 - Practical Aspects: Albumin in the Laboratory, in: T. Peters (Ed.), All About Albumin, Academic Press, San Diego, 1995, pp. 285-318.

[376] T. Peters, 3 - Ligand Binding by Albumin, in: T. Peters (Ed.), All About Albumin, Academic Press, San Diego, 1995, pp. 76-132.

[377] S. Brudar, B. Hribar-Lee, Effect of Buffer on Protein Stability in Aqueous Solutions: A Simple Protein Aggregation Model, J. Phys. Chem. B 125(10) (2021) 2504-2512.

[378] A. Salis, L. Cappai, C. Carucci, D.F. Parsons, M. Monduzzi, Specific Buffer Effects on the Intermolecular Interactions among Protein Molecules at Physiological pH, J. Phys. Chem. Lett. 11(16) (2020) 6805-6811.

[379] J. Meissner, A. Prause, B. Bharti, G.H. Findenegg, Characterization of protein adsorption onto silica nanoparticles: influence of pH and ionic strength, Colloid. Polym. Sci. 293(11) (2015) 3381-3391.

[380] T. Ditroi, J. Kalmar, J.A. Pino-Chamorro, Z. Erdei, G. Lente, I. Fabian, Construction of a multipurpose photochemical reactor with on-line spectrophotometric detection, Photochem. Photobiol. Sci. 15(4) (2016) 589-594.

[381] C.W. Gear, Numerical Solution of Ordinary Differential Equations: Is There Anything Left to Do?, SIAM Review 23(1) (1981) 10-24.

[382] G. Peintler, I. Nagypal, I.R. Epstein, Systematic design of chemical oscillators. 60. Kinetics and mechanism of the reaction between chlorite ion and hypochlorous acid, J. Phys. Chem. 94(7) (1990) 2954-2958.

[383] K.H. Chu, Revisiting the Temkin Isotherm: Dimensional Inconsistency and Approximate Forms, Ind. Eng. Chem. Res. 60(35) (2021) 13140-13147.

[384] T. Chen, X. Wang, Y. He, C. Zhang, Z. Wu, K. Liao, J. Wang, Z. Guo, Effects of cyclen and cyclam on zinc(II)- and copper(II)-induced amyloid beta-peptide aggregation and neurotoxicity, Inorg. Chem. 48(13) (2009) 5801-5809.

[385] J.D. Silversides, C.C. Allan, S.J. Archibald, Copper(II) cyclam-based complexes for radiopharmaceutical applications: synthesis and structural analysis, Dalton Trans. (9) (2007) 971-978.

[386] R.W. Hay, M.P. Pujari, The Dissociation of [Cu(Cyclen)]2+ in Acid-Solution - a Kinetic-Study, Inorg. Chim. Acta 100(2) (1985) L1-L3.

[387] K.S. Woodin, K.J. Heroux, C.A. Boswell, E.H. Wong, G.R. Weisman, W.J. Niu, S.A. Tomellini, C.J. Anderson, L.N. Zakharov, A.L. Rheingold, Kinetic inertness and electrochemical behavior of copper(II) tetraazamacrocyclic complexes: Possible implications for in vivo stability, Eur. J. Inorg. Chem. 2005(23) (2005) 4829-4833.

[388] K. Miyoshi, H. Tanaka, E. Kimura, S. Tsuboyama, S. Murata, H. Shimizu, K. Ishizu, Electrochemical and spectroscopic studies on copper(II) complexes of macrocyclic ligands as models for square-pyramidal metal active sites of copper(II) complexes of bleomycin and glutathione, Inorganica Chim. Acta 78 (1983) 23-30.

[389] M.H. Robbins, R.S. Drago, Activation of hydrogen peroxide for oxidation by copper(II) complexes, J. Catal. 170(2) (1997) 295-303.

[390] T.Y. Lin, C.H. Wu, Activation of hydrogen peroxide in copper(II)/amino acid/H2O2 systems: effects of pH and copper speciation, J. Catal. 232(1) (2005) 117-126.

[391] J. Li, A.N. Pham, R. Dai, Z. Wang, T.D. Waite, Recent advances in Cu-Fenton systems for the treatment of industrial wastewaters: Role of Cu complexes and Cu composites, J. Hazard. Mater. 392 (2020) 122261.

[392] H. Sigel, C. Flierl, R. Griesser, Metal ions and hydrogen peroxide. XX. On the kinetics and mechanism of the decomposition of hydrogen peroxide, catalyzed by the Cu2+-2,2'-bipyridyl complex, J. Am. Chem. Soc. 91(5) (1969) 1061-1064.

[393] G. Lente, Common Pitfalls, Deterministic Kinetics in Chemistry and Systems Biology: The Dynamics of Complex Reaction Networks, Springer International Publishing, Cham, 2015, pp. 111-129.

[394] R. Valenzuela, D. Contreras, C. Oviedo, J. Freer, J. Rodriguez, Copper catechol-driven Fenton reactions and their potential role in wood degradation, Int. Biodeter. Biodegr. 61(4) (2008) 345-350.

[395] R. Diószegi, D. Bonczidai-Kelemen, A.C. Bényei, N.V. May, I. Fábián, N. Lihi, Copper(II) Complexes of Pyridine-2,6-dicarboxamide Ligands with High SOD Activity, Inorg. Chem. 61(4) (2022) 2319-2332.

[396] Á. Martínez-Camarena, A. Liberato, E. Delgado-Pinar, A.G. Algarra, J. Pitarch-Jarque, J.M. Llinares, M.Á. Mañez, A. Domenech-Carbó, M.G. Basallote, E. García-España, Coordination Chemistry of Cu2+ Complexes of Small N-Alkylated Tetra-azacyclophanes with SOD Activity, Inorg. Chem. 57(17) (2018) 10961-10973.

[397] Z. Somosi, N.V. May, D. Sebők, I. Pálinkó, I. Szilágyi, Catalytic antioxidant nanocomposites based on sequential adsorption of redox active metal complexes and polyelectrolytes on nanoclay particles, Dalton Trans. 50(7) (2021) 2426-2435.

[398] A. Forgács, Z. Balogh, M. Andrási, A. Len, Z. Dudás, N.V. May, P. Herman, L. Juhász, I. Fábián, N. Lihi, J. Kalmár, Mechanistic explanation for differences between catalytic activities of dissolved and aerogel immobilized Cu(II) cyclen, Appl. Surf. Sci. 579 (2022) 152210.

ACKNOWLEDGEMENTS

I would like to express my sincere gratitude to all my co-authors and students with whom I have had the privilege to collaborate and cooperate on our scientific problems, projects and publications. Your insights, dedication, guidance, humor and joy have been invaluable. Working together has been inspiring and rewarding. I am grateful for your ideas and support.

MENTORS

Prof. István Bányai

Prof. István Fábián

Prof. Gábor Lente

THE RESEARCH TEAM (2020-2025)

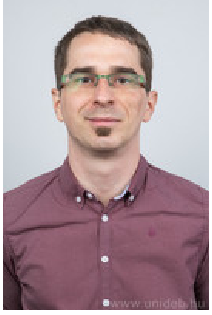

Dr. Attila Forgács
assistant prof.

Dr. Petra Herman
assistant prof.

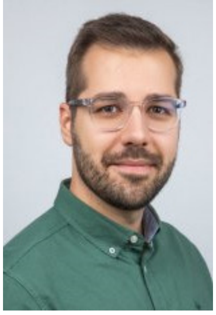

Dr. Krisztián Moldován
Ph.D. student

Dr. Zoltán Balogh
Ph.D. student

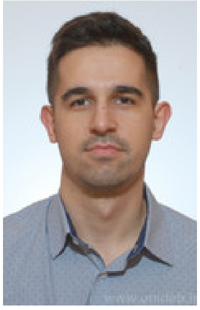

Dániel Pércsi
Ph.D. student

Marcell Tátrai
M.Sc. student

Balázs Bukta
M.Sc. student

Bertold Ecsédi
M.Sc. student

COLLABORATION PARTNERS IN HUNGARY

PHYSICS – SEM, XPS, XRD (UD and ATOMKI)

Prof. Csaba Cserháti

Dr. Tamás Fodor

Dr. Laura Juhász

Dr. Attila Csík

COORDINATION CHEMISTRY

Dr. Norbert Lihi

BIOLOGY AND PHARMACY

Dr. Gábor Király

Dr. Gábor Szemán-Nagy

CHEMICAL ENGINEERING

Dr. Péter Veres

NEUTRON SCATTERING (HUN-REN EK)

Dr. Adél Len

Dr. Zoltán Dudás

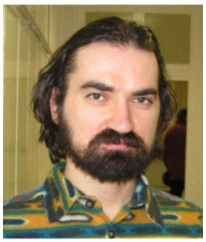

Dr. László Almásy

EPR (HUN-REN TTK)

Dr. Nóra May

Additional collaboration partners at UD

- **László István Orosz**
- **Dr. Gergő Vecsei**
- **Dr. István Csarnovics**
- **Prof. Zoltán Erdélyi**
- **Dr. István Lázár**
- **Dr. Mónika Kéri**
- **Dr. Vanda Papp**
- **Prof. Sándor Kéki**
- **Dr. Bernadett Biri**

INTERNATIONAL PARTNERS

Prof. Barbara Milow
German Aerospace Center, GERMANY

Prof. Ameya Rege
University of Twente NETHERLANDS

Prof. Pavel Gurikov
Hamburg University of Technology, GERMANY

Prof. C. A. García-González
Univ. Santiago de Compostela, SPAIN

Prof. Zoran Novak
University of Maribor, SLOVENIA

Prof. P. Paraskevopoulou
National Kapodistrian Univ. Athens, GREECE

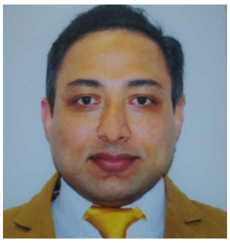

Prof. Geo Paul
Amedeo Avogadro University, ITALY

Prof. Jakub M. Gac
Warsaw University of Technology, POLAND

Prof. Cedric J. Gommes
University of Liège BELGIUM

PROJECTS & GRANTS

- **HUN-REN**
- **NKFIH: OTKA, NKKP**
- **GINOP**
- **EU HORIZON**
- **OPUS / DFG**
- **MTA Bolyai**
- **EU COST**

MAGYAR TUDOMÁNYOS AKADÉMIA · 1825 ·

EUROPEAN UNION
HORIZON EUROPE
#HorizonEU

AERoGELS
COST ACTION CA18125
environment | medicine | biotech | industry | academia

EKÖP
Egyetemi Kutatói Ösztöndíj Program

ÚNKP
Új Nemzeti Kiválóság Program

NATIONAL RESEARCH, DEVELOPMENT AND INNOVATION OFFICE
HUNGARY

PROGRAM FINANCED FROM THE NRDI FUND
MOMENTUM OF INNOVATION

NARODOWE CENTRUM NAUKI
Opus

DFG
Deutsche Forschungsgemeinschaft

SZÉCHENYI 2020
HUNGARIAN GOVERNMENT
European Union
European Regional Development Fund
INVESTING IN YOUR FUTURE

This research has been financially supported by following grants, scholarships and projects.

- National Research, Development and Innovation Fund of the Ministry of Culture and Innovation, Hungary: National Research, Development and Innovation Office (NKFIH) grants NKKP SNN_150561 and OTKA FK_17-124571.

- University of Debrecen Scientific Research Bridging Fund (DETKA), internal fund RH/751/2015 and University of Debrecen Program for Scientific Publication.

- János Bolyai Research Scholarship of the Hungarian Academy of Sciences (MTA).

- New National Excellence Program (ÚNKP) of the Ministry for Culture and Innovation of Hungary.

- The research was supported by the EU and co-financed by the European Regional Development Fund under Project GINOP-2.3.2-15-2016-00008 and project ENVIKUT (TÁMOP-4.2.2.A-11/1/KONV-2012-0043).

- HUN-REN-DE Mechanisms of Complex Homogeneous and Heterogeneous Chemical Reactions Research Group

I would like to express my deepest gratitude and love to my closest family – Betti, Mesi, Vili, Matyi – for their endless love, patience, and encouragement throughout my professional journey. Your belief in me, even during the most challenging moments, has been my greatest source of comfort and strength. Thank you for your understanding, sacrifices, and unwavering support. I could not have reached this point without you.